STATUS OF THESIS

Title of thesis: SYNTHESIS, CHARACTERIZATION AND ACTIVITY PATTERN OF CNFs-SUPPORTED Cu/ZrO_2 CATALYSTS FOR CO_2 HYDROGENATION TO METHANOL

I ISRAF UD DIN

hereby allow my thesis to be placed at the Information Resource Center (IRC) of Universiti Teknologi PETRONAS (UTP) with the following conditions:

1. The thesis becomes the property of UTP

2. The IRC of UTP may make copies of the thesis for academic purposes only.

3. This thesis is classified as

   ☐ Confidential

   ☑ Non-confidential

If this thesis is confidential, please state the reason:

The contents of the thesis will remain confidential for ______ years.

Remarks on disclosure:

Signature of Author

Permanent address: District Kohat
Tehsil Lachi Village & Post Office
Khader Khel, KPK, Pakistan

Date : 16/04/2015

Endorsed by

Signature of Supervisor

DR. MAIZATUL SHIMA SHAHARUN
Senior Lecturer
Fundamental & Applied Sciences Department
Universiti Teknologi PETRONAS PERAK

Dr. Maizatul Shima Shaharun

Date : 17/4/2015

UNIVERSITI TEKNOLOGI PETRONAS

SYNTHESIS, CHARACTERIZATION AND ACTIVITY PATTERN OF CNFs-SUPPORTED Cu/ZrO_2 CATALYSTS FOR CO_2 HYDROGENATION TO METHANOL

by

ISRAF UD DIN

The undersigned certify that they have read, and recommend to the Postgraduate Studies Programme for acceptance this thesis for the fulfillment of the requirements for the degree stated.

Signature:

DR. MAIZATUL SHIMA SHAHARUN
Senior Lecturer
Fundamental & Applied Sciences Department
Universiti Teknologi PETRONAS PERAK

Main Supervisor: Dr. Maizatul Shima Shaharun

Signature:

Professor Dr D Subbarao
Chemical Engineering Department
Universiti Teknologi PETRONAS

Co-Supervisor: Professor Dr. Duvvuri Subarao

Signature:

Dr Hanita Bt Daud
Head of Department
Department of Fundamental and Applied Sciences
Universiti Teknologi PETRONAS

Head of Department: Dr. Hanita Daud

Date: 13-04-2015

SYNTHESIS, CHARACTERIZATION AND ACTIVITY PATTERN OF CNFs-SUPPORTED Cu/ZrO_2 CATALYSTS FOR CO_2 HYDROGENATION TO METHANOL

by

ISRAF UD DIN

A Thesis
Submitted to the Postgraduate Studies Programme
as a Requirement for the Degree of

DOCTOR OF PHILOSOPHY
SCIENCE
UNIVERSITI TEKNOLOGI PETRONAS
BANDAR SERI ISKANDAR,
PERAK

APRIL 2015

DECLARATION OF THESIS

Title of thesis	SYNTHESIS, CHARACTERIZATION AND ACTIVITY PATTERN OF CNFs-SUPPORTED Cu/ZrO_2 CATALYSTS FOR CO_2 HYDROGENATION TO METHANOL

I ISRAF UD DIN

hereby declare that the thesis is based on my original work except for quotations and citations which have been duly acknowledged. I also declare that it has not been previously or concurrently submitted for any other degree at UTP or other institutions.

Witnessed by

Signature of Author

Permanent address: District Kohat
Tehsil Lachi Village & Post Office
Khader Khel, KPK, Pakistan

Date : 13-04-2015

Signature of Supervisor

DR. MAIZATUL SHIMA SHAHARUN
Senior Lecturer
Fundamental & Applied Sciences Department
Universiti Teknologi PETRONAS PERAK

Name of Supervisor
Dr. Maizatul Shima Shaharun

Date : 13-04-2015

DEDICATION

Dedicated to my beloved family

ACKNOWLEDGEMENTS

"**Read!** In the name of your Rabb (Only God and Sustainer) Cherisher, Who created — created man, out of a leech-like clot: **Read!** And your Rabb is Most Bountiful. He who taught (the use of) the Pen, taught man that which he knew not." (Qur'an 96:1-4)

I owe my profound thanks and deepest sense of gratitude to Allah S.W.T., who blessed me with potential and capability to carry out this work.

I would like to express vehement sense of thankfulness to my supervisor Dr. Maizatul Shima Shaharun for her kind guidance and invaluable support during the course of my Ph.D. studies. I am very grateful to my supervisor to give me an opportunity to undertake my Ph.D. research and help me to overcome all the hardships during the period of my studies.

I am thankful to my co-supervisor Dr. Duvvuri Subarao and field supervisor Dr. Abdul Naeem Khan for their immense help and support. Besides, I am also thankful to Salina Shaharun for Malay translation of my thesis abstract.

Lastly, I would like to express my great appreciation to Universiti Teknologi PETRONAS for providing the opportunity to study PhD. Program. Special thanks to staff of Fundamental and Applied Sciences Department, PG Office and all concerned laboratory technicians for providing me all the facilities to complete my work. Special thanks to Ministry of Higher Education Malaysia, FRGS No: FRGS/1/2011/SG/UTP/02/13 for providing financial support for this work.

ABSTRACT

~~In this work,~~ ~~a~~ A series of novel carbon nanofibers supported copper-zirconia [Cu/ZrO_2/CNFs-O (CZC)] catalysts were synthesized to investigate hydrogenation of CO_2 to methanol in a three phase reactor at a low~~er~~ pressure of 20 to 50 bar and temperature of 180 to 240 °C. The physicochemical characterizations of synthesized catalysts were studied by X-ray diffraction (XRD), inductively coupled plasma optical emission spectroscopy (ICP-OES), N_2 adsorption–desorption, N_2O chemisorption, high resolution transmission electron microscopy (HRTEM), temperature programmed reduction (TPR), X-ray photoelectron spectroscopy (XPS) and temperature programmed desorption (CO_2 & NH_3). The effects of temperature, total pressure and feed gas ratio on the methanol synthesis rate were also investigated. A highest methanol yield of 57 g/kg.cat.h and 12% CO_2 conversion were recorded at a reaction temperature of 220 °C and total pressure of 40 bar with catalyst active components composition of 15, 15 and 3 wt.% of Cu, ZrO_2 and ZnO, respectively. ~~With~~ For the reaction time of two hours, this catalytic system can be considered as a ~~reactive~~ active catalyst system. for CO_2 hydrogenation to methanol.

catalyst performance

The results showed that the methanol synthesis rate increased from 8 to 20 g/kg.cat.h with increasing Cu concentration from 5 to 15 wt.%, and was adversely affected with further Cu loadings. This could be attributed to the fact that the surface area of both the catalyst and Cu ~~were~~ increased significantly as the Cu contents ~~were~~ increased, and optimum values of 133 and 13.1 m^2/g, respectively were recorded for CZC catalyst with 15 wt.% Cu. Moreover, catalyst with 15 wt. % Cu exhibited sufficient number of catalytic active basic sites which played a key role in converting CO_2 to methanol. The effect of second active sites concentration was also investigated by modifying the 15 wt. % Cu/CNFs catalyst with varying concentration of ZrO_2 (5–25 wt.%). It was observed that BET surface area increased significantly from 130 to 152 m^2/g by increasing the ZrO_2 concentration from 5 to 15 wt.%, however it was less affected by further ZrO_2 loadings. Similarly, TPR investigations revealed a remarkable

increase from 18 to 68 % in a fraction of dispersed Cu by increasing ZrO_2 concentration from 5 to 15 wt.%. The reaction studies showed that methanol synthesis rate was further enhanced when zirconia was incorporated into Cu/CNFs catalyst and highest magnitude of 25 g/kg.cat.h was observed for 15 wt.% ZrO_2 loading. This trend could be attributed to the maximum number of active basic sites, high BET surface area and high fraction of dispersed Cu on the surface of the support. Furthermore, it was noted that BET surface area and fraction of dispersed copper were increased from 109 to 155 m^2/g and 59 to 71 %, respectively when the calcination temperature was increased from 350 to 450 °C. Similarly, rate of methanol formation was also observed to enhanced from 27 to 34 g/kg.cat.h when calcination temperature was raised from 350 °C to 450 °C. The characterization data and activity studies identified 450 °C as the optimum calcination temperature.

Different promoters such as Nb_2O_5 and ZnO were doped into $Cu/ZrO_2/CNFs$ catalyst to examine their effect on the catalyst structure and catalytic behavior. The results showed that 3 wt.% of ZnO significantly improved the methanol synthesis rate from 34 to 45 g/kg.cat.h. The ZnO-doped catalyst further enhanced the Cu dispersion and BET area as compared to Nb_2O_5. The rate was found to be the first order with respect to CO_2 conversion. The kinetic data was correlated using artificial neuron network model and the accuracy of prediction was within 10 %.

The work done has established the potential utilization of carbon nanofibers as catalyst support for CO_2 hydrogenation to methanol. The experimental results obtained in this study were in good agreement with the artificial neuron network model. The work also concluded that the CNFs based $Cu/ZrO_2/ZnO$ catalyst can be used to produce methanol at lower operating temperature and pressure.

ABSTRAK

Dalam tugasan ini, satu siri novel pemangkin karbon nanofiber disokong kuprum-zirkonia [Cu/ZrO_2/CNFs(CZC)] telah disintesis untuk mengkaji penghidrogenan CO_2 kepada methanol, dalam reaktor 3 fasa pada tekanan rendah iaitu 20 hingga 50 bar and suhu 180 hingga 240°C. Pencirian fizikokimia pemangkin yang telah disintesiskan dikaji melalui pembiasan sinar-X (XRD), spektroskopi sinaran optik plasma induktif (ICP-OES), penjerapan–nyahjerapan N_2, jerapankimia N_2O, mikroskopi transmisi elektron beresolusi tinggi (HRTEM), program pengurangan suhu (TPR), spektroskopi fotoelektron sinar-X (XPS) dan program suhu penjerapan (CO_2 & NH_3). Kesan terhadap suhu, jumlah tekanan dan nisbah gas suapan terhadap kadar sintesis metanol juga dikaji. Penghasilan metanol tertinggi untuk 57 g/kg.pemangkin.jam dan perubahan 12% CO_2 telah direkodkan pada suhu tindak balas 220°C dan jumlah tekanan 40 bar, dengan komponen pemangkin aktif berkomposisi 15,15 dan 3%berat Cu, Zr_2O dan ZnO masing-masing. ~~Dengan~~ Dalam masa tindak balas selama 2 jam, sistem pemangkinan ini boleh dianggap sebagai sistem mangkin yang reaktif. terhadap penghidrogenan CO_2 prestasi pemangkinan kepada metanol.

Keputusan menunjukkan kadar sintesis metanol meningkat dari 8 hingga 20g/kg.pemangkin.jam dengan peningkatan ~~kepekatan~~ muatan Cu dari 5 hingga 15%berat dan tidak memberi kesan lagi terhadap penambahlebihan Cu. Ini telah ditentukan oleh fakta di mana luas permukaan untuk kedua-duanya iaitu pemangkin dan Cu meningkat secara signifikan apabila kandungan Cu meningkat, dan nilai optimum telah direkodkan untuk pemangkin CZC dengan 15% berat Cu iaitu 133 dan 13.1 m^2/g, masing-masing. Tambahan, pemangkin dengan 15%berat Cu mempamerkan nilai tapak aktif asas pemangkinan secukupnya yang memainkan peranan penting dalam pertukaran CO_2 kepada metanol. Kesan ke atas kepekatan bahagian aktif kedua juga dikaji melalui pengubahsuaian pemangkin Cu/CNFs 15%berat dengan megubah kepekatan ZrO_2 (5-25%berat). Didapati bahawa luas permukaan BET meningkat secara signifikan daripada 130 hingga 152 m^2/g dengan peningkatan kepekatan ZrO_2 dari 5 hingga

15%berat, walaubagaimanapun ia hanya memberi sedikit kesan terhadap penambahlebihan ZrO_2 yang seterusnya. Dalam kajian TPR juga, menunjukkan satu peningkatan yang luarbiasa bagi pecahan serakan Cu iaitu dari 18 hingga 68% bagi peningkatan kepekatan ZrO_2 dari 5 hingga 15%berat. Kajian tindakbalas menunjukkan kadar sintesis metanol terus meningkat apabila zirconia digabungkan dengan pemangkin Cu/CNFs dan magnitud tertinggi untuk 25 g/kg.pemangkin.jam telah diperhatikan untuk penambahan 15%berat ZrO_2. Trend ini disumbangkan oleh bilangan maksimum tapak aktif alkali, luas permukaan BET yang tinggi dan pecahan serakan Cu atas permukaan sokongan. Tambahan lagi, didapati bahawa luas permukaan BET dan pecahan serakan Cu meningkat dari 109 hingga 155 m^2/g dan 59 hingga 71%, masing-masing apabila suhu pengkalsinan meningkat dari 350 hingga 450°C. Kadar penghasilan metanol juga dikaji untuk peningkatan dari 27 hingga 34 g/kg.pemangkin.jam apabila suhu pengkalsinan ditingkatkan dari 350°C hingga 450°C. Data pencirian dan kajian aktiviti telah mengenalpasti bahawa 450°C sebagai suhu pengkalsinan optimum.

Penggalak yang berbeza seperti Nb_2O_5 and ZnO telah didopkan ke dalam pemangkin $Cu/ZrO_2/CNFs$ untuk mengkaji kesan ke atas struktur pemangkin dan sifat pemangkinan. Keputusan menunjukkan bahawa 3%berat ZnO adalah mencukupi untuk membaikpulih kadar sintesis methanol dari 34 hingga 45 g/kg.pemangkin.jam. Pemangkin ZnO-dop dapat meningkatkan lagi serakan Cu dan luas permukaan BET berbanding dengan Nb_2O_5. Tertib kadar yang didapati bagi pertukaran CO_2 adalah tertib pertama. Data kinetik telah dikolerasi menggunakan model rangkaian neuron ciptaan dan kecekapan ramalan adalah dalam lingkungan 10%.

Kajian ini telah membuka potensi dalam penggunaan karbon nanofiber sebagai sokongan pemangkin untuk penghidrogenan CO_2 kepada metanol. Keputusan eksperimen yang didapati dalam kajian ini, adalah seiring dengan model rangkaian neuron ciptaan. Kajian ini menyimpulkan bahawa pemangkin $Cu/ZrO_2/ZnO$ bertapak CNFs boleh digunakan untuk menghasilkan metanol pada suhu dan tekanan operasi rendah.

TABLE OF CONTENT

LIST OF FIGURES

LIST OF TABLES

CHAPTER 1

INTRODUCTION

1.1 Methanol synthesis technologies

Currently methanol is exclusively synthesized on commercial basis from mixture of syngas (CO + H_2) and CO_2. The overall reactions of methanol synthesis by this route is given in reaction 1.1:

$$CO + 2H_2 \rightleftharpoons CH_3OH \qquad \Delta H^0{}_{298K} = -90.84 \quad kJ/mol \qquad (1.1)$$

For methanol synthesis, syngas is obtained from many carbonaceous sources like, coal, coke, heavy oils, petroleum, asphalt and natural gas. However, natural gas due to low cost, less impurities and higher content of H_2 is generally preferred over other sources. Syngas is produced by steam reforming of natural gas. The CO generated is reacted with more steam to produce some CO_2. In this way mixture of CO, H_2 and CO_2 is produced for methanol synthesis [1]. Industrially methanol synthesis by this route is carried at 220-300 °C and 5-10 MPa reaction temperature and pressure, respectively over Cu-ZnO/Al_2O_3 catalyst [2-4]. However, it is believed that methanol formation takes place mainly from CO_2, whereas CO acts as scavenger of surface oxygen [5-7].

Beside this traditional route, methanol can also be synthesized by pure CO_2 hydrogenation. Methanol synthesis by CO_2 hydrogenation is given in reaction 1.2.

$$CO_2 + 3H_2 \rightleftharpoons CH_3OH + H_2O \qquad \Delta H^0{}_{298K} = -49.5 \quad kJ/mol \qquad (1.2)$$

CO_2 hydrogenation to methanol is an exothermic process, therefore the reaction is thermodynamically favorable at low temperature. However, methanol can be produced via CO_2 hydrogenation with carbon utilization and reaction rate comparable to that of syngas route [8-10]. Likewise the role of CO_2 in methanol synthesis can also justified by the reported data where methanol was reported to be obtained exclusively from CO_2 hydrogenation over $Cu/ZnO/Al_2O_3$ catalyst. This was further supported by radioactively labeled carbon dioxide isotopes studies. More importantly, no methanol formation was observed by using a pure CO/H_2 mixture over Cu/ZnO and $Cu/ZnO/Al_2O$ catalysts [11]. Similarly, due to environmental impact, methanol synthesis by CO_2 received more attention than traditional syngas route [12]. In liquid phase hydrogenation, carbon dioxide is preferred reactant gas over carbon monoxide because the rate of hydrogenation of CO_2 is faster compared to CO [13]. Furthermore, methanol formation from atmospheric carbon dioxide hydrogenation has been declared as most economical after gas and oil [14, 15]. Recently, it has been reported that global surface temperature would remain almost constant for many centuries provided that CO_2 emissions are ceased [16-19]. Keeping in view the thermodynamic stability of CO_2, hydrogenation of CO_2 has been less investigated as compared to CO hydrogenation. CO hydrogenation to methanol is generally studied over $Cu\text{-}ZnO/Al_2O_3$ catalyst [2-4]. Nevertheless, application of this current methanol synthesis catalyst $CuO/ZnO/Al_2O_3$ does not look promising for CO_2 hydrogenation. This is because of the production of CO as a sequence of parallel reverse water gas shift reaction (RWGS) observed with CO_2 hydrogenation to methanol. Similarly, water formation during CO_2 hydrogenation lowers the activity profile of alumina based catalysts [2, 20, 21]. This triggered the investigations of new catalysts that are capable of producing methanol by CO_2 hydrogenation with enhanced activity and selectivity.

1.2 Methanol synthesis catalysts

Alumina based methanol synthesis catalysts have been extensively studied. Fujimoto et al. [22] investigated $Cu/ZnO/Al_2O_3$ for CO_2 hydrogenation to methanol. They reported greater activity and stability of the catalyst owing to stabilization of zero valent form of copper. However, due to poor performance of $Cu/ZnO/Al_2O_3$ catalysts, effective conversion of CO_2 to methanol has not been achieved [23, 24]. Moreover, CO_2 hydrogenation was depressed by strong hydrophilic character of Al_2O_3 [25-27]. Similarly, water formation during CO_2 hydrogenation lowers activity of alumina based catalysts. A gradual decrease of methanol yield from 8.1 % at 1 h to 4.4 % at 100 h was observed for alumina based Cu/ZnO catalyst [28]. This suggests the lower stability of alumina based catalyst for longer duration of reaction time.

Silica due to higher thermal stability and greater dispersion capacity has been extensively investigated as catalyst support for methanol production from CO_2 and H_2. Sugawa et al in 1995 investigated different active metals namely Cu, Ni, Co, Fe, Ag, Ru, Pt, Pd, Au, Rh, Ir, Os and Re supported on silica [29]. Activity studies were conducted at reaction conditions of 250 ^{0}C temperature, 5 MPa pressure and H_2/CO_2 ratio of 3. The study revealed higher selectivity of methane for Ni, Co, Rh, Os, and Rh based silica catalyst. On the other hand, Pt/SiO_2 showed higher selectivity towards CO formation. Only Cu/SiO_2, Ag/SiO_2, Pd/SiO_2 and Fe/SiO_2 were found with higher selectivity to methanol synthesis. Similarly, owing to higher surface area, the silica based catalysts showed higher activity and better selectivity for methanol production as compared to ZnO-based counterparts [30]. Nevertheless, despite the high surface area silica has been documented to be transformed to $Si(OH)_2$ in presence of steam at higher temperature which led to low thermal stability [31].

1.3 Potential new catalyst support: Carbon nanofibers

Carbon nanofibers (CNFs) were discovered in the last two decades [32]. CNFs have excellent potential as catalyst support because of their special physiochemical characteristics, tuneable and controllable texture [33, 34]. Furthermore, CNFs being pure, chemically inert and mechanically strong surpass other oxides catalyst supports like silica and alumina [35]. Moreover, in liquid phase reactions mass transfer plays a major role in determining the performance of the catalyst. As illustrated in Figure 1.1, CNFs due to the higher porosity and lower tortuosity will reduce mass transfer limitations [36]. Additionally, absence of micro pores in CNFs also mitigates the problem of mass transfer. CNFs being a combination of both active carbon and stable graphite, are considered as excellent contender as catalyst support. Moreover, the appreciable stability of carbon materials in acidic as well as basic conditions makes CNFs as suitable candidate for catalysts support. High external surface area and special morphology of CNFs allow rapid access of reactant molecules to the active metal sites.

Similarly, complete absence of bottled pores in CNFs, empowers 3D approach of the reactants to the entire volume of catalyst. Furthermore, CNFs due to higher thermal conductivity, efficiently remove heat generated during the reaction [37]. Likewise, Ledoux et al. [38] reported that greater thermal conductibility of CNFs enabled a rapid evacuation of heat generated during the course of reaction. This additional ability of CNFs will further support their application as catalyst support in exothermic reactions. Consequently, CNFs based catalysts showed better activity and selectivity as compared to traditional supported based catalysts [39].

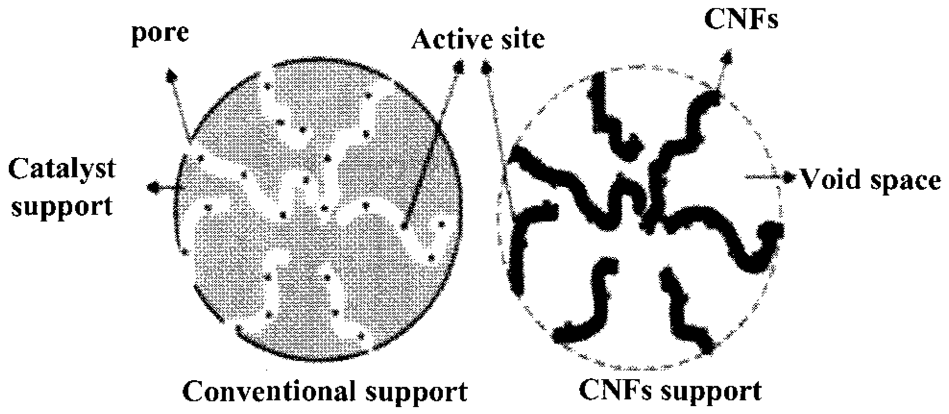

Figure 1.1: CNFs vs Conventional support [36]

In conclusion, combination of all these properties makes CNFs as competitive and attractive support in catalysis. This was also enforced by reactions studies where CNFs supported catalysts showed higher activities and selectivity as compared to the catalysts based on conventional supports [33, 40-43].

1.4 Reactor aspects

The following types of reactors have been utilized for methanol synthesis process in the literature.

1.4.1 Fixed-bed tubular reactors

CO_2 hydrogenation to methanol is extensively studied in fixed-bed type reactors. However, heat generated during reaction lowers activity and selectivity in such kind of reactors [44]. To overcome this problem, Rahimpour et al. [45] introduced two-stage bed reactor. This reactor is equipped with two beds with the first bed operated at higher temperature where synthesis gas was partly converted to methanol and in the second catalysts bed feed gas was pre-heated with heat generated at first bed. Consequently, the activity profile as well as lifetime of catalysts were improved in this modified bed reactors.

1.4.2 Membrane reactor

To overcome the limitations of fixed-bed reactors, Rahimpour et al. [46] in 2009 introduced dual type membrane reactor. In such kind of reactor, the reaction tube is shielded by palladium–silver membrane, which allows selective penetration of H_2 only. In this reactor system, partial pressure of H_2 is the driving force for penetration of hydrogen from feed gas to the reaction tube. A comparative study of the CO_2 hydrogenation to methanol in dual-type membrane reactor and conventional dual-type methanol reactor concluded that dual-type membrane reactor due to favorable temperature profile exhibited better activity and longer catalysts life as compared to conventional dual-type methanol reactor [46]. Similarly, simulation studied on the title reaction reported higher conversion of CO_2 in membrane reactor as compared to conventional bed reactor [47]. Likewise, Chen et al. [48] simulated the title reaction and concluded that conversion of CO_2 was ~~incremented~~ increased by 22 % when reaction was conducted in membrane reactor as compared to conventional bed reactor. Furthermore, membrane reactors are reported with increased selectivity of methanol from CO_2 hydrogenation than conventional bed reactors [49, 50]. However, the major limitation of membrane type reactor is its application in temperature range below 200 °C [47]. Similarly, because of the thermodynamic limitation, the economic efficiency of the current gas phase methanol synthesis is ~~unsatisfied~~ unsatisfactory [51].

1.4.3 Slurry reactor

To overcome thermodynamics limitations of the title reaction, liquid phase methanol synthesis technology was introduced in late 1970s by Chem Systems as LPMeOHTM technology [52]. Since then, this new low temperature methanol synthesis was intensively investigated [53]. Liquid phase methanol synthesis, due to higher heat transfer efficiency, excellent thermodynamic conditions, higher conversion of CO_2 and low operation cost is preferred over gas phase methanol process [51, 52, 54-56]. Different alcohol based reaction solvents were used by Zeng et al. [57] for liquid phase methanol synthesis. In their study, highest activity for methanol formation was recorded with ethanol as reaction solvent. The advantages of slurry reactor versus conventional fixed-bed reactor are provided in Table 1.1.

Table 1.1: Slurry reactors versus conventional fixed-bed reactors [58].

Features	**Slurry reactor**	**Fixed-bed reactor**
Overall reaction rate related to the catalyst mass	High	Low
Pressure	Low/Medium	Low/Medium/High
Operating costs	Low	High
Probability of runaways in exothermic Reactions	Low	Extremely high
Special measures against possible runaways in exothermic reactions	Not necessary	Nearly always necessary

1.5 Problem statement

Although, methanol synthesis by syngas has recorded good progress since its invention by BASF in 1923, however, no ultimate progress has been made to produce methanol by CO_2 hydrogenation at industrial level. Methanol synthesis by syngas is carried out over $CuO/ZnO/Al_2O_3$ catalyst. Nevertheless, application of this current methanol synthesis catalyst does not look promising for hydrogenation of pure CO_2

[59-63]. This is due to the production of CO as a sequence of parallel reverse water gas shift reaction (RWGS) observed with CO_2 hydrogenation to methanol. Similarly, since CO_2 hydrogenation to methanol is associated with water formation. Therefore, alumina-based catalysts have shown lower activities for CO_2 hydrogenation to methanol [8, 62, 64]. Furthermore, as the mechanistic understandings of the CO_2 hydrogenation to methanol are not yet well ~~comprehended so~~, understood, thus the knowledge of an appropriate catalyst designing is lacking. This is another reason why exploitation of a proper catalyst is not yet satisfactory. Similarly, supports of current methanol synthesis catalysts have drawbacks like low mechanical strength, poor thermal stability, toxicity and short life time [65, 66]. For instance, silica although having higher surface area but it has been documented to transform to $Si(OH)_2$ in presence of steam at higher temperature reported with low thermal stability [31]. Moreover, conventional supports like SiO_2, Al_2O_3 and TiO_2 are difficult to be reduced due to formation of the mixed metal-support oxides [67]. In addition, metal oxide supports face sintering problem at higher temperature during reduction which leads to reduce dispersion of active sites [68]. The above mentioned drawbacks led to lower activity and stability of methanol synthesis by CO_2 hydrogenation route. This whole scenario triggered the investigations of a new catalyst that is capable of producing methanol by CO_2 hydrogenation with enhanced activity and selectivity.

1.6 Research objectives

The aim of this work is to synthesize and evaluate CNFs based Cu/ZrO_2 catalyst for liquid phase methanol synthesis by hydrogenation of carbon dioxide using a slurry reactor. A number of experiments will be conducted to achieve best loadings of copper and zirconia components in terms of methanol production. The catalyst with best loadings of catalyst components will be tested at different calcinations temperature to obtain the most thermally stable and active catalyst. The optimized catalyst in terms of active metal loadings and calcination temperature will be selected for study of different promoters (Nb_2O_5 and ZnO) in the CO_2 hydrogenation to methanol. Finally the screened catalyst will be tested for kinetics study of CO_2 hydrogenation to methanol. Hydrogenation of CO_2 to methanol will also be optimized in terms of reaction conditions like reaction temperature, total pressure and feed gas ratio. The research objectives are summarized as below.

1. To synthesize CNFs based Cu/ZrO_2 catalyst by deposition precipitation method
2. To characterize the physiochemical properties of synthesized catalyst by different techniques
3. To optimize the catalyst for CO_2 hydrogenation to methanol in slurry reactor in terms of concentration of both active components (Cu and ZrO_2) as well as catalyst promoters like Nb_2O_5 and ZnO
4. To investigate kinetics of CO_2 hydrogenation over optimized CNFs based Cu/ZrO_2 catalyst

1.7 Research hypothesis

To address the above problems in methanol synthesis, our research is based on following hypothesis.

1. CNFs due to absence of bottles pores will provide 3D exposure of active sites to the reacting molecules. This will increase the reactivity of the catalyst
2. Higher mechanical properties (strength of 1.5 MPa) associated with CNFs will enable its application in bulk phase industrial applications
3. Due to exothermic nature of title reaction, methanol synthesis will be more favorable when it is carried out in liquid medium
4. Furthermore, mesoporus nature of CNFs will reduce the mass transfer limitation in liquid phase methanol synthesis

1.8 Scope of research

In the current work, herringbone type of carbon nanofibers GNF-100 produced by Carbon Nano-material Technology Co. Ltd. with diameter ranging from 50~100 nm having length of 10~30 um and specific surface area 100 ~ 300 m^2/g were used as catalyst support. CNFs based Cu/ZrO_2 catalysts were synthesized by deposition precipitation method. To study the effect of Cu loading, catalysts with 5, 10, 15, 20 and 25 wt.% Cu were prepared with fixed 10 wt.% loading of ZrO_2. After the optimum loading of Cu was achieved, catalysts with different loading of ZrO_2 (5, 10, 15, 20 and 25 wt.% ZrO_2) were prepared. To observe the effect of calcination temperature, optimized catalyst with respect to both active parts was calcined at different degree of calcinations temperatures 350, 450, 500 and 550 °C. Screened catalyst was incorporated with niobium and zinc oxide to investigate the influence of promoters.

In order to investigate physiochemical properties, catalysts were characterized by different analytical techniques. Composition of catalyst components was verified by inductively coupled plasma optical emission spectrometry (ICP-OES), phase identification of catalysts was performed by X-ray diffraction (XRD), functional groups were identified by Fourier transform infra-red spectroscopy (FT-IR), surface area and pore size were determined by N_2-physical adsorption (BET), surface chemistry of the catalyst components was investigated by X-ray photoelectron spectroscopy (XPS), morphology and particle size of catalyst particles were studied by transmission electron microscope (TEM), reduction behavior of catalysts was investigated by temperature program reduction (TPR), acidity and basicity of catalysts were studied by NH_3-TPD and CO_2-TPD respectively. Surface area and dispersion of metallic Cu was determined by N_2O chemisorption.

Activity of catalysts in CO_2 hydrogenation to methanol was evaluated in autoclave slurry reactor (Parr 4593 with a regulator Parr 4848). Ethanol was used as a reaction solvent. Activity of carbon nanofibers based Cu/ZrO_2 was evaluated at 180 °C and 30 bar reaction temperature and pressure, respectively. Kinetics study of the reaction was performed and the process was optimized in terms of operating parameters such as reaction temperature, pressure and feed gas ratio.

1.9 Organization of thesis

The dissertation has five chapters. Chapter 1 covers introduction and background of CO_2 hydrogenation to methanol. Chapter 2 describes literature review related to the current study. Chapter 3 covers the experiential and methodology sections of the current work. Chapter 4 describes the physiochemical study as well reactivity data of the title reaction. Chapter 5 describes the principal conclusion of the current work as well as recommendations for the future work.

CHAPTER 2

LITERATURE REVIEW

2.1 Synthesis of methanol

R.Dolye in 1661 discovered methanol for the first time by rectification of vinegar on lime milk [69]. At that time the new compound methanol, was named as adiphorus spiritus lignorum. The word methyl was first time introduced by Dumas and Leibig in 1835 when they established molecular identity of the compound as methanol. In well-established history, first successful synthesis of methanol was discovered by Berthelot in 1857 by dry distillation of wood. Hence, methanol was also called as wood spirit. Since then, investigations to produce methanol on commercial scale began by using different routes.

The first commercial methanol synthesis plant was constructed by BASF in 1923. In this process methanol was synthesized by syngas on zinc/chromia based catalyst with operating parameters of 300 bar pressure and temperature above 300 °C. This process of methanol production was prevailed for more than 40 years. However, thermodynamic limitations such as high temperature and pressure associated with this process led to the investigations of other techniques for synthesis of methanol. The high pressure limitation was mitigated by introducing highly active Cu/ZnO catalyst in 1960. This process was industrialized by Imperial Chemical Industries (ICI) and operated at pressure and temperature of 50-100 bar and 200-300 °C, respectively [11].

Currently, methanol has been produced industrially in gas phase from mixture of syngas and CO_2 over Cu-ZnO/Al_2O_3 catalyst at temperature and pressure of 220-300 °C and 5-10 MPa [15]. It is believed that methanol formation takes place mainly from CO_2, whereas CO acts as scavenger of surface oxygen [5-7]. However, due to the current environmental problems like global warming and demand for clean fuel, the usage of CO_2 as reactant gas instead of mixture of syngas and CO_2, has been extensively studied [70, 71]. Several ways like reduction of carbon dioxide emissions, CO_2 capture and storage and chemical transformation to valuable products were proposed to mitigate carbon dioxide. CO_2 hydrogenation to methanol is one of those chemical transformations which will not only mitigate this problem but will also produce environment-friendly methanol fuel.

Although CO_2 hydrogenation to methanol is not the ultimate solution to carbon conundrum, but still it is a feasible and economical way of CO_2 utilization. In 2005 Olah et al. [72, 73] introduced the concept of "Methanol Economy" where they proposed CO_2 recycling to methanol. Most recently in 2011 methanol production process was patented by Carbon Recycling International (CRI) company. CRI with joint adventure of Methanex Corporation constructed first ever plant of methanol synthesis by CO_2 hydrogenation at the Svartsengi geothermal power plant in Reykjanes Iceland. In this project hydrogen and carbon dioxide are utilized to produce methanol over copper–zinc oxide–alumina catalysts in temperature and pressure range of 220–250 °C and 10–30 bar, respectively. The present production capacity of the plant is 3500 tonnes/year which is planned to increase to 35000 per annum [71]. Similarly, Mitsui Chemicals of Japan has also constructed a pilot plant of CO_2 hydrogenation based methanol synthesis with production capacity of 100 tonnes per year [71].

2.2 Methanol synthesis strategies

Starting from destructive distillation of wood to the modern hydrogenation synthesis, a number of methods are applied for the synthesis of methanol. Similarly variety of feed stocks like wood, coal, forest and crop residue could be utilized to produce methanol. Here in this section some common methanol synthesis strategies will be discussed.

2.2.1 Methanol synthesis by syngas

Although methanol synthesis was originated from the destructive distillation of wood in 18th century, however the process did not sustain for longer period of time. Similarly other old methods like oxidation of hydrocarbons and synthol process also could not remain practical in industrial production of methanol. The effective hydrogenation of nitrogen to produce ammonia triggered the investigations of hydrogenating other molecules. A German scientist Matthias Pier working in BASF synthesized methanol from syngas for the first time.

Methanol synthesis by CO hydrogenation is given in Reaction 2.1 as below

$$CO + 2H_2 \rightleftharpoons CH_3OH \qquad \Delta H^0{}_{298K} = -90.84 \ \ kJ/mol \tag{2.1}$$

The negative value of ΔH^0 shows that reaction is exothermic in nature. Due to exothermic nature of reaction, CO hydrogenation is more favorable at lower reaction temperature. Similarly, standard Gibbs free energy (ΔG^0) is an important thermodynamic parameter which is applied to determine the spontaneity or non-spontaneity of the chemical reaction. Negative value of ΔG^0 for a particular reaction means that reaction is spontaneous and no external energy is required to carry out the reaction at a given temperature. Similarly positive value of ΔG indicates that reaction is non-spontaneous and reaction cannot be proceeded with any extra heat supply. In the case of CO hydrogenation to methanol, standard Gibbs free energy change (ΔG^0) (calculation are presented in brief in Appendix C (Table C1) resulted in negative value indicating the spontaneity of reaction. However, at higher temperature reaction becomes non-spontaneous with positive value of Gibbs free energy change as evident in Table 2.1. Generally in chemical reactions all reactants are not converted to products. In many cases reaction reaches a stage where concentrations of both reactants as well as products are present in equal concentration due to the equal rates of forward and backward reaction. This stage of reaction is termed as equilibrium state. Equilibrium constant (K) is another important thermodynamic parameter which is used to measure the extent of reactant conversion to products in equilibrium state. Hence, value of K point out the direction of the reaction at equilibrium condition. The higher the value of K, higher is the tendency of conversion of reactants to products. Reactants will be completely converted into products for reaction with K value greater than 10^5, similarly K lower than 10^{-5} shows zero conversion of reactants. In case of CO hydrogenation K >> 1 which indicates favorability of the reaction in forward direction and higher conversion of reactants to product. Impact of operating pressure is another important parameter for reaction in gas phase. As CO hydrogenation to methanol is mainly carried out in gas phase, study of change of operating pressure is essential. Effect of pressure is governed by Le Chartelier's principle which states that when a system in equilibrium is disturbed by any external change, the system will move in a direction to counteract the change. In the current case as evident from Reaction 2.1, the number of moles of reactants are higher than number of moles of product. So increase in pressure will shift the reactants to the product side. Thus CO hydrogenation to methanol is favorable at higher operating pressure. Thermodynamics data at two different temperature values are given in Table 2.1.

Table 2.1: Thermodynamic values of methanol synthesis reactions [69, 74]

Add . Equations to be clear

Equation	Thermodynamic values		
	T(C°)	ΔH° (kJ/mole)	ΔG° (kJ/mole)
2.1	25	-90.6	-25.3
	225	-97.9	+21.2
2.2	25	-49.5	+3.4
	225	-58.1	+41.5
2.3	25	+41.2	+28.6
	225	+39.8	+20.4

2.2.2 Methanol synthesis by bio gas

A flammable gas called biogas is produced by mammals, termites and some microorganisms during digestion of food. Similarly, biogas can also be obtained from wastes of microorganisms, accumulated rotten vegetation and animal manure. Biogas mainly composed of different ratios of 50–70 % methane and 30-40 % CO_2 and trace amount of H_2S. Currently, this gas is generally utilized for generation of heat and electricity. However, due to the presence of methane and CO_2 it is a potential candidate for producing methanol. Using biofuel technology, a methanol plant with methanol production capacity of 30000 L per day was planned in Utah by using manure of 250000 pigs [72]. Although methanol synthesis by this route is very cheap as compared to the current industrial process however, optimization of reactant gases for methanol synthesis is quite challenging due to different concentrations of CO_2 and methane in biogas obtained from various materials. Furthermore, in many cases syngas generated from biogas does not produce enough economical quantity of methanol without adding any H_2, and CO or combination of both gases [75].

2.2.3 Methanol synthesis by CO_2 hydrogenation

Methanol can be synthesized by CO_2 hydrogenation and detailed pathway of the reaction is given as below.

$$CO_2 + 3H_2 \rightleftharpoons CH_3OH + H_2O \qquad \Delta H^0{}_{298K} = -49.5 \ \ kJ/mol \qquad (2.2)$$

$$CO_2 + H_2 \rightleftharpoons CO + H_2O \qquad \Delta H^0{}_{298K} = +41.2 \ \ kJ/mol \qquad (2.3)$$

$$CH_3OH \rightleftharpoons CO + 2H_2 \qquad \Delta H^0{}_{298K} = +90.64 \ \ kJ/mol \qquad (2.4)$$

Like the previous reaction, CO_2 hydrogenation to methanol is also an exothermic reaction with negative ΔH^0 value (Reaction 2.2). Being an exothermic reaction, CO_2 hydrogenation to methanol will be best suited at lower temperature. However, unlike CO hydrogenation ΔG^0 value for CO_2 hydrogenation is positive at both lower and higher temperature, indicating that CO_2 hydrogenation is thermodynamically less favorable than CO hydrogenation. Similarly in case of methanol synthesis by CO_2 hydrogenation $K << 1$, implying that a lower conversion of reactants to products. Moreover, methanol synthesis by this route is also associated with reverse water gas shift reaction (RWGS) as shown in Reaction 2.3. In addition, methanol has also been reported to undergo decomposition at higher reaction temperature as given in Reaction 2.4. As a result of these two reactions an undesired CO is formed which can contribute to deactivation of methanol synthesis catalysts by this route. Furthermore, formation of water takes place during methanol synthesis as well as reverse water gas shift reaction. The formation of water during CO_2 hydrogenation is believed to be the one of main differences in two approaches. Nevertheless, formation of water during methanol synthesis is also reported to improve catalytic profile depending on the concentration of water [76].

However, despite all those thermodynamic limitations, in terms of kinetics CO_2 hydrogenation is faster than CO hydrogenation [59] . Furthermore, in the current industrial synthesis methanol is formed mainly by CO_2 hydrogenation and CO is believed to inhibit active sites of catalysts by acting as a scavenger to O_2 atoms from water [2, 3]. Comparative studies of CO and CO_2 hydrogenation revealed some facts that encourage the latter route. Although CO was believed to be the main source of carbon in the early days [77] however, isotope labeling experiment revealed that CO_2 is more preferentially hydrogenated to produce methanol [78, 79]. Similarly, Sahibzada et al. reported that intrinsic rate of methanol synthesis by CO_2 hydrogenation was 20 times faster as compared to CO hydrogenation [76]. They also found that rate of methanol synthesis was linear to CO_2 concentration. Similarly, under typical industrial conditions 2/3 of the total methanol produced was from CO_2 hydrogenation to methanol and contribution of CO hydrogenation was very low [80]. Similarly, CO_2 hydrogenation is preferred because of its high abundance, nontoxicity, low cost and greater potential as renewable energy source [81].

Industrially, methanol synthesis is carried out by a mixture of syngas and CO_2 [15]. Although CO hydrogenation to methanol has been extensively investigated, however, little attention was given to CO_2 hydrogenation. Mainly, this is because of the thermodynamic stability of carbon dioxide. Nevertheless, reduction of CO_2 as a greenhouse gas, demand for renewable energy sources and public awareness about cleaner environment highlighted CO_2 hydrogenation to methanol. Methanol synthesis from hydrogenation of atmospheric CO_2 has been declared as "most economical way after oil and gas" [14].

2.3 Catalysts in methanol synthesis

Catalysts with different compositions have been applied for CO_2 hydrogenation. Methanol synthesis was originated from zinc chromium oxide catalyst. In 1966 Cu based catalyst was introduced which showed better activity and selectivity to methanol synthesis. Currently almost entire methanol synthesis industry utilizes copper, zinc oxide, and alumina catalysts. Catalysts with different compositions of active components are described as below.

2.3.1 Active metal catalysts

A typical heterogeneous catalyst consist of three major components namely, active phase, support and promoter. An active phase is a part of catalyst where reaction is taken place. Generally transition metal and their oxides, nitrides, sulfides and carbides are employed for this purpose due to their unique abilities to catalyze chemical reactions. Due to multiplicity of low energy surface electronic states, the transition metals can readily accept or donate electrons hereby facilitating breaking or forming chemicals bonds at the surface [82].

A variety of metals based catalysts were studied for hydrogenation of carbon dioxide to methanol. Some common metals applied for methanol synthesis catalysts are described as below.

2.3.1.1 Ag based catalysts

Role of Ag as active part of methanol catalyst has been less investigated. The reason behind negligence of Ag is its ~~less~~ low activity to methanol synthesis as compared to Cu. However, literature regarding Ag role is not entirely univocal. Koppel et al. [83] reported higher selectivity for Ag/ZrO_2 as compared to Cu/ZrO_2 in low temperature (less than 500 K) methanol synthesis. Selectivity of CO_2 hydrogenation to methanol was observed to be enhanced by doping Ag to Cu/ZrO_2 with almost the same conversion of carbon dioxide [84]. Bell and Rhodes in 2005 [85] obtained 100% methanol selectivity for silver catalyst as compared to 75-90 % selectivity for Cu/ZrO_2 in the same reaction conditions. Similarly, Ag/ZrO_2 catalyst showed higher activity with low selectivity to methanol formation than Ag/ZnO catalyst at same reaction conditions. This implies that Ag/ZnO system is more selective to methanol as compared to Ag/ZrO_2 at given reaction conditions. Nevertheless, both activity and selectivity were remarkably increased when both oxide were mixed in $Ag/ZnO/ZrO_2$ system. However, all Ag-based catalysts showed better selectivity but lower activity as compared to $Cu/ZnO/ZrO_2$, indicating that Ag is less active than Cu in CO_2 hydrogenation to methanol. Interestingly, higher degree of Ag dispersion resulted in lower selectivity of methanol. This was recorded on account of linear relationship between dispersion degree of Ag and rate of reverse water gas shift reaction route instead of formate synthesis [84].

2.3.1.2 Pd based catalysts

Palladium (Pd) based catalysts have also been reported for methanol synthesis via hydrogenation of carbon dioxide. Pd based catalysts with different supports like SiO_2, Al_2O_3, La_2O_3 and ThO_2 were investigated for carbon dioxide hydrogenation to methanol. A higher selectivity of methanol (ca 90%) was recorded in reaction conditions of 12 MPa pressure and 623 K temperature over Pd/La_2O_3 catalyst. However, Pd supported on acidic supports showed methane as a main product instead of methanol [60]. Fan et al. investigated Pd based CeO_2 catalyst for reduction of carbon dioxide to methanol. According to their findings Pd/CeO_2 showed higher activity with longer period of life time when it was reduced at 500 °C [86]. Multi-walled carbon nanotubes supported Pd/ZnO catalyst showed excellent activity for hydrogenation of carbon dioxide to methanol [87]. Moreover, Pd/TiO_2 reduced at elevated temperature of 773 K, disclosed strong interaction between metal and support. This strong interaction resulted in higher activity and selectivity to methanol. However, methane was obtained as a main product when the same catalyst was reduced at 673 K [88]. This suggests that reducibility of catalyst is also an important parameter defining the selectivity of Pd based catalyst.

However, in comparison to Cu based catalyst, Pd/ZnO catalyst was found less active to methanol synthesis from CO_2 reduction [88]. Similarly, Pd based catalysts showed higher selectivity to methane whereby lowering methanol selectivity.

2.3.1.3 ~~Copper~~ Cu based catalysts

Role of copper as an active catalyst part has been extensively investigated for decades. Copper based catalysts have been declared as most active and selective catalysts for methanol synthesis by hydrogenation of CO_2 [29]. Some researchers even claim that methanol synthesis by CO_2 hydrogenation is not possible in the absence of copper [89].

Cu/ZnO is the most extensively catalyst system used for methanol synthesis. Generally this system is operated at higher temperature (more than 250 ^{0}C) and high pressure range (above 50 bar). Addition of ZnO to silica supported catalysts improved selectivity of methanol formation from H_2 and CO_2 [29]. Furthermore, the lattice oxygen vacancies of zinc oxide not only improve degree of dispersion of Cu but also provide greater stability to copper [90]. In addition, the lattice electron pair of ZnO is reported to be active for methanol production [12]. Higher dispersion of copper and generation of flat Cu species at the surface of zinc oxide resulted in higher activity and selectivity to methanol for Cu/ZnO system. Similar observations were also reported by Nitta et al. [91] where addition of ZnO not only increased surface area of catalyst but also improved dispersion of Cu, leading to enhanced activity at lower temperature. Metal dispersion is also promoted by strong interaction between Cu and ZnO. The interaction enhances redox profile of the catalyst which ultimately resulted in higher activity towards methanol formation [5]. Incorporation of Ga_2O_3 as a catalyst promoter to Cu/ZnO resulted in better performance of catalyst for hydrogenation of CO_2 to methanol. Small particles of Ga_2O_3 were recorded to facilitate reduction of Cu, leading to higher activity of the catalyst [30, 92]. Similarly, owing to strong synergy between Cu and ZnO, Cu/ZnO catalyst is believed to be more active than Cu/SiO_2, in CO_2 hydrogenation to methanol [93]. Although some researchers deny the presence of synergy effect in Cu catalysts and claim that solely metallic Cu is responsible for CO_2

hydrogenation and RWGS reaction [94, 95], however enough evidences are documented for persisting synergy effect of Cu with different oxides. This was further manifested by the double rate of methanol formation per Cu site on Cu/ZnO and $Cu/ZnO/Al_2O_3$ as compared to Cu dispersed on support in the absence of any oxide [61]. Furthermore, the existence of synergy effect can also be confirmed by stabilization of Cu^+ having neighboring oxides like ZrO_2 [96, 97], ZnO [30, 92] and ZnO/ZrO_2 [20] systems.

However, Cu-ZnO as compared to Cu/ZrO_2 system accelerates conversion of methanol to CO relatively at higher temperature resulting lower yield of methanol [98]. Moreover, Cu-ZnO system is observed with short life, where catalyst is deactivated after a short period of reaction time [3, 4].

$Cu/ZnO/Al_2O_3$ is most extensively studied catalysts for CO_2 hydrogenation to methanol. Currently almost entire methanol synthesis is based on $Cu/ZnO/Al_2O_3$ catalysts [59]. Fujimoto et al. [22] investigated $Cu/ZnO/Al_2O_3$ for CO_2 hydrogenation to methanol. They reported greater activity and stability of the catalyst owing to stabilization of zero valent form of copper. Zinc oxide plays a very interesting role in alumina based catalysts. Presence of zinc oxide mitigates the poisoning behavior of Cu by chlorides and sulphides impurities in feed gas. Similarly, ZnO not only improves dispersion of Cu particles on alumina surface but also exhibits refractory role by attenuating the agglomeration of active metal particles, hence increasing the overall stability of catalyst for long term operation. Moreover, ZnO being a basic oxide neutralize acidic character of alumina, thereby inhibiting conversion of methanol to dimethyl ether [30].

However, poor performance of $Cu/ZnO/Al_2O_3$ has limited the effective conversion of CO_2 to methanol [23, 24]. Moreover, CO_2 hydrogenation was depressed by strong hydrophilic character of Al_2O_3 as compared to $Cu/ZnO/ZrO_2$ [25-27].

Hydrogenation of carbon dioxide is practiced largely on Cu/ZrO_2 catalyst. In some cases addition of alumina to zirconia is reported to increase the activity and selectivity of catalyst towards methanol formation [99]. Zirconia due to abundant availability of oxygen at the surface and good ion exchange capacity is considered as a good candidate for hydrogenation reactions [65]. Moreover, higher stability of ZrO_2 in oxidizing and reducing environment enabled zirconia as an excellent support for methanol synthesis catalysts [2, 100]. Besides role of catalyst promoter, zirconia incorporated with copper, i.e. Cu/ZrO_2 catalyst showed higher activity and selectivity in methanol synthesis as compared to Cu/ZnO system [98]. Greater interaction between catalyst particles leads to higher activity and selectivity in methanol formation by Cu/ZrO_2 catalyst. Introduction of ZrO_2 to copper based catalyst also improved degree of dispersion and oxidation state of Cu, resulting in greater activity of catalyst [64, 93, 101]. Performance of ZrO_2 based catalysts is also affected by type of crystalline form of zirconia [102]. Transformation of polymorphic forms of zirconia is pH dependent during catalyst preparation, where tetragonal zirconia is predominantly form at pH 10 while at pH 7 monoclinic form of zirconia prevail [84, 85]. Furthermore, degree of calcination temperature also effect allotropic transformation of ZrO_2. Zirconia was exclusively found in tetragonal form below 500 °C, while fraction of tetragonal form was observed to transform to monoclinic polymorph with further elevation of calcination temperature [103]. Monoclinic ZrO_2 (m- ZrO_2) is reported to be 4.5 times more active than its tetragonal polymorph (t- ZrO_2). This is because t- ZrO_2 has more potential to adsorb active intermediate for methanol synthesis like CH_3O and HCOO than monoclinic zirconia [104]. Furthermore, owing to Ag^{+} stabilization effect associated with t- ZrO_2, activity profile of Ag/ZrO_2 catalysts to methanol formation was witnessed to enhance by increasing t-ZrO_2 content in the catalyst [84]. Similar observations were also recorded for Cu-based catalysts [97].

Comparative studies of Cu/ZrO_2 and Cu/ZnO catalysts concluded that former catalyst is more effective in CO_2 hydrogenation to methanol. Moreover, remarkable increase in catalyst activity was recorded when ZnO was added to Cu/ZrO_2 catalyst. The presence of ZrO_2 in ~~of~~ $Cu/ZrO_2/ZnO$ system led ~~the process~~ ~~for~~ to higher selectivity ~~to~~ for methanol formation, indicating that ZrO_2 is more selective to methanol synthesis than ZnO [91]. However addition of both ZnO and ZrO_2 enhance activity of catalyst by stabilizing Cu^{+} in Cu-based catalysts. In contrast, presence of ZnO did not affect the overall methanol formation rate in Ag-based catalyst, while only ZrO_2 addition amplified performance of catalyst to methanol formation. This discrepancy was resolved by noticing no substantial stabilization of Ag^{-} by neighboring ZnO [84].

Incorporation of B_2O_3 to Cu/ZrO_2 enhanced the CO_2 conversion with low selectivity values to methanol. In contrast, comparatively low conversion of CO_2 and higher selectivity to methanol was reported when Ga_2O_3 was unified to Cu/ZrO_2 [93].

added ?

2.4 Catalyst promoters

In heterogeneous catalysis, promoter is one of the three major components along with active metal and support. The promoter may not be itself active for a particular reaction but it can affect the active parts of the catalyst by facilitating the desired reaction or by depressing the formation of unwanted by-products. Thus both activity of the catalyst as well as selectivity of the product could be improved by application of promoters. Two kinds of promoters namely structure promoters and active promoters are generally used in catalyst industry. The promoter is termed as structural promoter when it provides stability to the catalyst in reaction condition generally by preventing sintering of the active catalysts particles. Such kind of promoters are inert in nature. The second kind of promoters are active promoters which influence the electronic structure of the active part of the catalysts by increasing number of active sites or facilitating reduction of active metals. Both kinds of promoters have been investigated for methanol synthesis by CO_2 hydrogenation. Some common promoters applied in methanol synthesis catalysts are discussed as below.

2.4.1 Gallium oxide

Gallium oxide (Ga_2O_3) enhances the activity of copper based catalyst for methanol formation by facilitating oxidation of copper to Cu^+ state [30]. Similarly, incorporation of Ga_2O_3 increased activity of the catalysts in methanol synthesis by CO_2 hydrogenation [21]. Moreover, addition of Ga_2O_3 to the Cu based catalysts improved catalytic profile of methanol synthesis catalysts by CO_2 hydrogenation [105] . Introduction of Ga_2O_3 has affected the structural changes in the catalysts and played a role of regulator by keeping the Cu^+/Cu^0 ratio constant throughout the reaction period [30].

2.4.2 Niobium oxide

It is intriguing that catalytic behavior of Niobium (Nb) is quite different from other family members due to its different periodic properties like electronegativity and atomic radius [106]. Niobium oxide (Nb_2O_5) has been used both as catalysts support as well as promoter. However, Nb_2O_5 has mainly been used as catalyst support [107]. Niobia-supported catalysts have been reported with higher activities and better selectivity [108]. The better performance of the niobia-supported catalysts was attributed to the formation of new active sites due to the greater interaction of support with the metal atoms. Likewise, niobia-supported catalysts have been reported with low acidity and strong metal support interactions [109]. Similarly, Nb_2O_5 based catalysts exhibited better activity and selectivity in hydrogenation reactions of CO and CO_2 [110-112].

Nevertheless, due to its strong acidic character it can also be effectively used as catalyst promoter [113]. In recent times, role of Nb_2O_5 as a promoter was investigated on silica and alumina based catalysts [114]. Incorporation of Nb_2O_5 resulted in drastic modification of catalytic as well as adsorptive profiles of the catalysts. Furthermore, Nb_2O_5 promoted catalysts not only showed better selectivity to olefins but also provided greater stability to the catalysts. Moreover, application of niobium-promoted iron catalysts in Fischer-Tropsch reaction resulted in higher selectivity towards formation of C_{5-} hydrocarbons and depressed catalysts activity to methane production [115]. Furthermore, application of Nb_2O_5 as catalyst promoter has not only incremented the activity profile of catalysts but it also increased catalysts life time [106]. Moreover, addition of Nb promoter has resulted in greater activity in liquid phase reactions [116]. In addition, Nb_2O_5 has exhibited better catalytic activity especially in the presence of water [113]. Keeping in mind this extra ability of Nb_2O_5, its application in the title reaction will have an extra advantage due to water formation during CO_2 hydrogenation to methanol.

Role of Nb_2O_5 as catalysts promoters has been hardly investigated for CO_2 hydrogenation reactions.

2.4.3 Zinc oxide

Zinc oxide (ZnO) has a dual application in methanol synthesis catalysts. It has extensively been reported that ZnO based catalysts worked effectively in CO_2 hydrogenation [20, 30, 117-119]. However, promoting effect of ZnO has also resulted in better activity profiles of methanol synthesis catalysts. Similarly, ZnO has also been reported to play a versatile role ranging from a spillover model to a model that could potentially affect the morphology of the active sites [120]. Introduction of ZnO facilitated catalyst preparation by forming appropriate precursors which consequently led to better dispersion of active components. Furthermore, a refractory behavior has been exhibited by ZnO in the presence of alumina and attenuated the unwanted agglomeration of active Cu component. In addition, incorporation of ZnO has also enabled Cu particles to resist against poison in the feed gas impurities like chlorides and sulfides. Additionally, being a basic oxide ZnO has partially neutralized acidity of the acidic support like Al_2O_3, thus helping to prevent the transformation of methanol to dimethyl ether [30]. Moreover, Arena et al. concluded that ZnO has a promoting effect on the dispersion of active phase, surface area and reducibility of catalysts for CO_2 hydrogenation to methanol [2]. More importantly, incorporation of ZnO to the Cu based catalysts resulted a synergism between Cu and ZnO. As a result of this synergetic effect the electronic interaction between Cu and $Zn^{(2-\delta)+}$ created active sites like Cu^{+}–O–Zn [121]. A similar observation of synergic effect between Cu and ZnO was also reported by Chen et al. in methanol synthesis reaction [122]. They also found that ZnO is acting as binding site for atomic hydrogen facilitating the adsorption of H_2 species. Furthermore, ZnO is believed to be involved actively in mechanistic studies of methanol synthesis by creating Zn-methoxy oxide. Methoxy oxide is one of the stable reaction intermediate which is converted to methanol on further hydrogenation [122].

Presence of sulphur is considered as poison for Cu based methanol synthesis catalysts. Addition of ZnO to the catalyst scavenge sulphur content irreversibly as ZnS, thus providing a protective role against deactivation of catalyst [59] . Introduction of ZnO also increases the absorption strength of reaction intermediates like HCO, H_2CO, and H_3CO and hence decreasing the energy barriers. Consequently, rate of methanol formation is enhanced [123]. Similarly, addition of ZnO to Cu based catalyst also facilitates reduction by adjusting itself to a partial oxidized state Zn^{+} [123].

2.5 Catalyst supports

In heterogeneous catalysis, the main objective of catalyst support is to disperse the active phase. Furthermore, different supports are also applied in order to provide the thermal stability to the active phase and to avoid sintering of metals particles.

A number of investigations revealed that activity and selectivity of methanol synthesis is affected by nature of catalyst support. Catalyst particles are dispersed on support to achieve higher exposure of active sites to the reacting molecules and also to avoid sintering phenomenon associated with high reaction temperature. However, different parameters associated with activity and selectivity of catalyst are modified by use of an appropriate catalyst support. Acidity or basicity of a support also alters the overall performance of catalyst for a particular reaction. Moreover, supports are not only responsible of stabilization of actives components but also for tuning surface interaction between the active components of catalyst [44]. Role of some common methanol catalyst supports is discussed as follow.

2.5.1 Silica

Due to higher thermal stability and greater dispersion capacity, silica has been extensively investigated as catalyst support for methanol production from CO_2 and H_2. Sugawa et al. in 1995 [29] experimented different metals namely Cu, Ni, Co, Fe, Ag, Ru. Pt. Pd. Au. Rh. Ir, Os and Re supported on silica. Activity studies were conducted at reaction conditions of 250 °C temperature, 5 MPa pressure and H_2/CO_2 ratio of 3. The study revealed higher selectivity of methane for Ni, Co, Rh, Os, and Rh based silica catalyst. On the other hand, Pt/SiO_2 showed higher selectivity towards CO formation. Only Cu/SiO_2, Ag/SiO_2, Pd/SiO_2 and Fe/SiO_2 were found with higher selectivity to methanol synthesis. Similarly owing to higher surface area, silica based catalysts showed higher activity and better selectivity for methanol production as compared to ZnO-based counterparts [30].

However, although silica possesses higher surface area, but it has been documented with low thermal stability due to its transformation to $Si(OH)_2$ in presence of steam at higher temperature [31]. Similarly, silica has been reported to undergo silicide formation during catalyst reduction at higher temperature [124]. Although in some cases, like in Pd-silicide system this silicide formation have resulted in higher selectivity for isomerization reaction of neopentane [125]. Nevertheless, formation of these metal-support oxides lowers the fraction of reduced metal as these are difficult to be reduced [67, 126].

2.5.2 Alumina

Alumina has been extensively studied as support for methanol synthesis catalysts by CO_2 hydrogenation. A gradual decrease of methanol yield from 8.1 at 1 h to 4.4% at 100 h reaction time observed for alumina based Cu/ZnO catalyst. This suggests the lower stability of alumina based catalyst for longer duration of reaction time. Furthermore, stability of $Cu/ZnO/Al_2O_3$ catalyst under prolong interval of time was increased by addition of zirconia to the parent catalyst [74].

However, the strong metal support interaction between transition metal oxide and amorphous alumina is the major drawback of alumina based catalysts [67]. Likewise, hydrophilic character of alumina is also one of the reasons for lower activity of alumina based catalyst in water forming reactions like CO_2 reduction to methanol.

2.5.3 Zirconia

Recently, comparative studies for zirconia and alumina supports for Cu/ZnO catalyst in methanol synthesis revealed higher conversion of CO_2 and better activity and selectivity for Cu/ZnO catalysts based on zirconia as compared to alumina support. However, catalyst performance was further enhanced by combination of both supports in $Cu/ZnO/ZrO_2/Al_2O_3$ system [28]. The increased performance was attributed to higher thermal stability and higher surface area associated with ZrO_2-Al_2O_3 system [127, 128]. Moreover, Cu/ZnO/ZrO_2 catalyst was found more resistant to water poisoning during methanol synthesis and was less affected in terms of catalyst activity and CO_2 conversion than Cu/ZnO/Al_2O_3 [28].

2.5.4 Carbon nanofibers

Carbon nanofibers (CNFs) are discussed in details as under.

2.5.4.1 Structure of CNFs

The structural unit of CNFs is composed of hexagonal carbon resembling the structure of graphite as indicated in Figure 2.1. Each carbon in CNFs is linked to four other carbon atoms, three of those four carbons are sp^2 hybridized with a bond length of 1.415 Å, while the fourth one is attached through loose interlamellar stacking with inter layer spacing of 3.35 Å. In case of sp^2 hybridized the electrons of carbon bonding are highly delocalized and are easily transported between different units. This is why CNFs have good electrical and thermal conductivity. The diameter of CNFs is ca. 100 nm. Furthermore, due to their small size and high aspect ratio, they hold very high surface area to volume ratio which makes them a good candidate for catalyst support. CNFs are different from vapor-grown carbon fibers (VGCFs) and conventional fibers as their diameters ranges in micrometers. Moreover, unlike carbon nanotubes (CNTs) CNFs are stacked in regular layers along the central axis.

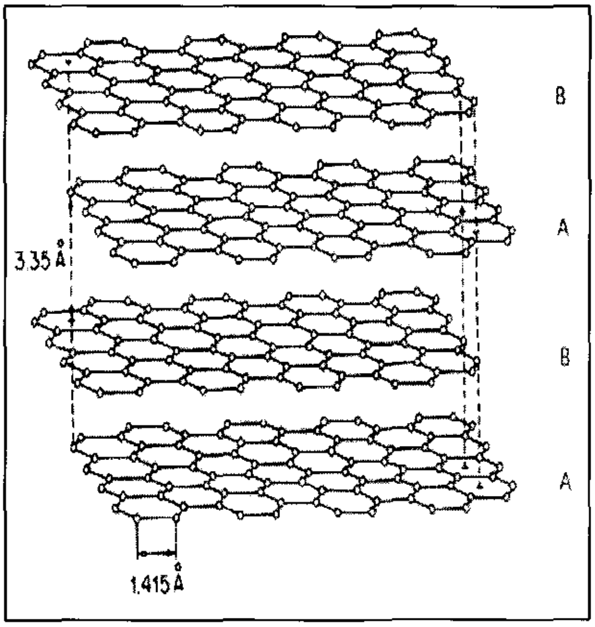

Figure 2.1: Graphite crystallite structures (the balls represent carbon atoms and the sticks represent the bonding) [129].

2.5.4.2 Types of CNFs

Based on orientation of graphene layers with respect to the central fiber axis, CNFs have been categorized in three different types like herringbone, platelet and ribbon type. In herringbone type CNFs, graphene layers are oriented obliquely with respect to the central fiber axis. They are also termed as fishbone type of CNFs. However, graphene layers are perpendicularly placed to the central fiber axis in case of platelet type of CNFs. Similarly, the type of CNFs is termed as ribbon, where the graphene layers are oriented in parallel to the central growth axis. Such CNFs are also called as tubular type CNFs. Structural arrangement of all three forms of CNFs is represented in Figure 2.2.

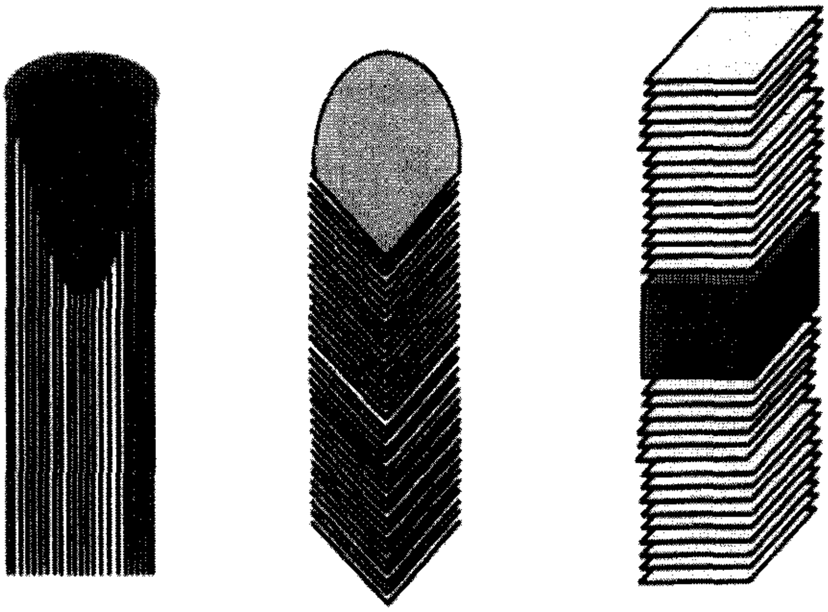

Figure 2.2: Types of CNFs adopted from [130]

Fishbone and platelet types CNFs are famous for their higher surface area as compared to the ribbon type. Similarly, surface edges in fishbone and platelet types are largely exposed as compared to tubular type, so the oxygen surface groups are more easily attached in the former types of CNFs. The metal–support interaction is generally dependent to the number of surface oxygen groups. Consequently, all those properties make fishbone and platelet types of CNFs more potential candidates in the field of catalysis than the ribbon type of CNFs [131].

2.5.4.3 Surface modification of CNFs

CNFs are chemically inert and hydrophobic. Due to their inertness, it is difficult to deposit the catalyst particles on their surface [132, 133]. When CNFs are treated with an oxidizing agent, like HNO_3, the oxygen-containing groups are created at the surface of the CNFs [134]. Nitric acid is used as most common oxidizing agent which incorporates oxygen containing groups like –CHO, –CO, –OH, –COOH to the surface of CNFs [135, 136]. In the oxidized carbon nanofibers (CNFs-O) the surface oxygen groups incorporate the active metal particles and act as anchoring sites for the catalyst particles [134]. This treatment is also responsible for the increased acidity and enhanced reactivity of CNFs [136]. It also introduces polarity at the surface of CNFs.

2.5.4.4 Deposition of catalyst particles without surface modifications

In general practice, CNFs are treated with oxidizing agent to create oxygen groups for adhering the catalyst particles. However, CNFs especially herringbone and platelets structures have potential reactive or functional groups to anchor the catalysts particles without any pre-treatment. This is because of the fact that CNFs have surface defects which work as anchoring site for deposition of catalyst particles. Baker et al. [40] conducted a comparative study of nickel deposition on unmodified CNFs, activated carbon and alumina support. TEM investigation revealed that well dispersed Ni particles with well-defined morphology was found on CNFs support. In contrast, less evenly distributed particles were observed on other two supports [33, 40, 135]. Similarly, different kinds of CNFs were used as catalyst support for deposition of Rh metal. Hexagonal shaped Rh particles were found to be located on the edges of CNFs. Irrespective of the type of CNFs, large sized particles were observed for all CNFs supports as compared to rhodium supported on silica support [137]. Furthermore, a 5 % (w/w) Platinum loading on the CNFs was investigated by Baker et al. [138]. They reported successful deposition of platinum with higher degree of (20 %) dispersion. Moreover, CNFs based iridium catalysts was synthesized by Vieira et al. [139]. They concluded that higher dispersed catalyst particles were observed due to the stronger interaction between the prismatic planes of CNFs and iridium catalyst particles.

2.5.4.5 Deposition of catalyst particles with surface modifications

Application of surface modified CNFs have shown better results in catalysis as compared to as-synthesized CNFs [140]. Many techniques have been applied for the surface modification of CNFs. Treatment of CNFs with some oxidizing agent like HNO_3 is one of those methods which are used for surface modification of CNFs. Oxidation of CNFs can be carried out in liquid as well as gas phase [141]. Nevertheless, liquid phase treatment with oxidizing agents is preferred over gas phase due to the better control and homogenous oxidation in former case [142]. This treatment is also responsible for the increased acidity and enhanced reactivity of CNFs [136]. Furthermore, the degree of active metal dispersion has a linear relationship with the amount of surface oxygen [143]. Interestingly, the exact sites of oxidation in CNFs are still debatable. According to some researchers the process is limited to the edges of graphite plans [144]. In contrast, oxidation has been reported to prevail through the whole length of CNFs [142, 145].

Prior to use as a catalysts support, Pham-Huu et al. treated CNFs with nitric acid solution for 2 hours at 80 °C. Catalyst having 5% (w/w) Pd particles was synthesized on the oxidized CNFs by impregnation method. They observed a homogeneous deposition on the surface of the modified CNFs and attributed this homogeneity to the metal-support interaction [41]. Similarly, 5% (w/w) Pd catalyst was prepared on nitric acid treated CNFs by Mojet et al. and reported a narrow size distribution of Pd catalyst particles of about 1.5 nm. [146]. XAFS analysis revealed the formation of palladium tetra amine complex with the surface of the CNFs. Interaction of carboxylic acid groups of the CNFs surface and π-electrons of the support were proposed to be stabilizing factor for the cationic palladium complex. More importantly, the role of surface oxidation can be recognized by the observations of Ros et al. where rhodium particles could not even be deposited on the surface of untreated CNFs due to the lack of interaction of between surface of CNFs and metal particles [147].

2.5.4.6 CNFs as a catalyst support

Majority of the industrial catalysts consist of supported metals. Choice of the right catalyst support is pivotal as any interaction between active catalyst phase and support can affect the overall activity of the catalyst. The desirable characteristics of a suitable catalyst support include stability under reaction conditions, chemical inertness, higher surface area and porosity, high mechanical strength in bulk phase application. CNFs are thermally stable at higher reaction temperatures (>1000 K). Moreover, higher thermal stability of catalyst support is desired to withstand the high degree of temperature in operating conditions. Thermo gravimetric analysis (TGA) is generally used to study the thermal stability of materials. TGA analysis revealed that CNFs are more resistant to oxidation and hence more thermally stables as compared to activated carbon [135]. Furthermore, CNFs are chemically inert and they show greater resistance in acidic as well as basic medium than conventional oxide supports like silica and alumina. Furthermore, surface area of the catalyst support should be of the magnitude to host adequate amount of active catalyst sites per unit volume. CNFs having higher surface area (100-200 m^2/g), larger porosity (0.5-2 cm^3/g) are very promising in this regard. Similarly, high external surface area and special morphology of CNFs allow rapid access of reactant molecules to the active metal sites. In the same way, complete absence of bottled pores in CNFs, empowers 3D approach of the reactants to the entire volume of catalyst. In addition, CNFs due to the higher porosity and lower tortuosity will reduce mass transfer limitations [36]. Additionally, absence of micro pores mitigates the problem of mass transfer. This makes CNFs as ideal candidate for catalyst support especially in liquid phase reactions [148]. CNFs being a combination of both active carbon and mechanically strong graphite, surpass other oxides catalyst supports like silica and alumina [35]. Furthermore, graphite like sp^2 hybridization provides a strong mechanical strength to the CNFs. Based on sp^2 hybridization, tensile modulus of CNFs is reported to be 1.06 TPa [149] while mechanical strength is calculated to be 130 GPa [129]. In addition, CNFs due to higher thermal conductivity, evacuate heat generated during reaction [37]. Furthermore, CNFs being good thermal conductors have an extra advantage as application of catalyst support in exothermic reactions [135]. Another extra feature associated with CNFs as catalyst support is the easy recovery of precious metallic phase by burning the carbon. Furthermore, being a carbonaceous material CNFs are provided with well-developed pore structure which is helpful in preventing sintering as well as to achieve good metal dispersions [150]. Additionally, CNFs are considered to be excellent catalyst support due to chemically active outer and inner end planes [151]. CNFs are preferred over conventional catalyst support like alumina and silica because of their higher thermal stability, higher surface area, resistance to corrosion in acidic and basic medium and ease in recovery of precious metal particles [38]. Moreover, CNFs due to their mechanical strength are very suitable as catalyst support [152, 153]. Because of all these properties CNFs are considered as excellent contender for catalyst support. Several reviews regarding role of CNFs as catalyst support has already been published [36, 135, 154, 155].

Baker et al. was the first group who started research on CNFs as a catalysts support in nineties [156]. They found a strong interaction between active phase and crystalline structure of the support. According to their findings, metal particles supported on CNFs behaved differently in terms of reactivity and adsorption strength as compared to those deposited on less structurally ordered supports. Since then, the same group explored the specific characteristics of this material compared to the traditional catalysts supports [40]. Later on this this material was investigated by many researchers with De Jong [157] , Ledoux [41], Geus [153] and Lefferts [133] are some of the main contributors in this field.

CNFs based catalysts showed higher activities for a variety of reactions as compared to traditional supported catalysts. Coelho et al. [37] in 2008 reported that CNFs has good metal/support interaction because of the prismatic planes on the surface of CNFs. Their study also revealed that high specific surface area of CNFs leads to a better contact between reactant and active site. Plomp et al. [158] in 2008 and Dusza et al. [159] in 2009 studied the deposition of CNFs on zirconia and reported that the addition of CNFs to ZrO_2 inhibits the growth of zirconia, which results in a very fine nanocrystalline zirconia surface. This was also enforced by reactions studies where CNFs based catalysts showed higher activities and selectivity as compared to conventional supports based catalysts [40-42, 160].

During the last two decades, applications of CNFs as catalyst support have been reported in various reactions. CNFs based catalysts have been extensively studied for hydrogenation reactions, both in gas phase as well as in liquid phase [135]. Rodrigues et al. in 1994 conducted comparative study on CNFs, activated carbon and alumina as catalyst support for ethene hydrogenation. Magnitude of higher activity was displayed by CNFs based catalyst as compared to alumina and active carbon based catalysts [155]. Interestingly, CNFs based catalyst showed higher performance than other counterparts, even if large sized metallic particles (6-8 nm) on CNFs as compared to 5.5 nm for activated carbon and 1.4 nm for alumina. These findings also indicate that catalytic hydrogenation is a structure sensitive reaction. Besides, morphological studies revealed that catalyst particles were widely spread on CNFs support which is generally believed to be the feature of strong metal-support interaction. Furthermore, strong metal-support interaction observed in CNFs supported catalysts, unveiled different strength of adsorption and reactivity than catalysts deposited over other less ordered supports. In addition, despite the lower content of metal, Pd doped CNFs catalyst displayed higher activity in hydrogenation reaction as compared to Pd/AC catalyst [161]. Moreover, nickel particles deposited on CNFs support exhibited greater activity in hydrogenation of lower alkenes [161]. Similarly, it has been demonstrated that due to the better interaction between support and liquid, Pd/CNFs have recorded a threefold increase in the activity of nitrobenzene hydrogenations [161]. Hydrogenation of cyclohexane by CNFs based rhodium (1-2 nm) nanocatalyst was studied by Ros et al. [147]. The catalyst was found extremely active even at low metal loading of ca 1%, low concentration of reactant (1% v/v) and lower pressure of H_2. Activity of the catalyst was claimed to be dependent on the influence of acidic groups of the surface rather than particle size. Similarly, Rh/CNFs catalyst, synthesized in mild conditions, exhibited good activities for the same process [162]. A comparative study was conducted for reduction of crotonaldehyde on CNFs and alumina based nickel catalysts [33]. CNFs based catalysts yielded higher amount of crotyl alcohol than the alumina based counterpart. The higher activity was attributed to location of nickel particles at the edges of CNFs: thus different crystallographic faces of metal exposed to the reactant molecules as compared to that of based on alumina. A ruthenium nanoparticles based on CNFs were investigated for hydrogenation of cinnamaldehyde [163]. The samples were heated in nitrogen flow for different degrees of temperature and reported that post-treatments of the samples have a crucial role in activity as well as selectivity profile of catalyst. Likewise, reduction of cinnamaldehyde to hydrocinnamaldehyde by palladium supported CNFs catalyst was studied [41, 154, 164, 165]. The higher selectivity of 90% was attributed to the reduction of mass transfer limitations, which is in turn due to mesoporous nature of CNFs. Previous work has shown that the activity of the catalyst increases dramatically for simple hydrogenation reactions when CNFs were used as a catalyst support as compared to corresponding alumina and active carbon supports [156].

All these examples underline the importance of CNFs and their successful application as a catalysts support for a variety of reactions. The economic studies on application of CNFs also revealed that CNFs is cost effective than CNT, as the market price for CNT is 100 times higher as compared to CNFs [166].

2.6 Catalyst synthesis methods

Catalysts have been the core part of manufacturing industry for decades. The desirable profile for any catalyst includes higher surface area, greater thermal stability, higher dispersion of active sites and longer life time. Choice of preparation method not only affects physiochemical parameters of catalyst but it also marks the overall activity profile of catalyst. Generally three different approaches are adopted for preparation of catalysts. In the first approach catalyst active components are deposited on support by precipitations, impregnation or ion exchange. This is followed by washing, drying, calcination and finally activation. In the second approach a high surface area carbonate or oxide containing active component is precipitated, followed by drying, calcination and activation. In the last approach non-porous alloy or compound having active components is prepared. In this case inactive material is extracted leaving behind high surface area porous compound. The first approach is simple and most commonly followed in preparation of methanol synthesis catalysts. Some common preparation methods for methanol synthesis are described as below.

2.6.1 Co-precipitation method

Co-precipitation method is commonly employed to prepare catalyst for methanol synthesis. Alkaline carbonates are employed as precipitating agents in this process. Generally catalysts prepared by this method show good activity in low pressure and low temperature methanol formation. Long duration of time more than 13 hours and difficulty in removing the alkaline content are some of the disadvantages of this technique. Moreover catalysts prepared by this method have been reported with low thermal stability, toxicity, poor mechanical strength and deactivation in longer time span of reaction [167, 168].

2.6.2 Impregnation method

Impregnation method is simplest and widely used method for catalyst preparation [169]. This method entails suspension of solid support in a solution of catalyst active elements or precursors. Deposition of catalyst particles depend on the concentration of impregnating liquid volume V_{imp} and pore volume of support V_p. Based on this relationship the process is termed as dry, capillary or incipient wetness, when V_{imp} is nearly equal to V_p whereas terms like ion exchange and equilibrium adsorption are entitled to the process when $V_{imp} > V_p$. Driving force for this method is capillary action which enables pores filling of porous support. Besides the simplicity the procedure is notoriously deficient in attaining uniform surface layer of precipitants on surface of support.

In carrying out wet impregnation technique, a support is wetted with a suitable solvent. Metal precursors are added to the solution and diffusion and adsorption govern the metal distribution. Capillary forces inside the support pores draw the metal precursors from the solution. The solvent from the pores of the support is evaporated by drying the impregnated sample. Furthermore, drying of impregnated sample also redistribute the metal precursors over the surface of support in order to create a strong interaction between metal and support. The dried impregnated catalyst is calcined at a particular temperature. In this way the catalyst is activated and its mechanical properties are stabilized.

Impregnation method has also been adopted in preparing CNFs supported catalysts. Bezemer et al. synthesized CNFs-supported cobalt catalysts for Fischer–Tropsch synthesis by impregnation technique [170]. They reported a successful loading of cobalt until 9.5 wt% loading with 8 % cobalt dispersion. Similarly, wet impregnation method was employed to prepare CNFs based ruthenium catalyst [131] . Different types of carbon nanofibers like platelet, fishbone and tubular were selected for the study and concluded that Ru loading was affected by the type of CNFs. They also found that deposition of ruthenium led to increase the specific surface area of tubular CNFs. According to their findings higher deposition of ruthenium on tubular CNFs was due to the increased numbers of acidic oxygen-containing groups as compared to the other CNFs types.

As mentioned earlier, impregnation method is simple; however efficiency of the method is affected by many factors like temperature, nature of solvent, rate of precursor addition and time for drying impregnated catalyst. Likewise, application of an impregnation method resulted in relatively lower metal loadings as compared to deposition precipitation method [96].

2.6.3 Deposition precipitation method

Catalyst particles can be deposited on the surface of CNFs by different methods like, impregnation and ion exchange methods [156, 164]. Deposition precipitation method (DP Method) is also one of the methods used for preparation of catalyst. Detailed description about DP method is given as below.

2.6.3.1 Short history of deposition precipitation method

Although DP method is well known from a longer period of time, however it was less investigated in the early days [171, 172]. This method was developed by Geus, Hermans, Van Dillen and De Jong [171, 173, 174]. Later on Burattin et al. utilized the method to deposit the nickel particles on the surface of silica [175]. Several reviews regarding application of DP method were published to highlight the advantages of this method [176]. Since then, DP method is extensively investigated for preparing different types of catalysts.

2.6.3.2 Principle of deposition precipitation method

Basically, DP Method is the modified form of precipitation technique. In this technique highly soluble metal precursors are converted to lower solubility substances and are precipitated specifically on the support avoiding precipitation in solution. This conversion could be done by increasing or decreasing the pH. Similarly electrochemical reactions could also be utilized where the conversion is completed by changing the valence state of the metal precursors [177]. However, the conversion of soluble metal precursors to less solubility substances is usually achieved by increasing the pH of the solution. Two basic conditions must be satisfied in order to deposit metal particles exclusively on the surface on the support.

I. There should be interaction between the surface of the support and metal particles.

II. To avoid the precipitation of metal precursors in solution, the concentration of the precursors must be retained between the concentration of super solubility curve (SS) and solubility curve (curve S).

The whole process is more elaborated with the help of following Figure.

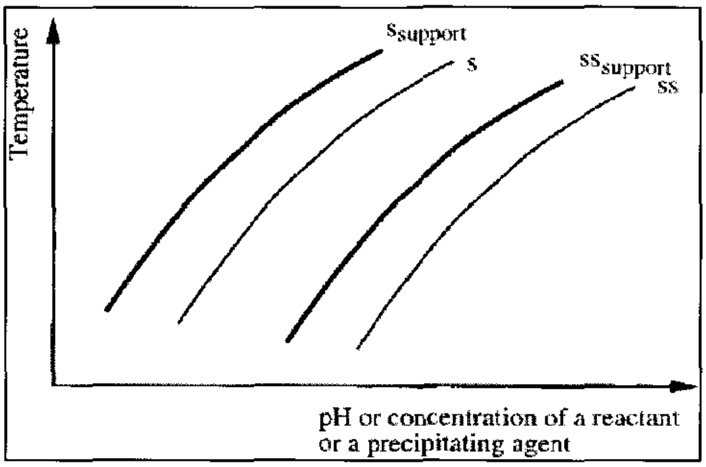

Figure 2.3: Phase diagram for a pure solution (solid lines) and in the presence of a support (bold lines) [178]

In Figure 2.3, phase diagram of solubility or saturation curve is represented by curve (S) represents the equilibrium curve separating the domain of two phases. Similarly, supersolubility or supersaturation is designated by curve (SS), which shows that nucleation and precipitation of metal precursor will occur if concentration is reached up to this mark. In the same way, curve ($S_{support}$) and curve ($SS_{support}$) correspond to solubility curve and supersolubility curve in the presence of support respectively. As shown in the Figure 2.3, the interaction of metal precursors with support has shifted both curve ($S_{support}$) and curve ($SS_{support}$) to the lower concentration. Similarly, concentration of precipitating agent is the key factor in DP method as its concentration above the supersolubility curve (SS) could nucleate the metal precursors in solution. Therefore, a gradual addition of precipitating agent to the stirring solution is recommended to avoid nucleation of metal precursors in solution. Furthermore, maintaining the concentration between solubility curve (S) supersolubility curve (SS) and metal-support interaction will avoid the nucleation. By keeping the concentration between curve ($SS_{support}$) and supersolubility curve (SS), metal precursors are exclusively deposited on the surface of support [179].

Main factors affecting the activity profile of catalyst like dispersion of active metal includes nature of precipitant and precursor and pH of the precursor solution [180, 181]. One of the most important parameters for DP method is the magnitude of solution precursor pH. Song et al. investigated the effect of pH on the preparation of Pt-doped TiO_2 catalysts and reported that catalysts with highest photocatalytic activity was synthesized at pH value around 7 [182]. Similarly, Yoon et al. synthesized Pt/Al_2O_3 catalysts by DP method at different pH values from 6.5 to 9.5 and concluded that increase in pH beyond 7.5 resulted in lower surface PtOx species as well as reduced dispersion of active metal. They also reported that catalysts particle size was affected by changes in pH and catalysts with best activity was found the one prepared with pH of 7.5 [180]. Contrary to this, according to Van der Lee et al. deposition precipitation started right from pH 3.5 and maximum deposition takes place at pH 5.8. Beyond this point, nucleation of metal precursors is started [157].

In general practice, metal precursors are dissolved in a solvent and catalyst support is suspended in solution. The suspension is heated to a desired temperature and thoroughly stirred. This is followed by addition of precipitating agent in controlled manner. The process is continued for a certain time, solid mass is collected by filtration, washed several times with distilled water and dried in oven for particular interval of time and calcined at desirable temperature.

2.6.3.3 Deposition precipitation with urea

As mentioned above, DP method is generally carried out with rising pH method. Similarly, it is also desirable to maintain the concentration below supersolubility curve

(SS) throughout the deposition process. This could be attained by using a base. Furthermore, a base is preferred with the ability to mix and generate the precipitate separately. Urea $CO(NH_2)_2$, being a delay-base provide mixing and basification of precipitates in two different stages. It permits mixing at room temperature and undergoes basification when solution temperature is exceeded beyond 60 °C. Urea $CO(NH_2)_2$ under goes hydrolysis at elevated temperature (~~A~~ a bove 60 °C) as shown below in Reaction 2.5

$$CO(NH_2)_2 + 3H_2O \rightarrow CO_2 + 2NH_4^+ + 2OH^- \quad (2.5)$$

As indicated by ~~the~~ Reaction 2.5, OH^- ions are generated by hydrolysis of urea which increases the pH of the solution. Since, hydrolysis of urea is a slow process, hence pH of the solution ~~is~~ gradually increased leading to deposition of metal precursors on the support. Kinetically, rate determining step is an important factor to speed up a particular process. Rate determining step for DP method is disputed in literature. According to Geus et al. hydrolysis of urea is the rate determining step in DP method [171]. In contrast, rate of DP method is claimed to be correspondent of to a pH, as lower steady state of pH resulted in higher deposition rate of nickel particles [157]. In DP method, a strong interaction of precipitating metals and the support lead to deposition of metals on the surface of support [171].

2.6.3.4 Mechanism of deposition precipitation method

The detailed step-wise study was conducted by van der Lee et al. in order to elaborate the insight of deposition of metal precursors on the support by DP method [157]. The schematic illustration is presented in Figure 2.4. Labels A-D represent the stepwise illustration of Ni deposition precipitation on silica whereas labels E-H symbolize mechanism of the Ni deposition on CNFs. In Ni deposition on silica support, there is no significant interaction between nickel hydroxide ions and the silanol groups of the support as indicated by label A. This clearly indicates that prior to nucleation, the deposition of nickel ions does not takes place. However, nucleation of nickel hydroxide ions takes place on the surface of the silica at pH value of 5.8, resulting in formation of Si-O-Ni (OH) $(OH_2)_4$ as shown by label B. Figure 2.4 further indicated that adsorption of nickel precursors coincides with the nucleation on the surface of the silica. Label C displays the formation of nickel hydroxide at pH value around 5.4 and finally nickel phyllosilicates is formed and demonstrated by label D. In contrast, nickel ions adsorption occurs from the very beginning at pH value of 3.5 in case of CNFs support as shown by label E. Carboxylic acid groups present on the surface of CNFs act as the binding sites for nickel ions. It is worth mentioning that in contrast to silica, deposition of nickel ions on CNFs takes place before nucleation phase. Furthermore, nearly all acid sites are reported to be occupied in the very beginning of the process at pH value of 3.5. The further steps labeled as F-H represent nucleation of nickel ions on the surface of CNFs and about 4 nickel ions per acid site have been reported to be adsorbed. Nucleation of nickel ions started at pH value of 5.8 as shown by label G. However, 22% of the nickel has already deposited on the CNFs until that point in strong conflict in case of silica.

The study concluded that acid groups played a vital role in successful deposition of nickel ions on the surface of CNFs. This was further supported by work of Toebes et al. where Pt metal loading was found directly proportional to the number of oxygen containing acidic groups on the surface of CNFs [160].

In addition, these mechanistic investigations also highlighted the importance of DP method for preparation of CNFs based catalysts.

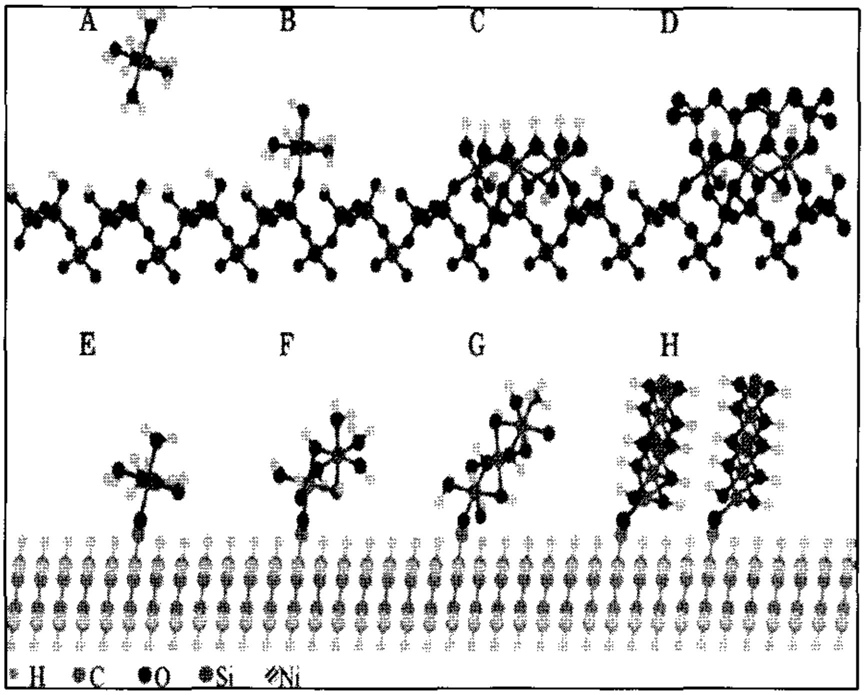

Figure 2.4: Schematic representation of mechanism of deposition precipitation [157]
[A – D ; Ni ~~deposited~~ ~~onto~~ in the complexation SiO_2 ; E – H , Ni ~~dep~~ complexation with CNF

2.6.3.5 Applications of deposition precipitation method

Deposition precipitation method has been widely utilized and developed for preparation of highly loaded and well-dispersed catalysts [183]. Moreover, comparative studies of catalysts preparation by deposition precipitation and impregnation method revealed that former route resulted in catalysts with better activities as compared to those prepared by latter method [182].

Deposition precipitation has hardly been studied for carbon supported catalysts. In case of preparation of CNFs based catalyst, this method was first applied to Ni/CNFs system [132]. Prior to metal loading, CNFs were activated by treating with oxidizing agent like HNO_3. By applying this technique 45 wt.% of Ni was successfully deposited on the surface of CNFs. Van der Lee et al. studied deposition precipitation of nickel hydroxide over CNFs and silica [157]. They reported that 20 % Ni was loaded successfully on CNFs. Deposition of Ni ~~was starts right~~ started immediately from the beginning of the process on CNFs, while the deposition of Ni on silica support was observed after 0.7 hours. Furthermore, kinetic study exposed that rate of Ni deposition is faster on CNFs as compared ~~to~~ on silica support. Similarly, Bezemer et al. deposited Co particles on the surface of CNFs by using DP method with urea decomposition [184] . They reported a selective deposition of cobalt precursors on the surface of CNFs. Cobalt metal particles with high interaction and metal dispersion of 12 % was achieved by carrying out the DP method at higher pH. Furthermore, Toebes et al. investigated synthesis of platinum catalysts on the surface of CNFs by DP method and ion adsorption technique [160]. The comparative study revealed that significantly higher platinum loadings were obtained with DP method as compared to ion adsorption method. The higher loading in case of DP method was suggested to be due to the creation of additional adsorption sites by hydrolysis of carboxyl groups of CNFs. Moreover, they also concluded that DP method is a suitable technique for preparing uniform and thermostable ruthenium particles on CNFs.

High~~ly~~ metal loading up to 45 % and well dispersed catalyst could be prepared by DP method [132]. Catalyst prepared by DP method showed better surface area and better performance towards methanol synthesis as compared to catalysts prepared by co-precipitation (CP) and impregnation method (IM) [96]. Moreover, catalyst prepared by DP method displayed greater yield of methanol with much higher selectivity and higher conversion of CO_2 as compared to catalysts prepared by conventional co-precipitated method [157].

2.7 Reactor aspects

In catalysis terms, a reactor is generally defined as a device which encloses catalyst and reaction medium. Reactor is actually a container where reactants are fed at particular reaction conditions for a specific time and the end products are removed at a particular time. In this way reactor provides a control of different reaction conditions like temperature and pressure. On the basis of charging and discharging operations, reactors are classified as either batch or steady state flow reactor. Similarly, on the basis of relative movement of the catalyst particles, reactors are categorized as fixed bed reactor where catalysts pellets are relatively fixed to each other and slurry reactor where catalysts suspended in some solvent are in motion to one another. Some common reactors used for methanol synthesis are discussed as below.

2.7.1 Fixed bed reactor

Fixed bed reactors are generally applied for gas phase reactions. Industrially methanol has been synthesized in gas phase. The process is very slow under normal reaction conditions. To improve gas phase methanol synthesis, a special reactor is designed to recycle the unreacted gases during the process.

Fixed-bed reactor has been extensively utilized for hydrogenation of carbon dioxide to methanol. A fixed-bed reactor was utilized for CO_2 hydrogenation at reaction conditions of 473 K temperature and 0.9 MPa pressure. Higher conversion of CO_2 with relatively low selectivity for methanol was documented with $Cu/ZrO_2/ZnO$ catalyst [91]. A recent study of Cai et al.[185] reported a higher CO_2 conversion and better selectivity by using fixed bed reactor for CO_2 hydrogenation to methanol over CuZnGa catalysts. Similarly, Bonura et al. [186] utilized fixed bed reactor for CO_2 hydrogenation to methanol over Cu-Zn-Zr catalysts. They found that catalyst activity was significantly altered by preparation method and concluded that gel-oxalate co-precipitation method has a superior functionality over co-precipitation with sodiumbicarbonate and complexation with citric acid methods. Furthermore, influence of Zr on the performance of Cu/Zn/Al/Zr catalysts was investigated in fixed bed reactor by Gao et al. [187]. According to their findings CO_2 conversion was directly related to the number of exposed Cu sites while methanol selectivity was more dependent on the number of basic sites of the catalyst. Similarly, the effect of fluorine on Cu/Zn/Al catalysts for CO_2 hydrogenation to methanol in fixed bed reactor was investigated [188]. In the course of study it was found that fluorine modified catalysts showed better activity for methanol synthesis in fixed bed reactor.

2.7.2 Slurry reactor

Catalyst deactivation is one of the common drawbacks of the catalysts in industrial processes. Many factors contribute to the deactivation of catalysts including poisoning, thermal degradation and compound formations as well as side reactions chemically and fouling, attrition/crushing mechanically [189]. Thermal degradation leads to catalyst deactivation especially in cases where heat is produced during reaction pathway. CO_2

hydrogenation to methanol is an exothermic reaction. This is why methanol synthesis catalysts are reported to be deactivated by heat generated due to the exothermic nature of the reaction. In such cases, in order to avoid catalyst deactivation heat generated must be reduced. One of the possible solutions is to carry out the reaction in liquid phase, where heat generated is absorbed by a reaction solvent with high values of heat capacity. Apart from avoiding catalyst deactivation, thermodynamically ~~to the~~ CO_2 hydrogenation to methanol is favored at low temperature liquid phase.

in

Slurry reactors are utilized to conduct the reaction ~~at~~ liquid phase. A comparative study of slurry reactor and fixed bed reactor for CO_2 hydrogenation was conducted by Kim et al. [190]. They concluded that application of slurry reactor increased more than by two folds conversion of CO_2 as compared to fixed bed reactor. Similarly selectively of unwanted CO formation in methanol synthesis was also reduced by using slurry reactor. Application of slurry reaction is advantageous in such reactions than conventional fixed bed reactors. Slurry phase methanol formation is preferred over traditional gas phase synthesis. This is because of controllable reaction temperature, high rate of reaction heat transfer, low cost of production and minimum cost of overall investment [191]. The potential advantages of the slurry reactors over fixed bed reactors are summarized as below.

a) Application of slurry ~~reactors~~ ensure uniform temperature as the reaction contents are well mixed.
b) Heat generated during reaction is absorbed by the slurry solvent leading to lowering reaction temperature. This also provides good heat control during the reaction.
c) Generally powder form of catalysts are applied in slurry reactors which is less expensive than pellet form.
d) ~~In~~ slurry reactors activity of the catalysts could be regenerated by withdrawing of a slip-stream.
e) Generally less reactor volume is needed in slurry reactor than fixed bed reactor in case of highly active catalysts.

Generally three types of slurry reactors have been reported in the literature. Type 1 is the stirred autoclave reactors which are commonly used in batch reactions. Type 2 slurry reactors are those where the reaction mixture is agitated with the help of a pump. In type 3 slurry reactors reactant gases are used to produce agitation. Although slurry reactors have been utilized for various reactions, however, history of slurry reactors applications for hydrogenation reactions is very old. First reported slurry reactor plant was constructed way back in 1964 at Institut du Petrole for catalytic hydrogenation of benzene to cyclohexane [192].

Liquid phase reactors were investigated to overcome thermodynamic limitations associated with methanol synthesis from CO_2 hydrogenation [53]. Owing to the exothermic nature of methanol formation, the reaction is thermodynamically more favorable at low temperature. Slurry reactors are utilized for hydrogenation of carbon dioxide to methanol, where a solvent absorbs heat produced during this process. Prior to use, thermal stability of a solvent is examined at typical reaction condition with given composition of reactant gases without catalyst. Any solvent with good heat capacity, inertness to the reactants and products, thermally stable at specified reaction conditions can be used as a slurry solvent. A variety of solvent has been investigated in this regard. Sun et al. used tetrahydroquinoline as a reaction medium for this process and reported excellent thermal stability of the solvent for methanol synthesis at temperature range of 598-698 K and total pressure of 14 MPa. Three different slurry solvents namely decahydronephthalene, tetrahydroquinoline and tetrahydronephthalene were tested for methanol syntheses. Tetrahydronephthalene resulted in higher rate of methanol formation as compared to other two solvents. Activity of ultra-fine CuB catalyst for hydrogenation of CO_2 to methanol was explored in slurry reactor under reactions conditions of 250 °C and 30 bar. Performance of CuB catalyst was enhanced by addition of Th, Cr and Zr as catalyst promoters [193]. Similarly, Chen et al. used *n*-hexadecane as a reaction solvent to carryout CO_2 hydrogenation to methanol in slurry reactor and obtain maximum yield at 275 °C [194]. The promoting effect of alcohols as reaction medium on the formation of methanol in Cu based catalyst was investigated by Zeng et al. [57]. They described a promoting role of alcohols which could be explained in reaction forms as follows:

$$CO_2 + \frac{1}{2}H_2 + Cu = HCOOCu \qquad (2.6)$$

$$HCOOCu + ROH = HCOOR + CuOH \qquad (2.7)$$

$$HCOOR + 2H_2 = CH_3OH + ROH \qquad (2.8)$$

In Cu based catalysts formate species are attached to the Cu as shown in reaction 2.6. In the presence of alcohols these formate species react with alcohol to form ester as presented by reaction 2.7. This ester on further hydrogenation is converted to methanol as displayed by reaction 2.8. The interesting thing about the alcohols solvents is that they not only participate in the reaction but are also reproduced in the end. So the net concentration of alcohol solvents is not disturbed. This behavior of alcohol solvents clearly indicates their catalytic role in the methanol synthesis. Eleven different types of alcoholic solvents namely ethanol, n-propanol, n-butanol, iso-butanol, t-butanol, n-pentanol, cyclo-pentanol, cyclo-hexanol, benzyl alcohol and ethylene glycol were investigated as reaction solvents for methanol synthesis. ~~A~~ the highest yield of methanol was reported with application of ethanol as reaction solvent.

Ethanol has been used as a slurry solvent in CO_2 hydrogenation to methanol. Ethanol has advantage over other slurry solvents as it plays a double role. Being a reaction solvent, it not only absorbs heat generated during reaction but it also plays a catalytic role in the process. Ethanol is actively involved in the CO_2 hydrogenation to methanol as presented below [195].

$$CO_2 + H_2 \rightarrow HCOOH \qquad (2.9)$$

$$HCOOH + C_2H_5OH \rightarrow HCOOC_2H_5 + H_2O \qquad (2.10)$$

$$HCOOC_2H_5 + 2H_2 \rightarrow CH_3OH + C_2H_5OH \qquad (2.11)$$

As it is evident from the reaction 2.9, formic acid is produced by hydrogenation of carbon dioxide. In reaction 2.10, formic acid reacts with ethanol solvent to produce ethyl formate. This reaction is well-known to be a fast reaction. In the last step reaction 2.11 methanol is produced by hydrogenation of ethyl formate. This last step is very

Reaction

well-known and is industrially operated at 180 °C and 30 bar ~~reaction temperature and pressure, respectively~~ [196]. Furthermore, the consumption of ethanol in step 2.10 and its regeneration with equal volumes step 2.11 confirm its catalytic role. The catalytic role of ethanol was further supported by the activity studies where methanol yield in the absence of ethanol was decreased to one-tenth of methanol produced in ethanol-accompanying system at the same reaction conditions. Moreover, this reaction pathway was further reinforced by the fact that rate of methanol synthesis was increased remarkably when ethyl formate was used as reactant with CO_2/H_2 reactant gases at the same reaction conditions [195]. The catalytic role of ethanol was further supported by Tsubak et al. [197] where methanol synthesis ~~even~~ did not even proceed when ethanol was replaced by cyclohexane as a reaction medium at 423 K reaction temperature. They further claimed that direct hydrogenation did not yield any methanol below reaction temperature of 483 K. However, addition of ethanol resulted in higher activity of the catalyst to methanol synthesis. They also reported that rate of reactants conversion as well as rate of methanol synthesis was increased by increasing concentration of ethanol to the reacting mixture. Similarly, they also found that besides the actively involvement, ethanol concentration remained the same and was not consumed when the reaction was accomplished. Active participation of ethanol in methanol synthesis reaction was also studied by Yang et al. [198]. They conducted in situ diffuse reflectance infrared Fourier-transform spectroscopy (DRIFTS) study to confirm the reaction mechanism and concluded that ethanol participated in nucleophilic addition–elimination reaction with formate adsorption species where ethanol played a part of nucleophilic reagent. They also concluded that reaction temperature was also decreased by introduction of ethanol and net concentration of ethanol remained constant due to its self-regeneration by hydrogenation of ethyl formate. Furthermore, they also found that addition of large quantity of ethanol increased the overall rate of reaction. Shi et al. [199] utilized ethanol as reaction solvent for methanol synthesis and also claimed that ethanol played a dual role of reaction medium as well as catalyst. As a consequent, higher activity and better methanol selectivity was observed by application of ethanol. In addition this dual role of ethanol in methanol synthesis has consistently been reported in the literature [57, 195, 197, 199, 200].

2.8 Effect of reaction parameters

A number of factors affect the rate of CO_2 hydrogenation to methanol. Some common parameters are discussed as below.

2.8.1 Effect of reaction temperature

Generally rate of reaction increases with increase in reaction temperature as it increases the average kinetic energy of the reacting molecules. However, as stated earlier methanol synthesis from CO_2 hydrogenation is exothermic in nature hence, it is favorable at low reaction temperature. On the other hand, higher activation energy is required to overcome the energy barrier of CO_2. Consequently, rate of CO_2 hydrogenation increases with the rise in reaction temperature but only up to certain degree. At higher temperature rate of CO_2 hydrogenation falls because of decrease in the thermodynamic equilibrium constant with increasing temperature. Therefore this reaction is not suitable at very high temperature. A suitable reaction temperature for CO_2 hydrogenation to methanol has been quite debatable in the literature. According to Fujitani et al. [201] rate of methanol synthesis by CO_2 hydrogenation increases by increasing temperature but only up to 493 K and any further rise in this temperature depresses the rate of reaction. Similarly 523 K was claimed to be the maximum temperature for CO_2 conversion and yield of methanol [202]. This discrepancy is quite understandable if we recall other associated reactions occurring along with the CO_2 hydrogenation to methanol. Reverse water gas shift (RWGS) is one important reaction taking place with CO_2 hydrogenation as shown in reaction 2.12.

State what temp ?

sup

$$CO_2 + H_2 \rightleftharpoons CO + H_2O \quad \Delta H^0{}_{298K} = +41.2 \ kJ/mol \qquad (2.12)$$

Due to the endothermic nature, this reaction is favorable at high temperature. So increase in reaction temperature will shift the CO_2 hydrogenation to reverse water gas shift reaction. Moreover, apparent activation energies of methanol synthesis and RWGS reaction are given at different reaction conditions in Table 2.2. The apparent activation energies of RWGS reaction are closely grouped at different reaction conditions. In contrast, methanol synthesis has widely placed apparent activation energies over the entire range of reaction conditions. This also indicates that reaction pathways are dependent on the reaction conditions like composition of catalyst and reaction conditions. Moreover, it also implies that methanol synthesis is more sensitive than RWGS reaction in terms of reaction condition. Additionally, in all cases the apparent activation energy of RWGS is more as compared to the methanol synthesis. This implies that rate of RWGS reaction is faster than methanol synthesis reaction with increasing temperature.

Similarly, methanol decomposition to CO is shown by ~~r~~Reaction 2.13

$$CH_3OH \rightleftharpoons CO + 2H_2 \qquad \Delta H^0{}_{298K} = +90\ kJ/mol \qquad (2.13)$$

This reaction too is endothermic and therefore is favorable at elevated temperature. So in this regard, ~~rise~~ increase in reaction temperature will decompose the methanol to produce CO. Ahouari et al. [89] reported that CO_2 conversion and methanol production was increased with increasing reaction temperature and maximum methanol yield was recorded at 250 °C and decreased beyond this temperature. They noticed that at higher temperature major part of CO_2 was converted to CO and only a small fraction was hydrogenated to methanol. They also described that methanol synthesis reaction was more sensitive to reaction temperature than the reverse water gas shift reaction. Furthermore they also found the evidence of methane formation at 350 °C. Similar investigations were also reported by Qi et al. [203] where rate of methanol formation was increased with increasing temperature and maximum yield of methanol was recorded at 240 °C. Beyond this point rise in reaction temperature declined the methanol synthesis rate and subsequently rate of CO formation was increased. They also concluded that reaction temperature was the controlling factor for transformation of reaction from kinetics to thermodynamics. In the same way, selectivity of methanol was declined from 37.6 % at 220 °C to only 2.1 % at 300 °C. However, CO_2 was further increased from 16.2 % at 220 °C to 28.3 % at 300 °C and consequently selectivity of CO increased from 62.3 % at 220 °C to 97.2 % at 300 °C. Indeed, it is quite evident from these results that reverse water gas shift reaction exceeds methanol synthesis at higher temperature [69]. Xin et al. [202] studied effect of temperature on performance of Cu/Zn/Al/Zr fibrous catalyst at a constant reaction pressure of 5 MPa in slurry reactor. Methanol synthesis and carbon dioxide conversion was tested in temperature range of 210 to 270 °C at 5 MPa constant reaction pressure and effect of reaction temperature on methanol yield as well as CO_2 conversion is presented in Figure 2.5. Methanol yield was observed to increase from 11.4 % at 210 °C to 17.9 % at 250 °C, while methanol yield was dropped with further increase of temperature. Because of thermodynamic constrains optimum yield of methanol was obtained at 250 °C. However, a linear relationship was observed between CO_2 conversion and degree of reaction temperature. Similar trend for CO_2 conversion was also reported by Tidona et al. [204]. More importantly the optimum value of reaction temperature is also dependent on the nature of catalyst. Chen et al. [194] investigated the role of reaction temperature for two different catalysts namely 20 % Cr-CuB and 20% Th-CuB. They found that reaction temperature played a vital role in productivity of methanol and maximum yield of methanol was obtained at 275 °C for 20 % Cr-CuB and 225 °C for 20 % Th-CuB catalysts.

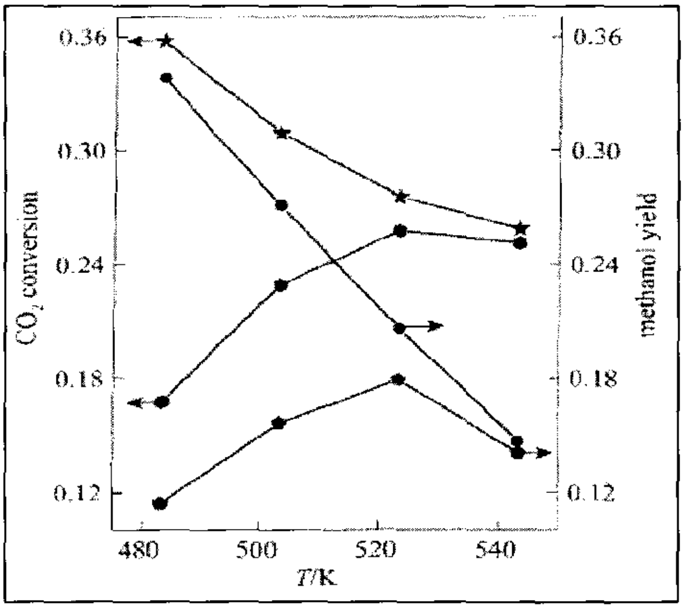

Figure 2.5: Relationship between reaction temperature and CO_2 conversion and methanol yield from experimental results and thermodynamic predictions [202]

Summary

In concl~~uding the discussio~~n, reaction temperature affects the catalyst activity as well as product selectivity. Reaction temperature was declared to be the main factor for catalysts activity as well as methanol selectivity.

Table 2.2: Activation energies of methanol synthesis and RWGS reactions [69]

Catalyst	E_A kJ/mol		Experimental conditions		Feed Gas
	Methanol synthesis	RWGS	T (°C)	P (bar)	
$Cu/ZnO/Al_2O_3$	104	109	170-220	50	H_2/CO_2
$Cu/ZnO/Al_2O_3$	65.2	123	210-245	15-50	H_2/CO_2
$Cu/ZnO/Al_2O_3$	54.3	-	200-280	60	$H_2/CO_2/CO$
$Cu/ZnO/Al_2O_3$	77.7	125	200-250	50-100	H_2/CO_2
Cu/ZnO	64	121	150-250	1	H_2/CO_2
Cu/ZrO_2	49.7	93.2	200-260	17	H_2/CO_2

2.8.2 Effect of reaction pressure

From thermodynamics point of view, hydrogenation of CO_2 to methanol is favorable at high pressure. Methanol synthesis as given in reaction 2.2 is molecular-reducing reaction, so according to Lishetliers principle it will best suited at higher reaction pressure. On the other hand, both RWGS (reaction 2.3) and methanol decomposition (reaction 2.4) being molecular-increasing reactions will be depressed by increasing reaction pressure. So indeed, in both cases methanol synthesis rate as well as selectivity will be enhanced thermodynamically. Furthermore, formation of water molecules during methanol synthesis also work as driving force to shift the RWGS to the left side decreasing the CO production. Nevertheless, increase in reaction pressure also accelerates oxygenate formation and oxygenates have been reported to increase selectivity for dimethyl ether synthesis rather than methanol at high pressure [205].

Le Chatelier

In the beginning, methanol synthesis was carried out at very high pressure when first started in 1920's by BASF. However, the reaction pressure was reduced to 50-100 bar by the introduction of ICI method in 1960. Graaf et al. in 1988 developed a low pressure methanol synthesis model. They claimed that their low pressure methanol synthesis model was more precise than all other previous reported models [206]. Similarly, Liu et al. [12] reported that methanol could be produced at as low pressure as 20 bar. Liaw et al. [193] investigated the effect of pressure at constant reaction temperature of 210 °C and found that methanol synthesis as well as CO_2 conversion increased with increasing pressure. Similarly, An et al. [202] studied effect of pressure on performance of Cu/Zn/Al/Zr fibrous catalyst in slurry reactor at constant reaction temperature of 523 K. The relationship between CO_2 conversion and methanol synthesis with respect to reaction pressure is presented in Figure 2.6. It is quite clear from the Figure that increase in reaction pressure favors the CO_2 conversion and methanol yield. Tidona et al. [204] investigated performance of Cu/Al_2O_3 and commercial $Cu/ZnO/Al_2O_3$ catalysts for CO_2 hydrogenation to methanol over wide range of pressure. They reported that increase in pressure from 50 to 360 bar resulted in three fold increase in methanol formation. Interestingly, methanol yield was independent of reaction pressure at temperature lower than 250 °C.

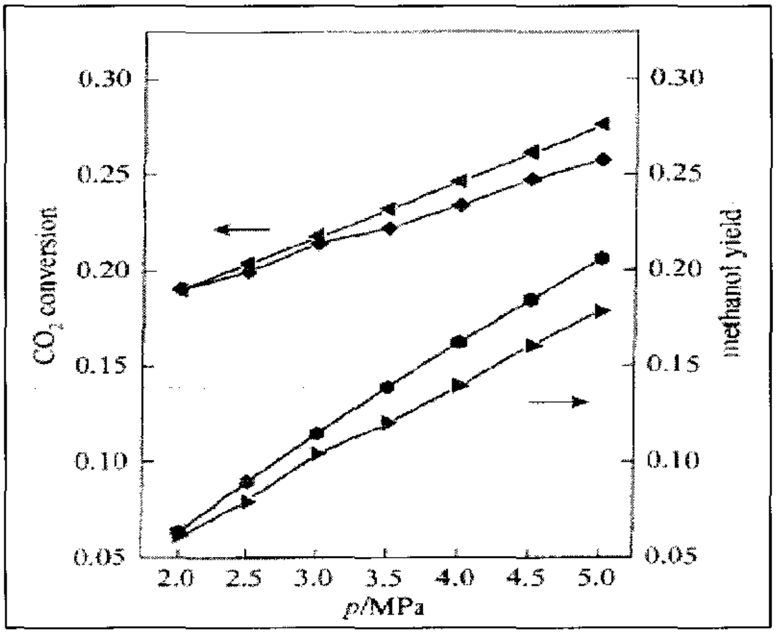

Figure 2.6: Relationship between reaction pressure and CO_2 conversion and methanol yield from experimental results and thermodynamic predictions [202]

Nevertheless, methanol synthesis at very high pressures is unsafe and it will also increase the production cost.

2.9 Effect of feed gases composition

Thermodynamically, feed gas ratio can be calculated by observing. CO_2 hydrogenation as below

$$CO_2 + 3H_2 \rightleftharpoons CH_3OH + H_2O \qquad \Delta H^0{}_{298K} = -49.5 \;\; kJ/mol \qquad (2.14)$$

As it is quite obvious from reaction 2.14 that one mole of CO_2 is reacting with three moles of H_2. So thermodynamically H_2/CO_2 = 3 will be favorable for CO_2 hydrogenation to methanol. However, in practical application this factor is quite debatable.

Conventionally, most of methanol synthesis has been carried out with stoichiometric value of H_2/CO_2 molar ratio of 3. Urakwa et al. [207] investigated methanol synthesis by varying the feed gas ratio at constant reaction pressure 360 bar and temperature 260 °C over $Cu/ZnO/Al_2O_3$ catalyst in tubular reactor. They documented a drastic increase in methanol synthesis as well as CO_2 conversion by switching the molar ratio of H_2/CO_2 from 3 to 10. This suggests that higher partial pressure of H_2 favors the methanol formation. Moreover, the methanol synthesis at higher pressure was found to thermodynamically controlled at $CO_2/H_2 = \geq 10$, whereas reaction is kinetically controlled at molar ratio of < 10. Shen et al. [208] conducted computational study to examine the effect of feed gas ratio on production of methanol. They investigated H_2/CO_2 ratio in the range of 0.5, 1, 2, 3, 4 and 5 at different degrees of reaction temperature at constant pressure and vice versa. The methanol yield was observed to ~~be~~ increased significantly with increasing ratio of H_2/CO_2 at each degree of reaction temperature (483 K, 523 K, and 563 K) with 3MPa constant pressure. Similarly, study of methanol synthesis at varied reaction pressure (1MPa, 2MPa, 3MPa, 5MPa, 7MPa and 9MPa) and constant reaction temperature 523 K revealed the same linear trend between ratio of H_2/CO_2 and methanol synthesis rates. Similar results were reported by Kim et al. [190] in their CO_2 hydrogenation investigation conducted in slurry reactors. They studied H_2/CO_2 ratio of 2-5 and higher CO_2 conversion rates were observed by increasing H_2/CO_2 ratio. This could be simply justified that as increase in H_2/CO_2 ratio actually increases the hydrogen part in the feed gas mixture so increasing

?

concentration of hydrogen will promote the hydrogenation process further leading to enhance both CO_2 conversion as well as methanol synthesis.

2.10 Artificial neural networks for kinetics modeling

Artificial neural networks (ANN) has been developed by McCulloh and Pitts in 1940s [209]. However, the model became more popular around 1985 when back propagation method for training neural networks was presented by Rumelhart et al. [210]. Since then ANN model has been extensively investigated for predicting rate of reactions, forecasting and recognizing patterns [211-213].

ANN is mathematical and computational model which performs parallel processing of informations. A neural network contains an interconnected group of artificial neurons and connectionist approach is used to process the information (Figure 2.7). In general practice each neuron acts as a processing unit which collects some numerical inputs, multiplies the inputs by adjustable parameters called weights, and the result is obtained by adding a scalar parameter termed as bias.

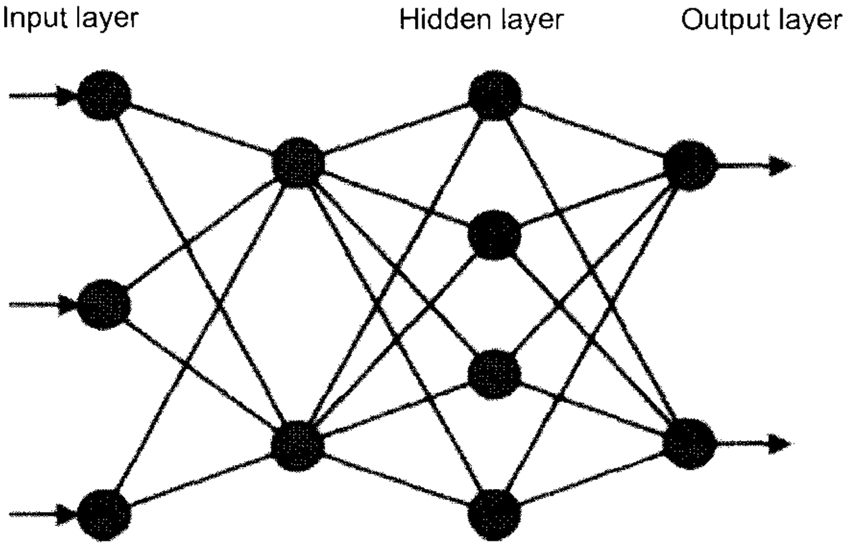

Figure 2.7: Structure of a typical multilayer perceptron neural network [214]

Structure of a typical artificial neuron is shown in Figure 2.8. In a typical experiment, when the sample (train) data is introduced to the network, the model adjusts its structure (the weights and biases) in such a way that finds the pattern between the input and output parameters called targets.

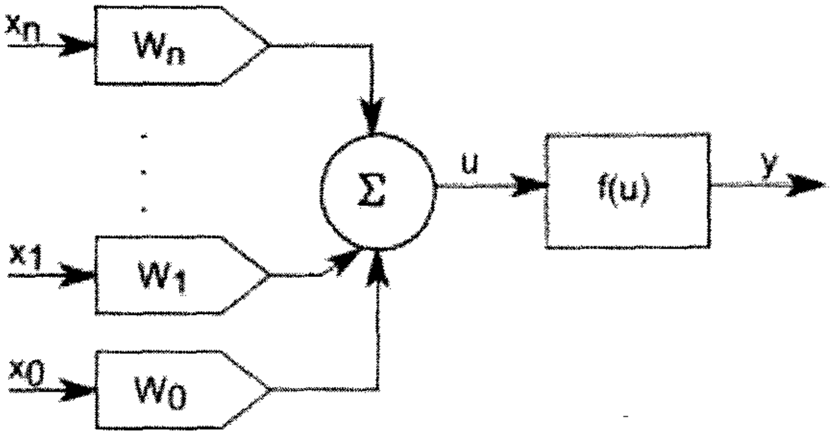

Figure 2.8: Structure of a typical artificial neuron [215]

ANN model has been declared as a promising technique, when complex reaction systems cannot be well understood or in case, where the basic knowledge of reaction mechanisms is not well known. Since CO_2 hydrogenation is a complex reaction and the exact mechanism is not yet identified, so the ANN model is best suited to be studied for finding the kinetics of reactions. Besides this, it has been reported that ANN model is 120–5000 times faster than phenomological models and therefore have an extra advantage of computation times [216]. Due to all these advantages ANN model has been widely investigated to formulate kinetic models for different biological and conventional chemical reactors [217, 218]. Recently, ANN model was employed to study reaction kinetics of methanol dehydration over nano Al_2O_3 catalyst by Alamolhoda et al. [214] in slurry reactor. It was concluded that rate estimation by ANN model significantly matched with the rate calculated on the experimental basis.

CHAPTER 3

RESEARCH METHODOLOGY

3.1 Background of chapter

This chapter focuses on the methodology and the experimental work performed during the study.

The overall process of research methodology is summarized in Figure 3.1.

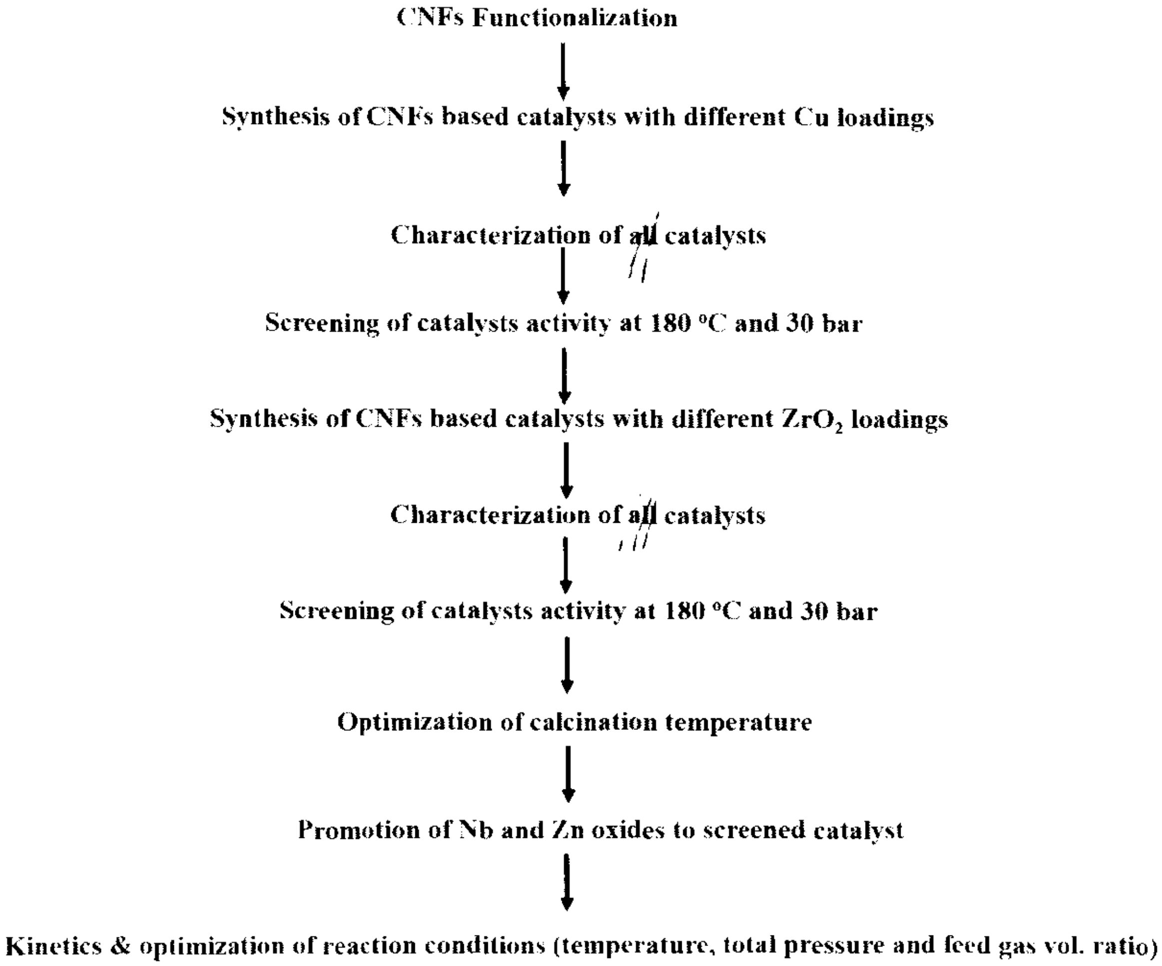

Figure 3.1: Research methodology layout

3.2 Materials

A variety of chemicals were used in the research. These are tabulated in Table 3.1.

Table 3.1: Chemicals and gases used in the study

Materials	**Supplier**	**Purity (%)**	**Purpose**
Cu $(NO_3)_2.3H_2O$	R&M Chemicals, UK	99	Catalyst precursor
$ZrO(NO_3)_2 \cdot xH_2O$	SIGMA-ALDRICH, USA	99	Catalyst precursor
Ammonium niobate (v) oxalate $(C_4H_4NNbO_9)$	SIGMA-ALDRICH, USA	99.99	Catalyst promoter
$Zn(NO_3)_2 \cdot 6H_2O$	SIGMA-ALDRICH, USA	99.9	Catalyst promoter
HNO_3	Merck	30	CNFs activation
CNFs	state name of company & brand Korea	99	Catalyst support
$5\%H_2/N_2$	Malaysian oxygen MOX	99.9	Reduction
H_2/CO_2	Malaysian oxygen MOX	99.9	Reactant gas
N_2O	Malaysian oxygen MOX	100	Chemisorption
NH_3	Malaysian oxygen MOX	99.9	Catalyst acidic profile
CO_2	Malaysian oxygen MOX	99.9	Catalyst basic profile

3.3 Methods

Deposition precipitation method was used for synthesis of catalysts. Prior to use as a catalyst support, carbon nanofibers (CNFs) were activated by an oxidizing agent. The detailed procedures are given as in the following sections.

3.3.1 Activation of CNFs

In typical experiment, CNFs were activated by refluxing 5 grams of CNFs with 35 vol.% nitric acid solution at 90 °C for 16 hours. The oxidized CNFs were filtered via vacuum filtration, and were washed with distilled water until the filtrate pH was more than five. The treated CNFs-O were dried overnight at 110 °C [140, 158, 219].

3.4 Synthesis of catalysts

All catalysts were synthesized by using the deposition precipitation method [132, 157, 175, 178, 183]. A schematic diagram is illustrated in Figure 3.2.

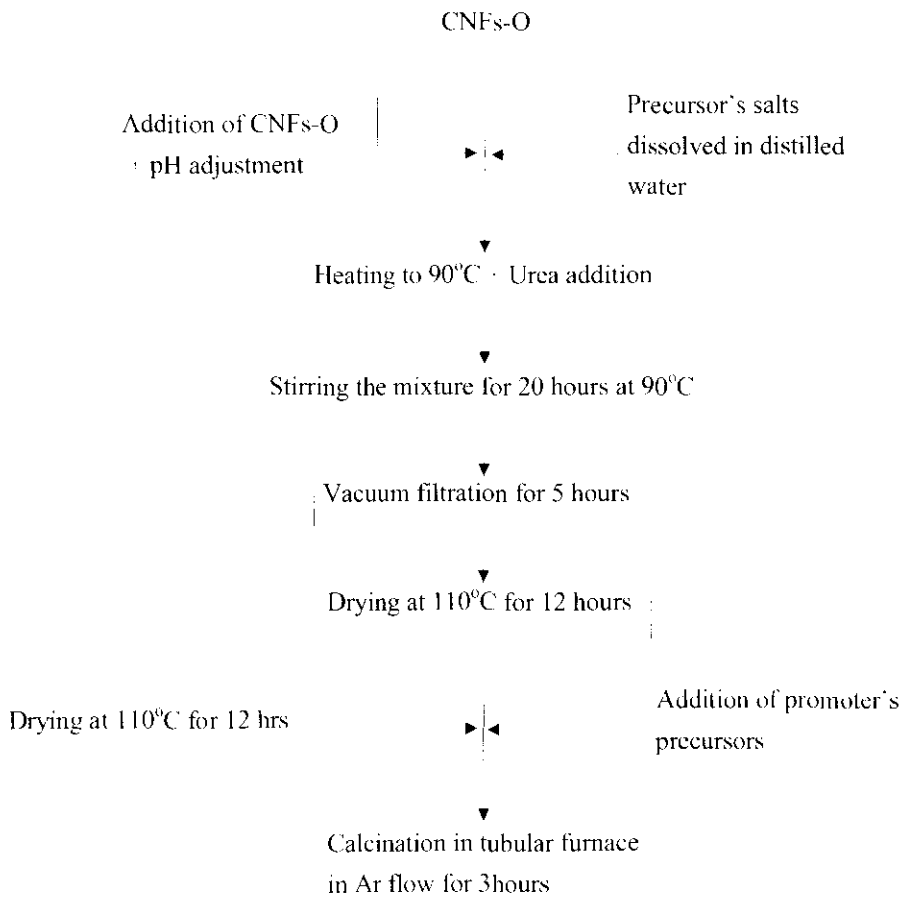

Figure 3.2: Flow chart for synthesis of CZC catalysts

Catalyst particles can be deposited on the surface of CNFs via different methods like impregnation and ion exchange methods [220, 221]. In the current work, deposition precipitation method had been employed [157, 160]. This method was selected for preparation of catalysts because it had been reported for preparation of highly loaded and well-dispersed catalysts [132, 175, 178, 183]. Nitrates salts were used as a precursor material for all metals due to their availability, higher solubility in water, easy removal of nitrates, and their rapid decomposition rate for formation of oxides compared to other precursors. The required amount of precursor was calculated to produce 5 grams of catalyst. Calculations for catalyst formulation are given in Appendix A (Section A1).

3.4.1 Preparation of bimetallic catalysts

Deposition precipitation method was employed to synthesize $Cu/ZrO_2/CNFs\text{-}O$ (CZC) catalysts [157, 160]. A required quantity of $Cu(NO_3)_2.3H_2O$ (R&M Chemicals, UK) was dissolved in 250 ml of distilled water. The solution was stirred for 10 minutes to obtain a clear solution. A 5 gram of oxidized CNFs were added to the solution and stirred. The pH of the solution was adjusted to 2.3 by adding dilute HNO_3. Next, the solution was heated to a temperature of 90 °C. 1 gram of urea (R&M Chemicals, UK) solution in 6 ml of distilled water was added to the solution as a precipitating agent. The solution was stirred for 20 hours. Later, the slurry was cooled to room temperature and it was filtered via vacuum filtration. The copper loaded CNFs were washed with distilled water and were dried at 110 °C for 12 hours.

The same procedure was repeated for the loading of ZrO_2. The dried copper loaded CNFs-O were added to a solution of zirconyl nitrate hydrate (SIGMA-ALDRICH, USA). The synthesized bimetallic catalyst was washed with deionized water, dried at 110 °C for 12 hours, and the dried samples were calcined in tubular furnace in Argon flow at 350 °C for 3 hours with temperature ramping of 5 °C/min.

3.4.2 Preparation of bimetallic catalysts with promoters

The bimetallic catalysts were later promoted with different loadings of Nb and Zn oxide promoters.

a) Nb promoted bimetallic catalysts

In order to investigate the effect of Nb oxide, different amounts of Nb_2O_5, namely 0.4, 0.8, and 1.2 wt%, were loaded on CZC catalyst. In the first step, the bimetallic catalysts were synthesized as discussed earlier. This parent catalyst was added to the solution of Nb precursor (ammonium niobate (v) oxalate hydrate 99.99% pure Aldrich). The slurry was stirred for 16 hours at lower pH with urea hydrolysis. Next, the modified catalysts were filtered, washed with distilled water, and dried at 110 °C overnight. The Nb_2O_5 loaded catalysts were calcined and reduced before reaction studies were carried out.

b) ZnO promoted bimetallic catalysts

The effect of ZnO promoter was also studied for CO_2 hydrogenation. CZC catalysts were loaded with four different concentrations of ZnO, namely 1, 2, 3, and 4 wt.%. The same procedure was adopted for ZnO as described in 3.4.2. (a). $Zn(NO_3)_2 \cdot 6H_2O$ sigma-Aldrich was used as Zn precursor in the study. All catalysts prepared in the course of study are listed in Table 3.2.

Table 3.2: List of prepared catalysts for the current study

No.	**Catalyst notation**	**Catalyst composition**	**1st Metal Cu wt%**	**2nd Metal**	**Promoters**	
				ZrO_2 wt%	**Nb_2O_5 wt%**	**ZnO wt%**
1	CZC5	Cu/ZrO_2/CNFs	5	10	-	-
2	CZC10		10		-	-
2	CZC15		15		-	-
4	CZC20		20		-	-
5	CZC25		25		-	-
6	5CZC	Cu/ZrO_2/CNFs	15	5	-	-
7	15CZC			15	-	-
8	20CZC			20	-	-
9	25CZC			25	-	-
10*	CZC350	Cu/ZrO_2/CNFs	15	15	-	-
11*	CZC450				-	-
12*	CZC500				-	-
13*	CZC550				-	-
14	CZC-Nb16	Cu.Nb/ZrO_2/CNFs	15	15	0.4	-
15	CZC-Nb32				0.8	-
16	CZC-Nb48				1.2	-
17	CZC-Zn1	Cu.Zn/ZrO_2/CNFs	15	15	-	1
18	CZC-Zn2				-	2
19	CZC-Zn3				-	3
20	CZC-Zn4				-	4

* CZC350, * CZC450, * CZC500, and * CZC550 are 15CZC catalysts calcined at 350, 450, 500 and 550 °C temperatures, respectively.

3.5 Characterization of catalysts

The activity and the selectivity of the catalysts had been affected by different physiochemical parameters. The prepared catalysts were characterized in order to investigate the physiochemical profiles of CZC catalysts. Bulk phase components, as well as surface components of catalysts, were characterized with different techniques. A brief description of the characterization techniques is given in Table 3.3, while the detailed procedure of each technique is briefly discussed in the following sections.

Table 3.3: Characterization techniques used for CZC catalysts

No.	**Technique**	**Instrument model**	**Purpose of investigations**
1	XRD	Brukar A&S D8 Advanced	Structure and phase studies
2	FT-IR	Perkin-Elmer spectrum one	Functional groups identification
3	TEM	Zeiss LIBRA 200 FE TEM	Morphology and particle size
4	N_2 adsorption-desorption	Micromeritics ASAP 2020	Surface are, pore size and pore volume
5	TGA	Perkin Elmer (Pyris 1)	Decomposition and calcination temperature
6	H_2-TPR	TPDRO (100 MS)	Reducibility of catalyst
7	CO_2-TPD	TPDRO (100 MS)	Basic sites determination
8	NH_3-TPD	TPDRO (100 MS)	Acidic sites determination
9	ICP-OES	Perkin Elmer	Metal loading
10	N_2O Chemisorption	TPDRO (100 MS)	Metal surface area (Cu^0)
11	XPS	Thermo-Fischer k-Alpha	Surface composition and oxidation states

[illegible]

3.5.1 X-ray diffraction (XRD)

X-ray diffraction (XRD) is one of the most widely used techniques for characterization of solid materials. Although x-rays were discovered way back in 1985 by W.C. Rontgen, the technique gained its popularity in the 1970s when the refinement method for powder structure was introduced by H.M. Rietveld [222].

In the present work, characterization of samples had been done using an X-ray diffractometer. The XRD technique was employed to investigate the structure and the phase of catalysts. Bruker A&S D8 Advanced Diffractometer was used at room temperature. The instruments had been fitted with CuKα as the radiation source was operated at 40 kV and 30 mA with scanning 2θ angle range of 10-80° with 1.2 °C/min of scanning speed. About 0.6 gram of sample quantity was used for analysis.

3.5.2 Fourier transform infra-red (FT-IR)

Fourier transform infra-red (FT-IR) analysis is based on molecular absorption spectrum generated by transmitted light. Fourier Transform Infrared Spectroscopy (FT-IR) is a useful tool for identification of functional groups. Both organic and inorganic functional groups can be identified via FT-IR. It can be utilized for quantitative, as well as qualitative analyses. Similarly, samples in solid, liquid, or in gas phase can be analyzed by using this tool. Besides, FT-IR has been extensively used in laboratories for identification of various compounds.

In the current study, Perkin Elmer Spectrum- I spectrometer was employed for FT-IR analysis. Prior to analysis, the samples were pelleted with KBr (Potassium Bromide) by using hydraulic pressurizing equipment and the characterization was performed in a wavelength range of 400-4000 cm^{-1}.

3.5.3 Diffuse reflectance spectroscopy

Diffuse Reflectance Spectroscopy (DRS), also known as Elastic Scattering Spectroscopy, is a non-invasive technique that measures the characteristic of reflectance spectrum produced as light passed through a medium. When incident light strikes a surface, the rays are diffracted. The diffracted rays may be symmetrical and appear in a normal line called specular reflection. In contrast, the incident light may be scattered in different directions, such as diffraction, and it is called diffuse reflection.

In the current work, Agilent Cary 100 UV-VIS Spectrophotometer was employed for this purpose. The samples were investigated in ultra violet regions from 200-400 nm and in visible regions from 400-800 nm.

3.5.4 Raman spectroscopy

Raman spectroscopy is a very powerful technique in understanding molecular structure. This technique is preferred over other techniques as it is simple and requires no special procedure for sample preparation and very little amount of sample is required for analysis.

HORIBA Jobin Yvon model HR 800 Raman Spectrometer with laser source of 514 nm and focal length of 800 nm was utilized for Raman study.

3.5.5 Inductively coupled plasma optical emission spectrometry

Inductively coupled plasma optical emission spectrometry (ICP-OES) is one of the most powerful and popular analytical techniques applied for the determination of trace metals.

In the current study, ICP-OES Perkin Elmer was used for metal analysis. The samples were digested in a mixture of nitric acid and hydrochloric acid with a volume ratio of 1:3 (Aqua Regia). The digestion was carried out in a digestive system for 45 minutes at 200 °C. The digested samples were then diluted with distilled water to a required volume. The diluted samples were tested with ICP-OES for metal analysis.

3.5.6 X-ray photoelectron spectroscopy (XPS)

As catalysis is a surface phenomenon, so the information regarding the surface of catalyst is vital in understanding the surface chemical profile of catalysts. X-ray photoelectron spectroscopy (XPS) is generally used to investigate the nature of chemical and the composition of catalysts surfaces. Furthermore, information pertaining to the elemental composition, oxidation states of active components, and their relative abundance is also obtained via XPS analysis. X-ray photoelectron spectroscopy (XPS) or electron spectroscopy for chemical analysis (ESCA) was first introduced by a Swedish physicist in 1960 and he was awarded the Nobel Prize in 1981 for his invention.

XPS is based on the photoelectric effect, whereby electrons from an X-ray source (AlK$_\alpha$, MgK$_\alpha$) ~~are~~ penetrated ~~in~~ the first few atomic layers (normally 2-20 atomic layers, depending on material) of sample, placed in Cu sample holder. In general procedure, photons with hv energy strike the surface atoms of the sample. This energy is absorbed by the surface atom which leads to eject a core or valence electron with binding energy E$_b$ and E$_k$ as kinetic energy. The binding energy of electron is equal to the difference of the two sets of energy with correction factor φ, as shown by Equation 3.1.

$$E_k = hv - E_b - \varphi \qquad (3.1)$$

where:

E_k is kinetic energy of the photoelectron, h is plank's constant, v is the frequency of excitation radiation, E_b is the binding energy of electron and φ is the work function of spectrometer.

Elements are identified based on their binding energy, as each element has its characteristic set of binding energies [223]. Binding energies of some elements/compounds are given in Table 3.3.

Table 3.3: Binding energies of some relevant elements/compounds

Element/compound	**Peak name**	**Binding energy (eV)**	**Reference**
Cu	$2p_{1/2}$	932.7	[224]
	$2p_{3/2}$	953	[224]
Zr	$3d_{3/2}$	184.6	[225]
	$3d_{5/2}$	182.2	[225]
Zn	$2p_{1/2}$	1046	[226]
	$2p_{3/2}$	1023	[226]
Nb	$3d_{3/2}$	210	[227, 228]
	$3d_{5/2}$	207	[227, 228]

In the current study, an X-ray photoelectron spectroscopy (XPS, Thermo-Fisher K-Alpha) was utilized for XPS investigations. The XPS was equipped with Alk source with ultimate energy resolution of ≤ 0.5 eV. The energy of the instrument analysis chamber was 50 eV, while it was pressurized to $3.81\text{x}10^{-7}$. The samples were placed in the sample holder with maximum capacity of 6 samples per tray. Identification of chemical state and peak fitting of the resultant XPS spectra were analyzed with Avantage software. Similarly, background correction was carried out by using Shirley background corrections. The atomic composition ratio of different metals was calculated by using a sample relation, as depicted in the following equation 3.2 [233, 234].

$$N1/N2 = (I1/S1)/(I2/S2) \qquad (3.2)$$

where, N is the composition, I is the peak area, and S is the sensitivity factor of the correspondence metal.

3.5.7 Thermal gravimetric analysis

Thermal stability is an important parameter in catalyst profile. Thermo gravimetric analysis (TGA) provides information of weight/mass loss of material under investigation as a function of degree of temperature and time. A suitable degree of calcination temperature of the catalyst can be identified via this technique [229].

TGA was carried out on Perkin Elmer (Pyris 1). About 20 mg of sample was analyzed for TGA in an inert environment of N_2 with a flow rate of 20 ml/min. The weight loss of the catalyst was evaluated ~~with~~ at a temperature range of 30-800 °C and at a heating rate of 10 °C, min.

3.5.8 H_2-temperature programmed reduction (H_2-TPR)

Reduction behavior is an important tool to determine the metal support interaction of catalyst. Hence, H_2-temperature programmed reduction (H_2-TPR) can be utilized to scrutinize the redox profile of catalysts. Besides, H_2-TPR also provides information about the interaction of metals with underlying support. Furthermore, particularly in bimetallic catalysts, alloy formation can also be characterized via TPR investigations. On top of that, addition of a second metal or incorporation of promoters to the parent catalyst can alter the redox properties of the catalysts, which can be verified with TPR analysis [230].

In this study, reducibility of the catalyst was conducted by using the H_2-TPR technique. TPDRO (1100 MS) was used for H_2-TPR investigations. 20 mg of catalyst was placed in a U-shaped quartz sample tube. The sample was pretreated in N_2 for one hour at 200 °C with a heating rate of 10 °C/min. After it cooled down, the adsorbing gas was switched to 5 % H_2 in N_2, and H_2-TPR was performed with 20 cm^3/min flow rate of gas. The H_2-TPR was studied for four hours with a temperature range of 30-900 °C with a heating rate of 10 °C/min. Meanwhile, a thermal conductivity detector (TCD) measured the amount of H_2 adsorbed during the course of the analysis.

3.5.9 Temperature programmed desorption (CO_2-TPD, NH_3-TPD & N_2O chemisorption)

Acidic and basic properties of catalysts are vital in heterogeneous catalysis. Furthermore, the nature and the strength of acidic and basic sites at the surface affect the catalyst activity as well as its selectivity. A number of techniques are available for measuring the types of acidic sites in catalysts. One of the methods is by using probe molecules like CO_2 and NH_3 for characterizing basic sites and acidic, respectively. TPD method, being simple, reproducible and rapid, is preferred over other techniques applied for the same purpose. As for the CO_2-TPD measurement, the sample was first cleaned by degassing at 200 °C with inert gas. After cooling the samples were reduced in 5 % H_2 in N_2 flow at 523 K for 2 h and subsequently flushed with pure helium (50 mL/ min) for 30 min to remove the excess hydrogen. The reduced samples were subjected to CO_2 and NH_3 at 150 °C for CO_2-TPD and NH_3-TPD analysis, respectively. The temperature was again dropped to room temperature. The adsorbed molecules were desorbed in helium flow at 800 °C with a heating rate of 10 °C/min [187, 231]

CO_2-TPD measurements were performed to calculate the basic sites, while the acidic sites were investigated via NH_3-TPD. In both cases, prior to analysis, the samples were degassed under helium flow at 200 °C with a heating rate of 10 °C/min. Then the reduced samples were subjected to pure CO_2 and NH_3 for CO_2-TPD and NH_3-TPD, respectively at 150 °C and were cooled down to room temperature in the flow of same gases. In the last step, two adsorbed gases were desorbed under helium gas flow at 800 °C with 10 °C/min heating rate.

The number of total acidic sites was evaluated from intensity of desorption peaks, while the number of total acidic sites divided by surface area produced the density of total acidic sites on the surface of catalyst [232]. The degree of temperature, at which ammonia is desorbed, is an indicator for strength of acidic sites in the catalysts, whereas concentration of acidic sites could be predicted from the intensity of desorption peak.

Meanwhile, the metal surface area plays an important role in forecasting and in elucidating the performance of catalyst for a particular reaction. Traditionally, metal surface area (MSA) of Cu is determined via nitrous oxide pulse method. Carbon monoxide and hydrogen have also been used as probe gases for determining Cu surface area. However, these methods are ~~have been~~ believed to be unreliable due to the uncertainties of the nature and the extent of different adsorption sites associated with adsorption of these two adsorbates. Hence, in the current work, N_2O chemisorption titration method ~~had~~ has been utilized.

N_2O chemisorption can be summarized in three chemical steps, as portrayed in the following equations 3.3-3.5:

$$CuO + H_2 \rightarrow Cu + H_2O \qquad (3.3)$$

In the first step, reaction (3.3) CuO is hydrogenated to Cu. The quantity of H_2 consumption is used to calculate the concentration of Cu^{2+}. This is a normal TPR study adopted for Cu based catalyst. In the second step, as indicated by reaction 3.4, two moles of Cu are reacted with N_2O to produce Cu_2O, while one mole of N_2 is liberated in the process.

$$2Cu + N_2O \rightarrow Cu_2O + N_2 \qquad (3.4)$$

In the final step, Cu_2O is hydrogenated to Cu, as shown in reaction 3.5 below.

$$Cu_2O + H_2 \rightarrow 2Cu + H_2O \qquad (3.5)$$

On the other hand, the dispersion of Cu (D_{Cu}) was calculated by reaction 3.6.

$$\%D_{Cu} = \frac{2C_2}{C_1} \times 100 \qquad (3.6)$$

Where C1 is the consumption of H_2 in equation 3.3, whereas C2 shows the H_2 consumption in reaction 3.5.

In calculating Cu surface area (S_{Cu}) and average copper particle size (d_{Cu}), a spherical shape of Cu particles was assumed. A chemisorption stoichiometry ratio of Cu:N_2O=2:1 was used with density of Cu atoms at 1.46×10^{19} Cu atom/m^2 was assumed. The detailed calculations are presented in Appendix C (section C1). Copper surface area was calculated by using formula 3.7 [233].

$$S_{Cu}(m^2/g) = (nCu \times N)/(1.4 \times 10^{19} \times W) \quad (3.7)$$

where S_{Cu} is the exposed copper surface area per gram catalyst, W is the weight of the reduced catalyst, n Cu is the number of moles of copper, N is Avogadro's constant (6.02×10^{23} atoms mol^{-1}), and 1.4×10^{19} is the number of copper atoms per square meter.

Besides, the average particle size (d_{Cu}) was obtained with a conventional formula 3.8 [2, 234].

$$d_{Cu}(nm) = \frac{104}{D_{Cu}(\%)} \quad (3.8)$$

In the experiment, the catalyst was first reduced in a flow of 5 vol.% H_2/Ar (30 mL/min), with a heating rate of 10 °C/min at 500 °C for 1 hour. The reduced catalyst was cooled to 60 °C in He flow (30 mL/min), and then was purged with He for 30 min. Then, pure N_2O (40mL/min) was introduced to the catalyst at 60 °C for 1 h. Subsequently, the residual N_2O was removed by purging the catalyst with He (30mL/min) for 1 h. In the last step, the sample was reduced again in a flow of 5 vol.% H_2/Ar (30 mL/min) at 500 °C with a heating rate of 10 °C/min for 1 hour [235].

3.5.10 Transmission electron microscopy (TEM)

Transmission Electron Microscopy (TEM) is used to examine the morphology of a catalyst. In investigations concerning nanomaterial, TEM is a very important characterization tool in determining the morphology and the size of nanoparticles. Furthermore, morphology, particle size, and distribution of catalyst particles on the support can be viewed by using this technique.

In this study, TEM was employed for investigations of morphology and particle size of catalysts. A number of images for each sample were recorded at magnitudes of 200 k magnifications. Zeiss LIBRA 200 FE TEM was utilized for TEM investigations. Before analysis, the samples were sonicated for one hour in a solution of n-hexane and the suspensions were dropped on Cu grid for analysis.

3.5.11 Surface area and pore size BET

Adsorption is a surface phenomenon. The process may occur when a solid material is contacted with gas or liquid molecules. The surface atoms of a solid tend to adsorb the approaching gas or liquid (fluid) molecules in order to diminish surface tension. The interaction of approaching molecules can be of two different types, and hence, adsorption can be categorized in two forms. In case of molecules interact at the surface through weak van der Waals forces and there is no change in the properties of adsorbate and adsorbent, the phenomenon is referred as physical adsorption or physiosorption. In contrast, the process is termed as chemical adsorption or chemisorption if there is strong chemical interaction with bond formation between the two reacting species. In chemisorption, unlike physiosorption, both adsorbate and adsorbent lose their individual identity.

As catalytic activity is related more to the surface chemistry of the catalyst, hence catalysts based on porous solids with higher surface area are prerequisite for achieving desirable activity. Structure and size of pore should be so that reactant molecules have easy access to the active sites within the pores of the solids and after reaction the product molecule produced should easily escape the pores. Adsorption desorption isotherms are generally studied for investigating textural properties of solids. According to IUPAC, adsorption isotherm relates amount of gas adsorbed as response to equilibrium pressure. However, isotherm is constructed as amount of gas adsorbed as a function of relative equilibrium pressure (P/P^o), if the analysis is performed below triple point [236]. Six types of adsorption isotherms have been identified according to IUPAC (Figure 3.3). Type I adsorption isotherm indicates monolayer adsorption on the surface of adsorbent. This kind of isotherm is exhibited by microporous solids whose pore size is almost equal to the molecular diameter of adsorbate. Adsorption of O_2 on carbon black at -90 K is the example of Type 1 adsorption isotherm. In Type II isotherm adsorption is not limited to monolayer but after a slight increase in relative pressure multilayer formation is observed. This kind of isotherm is displayed by nonporous adsorbents with a wide range of pore sizes. Adsorption of nitrogen gas on silica gel at -195 °C show Type II isotherm. Type III and V illustrate weak interaction between approaching adsobate and adsorbent. Similarly these kinds of isotherms can also be observed when adsorption is taking place in vapor conditions. Mesoporous materials (2-50 nm) show type IV adsorption isotherm. A very rare isotherm of type VI is observed for nonporous materials.

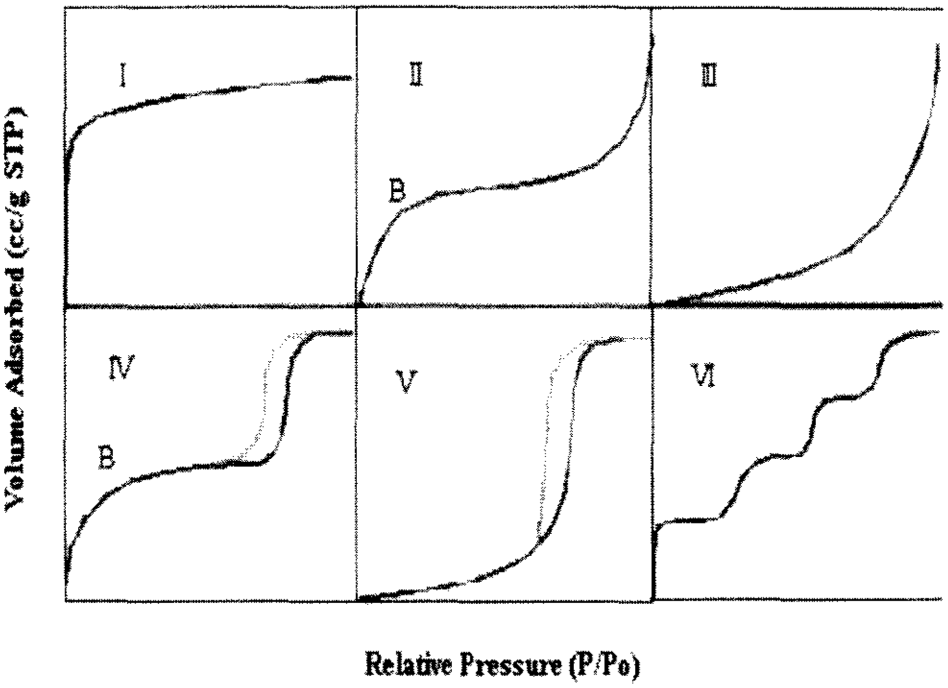

Figure 3.3: Types of adsorption isotherms

Brunauer-Emmett-Teller (B.E.T.) Model is basically an extended form of Langmuir equation [237].

BET model is based on some assumptions like

1. Adsorptions sites on adsorbent are of equal energy and placed in regular manner on the surface of adsorbent.
2. Adsorption takes place exclusively on these adsorption sites and is limited to these adsorption sites. Similarly adsorption and desorption prevail on exposed sites.
3. Adsorption is continuous phenomenon, where first layer adsorbs on the surface of adsorbent while each new layer is adsorbed on subsequent layer.

In terms of equation the BET model is expressed by equation 3.9

$$\frac{P}{V_{\propto}(P_O - P)} = \frac{1}{V_m C} + \frac{C-1}{V_m C}\left(\frac{P}{P_O}\right) \tag{3.9}$$

where,

P shows equilibrium pressure of adsorbate, P_o stands for saturation pressure of adsorbate, V_α and V_m are the total and monolayer adsorbent gas quantity, respectively. The constant C is given by correlation 3.10

$$C = \exp\frac{qi - ql}{RT} \tag{3.10}$$

Equation 3.10 ?

where,

qi qi represents the heat of adsorption of first layer on adsorbent, ql shows latent heat of condensation, R is gas constant and T is the absolute temperature.

A plot between $\frac{P}{V_{\propto}(P_O-P)}$ and $\left(\frac{P}{P_O}\right)$ gives a straight line with $\frac{1}{V_m C}$ is the intercept and $\frac{C-1}{V_m C}$ is the slope of the plot.

Finally surface area of the sample is determined after calculating volume of monolayer by following equation 3.11.

$$\sigma = (4)(0.866)\left[\frac{M}{4(2N_A\,\rho)^{\frac{1}{2}}}\right]^{\frac{2}{3}} \tag{3.11}$$

where,

σ is the area per molecule, M is the molecular weight, N_A is Avogadro's number and ρ is the density of liquid adsorbate.

Pore size distribution was determined by using Barret-Joyner-Halenda (BJH) model. Calculations of this model is summarized in equation 3.12.

$$V_{ads}(x_k) = \sum_{i-1}^{k} \Delta V_i[r_i \le r_c(x_k)] + \sum_{i-k+1}^{n} \Delta S_i t_i[r_i > r_c(x_k)] \tag{3.12}$$

where,

$V_{ads}(x_k)$ is volume of liquid adsorbate in cm^3/g at relative pressure, V denotes pore volume in cm^3/g, S represents surface area in cm^2/g, t is the thickness of adsorbed layer and r is the pore radius.

Prior to BET studies, the sample is degassed in order to eradicate any physically adsorbed materials like different contaminants and humidity. The degassing is generally carried out at a lower temperature to avoid degradation of materials. However, in some cases of highly thermally stable materials, it is conducted at higher temperature. It is, therefore, recommended to carry out TGA of the materials before BET analysis is performed. This technique encompasses surface area, surface porosity, and particle size, giving important information regarding surface characteristics of materials.

In the current study, Micromeritics, ASAP 2020 was used for surface investigations. Typically, 0.1 gram of sample was taken in quartz sample tube. The sample was degassed with N_2 flow to remove moisture and other impurities. The process was conducted at -196 °C, which is liquefaction temperature of nitrogen. The sample tube was refilled with N_2 and was weighed again to determine the actual sample mass before analysis. The surface area of material was evaluated by BET equation, while the pore size distribution was calculated via Barrett-Joyner-Halenda (BJH) method.

3.6 Reactor System

The activity of the catalysts was tested in slurry reactor. The details of the reactor systems are given as follows.

3.6.1 Gas supply

A mixture of H_2 and CO_2 with a volume ratio of 3:1 was used as reacting gas. Prior to reaction study, the reactor was purged with the reactant gases at room temperature.

The pressure of the reactant gases was controlled by using two pressure regulators. The reactant gases were then transferred to reactor with stainless steel tubing.

3.6.2 Slurry Reactor

The activity of catalysts in CO_2 hydrogenation to methanol was evaluated in autoclave slurry reactor (Parr 4593 with a regulator Parr 4848). The schematic diagram of reactor is displayed in Figure 3.4 while the reactor setup is shown by Figure 3.5. The detailed specifications of reactor are given in Appendix B (section B1). A mixture of reactant gases (CO_2 & H_2) in fixed volume ratio (1:3) was injected by using feed gas cylinder into the reaction cell, which contained catalyst samples suspended in ethanol solvent. Furthermore, the reactor cell was also equipped with a stirrer and a temperature probe to monitor the temperature during reaction. The reaction cell was wrapped by an electrical furnace that was capable of heating up to 500 °C. The reaction operating temperature and pressure were maintained by a temperature sensor and a pressure gauge, respectively. The reaction parameters were adjusted by a reactor controller, while the slurry reactor was provided with two outlets each one for obtaining gas and liquid samples. The reaction data were recorded in an attached computer.

In addition, a required amount of pre-reduced solid catalysts was suspended in ethanol. A screening study of catalysts with different concentrations of metals and promoters had been carried out at fixed 180 °C and 30 bar reaction temperature and pressure, respectively. The standard operating procedure is given in Appendix B (section B2).

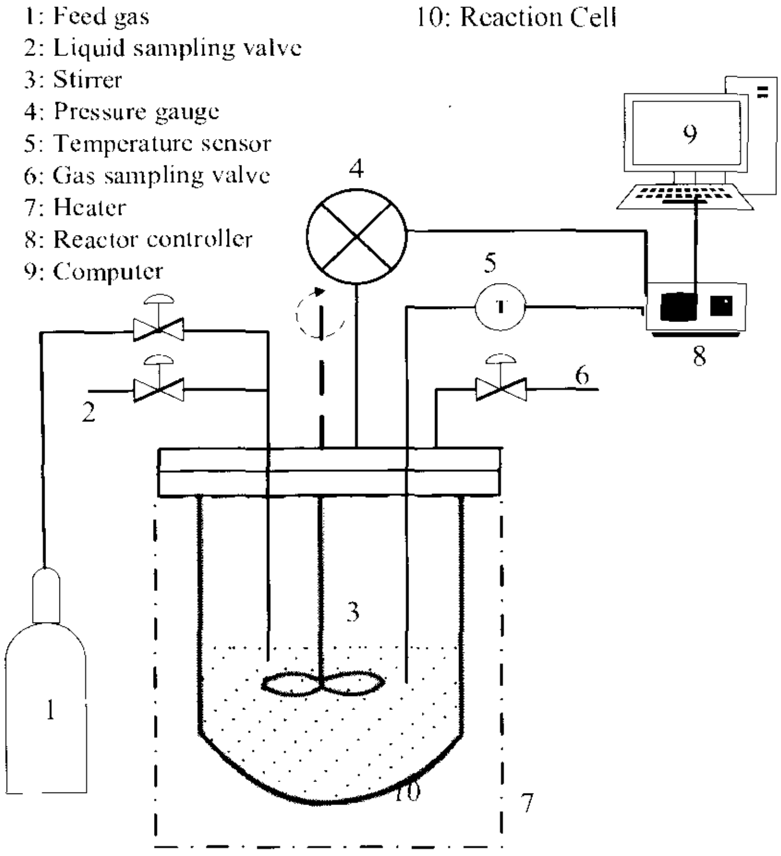

Figure 3.4: Schematic diagram of reactor

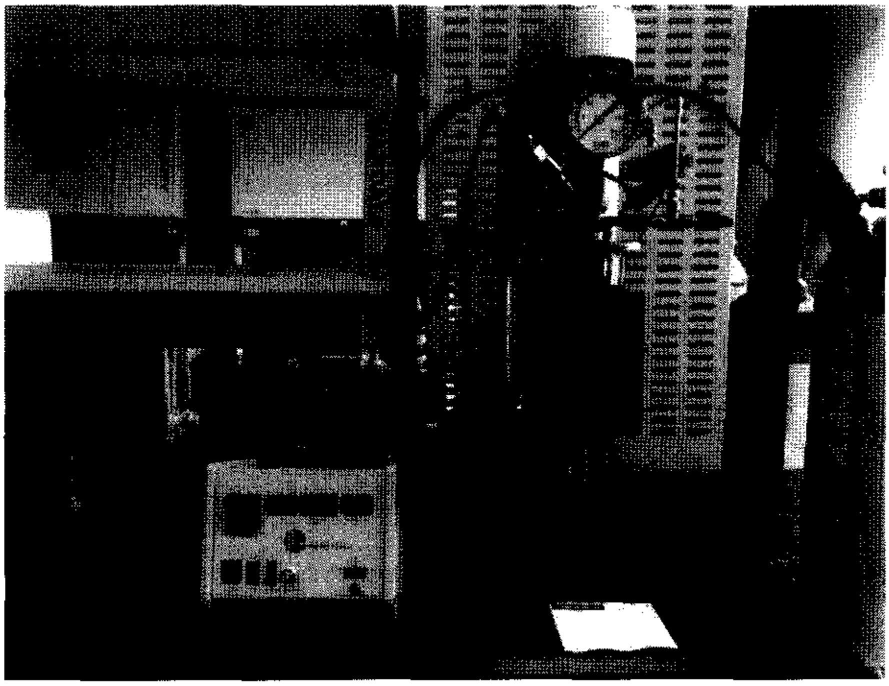

Figure 3.5: Slurry reactor setup

3.6.3 Gas chromatography

The reaction products were analyzed ~~via~~ [illegible] gas chromatography (Figure 3.6). Gaseous components of reaction were evaluated via gas chromatography thermal conductivity detector (GC-TCD), while liquid samples were analyzed with gas chromatography flame ionization detector (GC-FID). Prior to analysis, GC was calibrated with standard concentrations of CO_2 and H_2 gases. Their GC peaks were identified in terms of their retention time, while the intensity of GC peaks reflected their relative concentrations. Similarly, the system was also calibrated with methanol and ethanol concentrations for methanol evaluation. Details of GC column specifications are given in Table 3.4.

3.6.3.1 Details of GC system

Gas chromatography was used for quantification of gas and liquid products. Liquid products were analyzed by flame ionization detector (FID) back detector. Similarly, gas products were evaluated by thermal conductivity detector (TCD) front detector. The GC analysis was conducted for 20 minutes time.

a) Analysis of gas samples

The sampling valve was turned on for half minutes to pass the product gases through column and TCD (front) detector was used for identification and quantifications of gas molecules.

b) Analysis of liquid samples

Liquid samples were injected by liquid sampling valve. The valve was turned on for 0.01 minute to avoid entrance of any air. Liquid components were analyzed by FID (back) detector.

c) Calibration of GC

GC was calibrated by standard gas and liquid components provided by Refinery Gas Analysis (RGA). The standard gases were used to identify the retention time and peak area of each component. The chromatograms of both methanol and CO_2 are presented in Appendix B (Figures B1 and B2), respectively. The retention time of different components are given in Appendix B (Table B2).

Table 3.4: Specification of GC columns (supplied by J&W Scientific)

Column	Model	Dimension			Temp. limit (°C)	Flow (ml/min)
		Length (m)	I.D (µm)	Film (µm)		
DB-1	125-1034	30	530	3.0	280	5.0
HP-Plot U	19095P-U04	30	530	20	190	3.0
HP-MolSiv	19095P-MS9	15	530	50	300	3.0

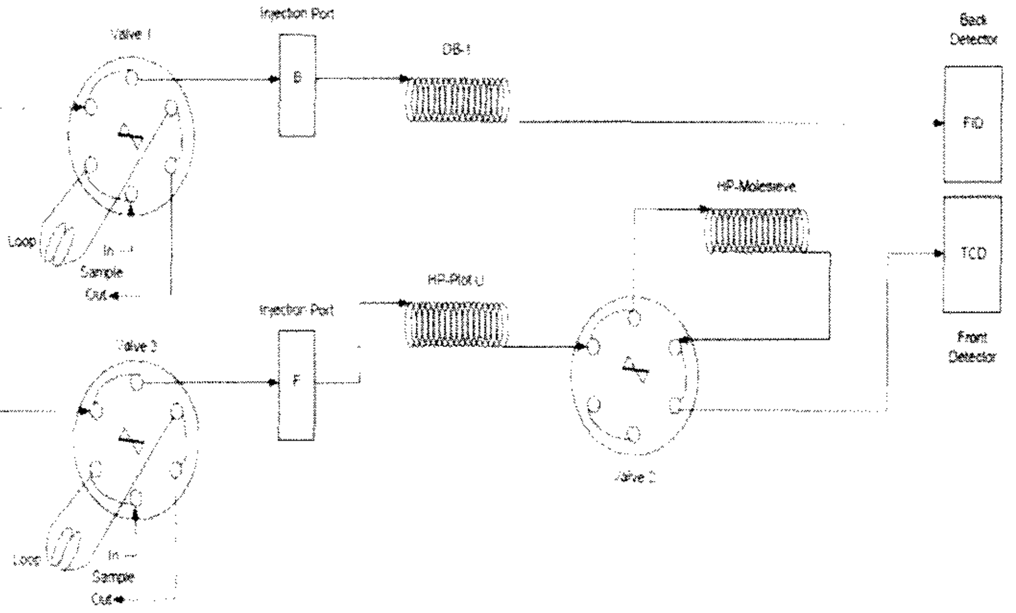

Figure 3.6: Gas Chromatography sampling valve diagram

3.6.4 Blank run

CNFs without metal loadings were tested for any possible contribution to CO_2 hydrogenation to methanol. The CNFs suspended in 25 ml ethanol were placed in a reactor and reactant gases were injected at 180 °C and 30 bar reaction temperature and pressure, respectively. No other product than CO_2 and H_2 were found in GC analysis.

3.6.5 Catalyst activation

In order to convert Cu^{2+} to metallic Cu, the catalysts were activated in H_2 with a flow rate of 2000 cm^3/h at 380 °C. The reduction process was continued for 6 hours. TPDRO (1100 MS) was used for activation of catalyst. Briefly, 0.5 gram of calcined catalyst was placed in a U-shaped quartz sample. The catalyst was held for 6 hours in H_2 with a flow rate of 2000 cm^3/h at 380 °C. The reduced catalyst was collected in a small vial and was placed in the reactor cell containing 25 ml of ethanol [191, 238-241]. The activation of catalyst was confirmed by using XPS analysis. As shown in Figure 3.7, two peaks were observed in XPS spectra for calcined catalyst.

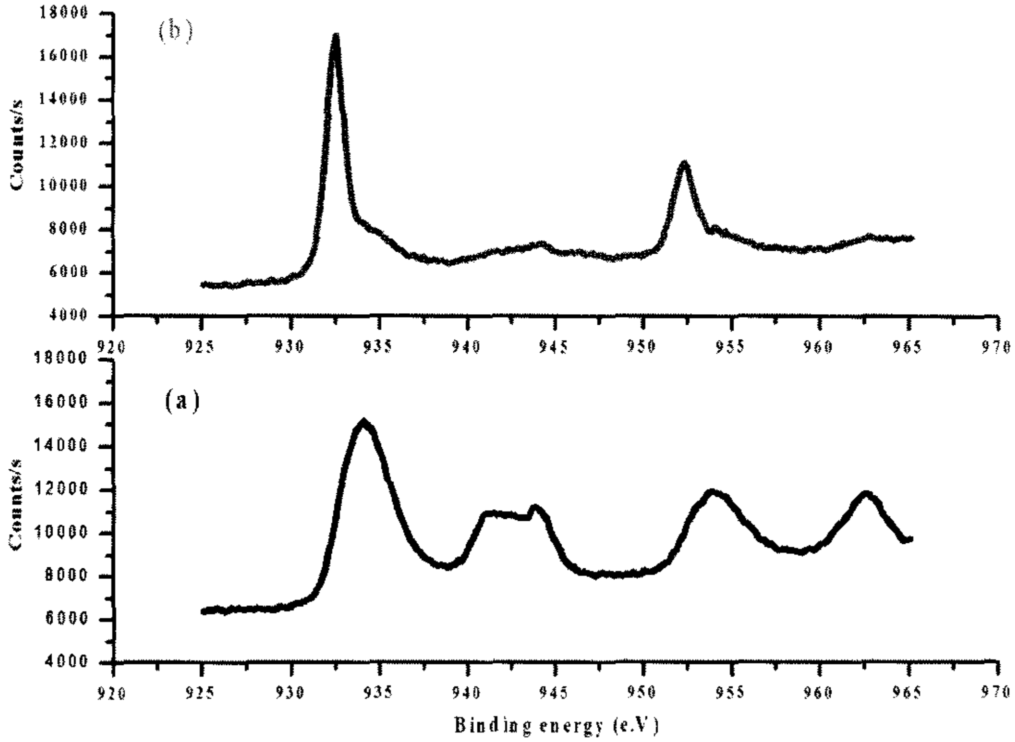

Figure 3.7: XPS Central level Cu $2p_{3/2}$ of (a) calcined and (b) reduced catalyst

The principal Cu $2p_{3/2}$ peak around 934 eV was ~~a~~ characteristic of Cu^{2+}, which was associated with satellite peak due to electron shake-up processes. When the sample was reduced by the above mentioned procedure, the satellite peak completely disappeared and the core electron peak was shifted to lower binding energy region. The disappearance of satellite peak and the subsequent shifting of core electron peak clearly indicated the reduction of CuO [242]. This verified the successful ex-situ reduction of catalyst prior to activity studies.

3.6.6 Catalyst testing

A 0.5 grams of activated catalyst was placed in a reactor vessel containing 25 ml of ethanol. The study was conducted in a batch reactor. The reactor was purged with reactant gases at room temperature before methanol synthesis reaction was carried out. The reactor was pressurized to 30 bar with a mixture of CO_2 and H_2 at a (v/v) ratio of 1:3. The reaction temperature was raised to 180 °C. The reaction mixture was agitated with a stirrer and a speed of 1300 rpm was selected to avoid mass diffusion constrains [200, 243]. Besides, the reactor was run in batch mode and the reaction was continued for 2 hours, while the products were analyzed via gas chromatography. GC chromatogram is displayed in Appendix B (Figure B3).

Rate of methanol synthesis was calculated as displayed by equation 3.13 [244].

$$Rate\ of\ methanol\ yield = g\ of\ methanol\ produced/Kg\ of\ catalyst \times h \quad (3.13)$$

Turnover frequency was calculated by formula 3.14 [89, 245].

$$TOF_{MeOH}(s^{-1}) = \frac{Number\ of\ molecules\ of\ methanol\ produced}{Time\ (s).number\ of\ mettalic\ copper\ atoms} = \frac{A.\mathcal{N}_a}{3600.S_{Cu}.N_a} \quad (3.14)$$

where, A represents methanol activity in mol/h g, $\mathcal{N}_a$ is Avogadro's number ($6.023\text{x}10^{23}$), S_{Cu} denotes metallic copper surface area in m^2/g and N_a designates number of Cu atoms in a monolayer ($Na = 1.469\text{x}10^{19}$ atoms/m^2).

Methanol selectivity was calculated as follows (E equation 3.15)

$$\overset{anol}{Meth.}\,selectivity = \left[\frac{moles\ of\ methanol\ produced}{total\ moles\ of\ products}\right] \times 100 \qquad 3.15$$

Similarly, CO_2 conversion was calculated by th~~e following~~ F formula 3.16.

$$\%\, CO_2\ conversion = \left[\frac{CO_{2_{in}} - CO_{2_{out}}}{CO_{2_{in}}}\right] \times 100 \qquad (3.16)$$

3.6.7 Kinetics study

A kinetics study of CO_2 hydrogenation to methanol was performed at 220 °C and 40 bar reaction temperature and pressure, respectively. A 0.5 gram of catalyst was suspended in 25 ml of ethanol and was placed in a reactor vessel. Mass transfer limitations were avoided by carrying out the reaction at 1300 rpm [200, 243]. The samples were analyzed with different intervals of time (20 minutes each) for CO_2 conversion and methanol synthesis.

3.6.8 Kinetics Modeling

Artificial neuron network (ANN) was used as a kinetics model for the CO_2 hydrogenation to methanol. The model was tested with four different reactor parameters, namely reaction temperature, pressure, time, and feed gas composition (Figure 3.7). The model was trained with the rate of reaction as a target value. Besides, back propagation method was employed for the predicted target values.

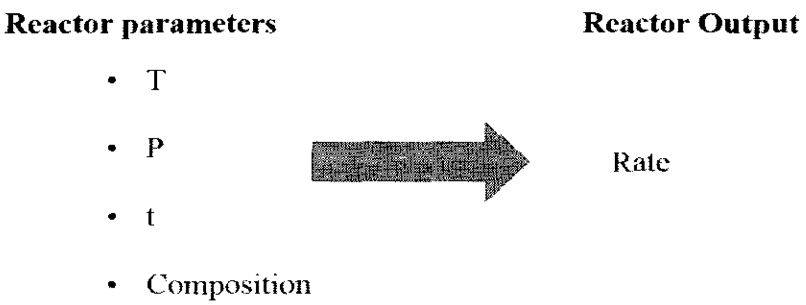

Figure 3.8: Scheme for application of ANN in kinetics modeling

In addition, four different training algorithms, namely trainlm, trainbr, traingda, and trainscg were used in the MATLAB platform to train and test the ANN model for methanol synthesis via CO_2 hydrogenation. Different numbers of hidden layer neurons were selected, and 10 hidden layer neurons showed the best ANN structure for estimating the training data in the current case.

3.7 Variation of reaction parameters

Methanol synthesis via CO_2 hydrogenation was first optimized in terms of reaction temperature. Hence, a range of reaction temperatures; 180, 200, 220, and 240 °C, had been selected at constant reaction pressure of 30 bar. After an optimized degree of reaction temperature was identified, methanol synthesis had been tested at different reaction pressures of 20, 30, 40, and 50 bar at a constant reaction temperature of 220 °C. Similarly, the effect of feed gas ratio was also studied by carrying out methanol synthesis at different H_2/CO_2 ratios of 0.8, 1.5, and 3 at 220 °C and 30 bar reaction temperature and pressure, respectively.

CHAPTER 4

RESULTS AND DISCUSSIONS

4.1 Functionalization of carbon nanofibers

Effects of oxidation of carbon nanofibers (CNFs) were investigated by using different characterization techniques, as discussed below.

4.1.1 X-ray diffraction study

X-ray diffraction patterns of as-received and modified CNFs are displayed in Figure 4.1. Both spectra showed diffraction bands at $2\theta = 26^\circ$ and $2\theta = 43^\circ$ corresponding to (002) and (100) of planes CNFs, respectively [87, 246].

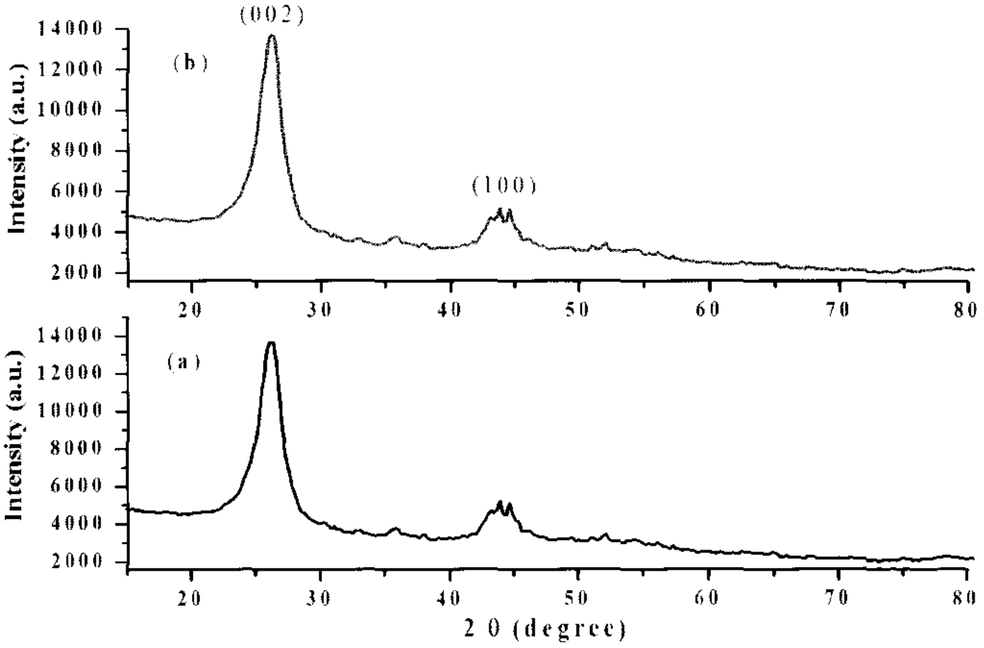

Figure 4.1: XRD spectra of (a) as-received and (b) modified CNFs

The intensity of 002 diffraction peak for modified CNFs was greater compared to the corresponding peak of as-received CNFs. This indicated that oxidation of CNFs improved the degree of graphitization of CNFs. Such observations were also reported by Ovejero et al. for HNO_3 treated carbon nanotubes [247].

4.1.2 Textural properties

Nitrogen adsorption desorption studies were conducted to analyze the influence of acid treatment on the textural profile of CNFs. Magnitudes of surface area, pore volume, and pore diameter are depicted in Table 4.1.

Table 4.1: Textural properties of CNFs

CNFs	**Surface area (m^2/g)**	**Pore volume (cm^3/g)**	**Pore diameter (nm)**
As-received	112	0.20	6.4
Treated	152	0.38	7.6

As evident from the tabulated data, the as-received CNFs had surface area of 112 m^2/g with 0.20 cm^3/g of pore volume, and pore diameter of 6.4 nm. Besides, oxidation of CNFs resulted in enlargement of surface area by 36 %. Similarly, pore volume and pore size diameter were also increased. The improvement of surface area with respect to HNO_3 treatment might be due to the creation of additional surface defects.

4.1.3 Thermo gravimetric analysis

Thermo gravimetric analysis (TGA) was performed to investigate the effect of oxidation on thermal stability of CNFs. TGA and DTG profiles of as-received and modified CNFs are presented in Figure 4.2. The first weight loss was observed in a temperature range of 40-120 °C. This was attributed to evaporation of water molecules from the surface of CNFs. Meanwhile, the as-received CNFs showed greater thermal stability before their sharp decrease in weight loss at 600 °C. This rapid weight loss was due to decomposition of CNFs. A total of 6 % weight loss was observed until 800 °C, which suggested high thermal stability of as-received CNFs. After oxidation, the position of TGA curve for oxidized CNFs on temperature scale remained almost unchanged. This indicated that thermal stability of CNFs was not much affected. However, two additional peaks were observed above 500 °C in derivative of modified CNFs. This minor weight loss was assigned to the decarboxylation and the removal of hydroxyl groups from the surface of modified CNFs [247].

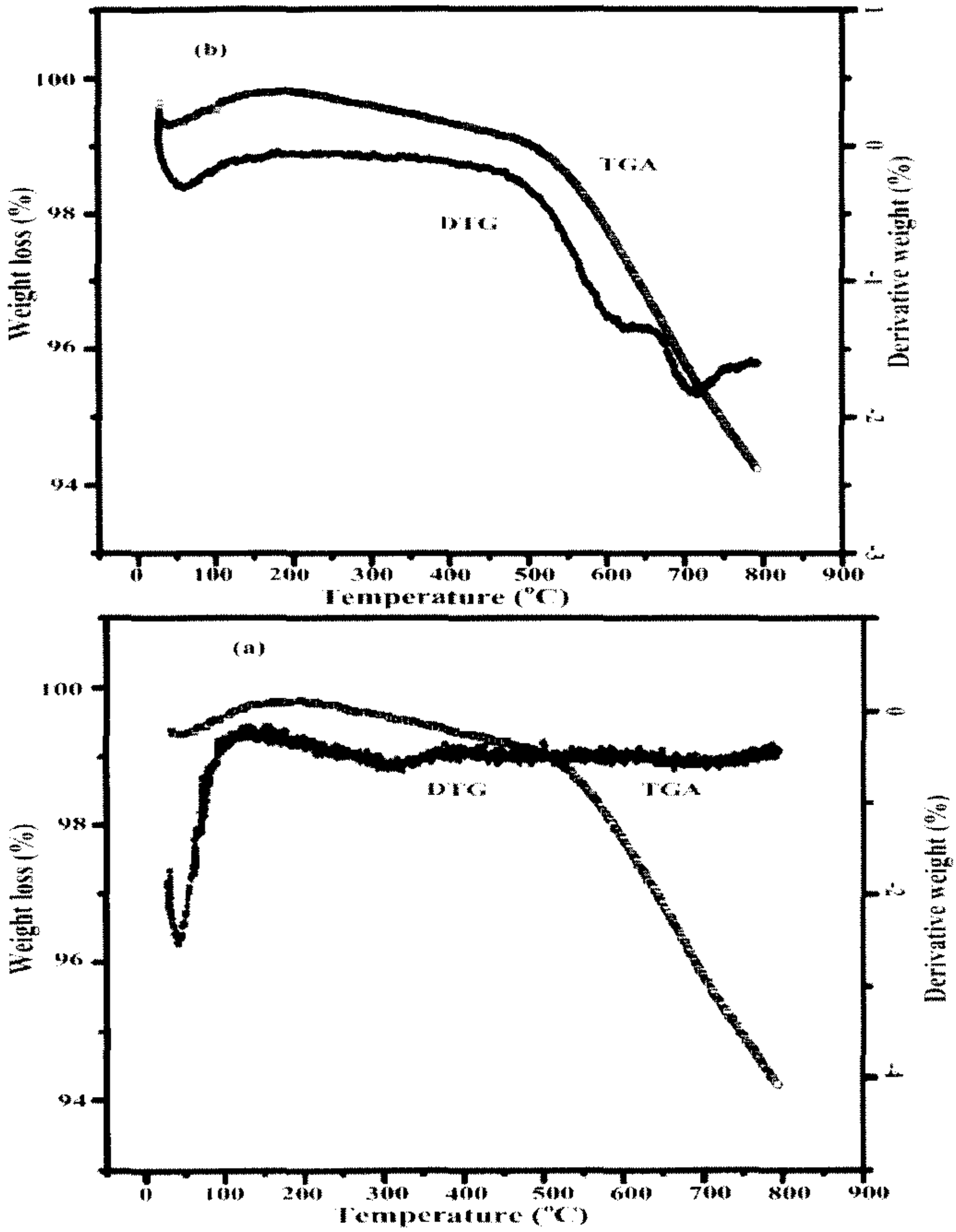

Figure 4.2: TGA curves of (a) as-received and (b) modified CNFs

4.1.4 Raman spectroscopy

Raman spectra for as-received and treated CNFs are displayed in Figure 4.3. Two prominent peaks were observed in both cases. Raman peak around 1365 cm^{-1} was ascribed to the defect-induced Raman band, generally called as D-band. It involved phonons near the K Brillouin zone boundary, which possessed a characteristic of disorderness in carbon materials. Similarly, another prominent peak was observed at 1600 cm^{-1}, which was assigned to tangential mode (G-band), representing the ordered graphite of CNFs. This Raman feature originated from the stretching vibrations of C-C bond in sp^2 hybridized graphitic materials. More importantly, these two characteristic peaks were also observed when as-received CNFs were oxidized. This suggested that HNO_3 treatment did not damage the surface of CNFs [248]. Nevertheless, after functionalization with nitric acid, G-band has slightly shifted upfield for ~4-5 cm^{-1}, as compared to that of the as received CNFs (Table 4.2). This slight shift indicated the presence of functional groups on the surface of the CNFs [129, 249]. The D to G-band intensity ratio (ID/IG) was calculated in order to gauge the defects on the surface of CNFs. As evident from the tabulated data, the ID/IG ratio was slightly increased with HNO_3 treatment for as-received CNFs. This is in accordance with the literature [248]. Furthermore, the increase in ID/IG intensity ratio suggested the introduction of some chemical groups that could be interpreted as defects on the surface of modified CNFs.

Table 4.2: Raman data of as-received and modified CNFs

Sample	D-band wavelength (cm^{-1})	G- band wavelength (cm^{-1})	I_D/I_G
As-received	1364	1601	1.15
HNO_3 treated	1368	1602	1.29

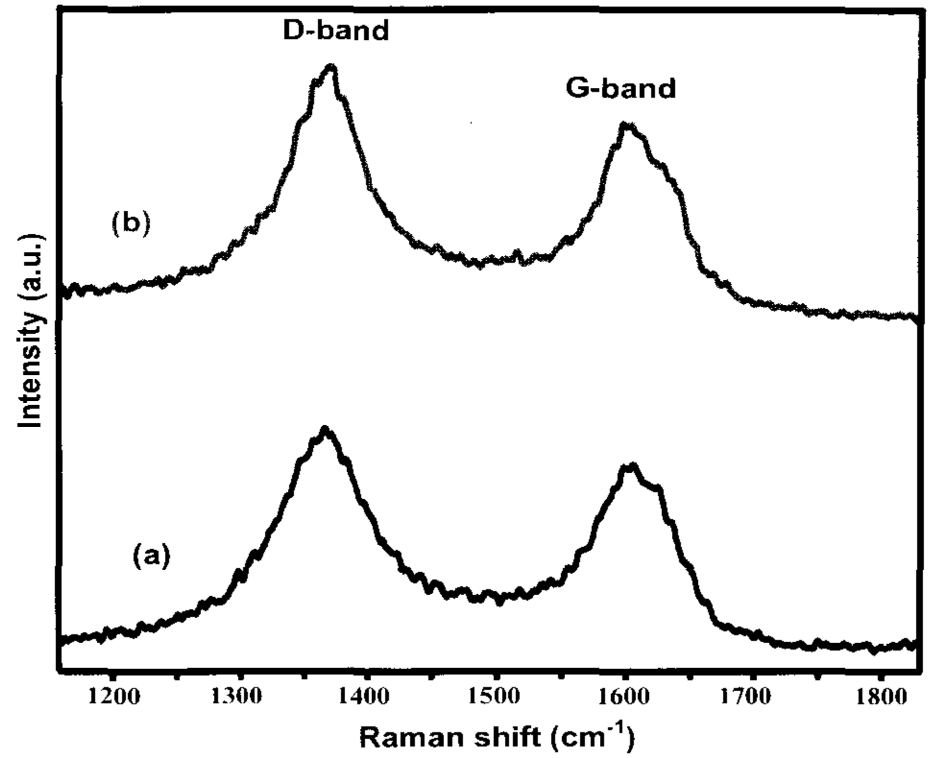

Figure 4.3: Raman spectra of (a) as-received and (b) modified CNFs

4.1.5 XPS survey

XPS spectroscopy was employed to investigate the effect of nitric acid treatment on the surface of CNFs. XPS Peak spectra of as-synthesized and modified CNFs are displayed in Figure 4.4. The only peak observed at 284.6 eV in XPS spectra for as-received CNFs, was a typical graphitized carbon peak. However, this typical graphitized carbon peak in modified CNFs was accompanied by a long tail in the higher binding energies region. In order to rationalize the surface chemistry during the acid treatment, C1s XPS Peak of modified CNFs was deconvolated into three major peaks. The new peaks were observed at 286.3 and 287.3 eV, indicating the existence of alcoholic (C-OH) and carbonyl (C=O) functional groups, respectively [250].

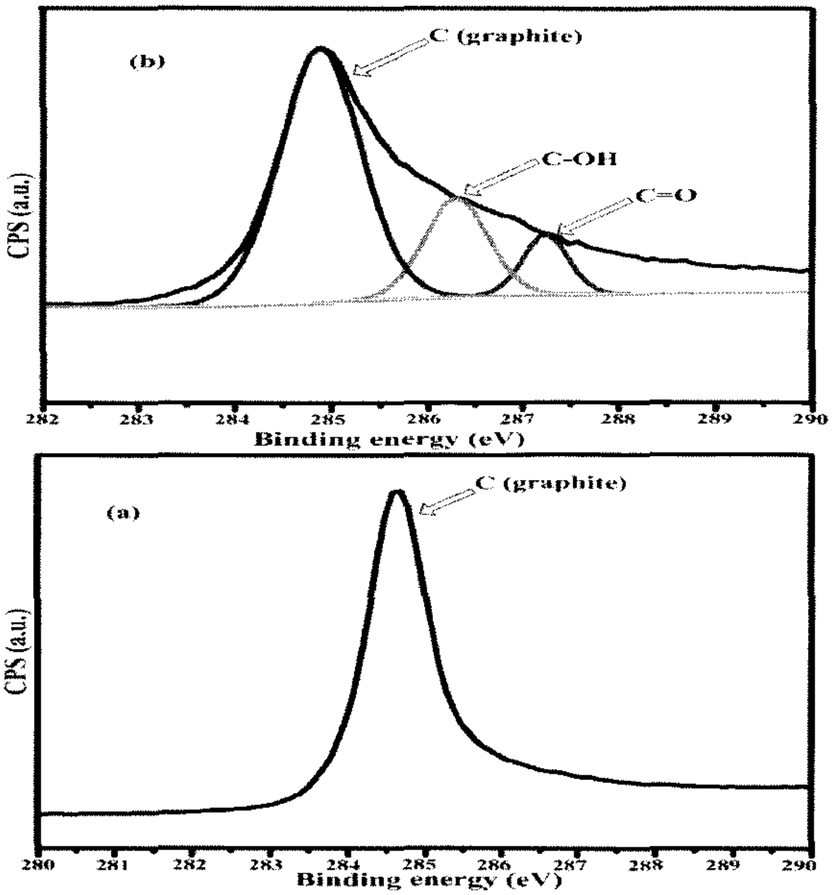

Figure 4.4: Raman spectra of (a) as-received and (b) modified CNFs

4.1.6 Functional groups identifications

FT-IR profiles for both as-received and modified CNFs are depicted in Figure 4.5. Two major peaks were observed in FT-IR profile for as-received CNFs. The absorption band at 1642 cm^{-1} was assigned to C=C domains of CNFs, while a broad FT-IR peak at 3440 cm^{-1} was ascribed to absorbed water. However, after oxidation, a number of additional absorption bands were found in wave length range of 1500-1000 cm^{-1}. The additional peaks were denoted as peak α, peak β, peak γ, and peak δ. Meanwhile, the absorption band at 1550 cm^{-1} (peak α) was assigned to carboxylate functional group. Similarly, the presence of hydroxyl functional groups was confirmed by a sharp absorption peak at 1415 cm^{-1} (peak β) [251]., whereas a small absorption band at 1312 cm^{-1} (peak γ) represented the incorporation of alcoholic group (C-OH) in modified CNFs [252]. Furthermore, two small absorption bands at 1081 and 1121 cm^{-1} (peak δ) were assigned to C-O stretching vibrations [253].

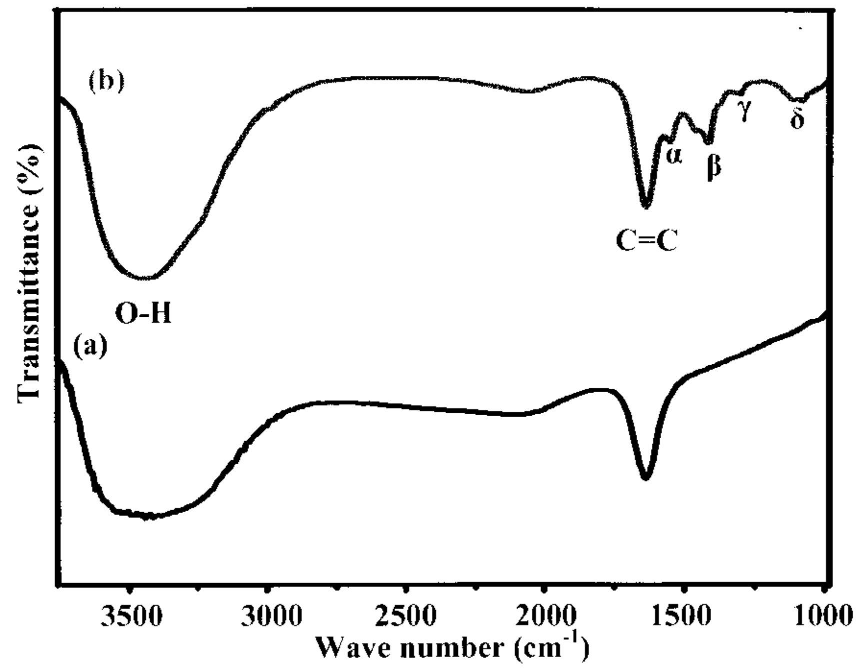

Figure 4.5: FT-IR profile of (a) as-received and (b) modified CNFs

4.1.7 Conclusions

Various characterization techniques revealed that the current applied method for functionalization of CNFs successfully introduced different functional groups (-OH, CO, C=O,) on the surface of CNFs. The main findings are summarized as

- BET results revealed larger surface area due to creation of surface defects as a consequent of oxidation.
- TGA showed additional weight loss for elimination of oxygenated functional groups by modified CNFs. [illegible] value
- Raman spectroscopy showed greater ID/IG ratio for modified CNFs. This is an indicator of functional groups creation at the surface of CNFs.
- XPS and FT-IR studies confirmed the incorporation of functional groups on the surface of CNFs.

4.2 Effect of Cu loadings

Effects of Cu loadings on the physicochemical properties and the activity pattern of parent catalyst were investigated. The results are briefly discussed as depicted in the following.

4.2.1 Effect of Cu loading on physicochemical properties

In order to investigate the influence of Cu loading on the physiochemical properties of prepared catalysts, catalysts with various amounts of Cu loadings were characterized by different techniques. These are briefly discussed in the following.

4.2.1.1 Quantification of catalysts components

Cu and ZrO_2 loadings were quantified via ICP-OES and the data are presented in Table 4.3 (the calculation is shown in Appendix A (Section A2). As evident from the tabulated data, the magnitudes of both bulk Cu, as well as ZrO_2 measured by ICP, were in very close agreement to the targeted values. This showed that the majority of active catalyst components (Cu & ZrO_2) were successfully deposited on the catalyst support. This in turn also supported the efficiency of DP method for synthesis of catalysts with higher loadings of active metals.

Table 4.3: ICP results of CZC catalysts with different Cu content

Sample	**Target Cu (%)**	**Cu (%) by ICP**	**Target ZrO_2 (%)**	**ZrO_2 (%) by ICP**
CZC5	5	4.54	10	9.51
CZC10	10	11.50	10	10.18
CZC15	15	14.39	10	9.29
CZC20	20	19.24	10	9.24
CZC25	25	24.8	10	9.17

4.2.1.2 Bulk phase analysis

Figure 4.6 displays the XRD patterns of calcined CNFs-O based Cu/ZrO_2 catalysts with different Cu loadings. For comparison, the diffraction pattern of bare CNFs-O was also included. Two prominent peaks were detected on 2θ scale at 26° and 44° with d spacing of 3.36 and 2.06, respectively. This indicated the diffractions of (002) and (100) planes of graphitic carbon nanofibers [87, 246, 254]. Likewise, a small diffraction peak visualized at 2θ = 30.3° was indexed as zirconia (t-ZrO_2, JCPDS 88-1007), whereas a small XRD peak at 2θ = 24.4° was recognized as monoclinic zirconia (m-ZrO_2) [255]. The XRD patterns at 32.6°, 35.5°, 38.7°, 48.8°, 58.3°, 61.67°, 66.4°, 68.1°, 72.3°, and 75.1° were found to be indexed as monoclinic-phased tenorite CuO with JCPDS card files No. 48-1548 (a = 4.62 Å, b = 3.43 Å, and c = 5.06 Å).

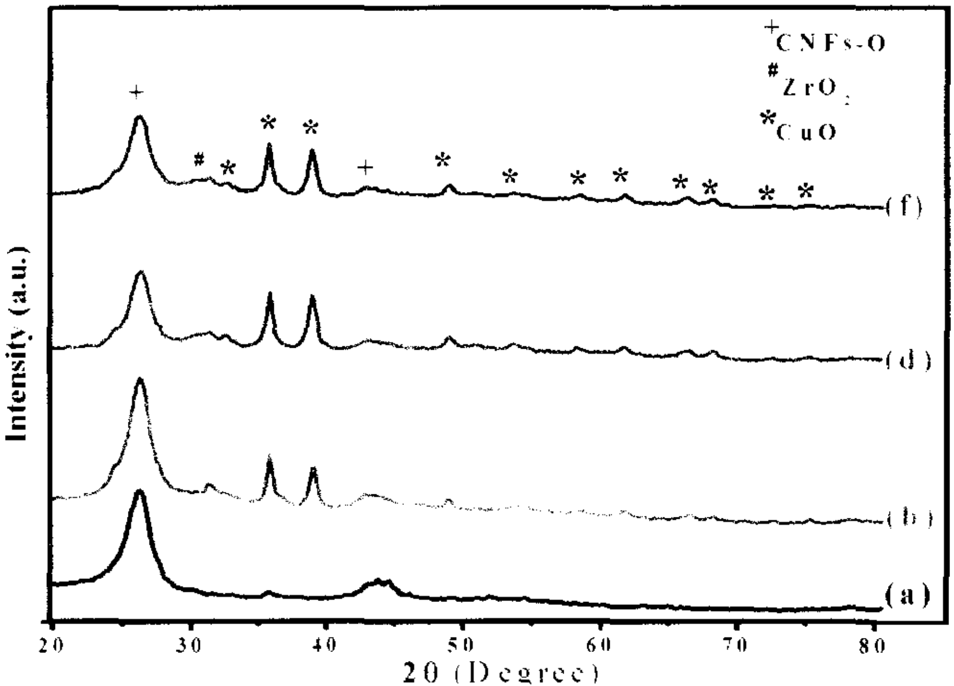

Figure 4.6: XRD pattern of (a) CNFs-O, (b) CZC5, (c) CZC10, (d) CZC15, (e) CZC20 and (f) CZC25 catalysts

These peaks were intensified when Cu loading was increased from 5 to 10 wt.%. This implied that the degree of CuO crystallization was enhanced by increasing the content of Cu. Another interesting observation was the intensification of t-ZrO_2 with the increase of Cu loadings. On the other hand, reflection of m-ZrO_2 observed in CZC5 catalyst disappeared in CZC10 catalysts. This disappearance of m-ZrO_2 and subsequent increment of t-ZrO_2 indicated that polymorphic transformation of zirconia had been facilitated by increased Cu content. In contrast, on further Cu increment (10-15 wt.%) the intensity of t-ZrO_2 peak was weakened and the reflection of m-ZrO_2 re-emerged. This lowering intensity of t-ZrO_2 peak and subsequent re-appearance of m-ZrO_2 suggested the back transformation of t-ZrO_2 to m-ZrO_2 form. Furthermore, the degree of CuO crystallization increased when Cu content exceeded 15 wt.%, while both zirconia phases almost disappeared. This could be due to stabilization of zirconia by Cu, as previously reported in the literature [256]. Similar observations were also reported by Ko et al. for Cu/ZrO_2 catalyst with increasing Cu content [256]. However, the intensity of CuO peak was reduced for CZC catalyst with maximum Cu content. More importantly, the CuO peak was slightly broadened with the increase of Cu from 5-10 wt.%, nevertheless, the peak width was progressively narrowed down as a function of increasing Cu loadings. This behavior of CuO, as a consequent of Cu loadings advocated agglomeration of CuO, which is in line with the literature [257]. Based on these observations, increase in Cu loadings promoted agglomeration of CuO. This trend was found satisfactory for all catalysts with exception of CZC10 catalyst, where agglomeration was depressed as compared to CZC catalyst with lower Cu content.

4.2.1.3 FT-IR investigations

Structural elucidation and confirmation of different functional groups in CZC catalysts were carried out via FT-IR analysis. FT-IR spectra of CZC catalysts with different Cu loadings are depicted in Figure 4.7. An absorption band for Cu-O was observed at 600 cm^{-1} [258, 259]. Similarly, a small absorption band at 750 cm^{-1} reflected the characteristic band of Zr-O bonds [260]. Meanwhile, a sharp FT-IR band at 1600 cm^{-1} was ascribed to C=C domain of CNFs [261]. All characteristic bonds observed in the FT-IR study confirmed the structure elucidation of CZC catalysts. Besides, incorporation of increasing Cu content revealed a progressive intensification FT-IR band at 600 cm^{-1} as a function of increasing Cu content.

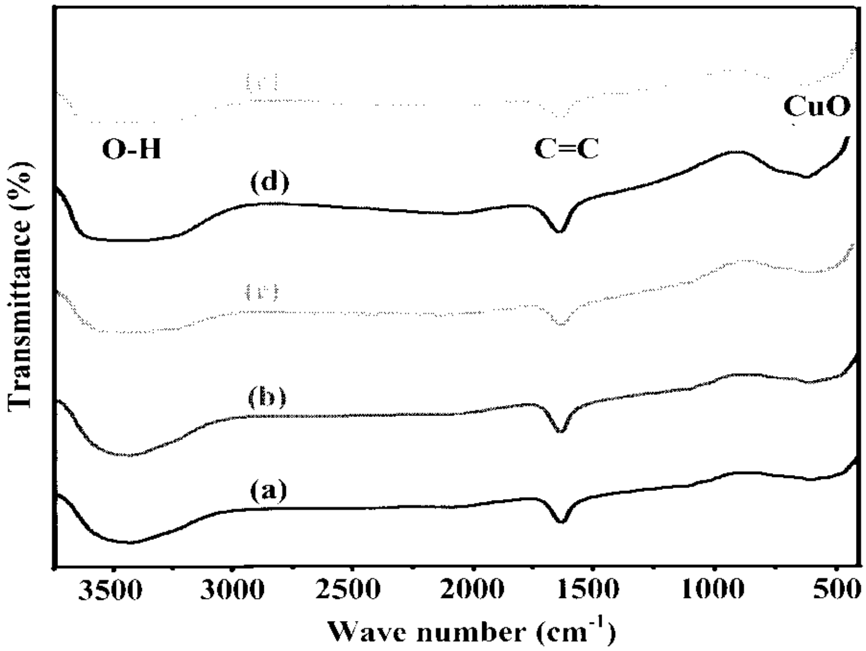

Figure 4.7: FT-IR spectra of (a) CZC5, (b) CZC10, (c) CZC15, (d) CZC20 and (e) CZC25 catalysts

4.2.1.4 DRS UV-Visible study

The diffuse reflectance of UV spectra for catalyst with different Cu loadings are shown in Figure 4.8. For each catalyst, a broad absorption valley was observed. UV absorption started from 210 nm and continued through the entire Ultraviolet range with a shoulder at 270 nm and a sharp peak at 350 nm. The absorption band between 210-270 nm was due to ligand-to-metal charge-transfer transition of $O^{2-} \rightarrow Cu^{2+}$, indicating the occurrence of Cu at isolated sites on the surface of support [262]. Similarly the absorption band at 350 nm was a clear manifestation of $(Cu\text{-}O\text{-}Cu)^{2+}$ cluster formation, indicating the presence of Cu in highly dispersed form.

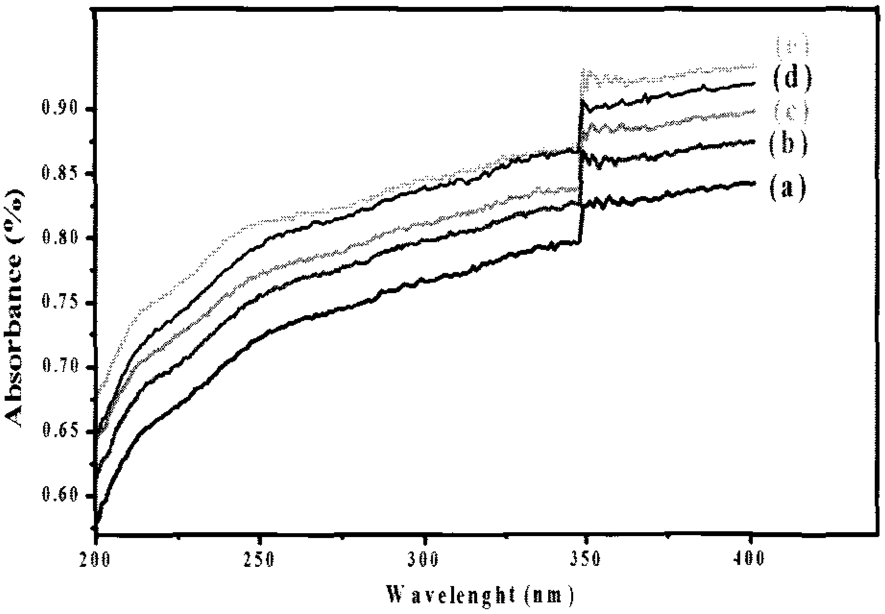

Figure 4.8: DRS UV spectra of (a) CZC5, (b) CZC10, (c) CZC15, (d) CZC20 and (e) CZC25 catalysts

A DRS-visible spectra of CZC catalysts with different Cu loadings are presented in Figure 4.9. A long and no ending absorption profile was observed in the entire visible region of the studied catalysts. This is because; CNFs possessed the property of absorbing visible radiations. In addition, Xie et al. studied DRS-visible spectrum of carbon nanotubes and recorded similar observations [263].

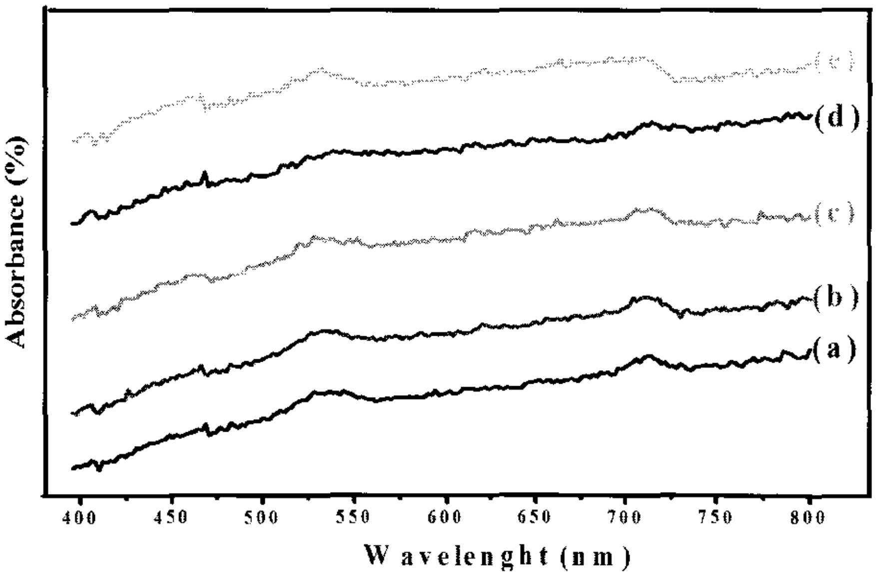

Figure 4.9: DRS Visible spectra of a) CZC5, (b) CZC10, (c) CZC15, (d) CZC20 and (e) CZC25 catalysts

Apart from that, two more absorption shoulders were observed in the current study. An adsorption peak centered at 540 nm with energy band gap of 2.3 eV suggested the presence of tetragonal form of ZrO_2. Similarly, the absorption band around 720 nm with energy band gap of 1.74 eV was assigned to 2Eg → 2T2g transitions of Cu^{2-}, indicating octahedral symmetry of Cu. Moreover, this absorption band was also attributed to the crystalline and the bulk phase copper [262].

4.2.1.5 Morphology investigations

TEM images of CZC catalysts with different ZrO_2 loadings are shown in Figure 4.10. Dark black spherical shaped particles were identified as copper particles, whereas tetragonal shaped light colored particles were recognized as zirconia particles [264-267]. The identification of particles was also supported by XRD findings, whereby spherical and tetragonal shaped structures were found for copper and zirconia particles, respectively. Besides, TEM investigations revealed well-dispersed particles for both Cu and ZrO_2. Furthermore, a uniform particle distribution was observed for catalysts with lower loading of Cu and most of the CNFs surface laid bare, indicating a higher potential of catalyst support for anchoring catalysts particles. This uniformity and dispersion of catalysts components had been persisted with further Cu loadings, while an optimum dispersion was observed in the case of CZC15 catalysts. However, both dispersion and particle size were adversely effected with the excess of Cu loadings. This was manifested by densely populated and poorly dispersed catalysts particles with further increase in Cu content.

Table 4.4: Average particle size of catalysts components with variant Cu content

Catalysts	Copper average particle size	Zirconia average particle size
CZC5	2	3
CZC10	3	5
CZC15	5	7
CZC20	8	10
CZC25	10	13

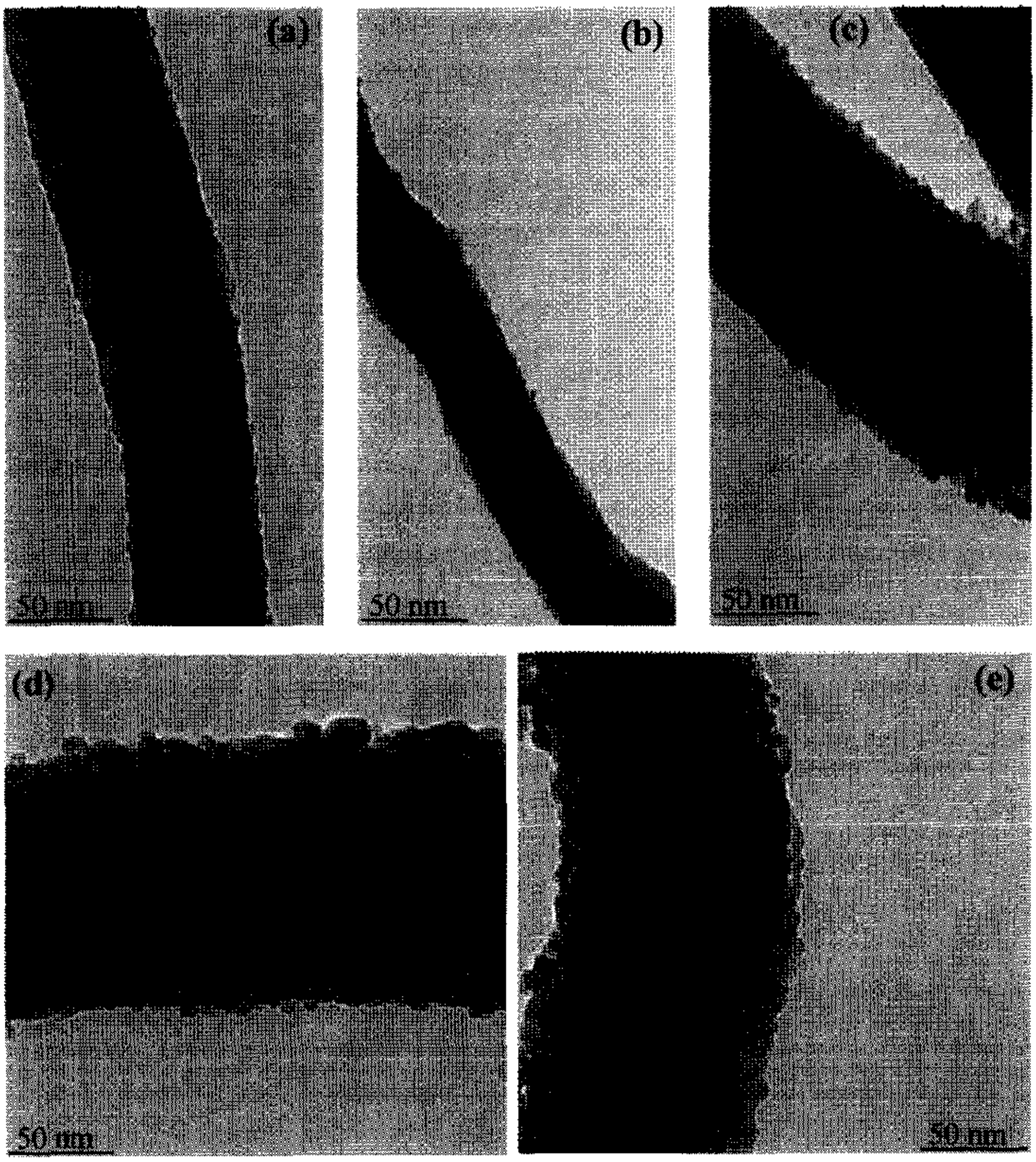

Figure 4.10: TEM images of (a) CZC5, (b) CZC10, (c) CZC15, (d) CZC20 and (e) CZC25 catalysts

The average particle size of both catalysts components in catalysts with various Cu contents is documented in Table 4.4. As evident from the tabulated data, the average particle size of both Cu and ZrO_2 experienced some variations with respect to Cu loadings. In the beginning, Cu average particle size almost remained the same for the first three variations in Cu contents. However, the average particle size increased with further addition of Cu. Similar observations were also recorded for ZrO_2 average particle size. Besides, these results were in very good agreement with the XRD investigations.

4.2.1.6 Textural properties

Nitrogen adsorption desorption isotherms of CZC catalyst with different Cu contents are displayed in Figure 4.11, while the image for pore size distribution is presented in Figure 4.12. Similarly, BET surface area and pore size volume are documented in Table 4.5. Each catalyst showed typical type-IV isotherms with H4 type hysteresis loops having sharp inflection between p/po ranges of 0.83–0.96. This revealed mesoporous nature of catalyst support. P/P

Table 4.5: Copper metal and catalysts surface area of CZC catalysts with different Cu loadings

Sample	**BET surface area (m^2/g)**	**Total pore volume (cm^3/g)**	**Average pore diameter (nm)**
CZC5	109	0.29	10.7
CZC10	123	0.32	10.4
CZC15	133	0.36	10.8
CZC20	92	0.29	12.9
CZC25	88	0.27	12.4

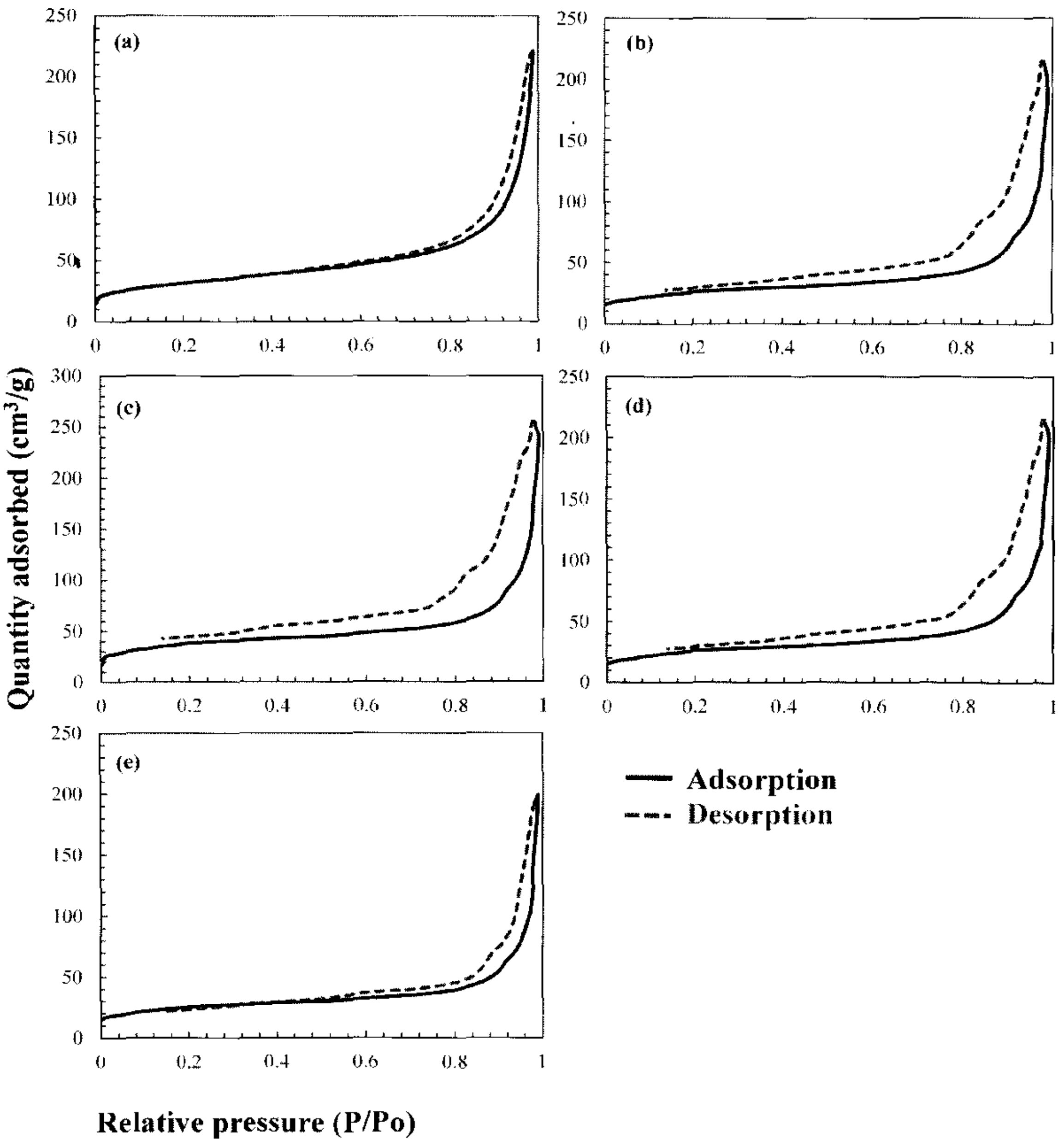

Figure 4.11: N_2 adsorption-desorption isotherms of (a) CZC5, (b) CZC10, (c) CZC15, (d) CZC20 and (e) CZC25 catalysts

Both BET surface areas, as well as pore volume, increased with the increase of Cu loading from 5 to 15 wt.%. The enlargement of surface area with the increase of Cu content was also observed by Grift et al. [172]. However, both BET surface areas and pore volume reduced progressively with further Cu loadings and had the lowest values of 88 m^2/g and 0.27 cm^3/g, respectively with maximum Cu content. The decline in surface area and pore volume indicated a partial blockage of the support pores at higher Cu loadings. The trend of surface area and pore volume as a function of increasing Cu content could also be due to copper agglomeration at Cu content >15 wt.% [257].

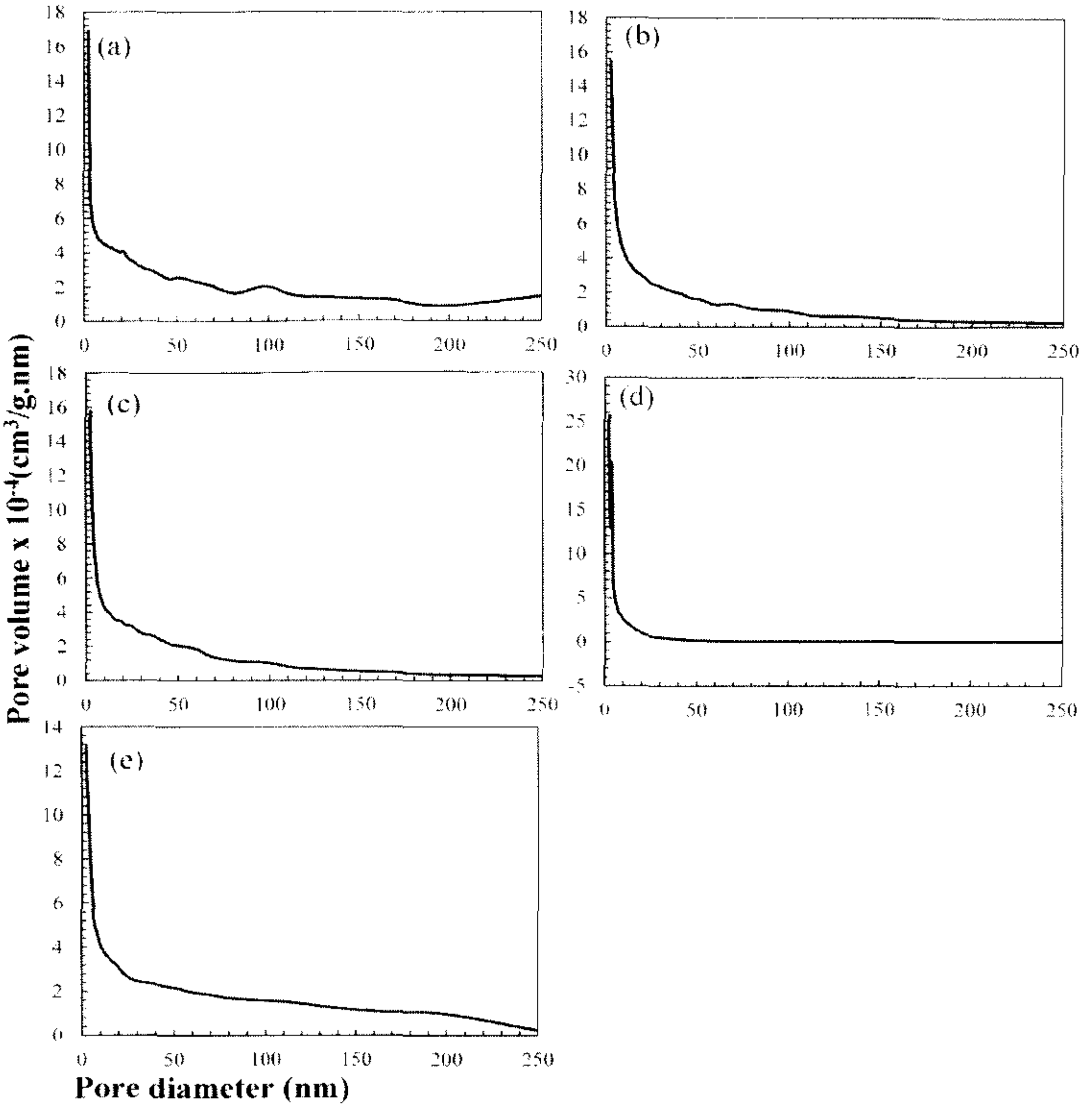

Figure 4.12: Pore size distribution of (a) CZC5, (b) CZC10, (c) CZC15, (d) CZC20 and (e) CZC25 catalysts

This conclusion was further manifested by XRD results. Contrary to the BET surface area, the average pore diameter gradually decreased with the increase of Cu loadings and increased when Cu content > 15 wt. %. Nevertheless, position of hysteresis loop on p/p^0 scale is not affected, indicating that average pore diameter was not affected and remains almost constant throughout the concentration range of copper content as evident from Figure 4.12.

4.2.1.7 Surface area and dispersion of copper

The surface area of metallic copper (S_{Cu}), Cu dispersion (D_{Cu}), average particle size (d_{Cu}), and relative distribution of metallic copper (R_{Cu}) measured via N_2O chemisorption are presented in Table 4.6. As evident from the tabulated data, the increase in Cu content had a marked influence on the surface properties of Cu. Besides, the copper surface area progressively increased with incorporation of Cu content in the parent catalyst and an optimum S_{Cu} was obtained for CZC15 catalyst. However, the metallic surface area was depressed with further rise in concentration of Cu content. These observations clearly suggested agglomeration of CuO at Cu content $\geq$15 wt.%. This was also supported by TEM and XRD results of the respective catalysts. Such a correlation between Cu concentration and S_{Cu} was also reported elsewhere [235]. On the other hand, D_{Cu} initially decreased, and then, increased with the increase in Cu loading from 5-10 wt.% and 10-15 wt.%, respectively. Generally, a linear relationship is observed for surface area and dispersion of copper. In the current case, the correlation remained in line with exception of CZC5 catalyst, whereby low Cu surface area was witnessed despite of higher Cu dispersion. This could be due to the higher interaction between Cu and ZrO_2 components. More recently, similar observations were also recorded by Freitas et al. for Cu/ZrO_2 catalyst with varying Cu content [257].

In contrast, the magnitude of d_{Cu} showed an opposite trend with corresponding catalysts. This had been quite obvious as smaller particles exhibited higher dispersion and vice versa. The growth in particle size and the concomitant decline in dispersion with Cu content beyond 15 wt.% was a clear manifestation of Cu agglomeration with higher loadings.

Table 4.6: N_2O chemisorption data of CZC catalysts with different Cu content

Sample	S_{Cu} **(m^2/g)**	D_{Cu} **(%)**	d_{Cu} **(nm)**	R_{Cu}
CZC5	5.7	17.7	5.9	1.0
CZC10	9.8	13.25	7.8	0.8
CZC15	13.1	16.0	6.5	0.6
CZC20	12.3	11.0	9.5	0.6
CZC25	11.0	8.5	12.2	0.5

These results were further justified by TEM investigations. Similarly, distribution of metallic Cu (R_{Cu}) was affected by Cu content in the parent catalyst. In addition, value of unity was observed for catalyst with the lowest Cu concentration and it gradually decreased with the increase of Cu content. This implied that Cu was partially embedded in the ZrO_2 phase and the process continued until the lowest R_{Cu} value was recorded for catalysts with maximum Cu loadings. Besides, it could be further inferred that increasing Cu content and subsequent embedding provided less exposed Cu surface and more Cu–ZrO_2 interfacial surface area. Furthermore, due to large interfacial surface area, this feature also revealed better Cu–ZrO_2 interactions as a function of increasing Cu content.

4.2.1.8 Reducibility studies

H_2-TPR analysis was conducted in order to identify and quantify Cu species in the catalysts. H_2-TPR profile of Cu loaded catalysts is given in Figure 4.13, while total H_2-uptake, extent of reduction (H_2/Cu), position and distribution of reduction peaks, as well as relative abundance of dispersed copper are listed in Table 4.7.

[illegible] %

Confirm → - with [illegible]

- mechanism of Cu reduction. exp ?

$Cu^{2+} \rightarrow Cu^0$; $Cu^{2+} \rightarrow Cu^{1+}$

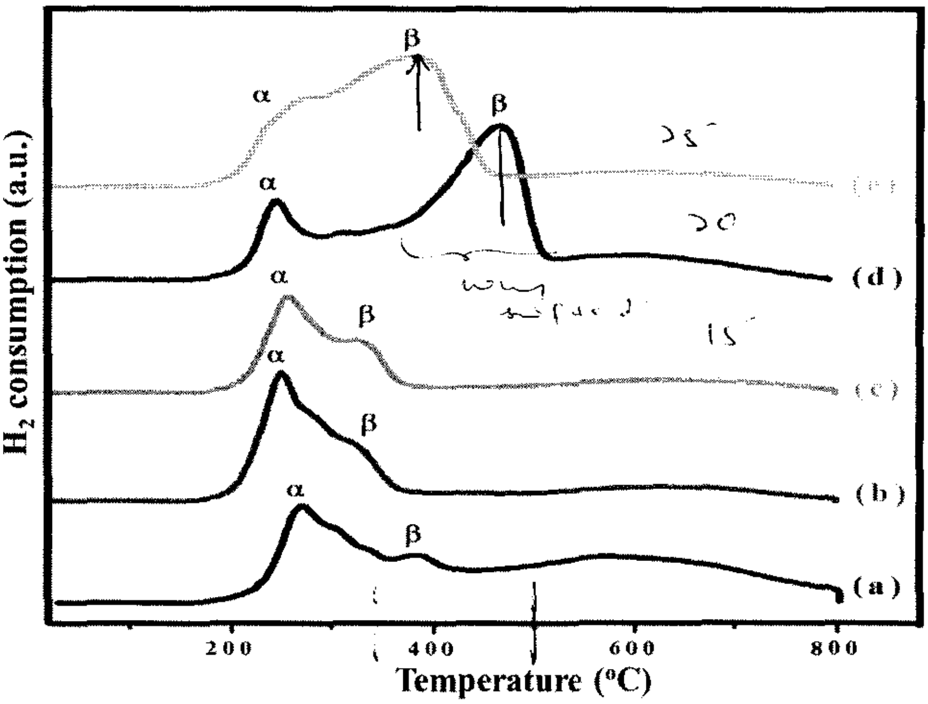

Figure 4.13: TPR profile of (a) CZC5, (b) CZC10, (c) CZC15, (d) CZC20 and (e) CZC25 catalysts

Two reduction peaks were observed in the TPR profile of CZC catalysts, which had been consistently reported for Cu/ZrO_2 system. The reduction peak at lower temperature range of 250-280 °C (peak α) was ascribed to dispersed copper, while the reduction peak observed in temperature range of 350-500 °C (peak β) was due to bulk phase copper. Furthermore, the presence of two reduction peaks had also been reported and attributed to stepwise reduction of Cu ($Cu^{2+} \rightarrow Cu^{+} \rightarrow Cu$) [268]. Likewise, lower reduction peak indicated stronger interaction between Cu and ZrO_2, while the reduction peak at higher temperature was designated to weaker interaction between the two interacting metal oxides. In the current study, both reduction peaks were slightly shifted to relatively lower temperature by increasing Cu loading up to 15 wt.% (Table 4.7). The trend of reduction peaks shifting to lower temperature with increasing Cu content was due to the formation of dimeric Cu-species [269]. Moreover, shifting of reduction peaks with respect to increasing Cu loading clearly showed that Cu reduction was facilitated by promotion of Cu content. On the other hand, reduction maxima of both peaks were shifted to higher temperature when Cu content exceeded above 15 wt.%. This in turn, indicated diminishing interaction between Cu and ZrO_2 as a consequent of increasing Cu content [256].

Table 4.7: TPR results of CZC catalysts with different Cu loadings

Sample	**Total H_2 consumed (μmoles/g)**	**H_2/Cu**	**Red [illegible] temperature (°C)**		**H_2 consumed (μmoles/g)**		**$A_{(\alpha)}/(A_{(\alpha)} + A_{(\beta)})^*$ (%)**
			Peak α	**Peak β**	**Peak α**	**Peak β**	
CZC5	709	0.90	268	385	503	205	71
CZC10	1752	1.11	254	333	1260	491	72
CZC15	2145	0.90	258	337	1455	689	68
CZC20	2715	0.86	256	474	1038	1676	38
CZC25	3162	0.80	283	400	734	2427	23

* Fraction of dispersed Cu

increased

Obviously, the magnitude of total H_2-uptake ~~was increased~~ by increasing Cu content. However, the extent of Cu reduction (H_2/Cu) is an important parameter to assess the fraction of reducible form of CuO in such cases. Besides, H_2/Cu ratio was calculated for each catalyst, assuming that Cu was present as CuO in each catalyst and completely reduced to Cu. In addition, based on stoichiometry of CuO reduction ($CuO + H_2 \rightarrow Cu + H_2O$), a value of H_2/Cu near 1 would mean that Cu is entirely [illegible] present in Cu^{2+} state and had been completely reduced to Cu, while H_2/Cu ratio near 0.5 would show that Cu^{+} is the dominant state of Cu or it is not completely reduced. Although no proper trend in the extent of Cu reduction was observed in the study, the H_2/Cu ratio was improved from 0.92 to 1.11 by increasing the Cu content from 5 to 10 wt.%. Meanwhile, in the Cu/ZrO_2 system, it had been reported that some quantity of Cu^{2+} was incorporated in Zr^{4+} lattices, which was difficult to be reduced [256]. In this regard, improvement of Cu reduction can be justified with the increment of Cu fraction outside these lattices by increasing Cu content from 5 to 10 wt.%. Approximately, 100% Cu reduction was obtained for catalysts up to 15 wt.% Cu loading, which not only confirmed our assumption in calculating the extent of Cu reduction, but it also revealed that Cu^{2+} was completely reduced to Cu instead of Cu^{1+}. Similar observations were also recorded by Lo´pez-Sua´rez et al. in Cu/Al_2O_3 catalyst [270].. Nevertheless,

H_2/Cu ratio was declined when Cu exceeded beyond 15 wt.%. The decline in H_2/Cu ratio clearly indicated the agglomeration of copper.

Furthermore, the distribution of reducible copper was also affected by Cu promotion in the parent catalyst. Peak α remained the major reduction peak in H_2-TPR profile of catalysts with Cu loading up to 15 wt.%. Nevertheless, the intensity of Peak α was reduced, and consequently, peak β was enhanced as the Cu content was increased beyond 15 wt.%. This indicated that Cu experiences phase transformation from Cu^{2+} to Cu^{+} by further increasing Cu loading. Likewise, the relative contribution of highly dispersed CuO also remained constant until CZC15 catalysts. However, it was a remarkable decrease with the excess of Cu contents. This is in accordance with the N_2O chemisorption results.

4.2.1.9 Metal-metal interaction and surface analysis

XPS spectra of Cu 2p of CZC catalysts with different Cu contents are depicted in Figure 4.14. Each catalyst exhibited Cu $2p_{3/2}$ parental peak at 934.4 eV, accompanied by a broad satellite peak around 943 eV, and another parental peak for Cu $2p_{1/2}$ at 954 eV associated with a shake-up peak at around 962 eV. The occurrence of satellite peaks in concomitant to the parental peaks confirmed that Cu predominantly existed as Cu^{2+} in all calcined samples. More importantly, Cu $2p_{3/2}$ was observed at 934.4 eV for each sample, which suggested the highly dispersed state of copper whereas it is generally observed at about 933 eV in the case of bulk copper [271].

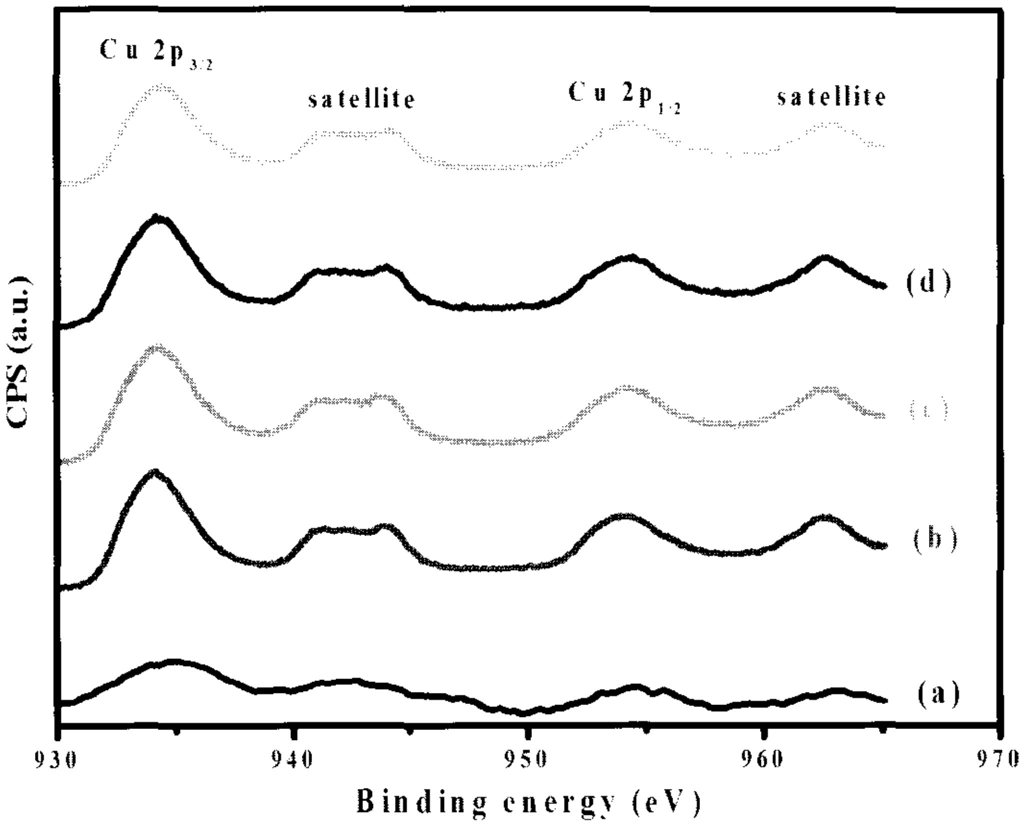

Figure 4.14: XPS Cu2p profile of (a) CZC5, (b) CZC10, (c) CZC15, (d) CZC20 and (e) CZC25 catalysts

Similarly, XPS spectra of Zr 3d is shown in Figure 4.15. Two prominent XPS peaks were identified as Zr $3d_{5/2}$ and Zr $3d_{3/2}$ at 182.2 and 184.6 eV, respectively. The presence of two XPS peaks with an energy gap of 2.4 eV indicated the existence of two different types of zirconium ions. Lower binding energy peaks ($3d_{5/2}$) at 182.2 eV confirmed the existence of Zr^{4+} as ZrO_2, whereas higher binding energy peak ($3d_{3/2}$) at 184.6 eV symbolized Zr^{2+} species [225, 272].

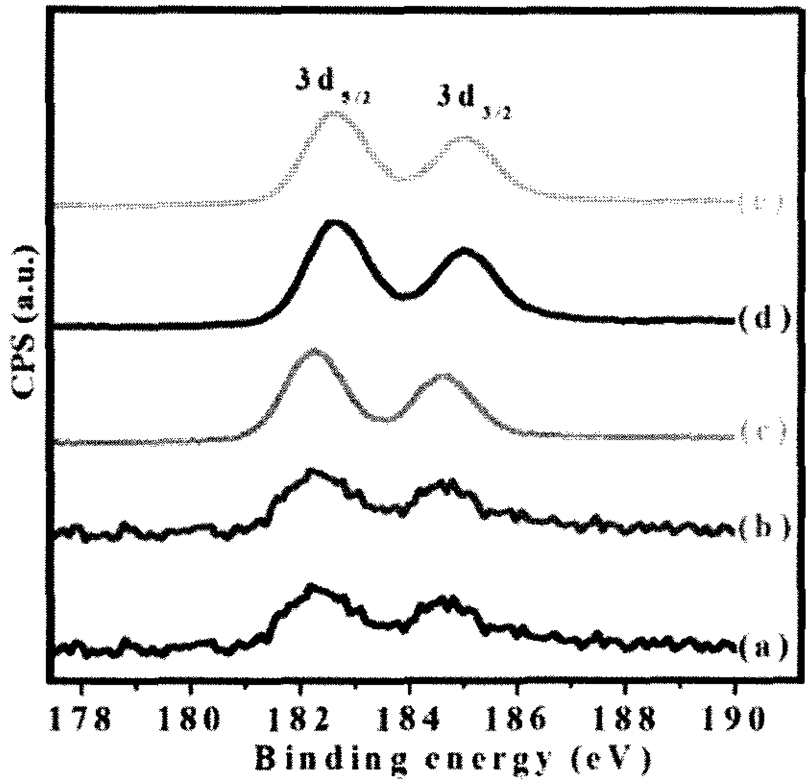

Figure 4.15: XPS of Zr 3d of (a) CZC5, (b) CZC10, (c) CZC15, (d) CZC20 and (e) CZC25 catalysts

The binding energies of Cu $2p_{3/2}$ and Zr $3d_{5/2}$ core electrons and their full width at half maximum (FWHM) values, along with Cu/Zr atomic ratio, are summarized in Table 4.8. As evident from the tabulated data, the binding energies of Cu $2p_{3/2}$ slightly shifted from 934.45 to 934.23 eV by increasing Cu concentration from 5 to 15 wt.%, respectively. This shift of binding energies from higher to lower magnitude with the increase of Cu loading indicated intensification in interaction between Cu and ZrO_2 on one hand, and on the other hand, it was also a clear manifestation of increasing copper dispersion [232]. However, both interaction and dispersion of copper were adversely affected when the Cu loadings reached beyond 15 wt.%. These findings further validated chemisorption and TEM results. Moreover, such variation in binding energies, as a consequent of increasing Cu loadings, was also reported by Liu et al., where lower binding energies were related to dispersed CuO and higher binding energies were declared for crystalline CuO [272]. In contrast, binding energies of Zr $3d_{5/2}$ were less affected by increment in Cu concentration up to 15 wt.%. However, further increase in Cu content shifted the position of Zr $3d_{5/2}$ to slightly higher binding energies, suggesting diminishing the mutual interaction and reducing Zr dispersion with the increase in Cu content [273].

Table 4.8: XPS data of CZC catalysts with different Cu contents

Sample	**Binding energies (eV)**		**FWHM (eV)**		**Atomic Cu/Zr ratio**
	Cu $2p_{3/2}$	**Zr $3d_{5/2}$**	**Cu $2p_{3/2}$**	**Zr $3d_{5/2}$**	
CZC5	934.45	182.18	4.15	4.41	0.56 (0.6)
CZC10	934.20	182.20	4.05	4.42	0.71 (1.35)
CZC15	934.23	182.24	4.22	4.43	1.3 (2.02)
CZC20	934.32	182.60	4.22	4.40	0.73 (2.7)
CZC25	934.43	182.62	4.17	4.42	0.65 (3.37)

Besides, CuO has a nearly square-planar symmetry, where Cu^{2+} ion is surrounded by four oxygen anions. So, in such a system when the symmetry of Cu^{2+} ion is distorted, other charge-transfer excitations may take place due to electron correlation effects [274]. The broad shake-up satellite peak observed in the current case could be due to the slight distortion of CuO symmetry. This could be further elaborated by examining the change in FWHM value of parent Cu $2p_{3/2}$ peaks as a function of Cu addition. The magnitude of FWHM slightly increased by increasing Cu loadings and maximum values were recorded for catalysts with 15 and 20 wt.% of Cu content. Therefore, it could be infirmed from the XPS data that addition of Cu content led to the formation of additional weak Cu^{2+}–Cu^{2+} bonding with neighboring O^{2-} ions, which consequently distorted coordination symmetry of Cu^{2+} ion towards a highly distorted octahedral symmetry [97]. On the other hand, FWHM values of parent Zr $3d_{5/2}$ were found to be invariant throughout the range of Cu concentration. Therefore, no particular information pertaining to bonding and the nature of Zr^{4+} ions could be obtained.

Furthermore, relative atomic ratio of Cu/Zr is also presented in Table 4.8, whereby the values in parentheses are nominal ratio of the two metal in parent catalysts. This atomic ratio increased with the increase of copper content, but as for the bimetallic catalyst with higher loadings, it was significantly lower than the nominal ratio. This showed depletion of surface Cu and subsequent enrichment of surface Zr content. This was due to agglomeration at higher loadings and had been consistent with the agglomeration of the copper particles observed by XRD at higher content. Recently, similar results were also reported by Martin et al. for Cu–ZrO_2 with increased Cu content [225].

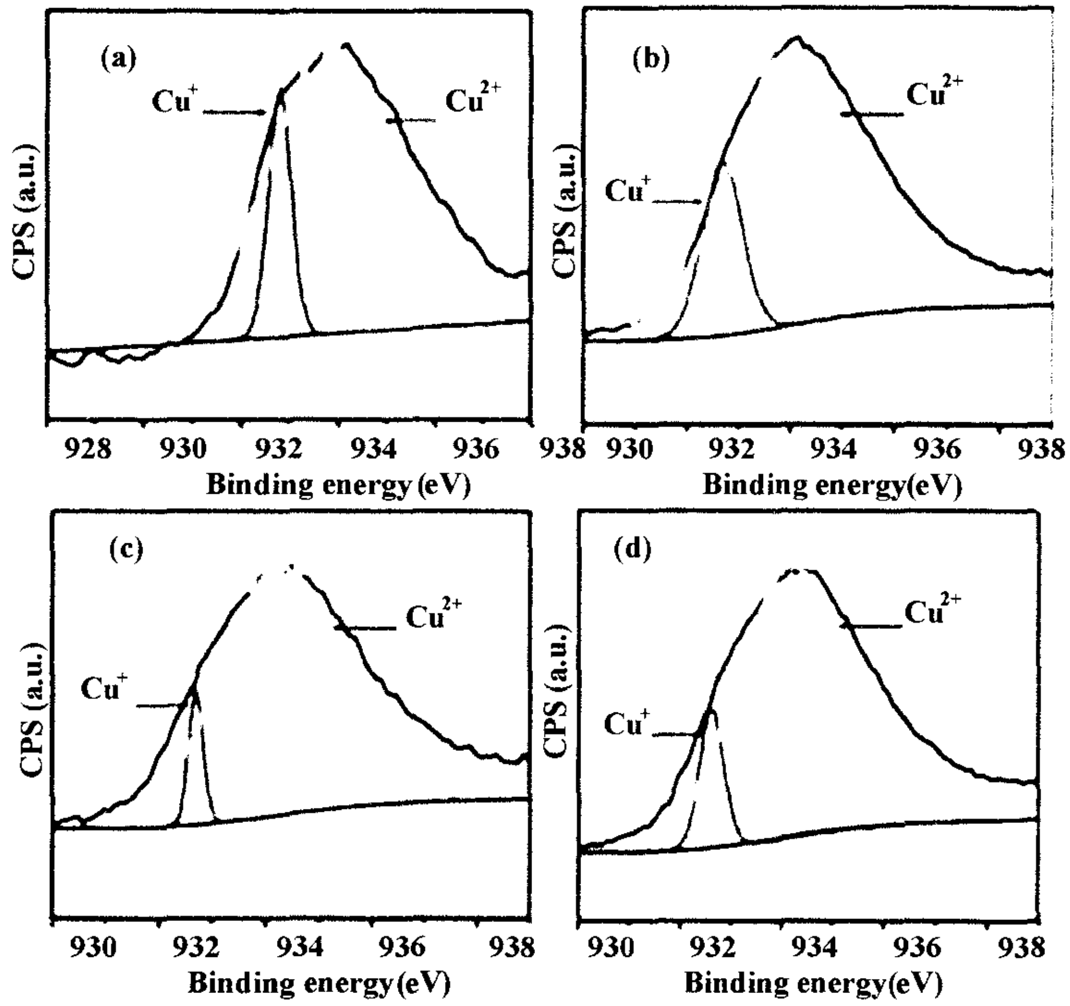

Figure 4.16: XPS Cu 2p peak fitting curves of (a) CZC10, (b) CZC15, (c) CZC20, and (d) CZC25 catalysts

In order to identify the different Cu species, Cu $2p_{3/2}$ peak of each catalyst was resolved in different peaks and is displayed in Figure 4.16. Cupric ion can easily be recognized owing to its characteristic coupling phenomenon between unpaired

[illegible]

electrons. However, binding energies of Cu and Cu^{+} are so close that they could not be differentiated. In the current study, higher energy of Cu $2p_{3/2}$ peak observed at 933.7 eV was assigned to Cu^{2+} ion, whereas low energy peak at 932.7 eV was ascribed to Cu^{+} ions. The appearance of two different CuO species in XPS analysis strongly supported the H_2-TPR findings, where step-wise reduction of CuO was recognized.

4.2.1.10 Basicity and acidity studies

Moreover, in order to obtain insight concerning the basic sites of the catalysts, CO_2-TPD was performed. CO_2-TPD profile of catalysts with different copper loading is presented in Figure 4.17. Similarly, the number of basic sites and their respective densities are documented in Table 4.9. A wide distribution of basic sites was observed, ranging from 100 to 700 °C. The basic sites were classified as medium (below 450 °C) and strong (above 450 °C).

bases assigned as medium b.s. ?

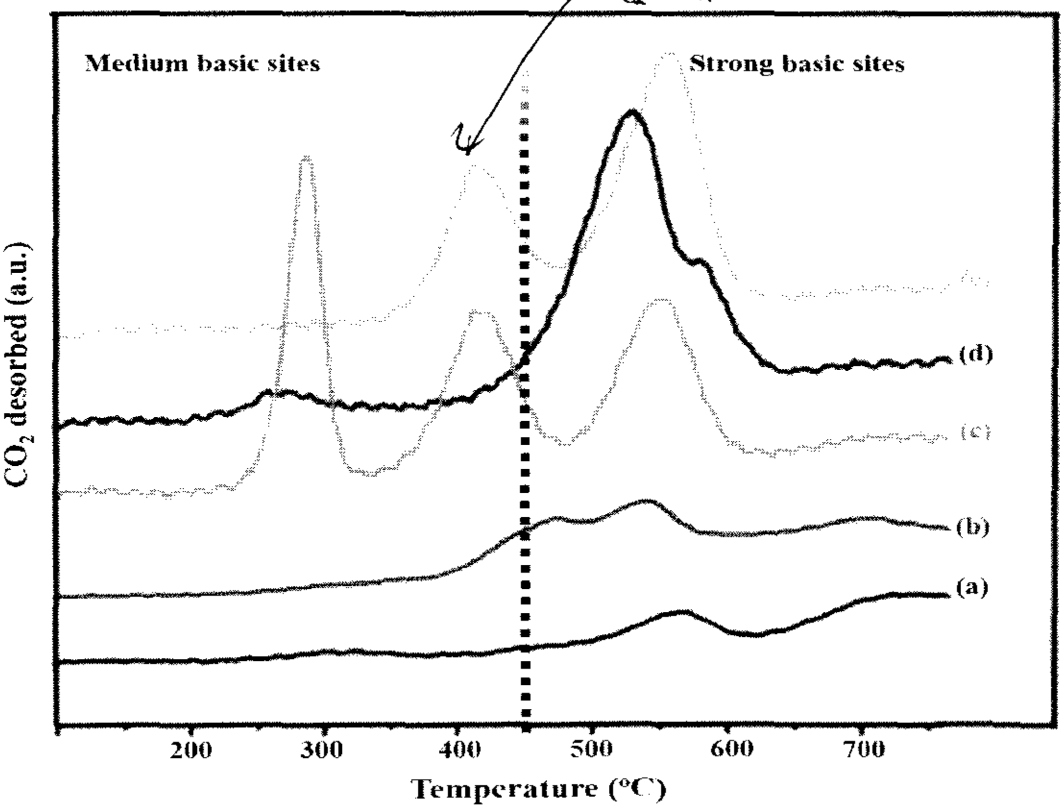

Figure 4.17: TPD-CO_2 profile of (a) CZC5, (b) CZC10, (c) CZC15, (d) CZC20 and (e) CZC25 catalysts

earlier

In addition, the total amount of desorbed CO_2 increased with the increase of Cu content in the CZC catalysts. This linear relationship was maintained with the addition of Cu up to 20 wt.%. However, it was depressed on further Cu loading. This increase in intensity of basic sites with increasing Cu loading is in line with ~~the~~ literature [275]. Since CuO has been reported to be the adsorption site of CO_2 [275], hence it is quite understandable that CO_2 adsorption is improved by increasing Cu loading in CZC catalysts. Besides, the distribution of basic sites was ~~remarkably~~ significantly affected by variation in Cu loadings. A small shoulder at 300 °C confirmed the presence of basic sites with medium strength, but basic sites were predominantly distributed in strong and very strong adsorption regions, as indicated by desorption peaks at 480, 560, and 700 °C for CZC5 catalyst. Meanwhile, the incorporation of Cu content to 10 wt.% created a new desorption peak in the weak basic sites region with desorption max at around 421 °C. However, the majority of basic sites were still distributed at higher temperature regions in CZC10 catalyst. A distinct ~~and~~ a ~~remarkable~~ shift of basic sites from higher temperature region to lower temperature region was observed when Cu content was increased to 15 wt.%.

Table 4.9: Acidic and basic properties of CZC catalysts with different Cu loading

Catalyst	Number of total basic sites (mmol/g.cat)	Density of total basic sites (mmol/m²)	Number of total acidic sites (mmol/g.cat)	Density of total acidic sites (mmol/m²)
CZC5	9.40	0.08	0.85	0.007
CZC10	11.2	0.09	0.94	0.007
CZC15	15.81	0.12	2.36	0.017
CZC20	17.04	0.18	2.53	0.027
CZC25	15.83	0.17	2.05	0.023

< highest
- expt error
- if so, [illegible]
- what is [illegible] fraction, LA or BA ?

Nevertheless, on further increasing of Cu content, the distribution of basic sites was shifted to the right side of the TPD spectra. A similar trend was observed for density of basic sites variation as a function of Cu content. Furthermore, the addition of Cu loading also effected the distribution of acidic sites strength (Figure shown in Appendix C (Figure C2). A small shoulder around 300 °C and a TPD-NH_3 peak near 580 °C indicated the presence of medium and strong acidic sites in CZC5 catalysts, respectively. However, further addition of Cu content did not only shift the latter peak to slightly lower temperature, but also generated another TPD peak in lower temperature region at around 490 °C. Interestingly, a remarkable increase in TPD peak in medium acidic sites region was observed when Cu content was increased to 15 wt.%. The increment of medium acidic sites with increasing Cu loading indicated that the distribution of medium acidic sites had been facilitated by copper. Similar correlation of medium strength acidic sites with respect to the increase of Cu content was also reported by Mihai et al. [276]. However, this trend was no longer observed for further addition of Cu content and substantial decrease in magnitude of medium acidic sites and subsequent increase in the number of acidic sites with higher strength had been recorded when the Cu loading exceeded 15 wt.%. The agglomeration of catalysts particles may be one of the reasons for the depressing amount of acidic sites with respect to higher Cu loading.

Meanwhile, the total NH_3 uptake was increased by increasing the Cu content in the catalysts (Table 4.9). This trend of increasing number of total acidic sites as a function of increasing Cu loading is in line with the literature [276, 277]. This also suggested the adsorption of NH_3 on the surface of Cu, which has previously been reported elsewhere [276]. Therefore, the higher the Cu loading, the higher the amount of ammonia adsorbed. Moreover, the trend can also be justified by considering the strong capability of Cu to oxidize NH_3 to NO and/or N_2. Besides, the number of total acidic sites increased from 0.85 to 2.53 mmol/g.cat when Cu loading was increased from 5 to 20 wt.%. However, further addition of Cu resulted in lowering magnitude of acidic sites, which could be due to agglomeration of Cu particles or formation of Cu crystallites at higher loading. Likewise, the density of basic sites was also enhanced through the elevation of Cu content and an optimum value was recorded for CZC20 catalyst.

?

In conclusion, both acidic and basic profiles of CZC catalysts were promoted with the addition of Cu content in CZC catalysts and optimum quantities of acidic and basic sites were observed for CZC20 catalyst.

4.2.2 Effect of Cu loadings on activity profiles

Table 4.10 presents activity data of CZC catalysts with different Cu loadings. Methanol synthesis rate was improved with incorporation of Cu content up to 15 wt.%, however its rate ~~was~~ declined on further addition. A sharp increase in menthol synthesis rate was observed by increasing Cu content from 5 to 10 wt.%. The trend was continued with further addition of Cu and optimum activity was recorded for catalysts with 15 wt.%. However, when the Cu content was increased further, the additional amount of Cu led to a decline in the methanol activity. The trend in methanol synthesis with respect to Cu content had been closely associated with the variations in Cu surface area and dispersion. Similar observations were also observed by Rhodes et al. [85]. Methanol selectivity ~~was~~ increased with the first three variation of Cu loadings, however, it ~~was~~ decreased when Cu content was increased beyond 15 wt% in parent CZC catalyst. Besides methanol, ethane, hexane and acetone were found as by-products in the reaction mixture.

how do u explain its formation. Rxn scheme?

In terms of methanol synthesis, the production rate of almost similar magnitude was reported by Sloczynski et al., for $Ag/ZnO/ZrO_2$ and $Au/ZnO/ZrO_2$ catalysts [278]. Similarly, CO_2 conversion gradually increased with the increase of Cu content and maximum conversion was achieved with CZC20 catalyst. The discrepancy of greater CO_2 conversion with higher Cu content could be understood by the fact that CO_2 conversion is more related to the ZrO_2 component of the catalyst. In case of TOF, although maximum value was recorded for CZC15 catalyst, no proper variation was observed with varying Cu content.

Table 4.10: Catalytic activity of CZC catalyst with different Cu loadings

Catalyst	Meth~~.~~anol activity (g/kg.cat.h)	CO_2 conversion (%)	Meth~~.~~anol selectivity (%)	$TOF_{MeOH} \times 10^{-4}$ (s^{-1})
CZC5	08	4	41	5.0
CZC10	13	7	49	4.7
CZC15	20	11	54	5.4
CZC20	18	12	42	5.2
CZC25	16	09	39	5.1

~~On top of that, the~~ And BET surface area is an important parameter in ~~discussing the~~ correlating catalyst activity ~~in~~ a particular reaction. In the current work, a correlation of BET surface area with methanol productivity as a consequent of varying Cu content was investigated.

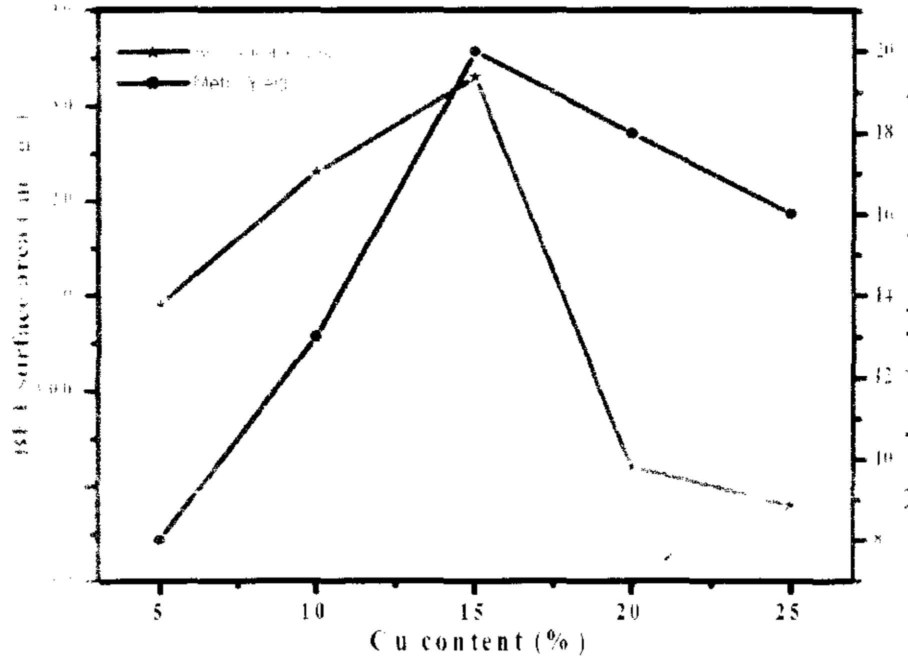

Figure 4.18: Correlation of Cu content with BET surface area and methanol productivity rate

As shown in Figure 4.18, increase in Cu content tended to ~~enlarge~~ boost the BET surface area of the catalyst, which subsequently improved the methanol productivity rate. The trend continued with further Cu addition and optimum values of both BET surface area and methanol productivity rate were obtained for catalyst with 15 wt.% of Cu content. However, further augmentation of Cu content reduced the BET surface area, and consequently, methanol productivity rate was depressed. This ~~pointed out~~ suggested that BET surface area ~~had been~~ has a predominant contribution factor in activity profiles of CZC catalyst to methanol formation. Similar observations were also documented for methanol production over Cu/ZnO catalyst by Pan et al. [279].

Based on the reported mechanistic studies, Cu surface area (S_{Cu}) is an important parameter in CO_2 hydrogenation to methanol. In order to assess the role of copper surface area (S_{Cu}) on the activity pattern of CZC catalysts, a graph portraying S_{Cu}, methanol production, and turnover frequency (TOF) is depicted in Figure 4.19.

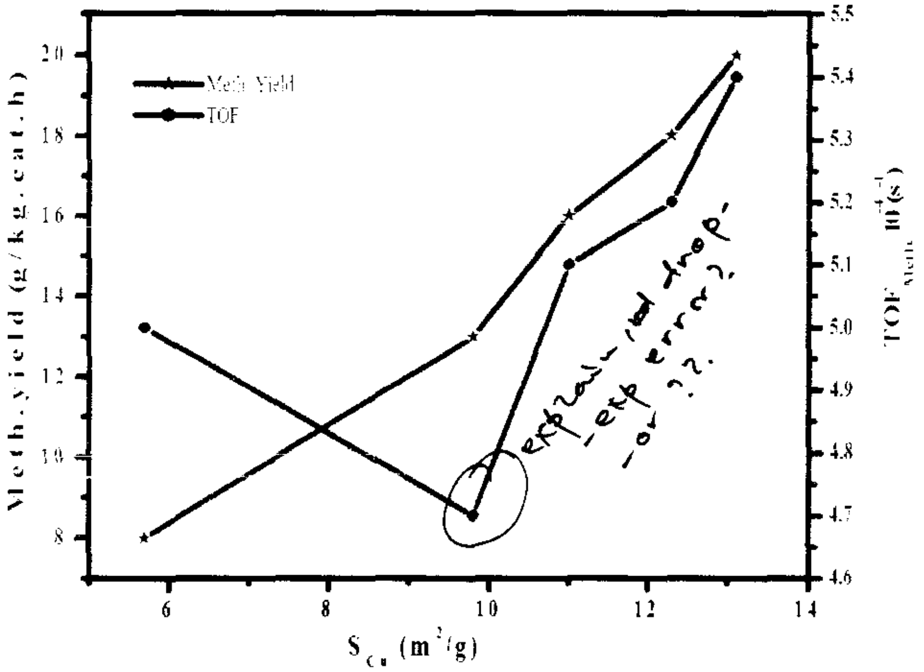

Figure 4.19: Correlation of S_{Cu} with methanol production and TOF

As evident from the graph, methanol yield exhibited a volcanic variation trend with the increase of S_{Cu}. The promotion of methanol yield by increasing S_{Cu} is in accordance with the literature [280]. Obviously, promotion in S_{Cu} provided more atomic hydrogen.

Consequently, more atomic hydrogens were supplied to the ZrO_2 sites for reduction of CO_2 adsorption, which led to higher production rate. However, TOF variation was not totally aligned with variant S_{Cu} values. As evident from the graph, TOF decreased with initial increase in copper surface area, however it was enhanced with further increase in S_{Cu}. Generally activity of the copper based catalysts increases linearly with increasing S_{Cu}. However conflicting results have also been reported in the literature [281, 282]. Based on Boudart's theory, a straight line should be obtained between S_{Cu} and TOF in case where catalyst activity is only dependent on S_{Cu} [102]. Based on this observation, it could be inferred that in the current case, although the rate of methanol synthesis was accelerated by increasing S_{Cu}, however it was not the sole factor that tailored the activity profile.

Due to the acidic nature of CO_2, the number of basic sites played an important role in CO_2 conversion reactions.

explain more

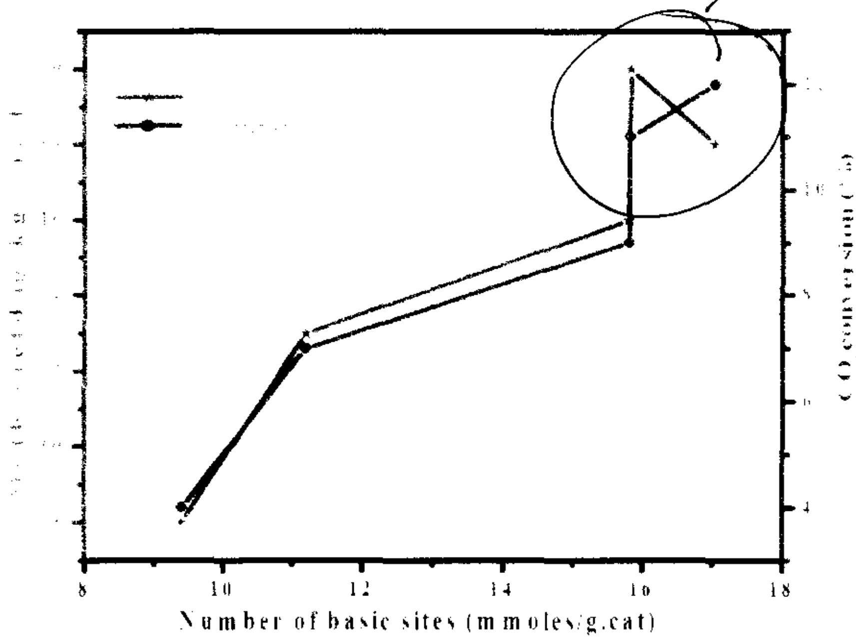

Figure 4.20: Catalysts performance versus number of basic site

As shown in Figure 4.20, the performance of catalysts was significantly altered by the number of basic sites. The rate of methanol productivity was increased by increasing the number of basic site with an exception of increase in basic sites from 15.8 to 17.04 mmoles/g.cat, which led to a decrease in methanol productivity from 20 to 18 g/kg.cat.h, respectively. However, a linear relationship was observed in the number of basic sites and CO_2 conversion. This signified the vital role of magnitude of basic sites in CO_2 conversion. Similar relation of improved CO_2 conversion as a function of the number of basic sites had also been previously reported [283].

4.3 Effect of ZrO_2 loadings

Effects of ZrO_2 loadings on the physicochemical properties and activity pattern of parent catalyst were investigated. The results are briefly discussed. ~~in the following~~

4.3.1 Effect of ZrO_2 loadings on physiochemical properties

Different techniques were employed to investigate the effects of ZrO_2 loadings on the physicochemical properties. These are described in the following.

4.3.1.1 Quantification of catalyst components

ICP-OES was employed to quantify Cu and ZrO_2 loadings and the data are presented in Table 4.11. Magnitudes of both bulk Cu, as well as ZrO_2 measured by ICP, were in very close agreement to the targeted values. This implied that almost all metal components (Cu & ZrO_2) were successfully deposited on the catalyst support. This in turn also indicated the efficiency of DP method for preparing catalysts with higher loadings of active metals.

Table 4.11: ICP results of CZC catalysts with different ZrO_2 content

Sample	**Target Cu (%)**	**Cu (%) by ICP**	**Target ZrO_2 (%)**	**ZrO_2 (%) by ICP**
5CZC	15	14.54	5	4.51
10CZC	15	15.50	10	9.78
15CZC	15	14.89	15	15.29
20CZC	15	14.24	20	19.24
25CZC	15	14.81	25	24.17

4.3.1.2 Bulk phase analysis

Figure 4.21 displays the diffraction patterns of calcined CNFs based Cu/ZrO_2 catalysts with different ZrO_2 loadings. For comparison, diffraction of bare CNFs is also shown in the Figure. Two prominent peaks were detected at $2\theta = 26°$ and 44° with d spacing of 3.36 and 2.06 respectively, indicating the diffractions of (002) and (100) planes of graphitic carbon nanofibers [87, 246]. The presence of zirconia was pointed out by two diffraction peaks at 24.3° and 30.3°, ~~each one for~~ monoclinic zirconia (m-ZrO_2) and tetragonal zirconia (t-ZrO_2), respectively [284]. Similarly, the diffraction patterns at 32.6°, 35.5°, 38.7°, 48.8°, 53.6°, 58.3°, 61.67°, 66.4°, 68.1°, 72.3°, and 75.1° had been identified, which was indexed as monoclinic-phased tenorite CuO with JCPDS card files No. 48-1548 (a = 4.62 Å, b = 3.43 Å, and c = 5.06 Å). It was observed that ~~With closer look,~~ by increasing ZrO_2 content up to 15 wt.%, the intensity of the CuO diffraction peaks gradually decreased while the width of the diffraction peak slightly broadened with respect to ZrO_2 promotion, indicating a reduction of CuO crystallization degree and improvement of copper dispersion. However, further addition of ZrO_2 led to intensify CuO diffraction peaks sharply, suggesting increase in the degree of crystallization and reduction in copper dispersion. Moreover, no diffraction peak was observed for zirconia phase in catalysts with ZrO_2 loadings up to 15 wt.%. This suggested a well-dispersed and amorphous form of zirconia. Nevertheless, sharp diffraction peaks were identified when ZrO_2 concentration surpassed beyond 15 wt.%, displaying the amplification of crystallization and the decline in ZrO_2 dispersion. By summarizing the XRD results, ZrO_2 addition resulted in higher dispersion and reduced crystallization for both active components (CuO and ZrO_2) with optimum values for 15CZC catalyst. Besides, the highly dispersed forms of active components are desirable for improved performance of catalysts [285]. Hence, XRD findings envisaged 15CZC to be the most active catalyst amongst the studied catalysts.

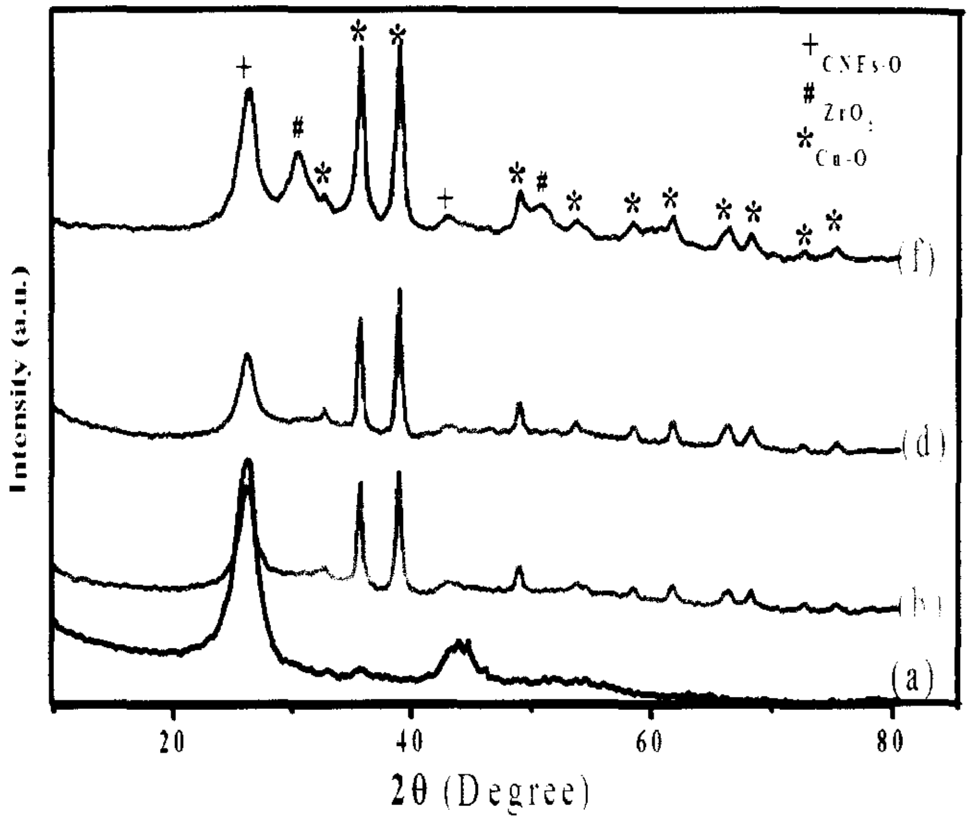

Figure 4.21: XRD spectra of (a) CNF-O, (b) 5CZC, (c) 10CZC, (d) 15CZC, (e) 20CZC and (f) 25CZC catalysts

4.3.1.3 Morphology investigations

TEM images of CZC catalysts with different ZrO_2 loadings are shown in Figure 4.22. CuO and ZrO_2 individual particles were identified as mentioned in the previous section 4.2.2.5. TEM investigations revealed that the particles of the catalysts were uniformly distributed in CZC catalysts with lower ZrO_2 content. However, aggregation of particles was observed when ZrO_2 content was increased above 15 wt.%. Besides, aggregation and growth of particles adversely affected the dispersion of active components over the surface of CNFs. This is exactly in line with the results of N_2O chemisorption. Besides, TEM investigations had been consistent with the XRD and TPR findings. Next, particle size was calculated to identify the average particle size of copper and zirconia, and the details are depicted in Table 4.12. Although the size of the average Cu particles progressively increased with the increase in ZrO_2 content with the first three ZrO_2 variations, however, remarkable growth of the average Cu particles was observed for catalysts with 20 and 25 wt.% of ZrO_2 content. These TEM observations were in line with the XRD and the N_2O chemisorption results. Similarly, the average particle size of zirconia was increased from 4 to 7 nm by increasing ZrO_2 concentration from 5 to 15 wt.%, respectively. The growth of ZrO_2 particles persisted with further ZrO_2 addition and the average particle size was doubled as ZrO_2 was promoted from 15 to 25 wt.% in the parent catalyst.

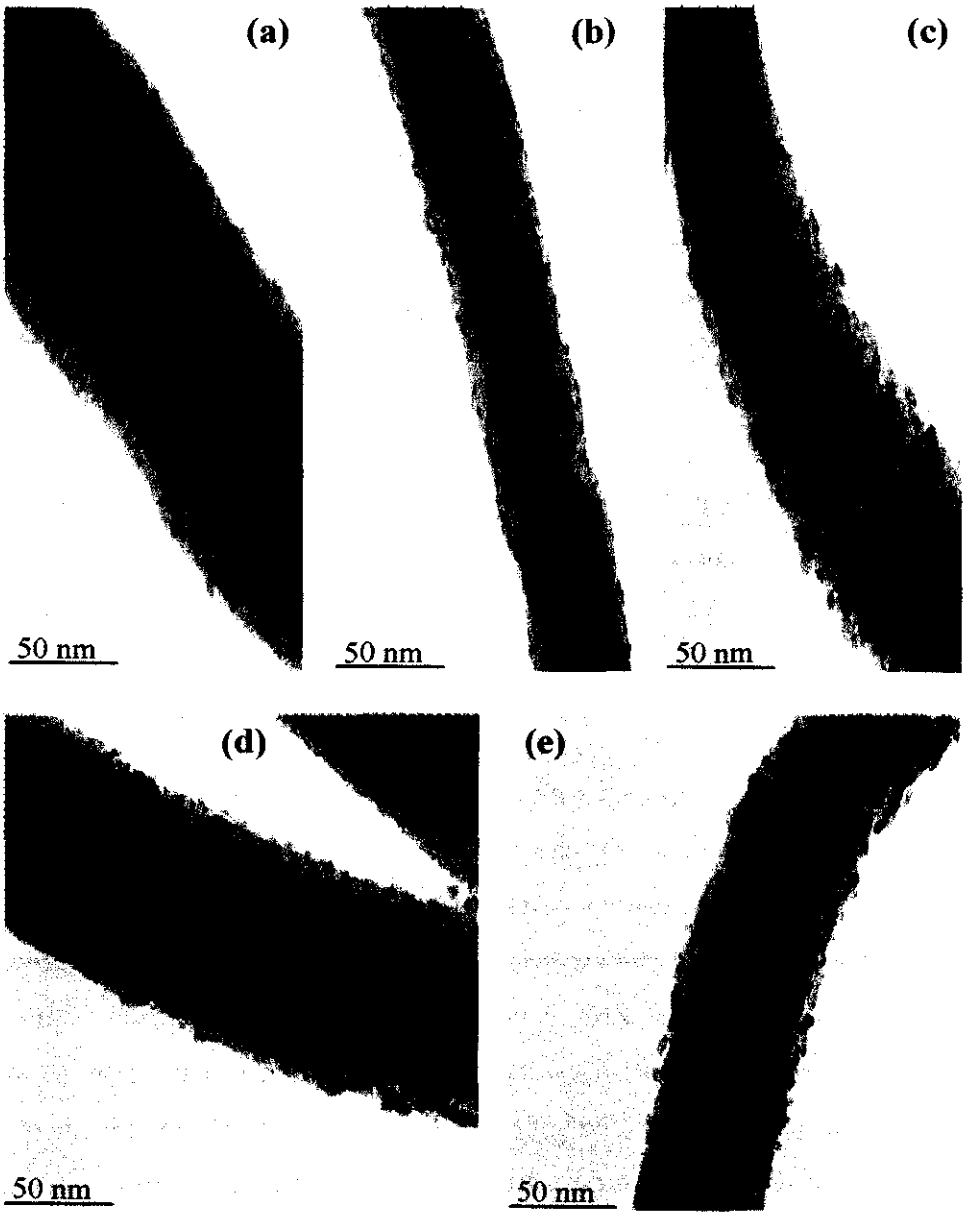

Figure 4.22: TEM images of (a) 5CZC, (b) 10CZC, (c) 15CZC, (d) 20CZC and (e) 25CZC catalysts

Table 4.12: TEM catalyst particle size

Catalysts	**Copper average particle size**	**Zirconia average particle size**
5CZC	3	4
10CZC	4	5
15CZC	5	7
20CZC	8	10
25CZC	10	12

4.3.1.4 Textural properties

In order to investigate the textural properties of catalysts N_2 adsorption-desorption technique was employed. N_2 adsorption-desorption isotherms and pore size distributions of CZC catalyst with different ZrO_2 loadings are illustrated in Figures 4.23 and 4.24, respectively. Likewise, their textural properties are summarized in Table 4.13. Each catalyst showed type-IV isotherms with H4 type hysteresis loops with a sharp rise between P/P_0 at 0.90. This represented the mesoporous nature of the catalyst. A very narrow pore size distribution, centered at around 10 nm, was found for each catalyst (Figure 4.24). This suggested that pore size distribution was not affected with the addition of ZrO_2. On the other hand, surface area was significantly altered with the addition of ZrO_2. Nevertheless, pore volume and average pore diameter were less affected with the incorporation of ZrO_2. As evident from the tabulated data, a sharp increase in surface area was observed from 130 to 140 m^2/g when ZrO_2 content was doubled from 5 to 10 wt.% and reached 152 m^2/g with further addition of ZrO_2 content. However, the surface area first decreased, and then, remained almost constant when ZrO_2 loading was increased beyond 15 wt.%. This could be due to the lower dispersion and agglomeration of catalysts particles with the excess amount of ZrO_2. Furthermore, agglomeration of catalysts particles and subsequent lower dispersion at higher ZrO_2 loadings could also be visualized from TEM images of the respective catalysts.

How do u explain SA & pore vol [illegible]

Should relate [illegible]

Hence, in summarizing the BET results, ZrO_2 promotion facilitated the surface area of CZC catalysts remarkably up to 15 wt.% of ZrO_2 content, and then, remained unchanged with further ZrO_2 addition. In addition, a similar trend was also reported by Gao et al., for Cu/Zn/Al/Zr catalysts with different ZrO_2 loadings [187].

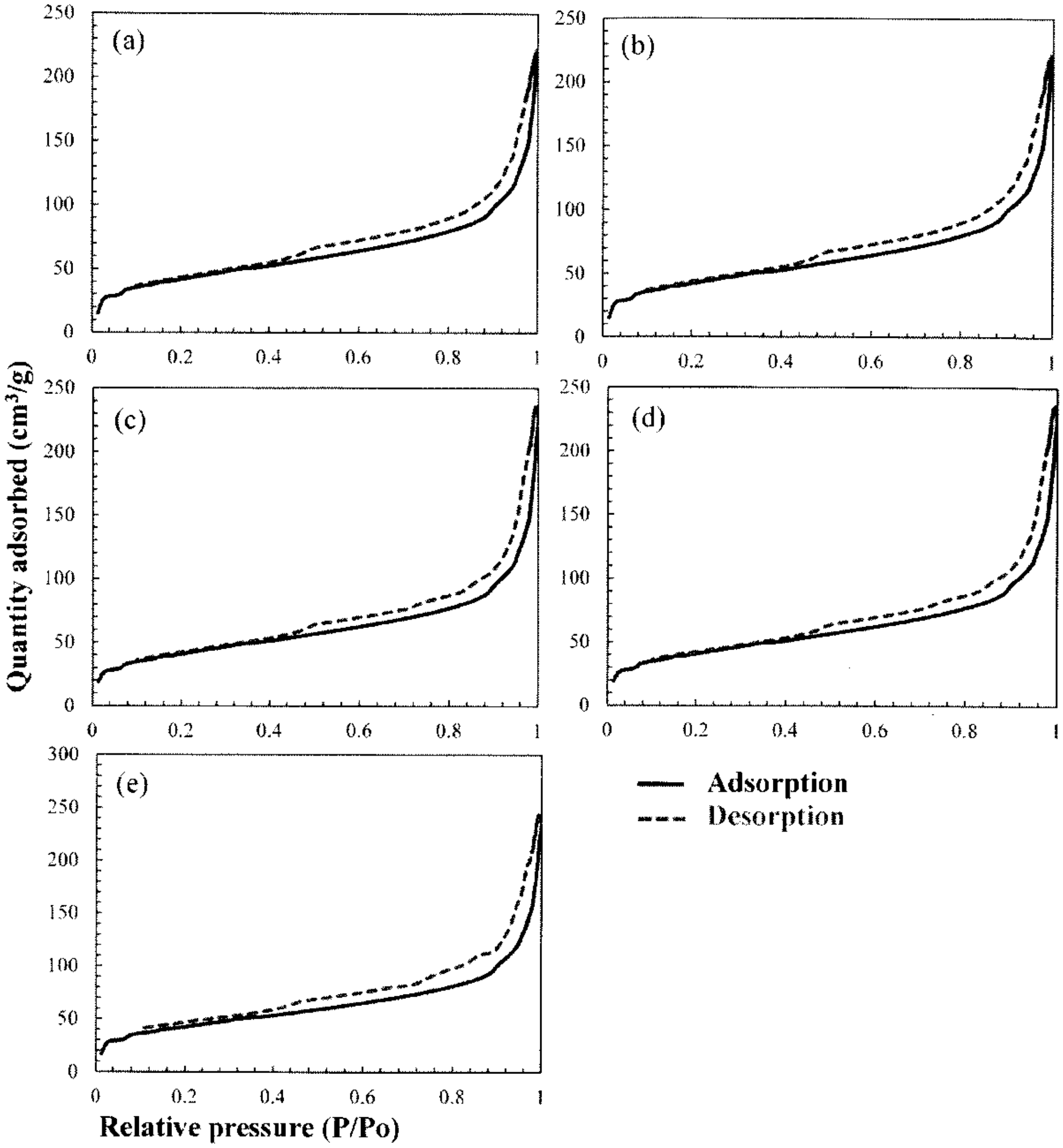

Figure 4.23: N_2 adsorption-desorption isotherms of (a) 5CZC, (b) 10CZC, (c) 15CZC, (d) 20CZC and (e) 25CZC catalysts

Table 4.13: Textural properties of CZC catalysts with different ZrO_2 loadings

Sample	BET surface area (m^2/g)	Total pore volume (cm^3/g)	Average pore diameter (nm)
5CZC	130	0.32	10.8
10CZC	141	0.30	10.6
15CZC	152	0.28	10.5
20CZC	149	0.31	11.6
25CZC	155	0.29	10.6

what do they tell ?

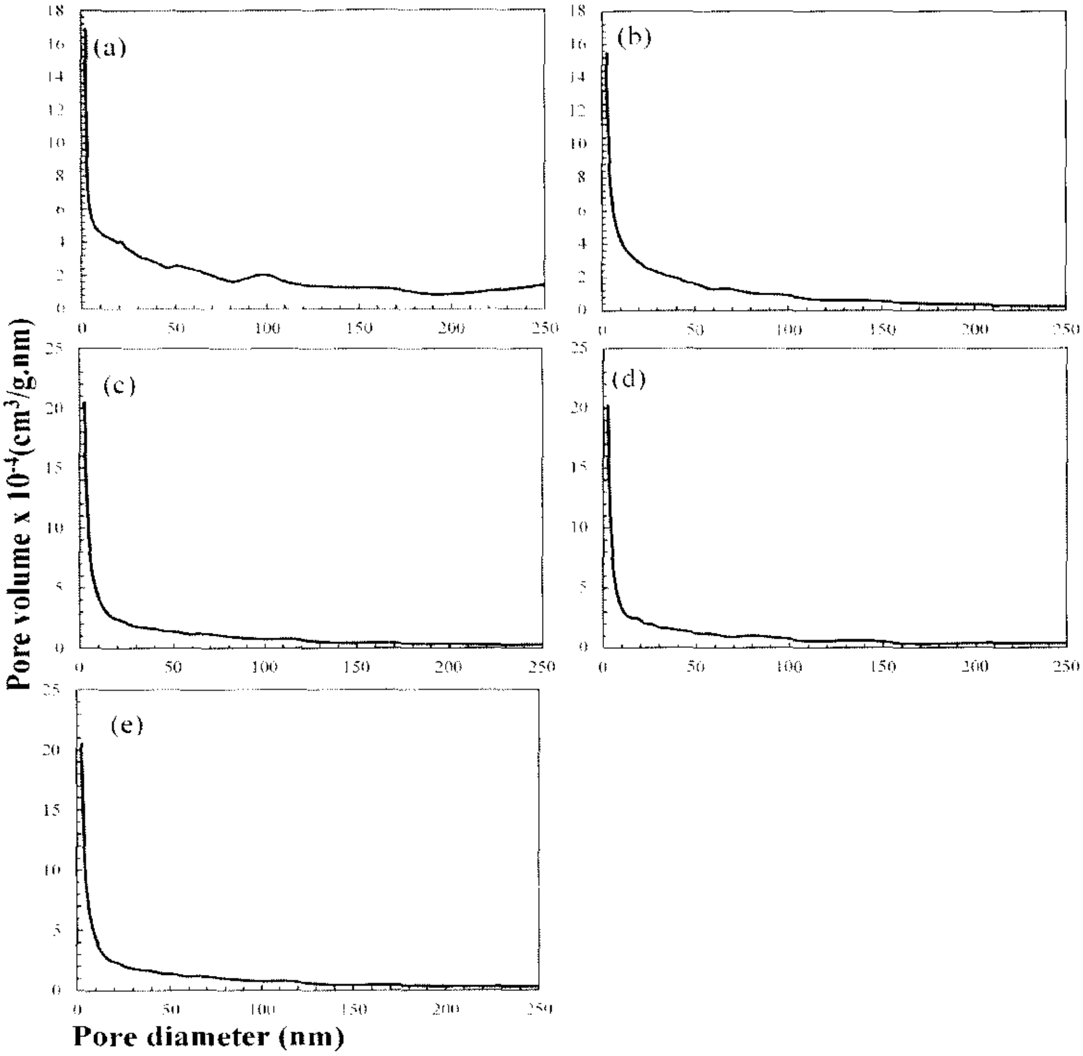

Figure 4.24: Pore size distribution of (a) 5CZC, (b) 10CZC, (c) 15CZC, (d) 20CZC and (e) 25CZC catalysts

4.3.1.5 Surface area and dispersion of copper

The surface area of metallic copper (S_{Cu}), Cu dispersion (D_{Cu}), average particle size (d_{Cu}), and relative distribution of metallic copper (R_{Cu}) were measured via N_2O chemisorption. The N_2O chemisorption data are presented in Table 4.14. As evident from the tabulated data, increase in ZrO_2 content had a marked influence on the surface properties of Cu. Copper surface area initially increased from 8.1 to 9.9 m^2/g with the incorporation of ZrO_2 in the parent catalyst from 5 to 10 wt.%. However, the metallic surface area progressively depressed when ZrO_2 addition exceeded 10 wt.%. Nevertheless, CZC catalyst with the largest Cu surface area (10CZC) did not show the highest activity, and unexpectedly, CZC catalyst with relatively lower S_{Cu} (15CZC) displayed the highest catalytic activity. This discrepancy could be resolved by taking into account the amount of active copper. In the current case, it could be inferred that the Cu on the surface of 10CZC catalyst displayed lower activity than the Cu particles on the surface of the 15CZC catalysts or in other words, lesser amount of surface copper was active in 10CZC catalyst as compared to that of 15CZC catalyst. Besides, similar observations of conflicting correlation between Cu surface area and catalyst activity were reported by Jones et al. for Cu/ZnO/nano Al_2O_3 catalyst [273]. The decline of S_{Cu} by increasing ZrO_2 content suggested crystallization and agglomeration of Cu particles. This supported the intensification and broadening of XRD peaks when ZrO_2 concentration exceeded 15 wt.%. Likewise, a similar trend was discovered for Cu dispersion with the increased ZrO_2 content. Although the magnitude of Cu dispersion initially increased and then decreased by increasing ZrO_2 loadings from 5-10 and 10-15 wt.%, respectively, there was no substantial difference between magnitudes of D_{Cu} for the corresponding catalysts. In contrast, the amount of D_{Cu} significantly declined when ZrO_2 concentration surpassed 15 wt.%. These observations had been in line with TEM results. Nonetheless, contrary to S_{Cu} and D_{Cu}, d_{Cu} showed an opposite trend with the increase of ZrO_2 content. Obviously, particle size and surface area are reciprocal to each other, hence smaller particles exhibit higher surface area and vice versa. Furthermore, the growth in Cu particle size and the concomitant decline in its surface area, as well as the dispersion with ZrO_2 content beyond 15 wt.% had been a clear manifestation of Cu agglomeration with higher ZrO_2 loadings. These results were further justified with TEM investigations. Similarly, the distribution of metallic Cu was affected with the addition of ZrO_2 content in the parent catalyst. Besides, the contribution of surface metallic copper was increased from 0.41 to 0.46 with the increment of ZrO_2 loading from 5-10 wt.%. Nevertheless, it progressively declined with further addition of ZrO_2 content. The decrease in surface Cu as a consequent of increasing ZrO_2 content implied that Cu was partially embedded in the ZrO_2 phase and the process lingered until the lowest R_{Cu} value was recorded for catalysts with maximum ZrO_2 loadings. More importantly, increasing ZrO_2 content and subsequent Cu embedding offered less exposure to Cu surface, but more Cu– ZrO_2 interfacial surface area. Furthermore, due to large interfacial surface area, this feature also revealed better Cu– ZrO_2 interactions as a function of increasing Cu content.

Table 4.14: N_2O chemisorption data

Sample	**S_{Cu} (m^2/g)**	**D_{Cu} (%)**	**d_{Cu} (nm)**	**R_{Cu}**
5CZC	8.1	11.6	9	0.41
10CZC	9.9	13.2	8	0.46
15CZC	9.5	12.9	8	0.41
20CZC	5.9	6.7	15	0.25
25CZC	4.3	5.8	18	0.19

4.3.1.6 Reducibility studies

TPR measurements were carried out in order to investigate the reduction behavior of catalysts as a function of ZrO_2 promotion. TPR profile of CZC catalyst with different ZrO_2 loadings is depicted in Figure 4.25. Similarly, the magnitude of total H_2 uptake, extent of reduction, and relative distribution of dispersed Cu are presented in Table 4.15. As evident from the Figure, two main reduction peaks were observed for all CZC catalysts. Low-temperature peak (peak α) was ascribed to the reduction of dispersed CuO, whereas the high temperature peak (peak β) was due to reduction of bulk phase CuO [85]. With a closer look, one could observe that peak α centered at 240 °C for 5CZC catalyst was shifted to a higher temperature of 260 °C as the ZrO_2 content was doubled, suggesting lesser interaction between CuO and ZrO_2 in the latter case. However, further addition of ZrO_2 facilitated the reduction of CuO by demonstrating a slight shift towards lower temperature.

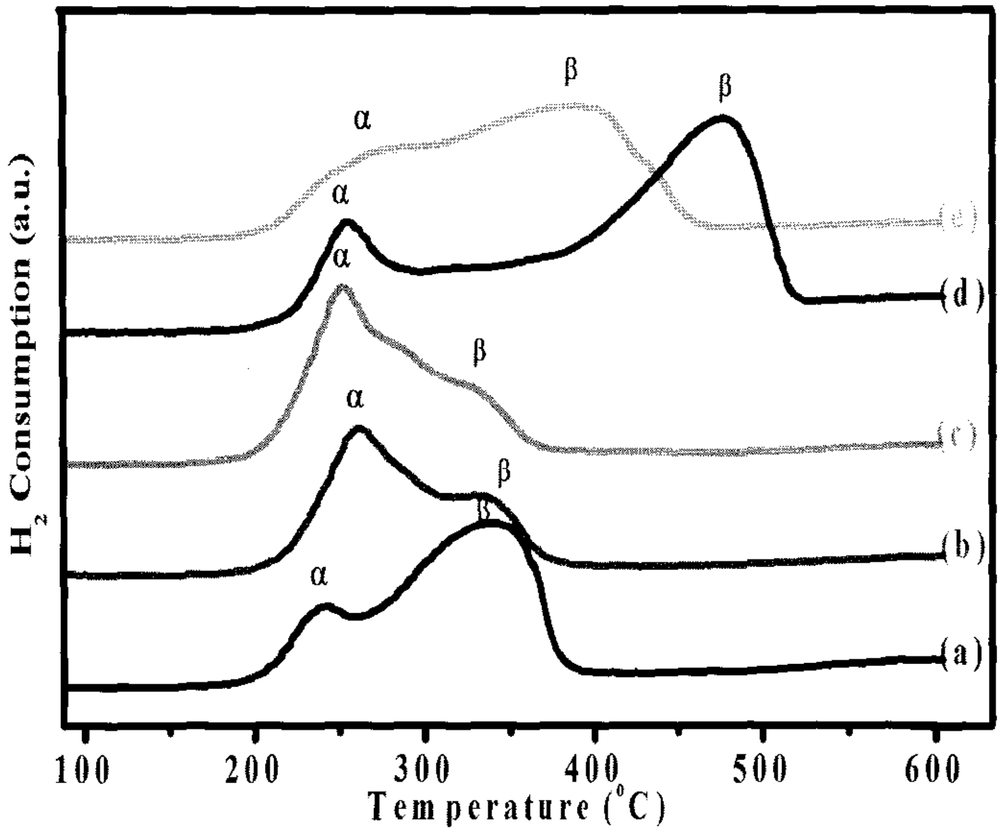

Figure 4.25: TPR Spectra of (a) 5CZC, (b) 10CZC, (c) 15CZC, (d) 20CZC and (e) 25CZC catalysts

In contrast, peak β observed a consistent lower-temperature shift as a consequence of ZrO_2 addition up to 15 wt.% of ZrO_2 loading, and a reverse shift was witnessed with further ZrO_2 promotion. This indicated that ZrO_2 addition improved the reduction of bulk phase CuO and maximum improvement was observed for catalysts with 15 wt.% of ZrO_2 content. In addition to these two common reduction peaks, another small shoulder centered at 286 °C was observed for 15CZC catalysts, suggesting the formation of a new Cu phase. However, this new phase was diminished with further ZrO_2 addition. Generation of such a new Cu phase in Cu/ZrO_2 system has been previously reported and attributed to dissolution of zirconium ions in CuO phase [97]. More interestingly, this new phase was claimed to contribute more significantly in

If so, what is it
Could it Cu^{1+}

methanol synthesis. Based on this observation, the highest activity of 15CZC catalyst could also be correlated to this new CuO phase.

Highly dispersed Cu had been believed to be the most active phase of copper in Cu-based catalysts. In the current study, distributions of highly dispersed and bulk phase Cu were significantly affected by ZrO_2 promotion. As evident from the tabulated data, contribution of highly dispersed phase was incremented by ZrO_2 addition and optimum contribution was recorded for 15CZC catalysts. This could also be one the reasons for higher activity of the catalyst amongst all studied catalysts for methanol synthesis. Similar correlation of catalyst activity to methanol synthesis as a function of magnitude of dispersed Cu was also reported by Suh et al. [97]. Furthermore, the presence of two reduction peaks had also been reported and attributed to stepwise reduction of Cu, from Cu^{2+} to Cu^{+}, and subsequently from Cu^{+} to Cu^{0} [268, 286-288]. In this respect, peak α was attributed to the reduction of Cu^{2+} to Cu^{+}, while peak β was assigned to the reduction of Cu^{+} to Cu [270, 289, 290].

Besides, the extent of copper reduction (H_2/Cu) was calculated to assess the influence of increasing ZrO_2 content on the overall Cu reduction. Almost 90 % of total Cu was found in reduced form with ZrO_2 loading up to 15 wt.%. Furthermore, the magnitude of $H_2/Cu \approx 1$ also indicated that regardless of ZrO_2 content, copper predominantly existed as CuO in catalysts up to 15 wt.% of ZrO_2 content. Nevertheless, the extent of Cu reduction was depressed when ZrO_2 content exceeded 15 wt.%. As less fraction of agglomerated Cu was available for reduction, this trend suggested the growth and the agglomeration of Cu with increased ZrO_2 loadings. Likewise, this behavior of Cu growth and agglomeration was also supported by XRD results and N_2O chemisorption studies.

Table 4.15: TPR data of CZC catalysts with different ZrO_2 loadings

Sample	**Total H_2 consumed (μmoles/g)**	**H_2/Cu**	**Red.Temp (°C)**		**H_2 consumed (μmoles/g)**		**$A_{(\alpha)}/(A_{(\alpha)}+A_{(\beta)})^{*}$ (%)**
			Peak α	**Peak β**	**Peak α**	**Peak β**	
5CZC	2265	0.95	240	341	420	1845	18
10CZC	2089	0.88	260	334	706	1383	33
15CZC	2145	0.90	250	326	1455	689	68
20CZC	1790	0.75	255	476	640	1150	35
25CZC	1331	0.56	270	400	600	731	45

* Fraction of dispersed Cu

4.3.1.7 Metal-metal interaction and surface analysis

XPS spectra of Cu 2p of CZC catalysts with different ZrO_2 content are illustrated in Figure 4.26. Each catalyst showed core electron peaks at 934 and 954 eV, representing Cu $2p_{3/2}$ and Cu $2p_{1/2}$ parental peaks, respectively. Similarly, each core electron peak was accompanied by another satellite peak with binding energy gap of 8-9 eV at 943 and 962 eV, respectively. The occurrence of shake-up peaks in concomitant to the parental peaks confirmed that Cu predominantly existed as Cu^{2+} in all calcined samples.

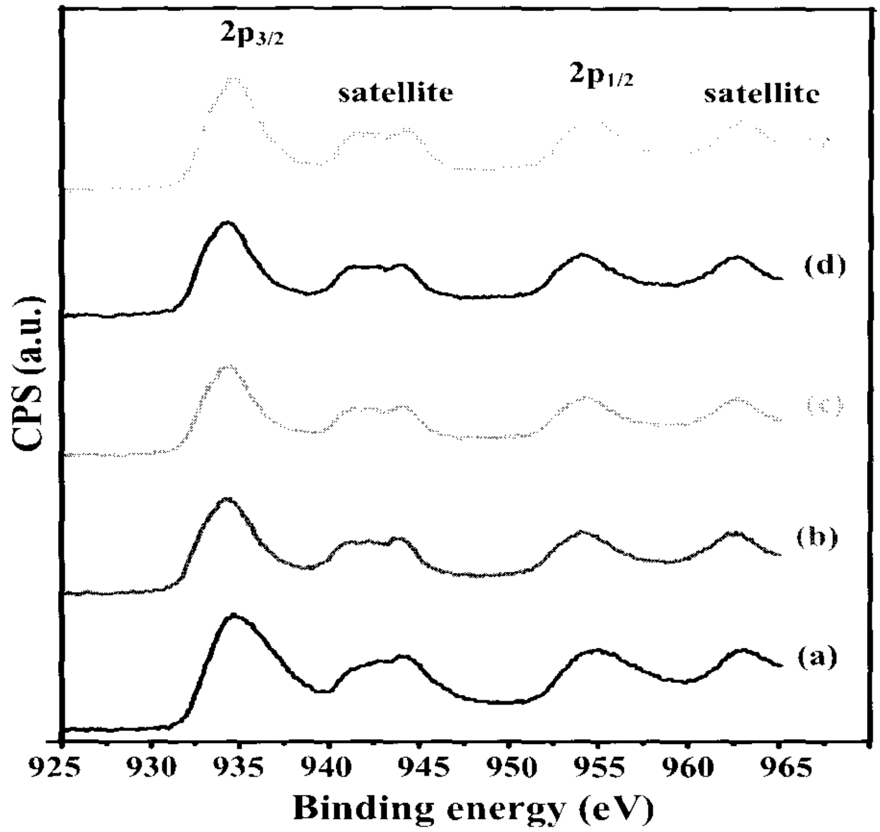

Figure 4.26: XPS Cu2p profile of (a) 5CZC, (b) 10CZC, (c) 15CZC, (d) 20CZC and (e) 25CZC catalysts

Similarly, XPS profile of Zr 3d is depicted in Figure 4.27. Two prominent peaks were observed in binding energy range of 182-185 eV. The occurrence of two XPS peaks with energy gap of 2.4 eV indicated the presence of two different types of zirconium ions. XPS peaks at 182.2 eV was assigned to Zr $3d_{5/2}$ core electrons and another core electrons peak for Zr $3d_{3/2}$ was observed at 184.6 eV. Lower binding energy peaks at 182.2 eV confirmed the existence of Zr^{4+} as ZrO_2, whereas higher binding energy peaks (184.6 eV) symbolized Zr^{2+} species [225, 272].

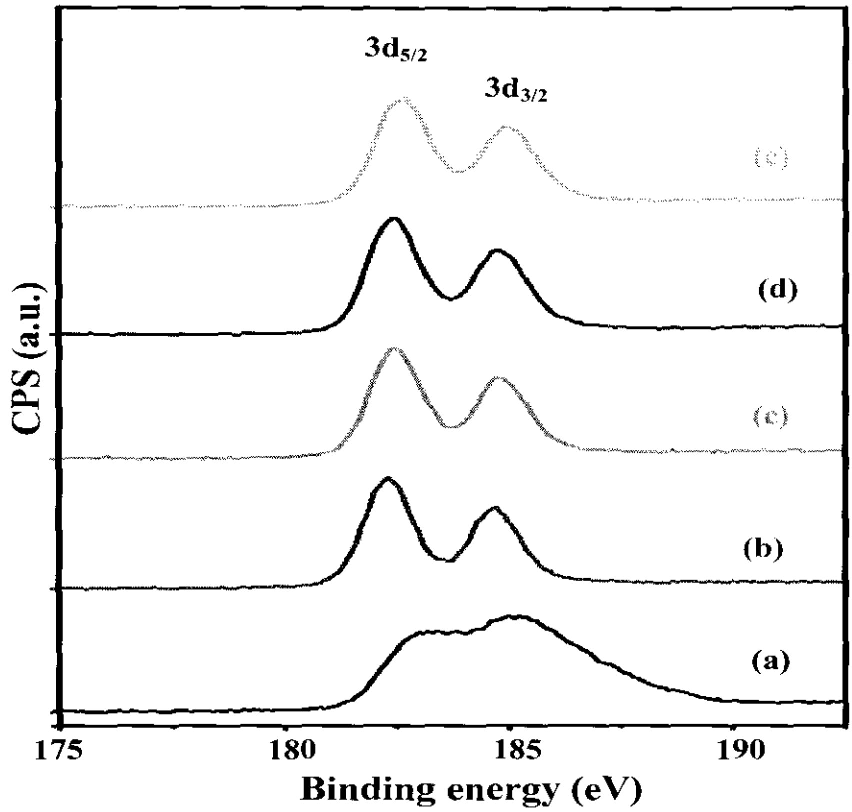

Figure 4.27: XPS Zr 3d spectra of (a) 5CZC, (b) 10CZC, (c) 15CZC, (d) 20CZC and (e) 25CZC catalysts

The binding energies of Cu $2p_{3/2}$ and Zr $3d_{5/2}$ core electrons and their full width at half maximum (FWHM) values, along with Cu/Zr atomic ratio, are summarized in Table 4.16. As evident from the tabulated data, promotion of ZrO_2 content from 5 to 10 wt.% shifted the binding energies of Cu $2p_{3/2}$ from 934.72 to 934.31 eV, respectively. This shift from higher to lower binding energies with increasing ZrO_2 content showed the strengthening of the interaction between Cu and ZrO_2. In addition, it also advocated better copper dispersion. This shifting trend of Cu $2p_{3/2}$ peak position to lower binding energies continued with further ZrO_2 addition. However, both metal-metal interaction and copper dispersion was adversely affected by ZrO_2 incorporation that exceeded 15 wt.%. This was demonstrated by back shifting of Cu $2p_{3/2}$ peak from lower to higher binding energies. These XPS findings were exactly in line with the results of N_2O chemisorption and TPR studies. On the other hand, the magnitudes of binding energies of Zr $3d_{5/2}$ core electron levels are in good agreement with the published literature for Zr^{4+} cations [291]. Meanwhile, position of peak maxima of Zr $3d_{5/2}$ on binding energy scale was also influenced by variation in ZrO_2 content. Increase in ZrO_2 content from

5 to 10 wt.% shifted the peak to lower binding energy, suggesting greater interaction between Cu and ZrO_2. Nevertheless, further promotion of ZrO_2 content shifted back the Zr $3d_{5/2}$ to slightly higher binding energy region. Although binding energies of Zr $3d_{5/2}$ were shifted to higher energies when ZrO_2 content was increased beyond 10 wt.%, the highest values of binding energies of Zr $3d_{5/2}$ (183.81 eV) were recorded for catalysts with the lowest ZrO_2 content, suggesting variation of coordination number of Zr atoms. Such observations were also reported by Damyanova et al. for CoMo/ZrO_2-Al_2O_3 catalyst with varying ZrO_2 content [292]. Besides, the molecule of CuO had a nearly square-planar symmetry, whereby Cu^{2+} ion was surrounded by four oxygen anions. So, charge-transfer excitations may occur in such a system due to electron correlation effects when the symmetry of Cu^{2+} ion is distorted. The broad shake-up satellite peak observed Cu 2p profile of CZC catalyst with different ZrO_2 content could be due to the slight distortion of CuO symmetry. To elaborate this further, variation in FWHM values of parent Cu $2p_{3/2}$ peaks as a function of ZrO_2 addition were examined. Initially, the magnitude of FWHM slightly decreased by increasing ZrO_2 loadings from 5 to 10 wt.%. However, the FWHM values increased with further incorporation of ZrO_2 content and maximum values were recorded for catalysts with 15 and 20 wt.% of ZrO_2 content. Hence, it implied that the addition of ZrO_2 distorted the coordination symmetry of Cu^{2+} ion towards a highly distorted octahedral symmetry. The FWHM values of Zr $3d_{5/2}$ initially decreased with increasing ZrO_2 content from 5 to 10 wt.%. However, they were less affected by further rise of ZrO_2 concentration. The lacking of variations in FWHM values of Zr $3d_{5/2}$ as a consequent of increasing ZrO_2 content, did not allow to get information about the nature of ZrO_2 bonding. Furthermore, relative atomic ratio of Cu/Zr is also presented in Table 4.16. The nominal ratio of the two metals in parent catalysts is given in parentheses. Apparently, atomic ratio decreased with the increase in ZrO_2 content, however in all cases, it was significantly lower than the nominal ratio for the bimetallic catalyst. This clearly demonstrated depletion of surface Cu and subsequent enrichment of surface ZrO_2 content. One of the possible reasons was the agglomeration of Cu at higher ZrO_2 loadings and this had been consistent with earlier (XRD, TEM, and N_2O) investigations. Of course, embedding of Cu in zirconia framework could be the major reason for lower Cu/Zr ratio.

Table 4.16: XPS data of CZC catalysts with different ZrO_2 content

Sample	**Binding energies (eV)**		**FWHM (eV)**		**Atomic Cu/Zr ratio**
	Cu $2p_{3/2}$	**Zr $3d_{5/2}$**	**Cu $2p_{3/2}$**	**Zr $3d_{5/2}$**	
5CZC	934.72	183.81	4.15	5.15	3.1 (4)
10CZC	934.31	182.38	4.05	4.36	1.4 (2)
15CZC	934.26	182.45	4.22	4.39	0.8 (1.3)
20CZC	934.29	182.60	4.22	4.40	0.6 (1)
25CZC	934.60	182.68	4.17	4.41	0.5 (0.8)

In order to identify the different Cu species, Cu $2p_{3/2}$ peak of each catalyst was resolved in different peaks. The deconvoluted profile of Cu $2p_{3/2}$ peak for each catalyst is displayed in Figure 4.28. Cupric ion can easily be recognized owing to its characteristic coupling phenomenon between unpaired electrons. However, the binding energies of Cu and Cu^+ were too close to be differentiated. In the current study, three different XPS peaks were observed. Lower binding energy XPS peak at 932.6 eV was attributed to Cu^+, while higher binding energy peaks at 933.7 and 935.5 eV were assigned to Cu^{2+} [293]. The appearance of more than one CuO species via XPS analysis strongly supported the H_2-TPR findings, where step-wise reduction of CuO was recognized.

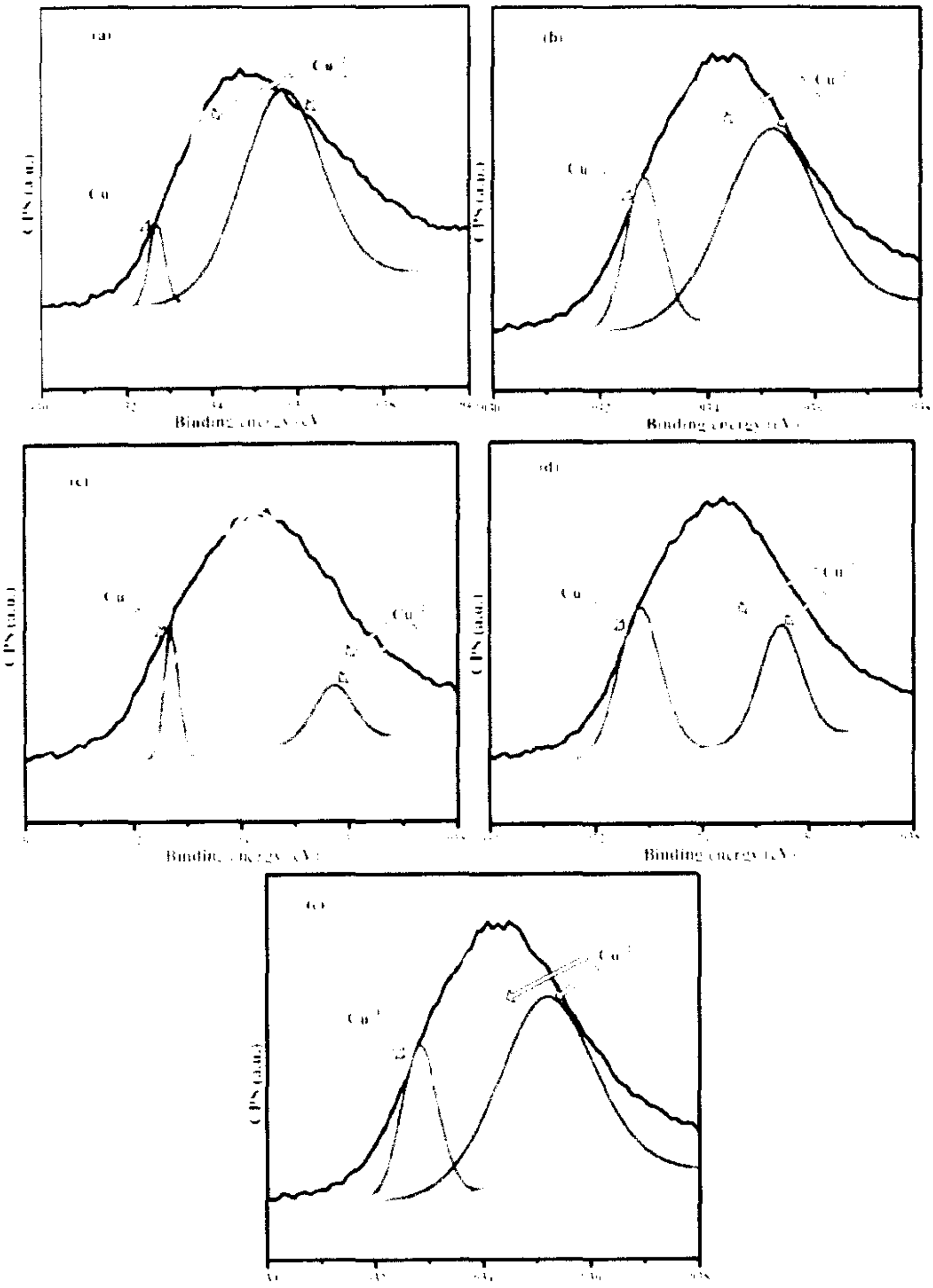

Figure 4.28: XPS Cu $2p_{3/2}$ fitting curves (a) 5CZC, (b) 10CZC, (c) 15CZC, (d) 20CZC and (e) 25CZC catalysts

Cu^{1+}

Cu^{2+} [illegible] / [illegible] = [illegible]

4.3.1.8 Basicity studies

CO_2 TPD was performed to investigate the nature and the strength of basic sites in CZC catalysts with variant ZrO_2 content. TPD-CO_2 profile of catalysts with different zirconia loadings is presented in Figure 4.29. Similarly, the number of basic sites and their respective strength are given in Table 4.17. Basic sites were found to be distributed over a wide range of temperature (100 °C to 700 °C). The basic sites below 450 °C were classified as weak and medium had been symbolized as α region, whereas basic sites above 450 °C were categorized as strong basic sites and were denoted as β region.

what is the basis of 450°C

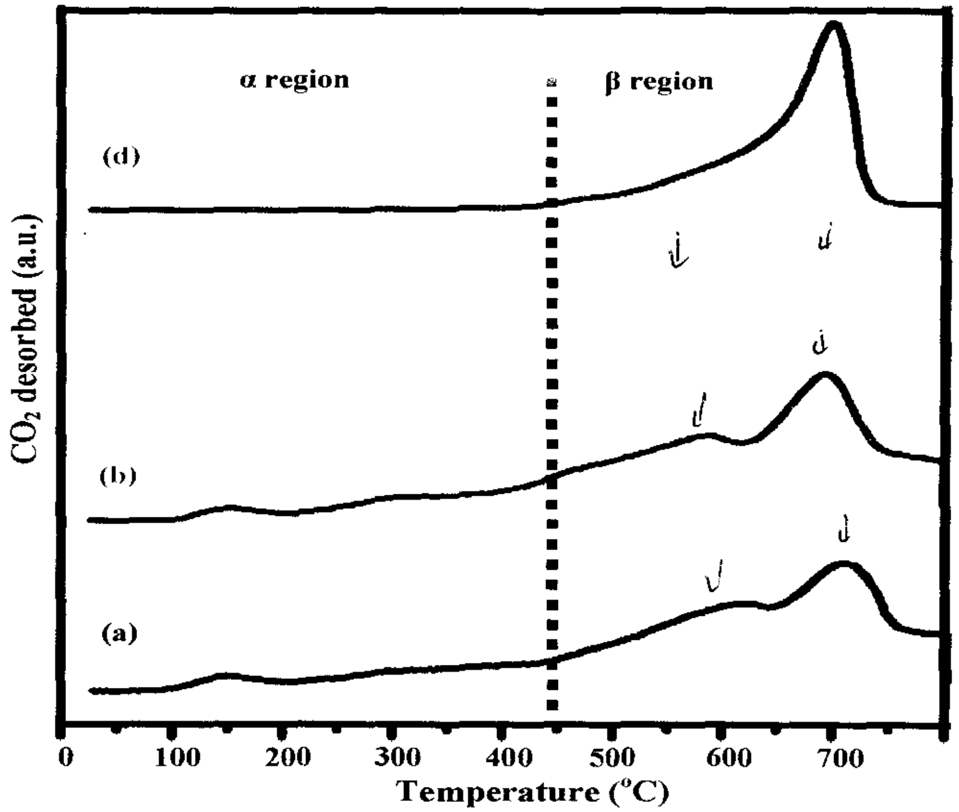

all basic sites?

Figure 4.29: CO_2 TPD profile of (a) 10CZC, (b) 15CZC, (c) 20CZC and (d) 25CZC catalysts

Nevertheless, no adequate amount of basic sites was found for CZC catalyst with 5 wt.% of zirconia. Therefore, 5CZC catalyst was excluded from the basicity profile. Irrespective of the ZrO_2 content, the majority of the basic sites of each catalyst were distributed in strong basic site region. As it is evident from the Figure above, a small and long desorption band centered at 150 °C was observed in CO_2 TPD profile of 10CZC catalyst, indicating the presence of weak basic sites. However, a majority of basic sites had been found in β region. The promotion of ZrO_2 content developed additional desorption peak around 300 °C. This suggested that ZrO_2 addition improved the weak and the medium basic sites. A broad desorption peak was observed starting from 320 °C in α region with a tail in β region when ZrO_2 content was increased to 20 wt.%. Nevertheless, the basic sites were observed exclusively in β region with no basic site in α region where ZrO_2 was increased to 25 wt.% in parent CZC catalyst.

Similarly, the relative distribution of basic sites was also quantified and portrayed in Table 4.17. The number of total basic sites gradually increased with the increase of ZrO_2 content. Obviously, ZrO_2 was an adsorption site for CO_2, and increase in ZrO_2 increased CO_2 adsorption capacity. Meanwhile, the density of total basic sites remained almost invariant throughout the range of ZrO_2 content. The number of basic sites in both α and β regions were incremented by increasing ZrO_2 content in the CZC catalysts. However, basic sites were exclusively found in 25CZC catalyst. This factor could be contributed to the lower activity of the aforementioned catalyst.

Table 4.17: CO_2 TPD data of CZC catalysts with different Zr content

Catalyst	**No. of total basic sites (mmol/g.cat)**	**Density of total basic sites (mmol/m^2)**	**No. of weak basic sites (mmol/g.cat)**	**No. of strong basic sites (mmol/m^2)**
10CZC	9.40	0.08	1.8	7.6
15CZC	13.21	0.08	2.2	11
20CZC	14.60	0.09	2.47	12.12
25CZC	15.85	0.10	0	15.85

4.3.2 Effect of ZrO_2 content on the activity of catalysts

The catalytic performances of the bimetallic catalysts for CO_2 hydrogenation to methanol have been summarized in Table 4.18. The activity profile of the current catalysts was comparatively better to those recently reported for Ag/ZrO_2 and Ag/ZnO catalysts by Grabowski et al. [84]. Likewise, the magnitudes of catalyst activity had been very much comparable to the results of Liang et al. [87] reported for CO_2 hydrogenation to methanol over carbon nanotubes supported Pd/ZnO catalysts. On the other hand, the rate of methanol synthesis was not so affected by variation of ZrO_2 content in the parent catalyst. Methanol synthesis rate remained almost constant when ZrO_2 content was doubled. Nevertheless, a slight increase in methanol production rate was observed for catalysts with 15 wt.% of ZrO_2 loadings. However, the rate of methanol synthesis declined on further addition of ZrO_2 content. Selectivity data shows that methanol selectivity was less effected with incrementing ZrO_2 content from 5-10 wt. %. Maximum value was recorded for CZC catalyst with 15 wt.% ZrO_2 content and was decreased with further increasing ZrO_2 content. Meanwhile, increment in ZrO_2 content had a strong promoting effect on CO_2 conversion. Besides, CO_2 conversion had significantly increased by increasing ZrO_2 content and an optimum conversion was obtained for catalysts with 20 wt.% of ZrO_2. Recently, similar correlation between ZrO_2 content and CO_2 conversion was also reported by Gao et al., for CO_2 reduction to methanol over Cu/Zn/Al/Zr catalysts [187].. Moreover, the TOF of methanol production decreased when the ZrO_2 concentration was doubled from 5 to 10 wt.%. However, further addition of ZrO_2 to the parent catalyst enhanced the TOF.

Table 4.18: Catalytic activity of CZC catalyst with different ZrO_2 loadings

Catalyst	**Meth. activity (g/kg.cat.h)**	**CO_2 conversion (%)**	**Meth. selectivity (%)**	**$TOF_{MeOH} \times 10^{-4}$ (s^{-1})**
5CZC	18	3	55	7.9
10CZC	19	7	49	6.8
15CZC	25	10	67	9.3
20CZC	21	11	53	12.6
25CZC	22	09	48	18.2

In addition, the BET surface area plays an important role in defining the catalyst activity for a particular reaction. In the recent study, the relationship between BET surface area and methanol productivity, as a consequent of varying ZrO_2 content, was examined and is shown in Figure 4.30. Addition of ZrO_2 content had the tendency to amplify the BET surface area of the catalyst, which subsequently improved the methanol productivity rate. The trend continued with further ZrO_2 addition and optimum values of both BET surface area and methanol productivity rate were obtained for 15CZC catalyst. However, further increase of ZrO_2 content reduced the BET surface area, and consequently, methanol productivity rate was depressed. This dependence of catalysts activity advocated the BET surface area as a prominent contributing factor for CZC catalyst in methanol formation.

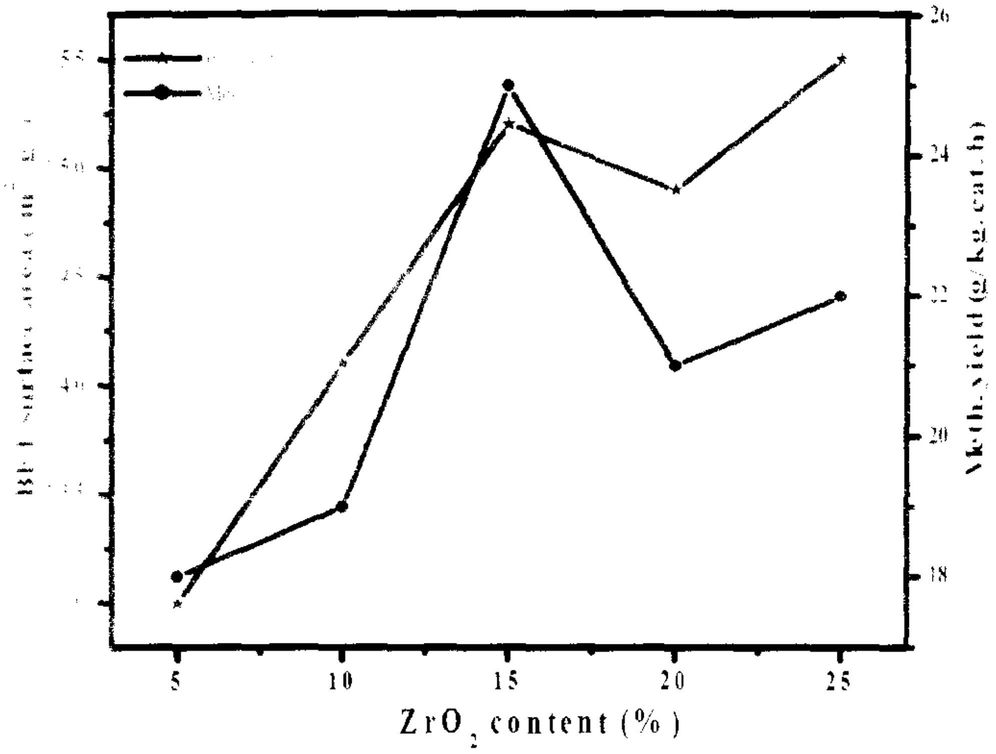

Figure 4.30: Correlation of ZrO_2 content, BET surface area and methanol productivity

The correlation of dispersed Cu with the performance of CZC catalysts has been depicted in Figure 4.31. As expected, a linear relationship was observed between the percentage of reduced Cu and the rate of methanol production. This had been quite straight forward as the increase in Cu dispersion exposed more active Cu to the reacting molecules, and thus, the methanol synthesis rate was improved. Likewise, a linear relationship was observed between the degree of reduced Cu and CO_2 conversion. As a well-established fact, highly dispersed Cu is considered as a more active form of Cu.

So, by increasing the degree of Cu dispersion, more H_2 molecules were dissociated to atomic hydrogen and had been supplied to the ZrO_2 sites for hydrogenation of the adsorbed carbon-containing species, and subsequently, CO_2 conversion was improved.

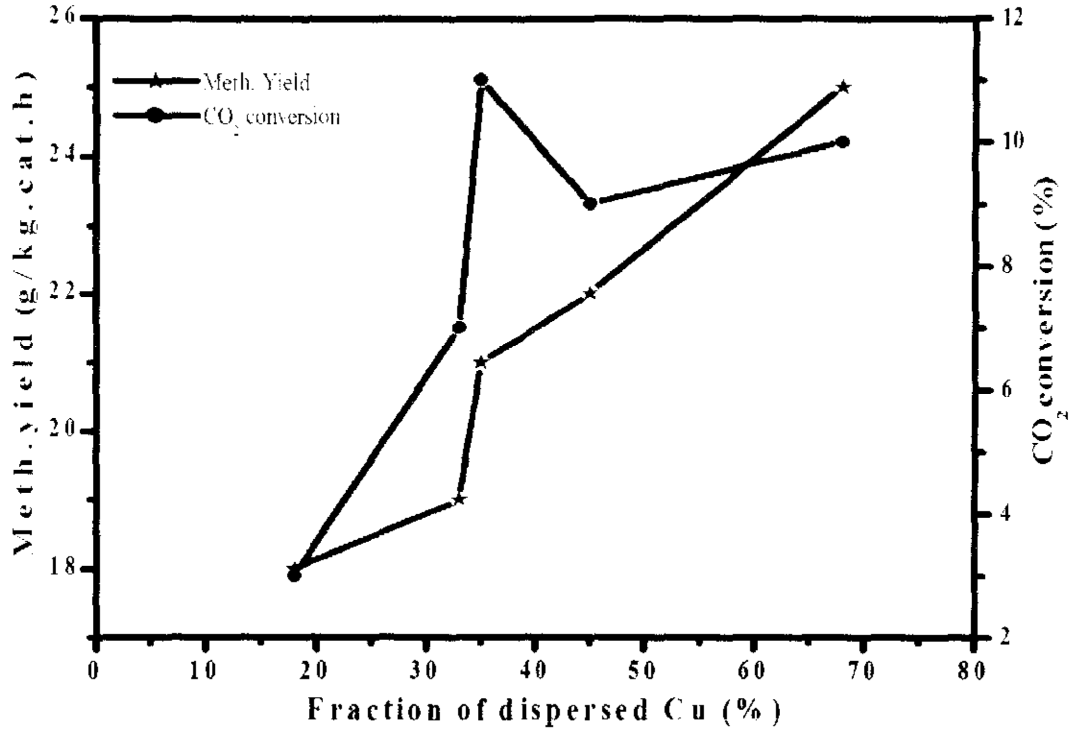

Figure 4.31: Performance of CZC catalysts versus Cu dispersion

4.4 Effect of calcination temperature

Effects of calcination temperature on the physicochemical properties and activity pattern of parent catalyst were investigated. The results are briefly discussed as follows.

4.4.1 Influence of calcination temperature on physicochemical properties of CZC catalysts.

Various analytical techniques were used to investigate the influence of calcination temperature on the physicochemical properties of CZC catalysts. The brief description is presented as follows.

4.4.1.1 Bulk phase analysis

Phase analysis of catalyst components were investigated by XRD technique. XRD profile of catalysts calcined at different temperatures is shown in Figure 4.32. For comparison an XRD spectrum of bare oxidized CNFs was also included. Two prominent peaks were detected at 2θ values of 26° and 44° indicating the hexagonal graphitic planes of CNFs (JCPDS No. 41-1487). Similarly, diffraction pattern with peaks at 32.6°, 35.5°, 38.7°, 48.8°, 53.6°, 58.3°, 61.67°, 66.4°, 68.1°, 72.3° and 75.1° on 2θ scale was found which is indexed as monoclinic phased tenorite CuO with JCPDS card files No. 48-1548 (a = 4.62 Å, b = 3.43 Å, and c = 5.06 Å). Phase distribution was affected by the degree of calcination temperature. Catalysts calcined at lower temperature were less crystalline as disclosed by low intensity peaks of CZC350 and CZC450 catalysts.

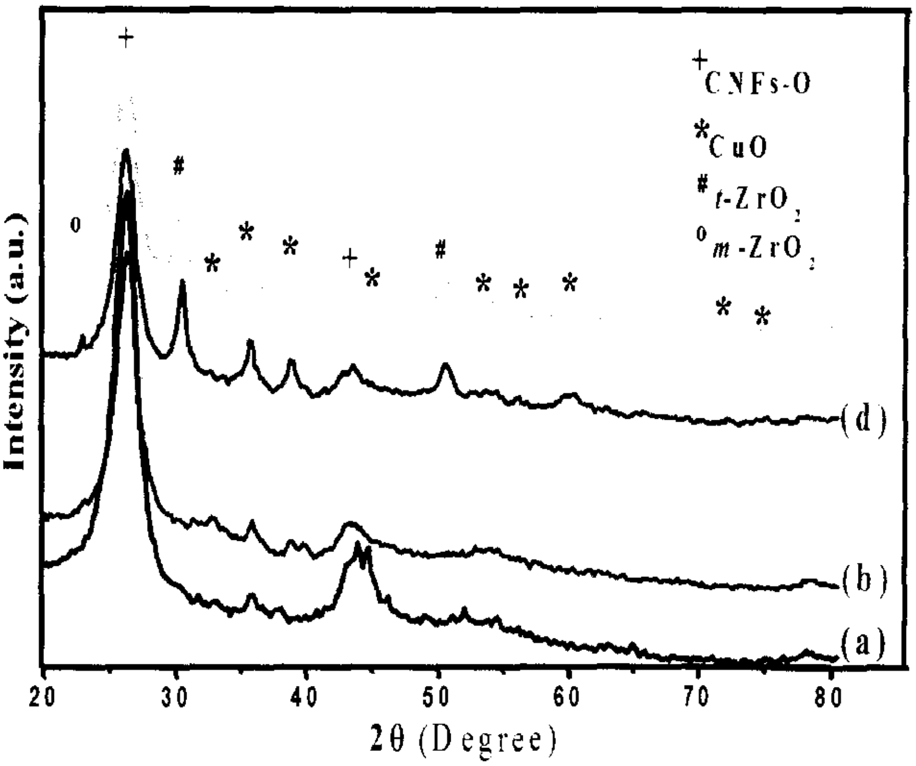

Figure 4.32: XRD profile of (a) CNFs-O, (b) CZC350, (c) CZC450, (d) CZC500 and (e) CZC550 catalysts

The lower crystallinity indicates a well dispersed and highly amorphous phase of CuO component at lower calcination temperature. Furthermore, no peak was observed for ZrO_2, suggesting that ZrO_2 is either in amorphous phase or exists in very fine crystalline form which could not be detected by XRD. However, further rise in calcination temperature not only increased CuO crystallinity but it also developed two additional reflections in CZC500 and CZC550 catalysts around 24° on 2θ scale, indicating the presence of monoclinic zirconia [255]. Similarly, existence of tetragonal polymorph of zirconia was also identified by sharp reflections at 30.3° and 50.4° on 2θ scale at higher calcinations [284].

4.4.1.2 Diffuse reflectance UV.Visible spectroscopy

Diffuse reflectance visible spectra of CZC catalyst calcined at different temperature is presented in Figure 4.33. An absorption peak was observed around 540 nm. This could be attributed to the tetragonal form of ZrO_2 with energy band gap of 2.3 eV.

Interestingly, absorption band at 540 nm was weakened and subsequently a new small peak around 410 nm was appeared when calcination temperature was raised to 500 °C and ~~beyond~~ above. This small absorption peak around 410 nm with energy band gap of 3.0 eV was assigned to monoclinic polymorphic form of ZrO_2. Similar observations were also recorded by Botta et al. in UV analysis of Fe/ZrO_2 semiconductors [294]. Thus diffuse reflectance visible investigation not only ~~ratifies~~ supports the existence of ZrO_2 in CZC catalysts but it also reveals the phase transformation of ZrO_2 from tetragonal to monoclinic polymorph.

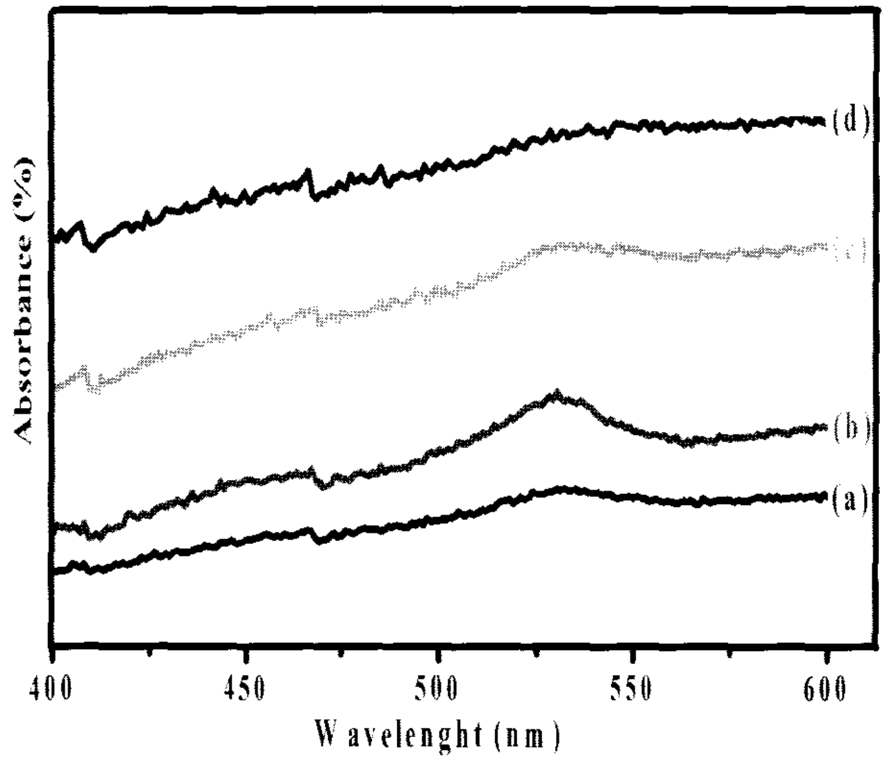

Figure 4.33: DRS-Visible spectra of (a) CZC350, (b) CZC450, (c) CZC500 and (d) CZC550 catalysts

4.4.1.3 Morphology investigations

Transmission electron microscopy was utilized to study the morphology of the catalyst. TEM images of studied catalysts with magnification of 200 K are presented in Figure 4.34. TEM studies revealed well distributed particles for CZC350 and CZC450 with average particle size of 3 nm and 5 nm respectively. However, agglomeration as well as growth of catalysts particles was observed when calcination temperature was increased beyond 450 °C. Consequently, a twofold increased was observed in average particle size for CZC500 and CZC550 catalysts (Table 4.19). This growth of particle with increasing calcination temperature is due to agglomeration of particles and has been consistently reported in literature [295]. By a closer look at Figure 4.34, one can see that intensification of calcination temperature beyond 450 °C has resulted sintering phenomenon, as evident from in set images of CZC500 and CZC550 catalysts.

Table 4.19: TEM catalyst particle size

Catalysts	**Copper average particle size**	**Zirconia average particle size**
CZC350	3	3
CZC450	5	6
CZC500	6	10
CZC550	10	12

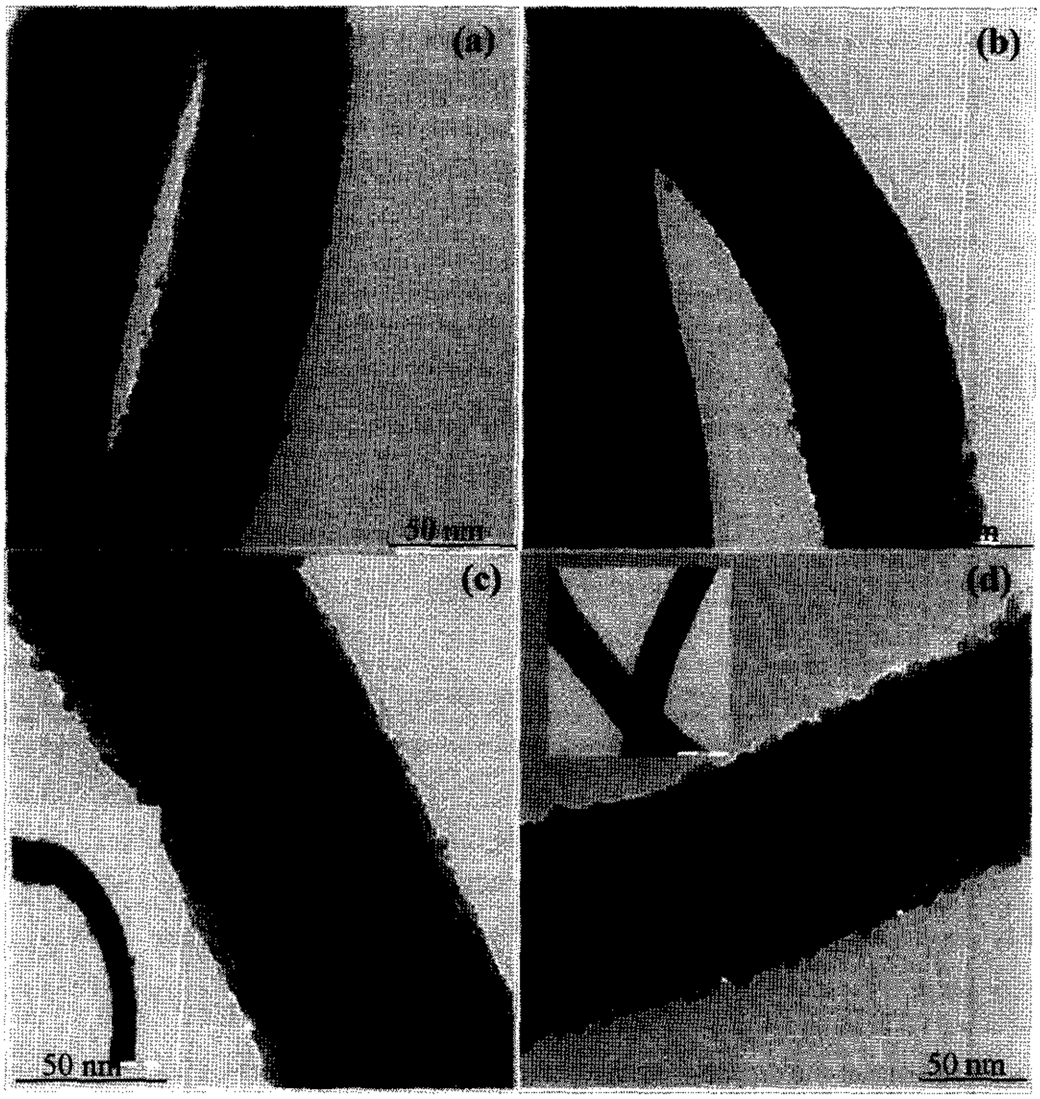

Figure 4.34: TEM images of (a) CZC350, (b) CZC450, (c) CZC500 and (d) CZC550 catalysts

4.4.1.4 Textural properties

Surface area is an important parameter in determining the activity of the catalyst. The N_2 adsorption-desorption isotherms of the catalyst at different calcination temperature are shown in Figure 4.35. All samples exhibited typical type-IV isotherms with H4 type hysteresis loops having sharp inflection between p/p^0 ranges of 0.75–0.94, implying mesoporus nature of catalyst support. In the current study, a sharp increase in BET surface area was observed by increasing degree of calcination temperature from

P/P_o

350 to 450 °C as shown in Table 4.20. Consequently, total pore volume was increased from 0.29 0.39 cm^3/g. This increase in surface area can also be justified by a remarkable increase of total adsorbed gas from 225 to 293 cm^3/g for CZC350 and CZC450 respectively. However, this trend was not lasted for samples calcined at more elevated temperature.

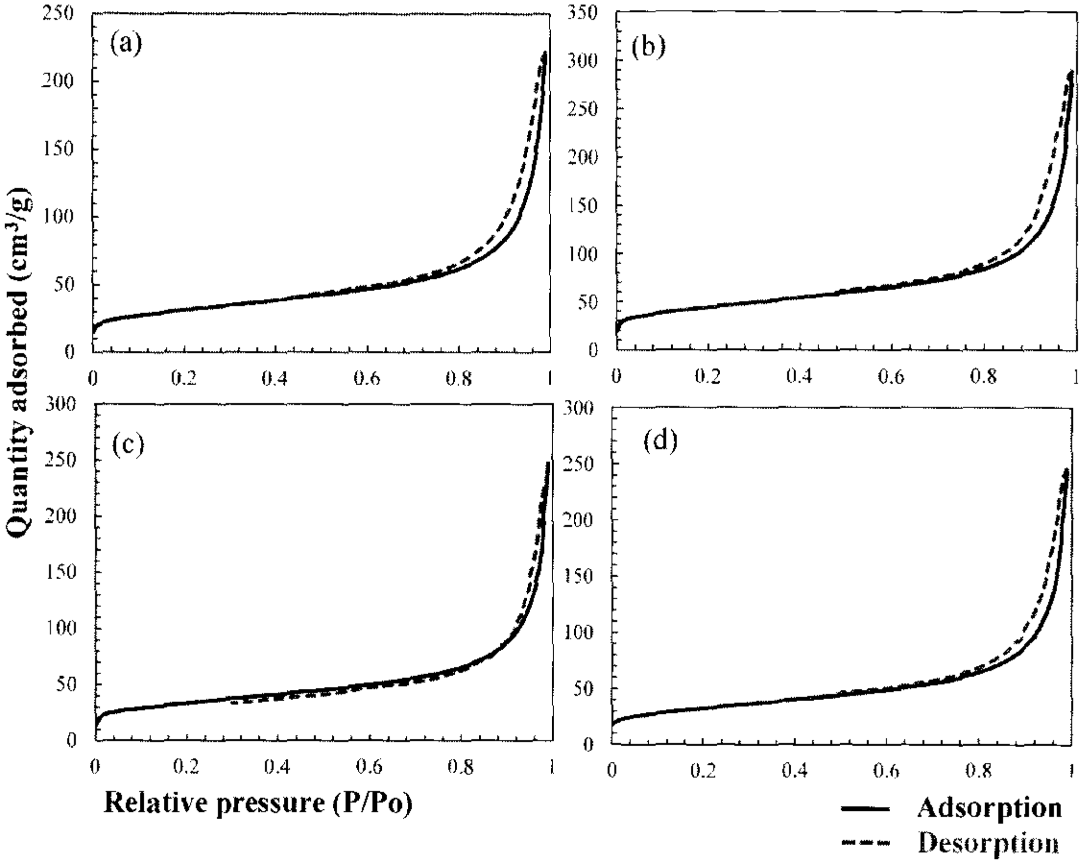

Figure 4.35: N_2 adsorption-desorption of (a) CZC350, (b) CZC450, (c) CZC500 and (d) CZC550 catalysts

Contrary to the earlier trend, BET surface area was observed to be reduced with further rise in degree of calcination temperature. This could be ascribed to sintering phenomenon and growth of catalyst particles at higher calcination temperature [296]. Similarly, decline in surface area could also be attributed to sintering of zirconia associated with the mobility of Zr ions on the surface of the support at elevated temperature [297] . Sintering of catalyst particles at elevated temperature was also evident from TEM images of the respective catalysts.

Table 4.20: Textural properties of CZC catalysts calcined at different temperature

Sample	Ads. gas ($cm^3 g^{-1}$)	BET surface area (m^2/g)	Total pore volume (cm^3/g)	Average pore diameter (nm)
CZC350	225	109	0.29	10.7
CZC450	293	155	0.39	10.1
CZC500	250	118	0.33	11.2
CZC550	250	114	0.32	11.2

4.4.1.5 Surface area and dispersion of copper

Investigations of Cu surface area, variation of Cu size as well as dispersion of active sites are crucial as they have a pivotal role in the performance of catalysts for structure sensitive reactions like CO_2 reduction to methanol. Tabulated values of Cu surface area (S_{Cu}), Cu dispersion (D_{Cu}), Cu particle size (d_{Cu}) and fraction of surface Cu (R_{Cu}) are documented in Table 4.21.

Table 4.21: N_2O chemisorption data

Catalyst	S_{Cu} (m^2/g)	D_{Cu} (%)	d_{Cu} (nm)	R_{Cu}
CZC350	8.6	23	4	0.52
CZC450	8.0	22	5	0.34
CZC500	4.2	14	8	0.23
CZC550	3.6	18	10	0.21

Although magnitudes of S_{Cu}, D_{Cu}, and R_{Cu} were less affected by increasing calcination temperature from 350 to 450 °C, however values of all three parameters were significantly dropped with further rise. Generally, homogenous distribution of copper on catalyst support resulted in higher surface area of copper. In current study,

S_{Cu} was witnessed to ~~be~~ decrease~~d~~ by raising ~~degree of~~ calcination temperature. This indicates that homogeneity of Cu is adversely affected by increase in calcination temperature. This may also be attributed to growth of Cu particles at elevated temperature. Contrary, size of Cu was twofold increased when calcination temperature was raised from 350 to 550 °C. This is mainly due to agglomeration of Cu at higher degree of temperature as shown by TEM images. This trend is also in agreement with the previous reported data [298-300]. Nevertheless, dispersion of Cu was adversely effected by intensification of calcination temperature. This could be due to sintering of Cu particles at elevated temperature. As shown in Table 4.21, distribution of Cu has been affected by variation in calcination temperature. R_{Cu} was progressively decreased with increasing calcination temperature and lowest R_{Cu} value was recorded for catalysts calcined at maximum calcination temperature. This implies that Cu is partially embedded in the ZrO_2 phase and the process accelerates with further rise in calcination temperature. Moreover, it could be further inferred that intensification of calcination temperature and subsequent Cu embedding provide less exposed Cu surface and more Cu–ZrO_2 interfacial surface area. Furthermore, due to large interfacial surface area this feature also reveals better Cu-ZrO_2 interactions as a function of increasing calcination temperature.

At ~~In~~ the end of this discussion, an interesting correlation was developed by these three parameters in a sense that larger d_{Cu} exhibited lower S_{Cu} which resulted in reduction of D_{Cu}.

4.4.1.6 *Reducibility of catalysts*

In order to get insight into metal support interaction, TPR profiles of all studied catalysts is presented in Figure 4.36. TPR bands are deconvoluted into three reduction peaks, denoted as peak (α), peak (β) and peak (γ). Reduction peak (α) around 260 °C is ascribed to highly dispersed copper [301]. Peak (β) is assigned to reduction of bulk – like CuO while peak (γ) shows gasification of carbon nanofibers at ~~in~~ high~~er~~ temperature range [170, 302, 303]. In fact by close inspection, the reduction peaks of both dispersed and clustered copper were observed at relatively higher temperature as compared to those observed for traditional catalyst supports like alumina and zirconia. This is because of the electronegativity gradient (χ_{Cu}- χ_S) between copper and corresponding catalyst support Table 4.22.

Table 4.22: Electronegativity Gradient of Common catalyst supports with copper

Element	**Electronegativity (χ)**	χ_{Cu}- χ_S
Al	1.61	0.29
Zr	1.33	1.57
C	2.55	-0.65
Cu	1.90	

In case of alumina and zirconia, copper accepts electrons from the support whereas in case of CNFs electrons are donated by copper, thus making the reduction of CuO difficult in this case [304]. In turn, this also suggests strong interaction of copper and carbon nanofibers as compared to other traditional catalyst support. Shifting of reduction peak to higher temperature can also be attributed to interaction of copper and zirconia at the surface of CNFs. Because of high work function of ZrO_2 than Cu, interaction between the two creates electron deficiency in Cu. Hence reduction of copper is observed at higher temperature [65]. Likewise, total hydrogen uptake, extent or degree of reduction (H_2/Cu), position of TPR peak, number of dispersed and bulk phase Cu and their relative abundance are documented in Table 4.23. Total hydrogen uptake was observed in order of CZC350> CZC450> CZC500> CZC550, which indicates that H_2 uptake is suppressed by increase in degree of calcination temperature. Moreover, ~~R~~reduction peak of copper was shifted to higher temperature with increasing the ~~degree of~~ calcination temperature. This is because of the catalyst particle size variation associated with the calcination temperature. Copper with small size is easily reduced at the surface of the support as compared to the large one [305].

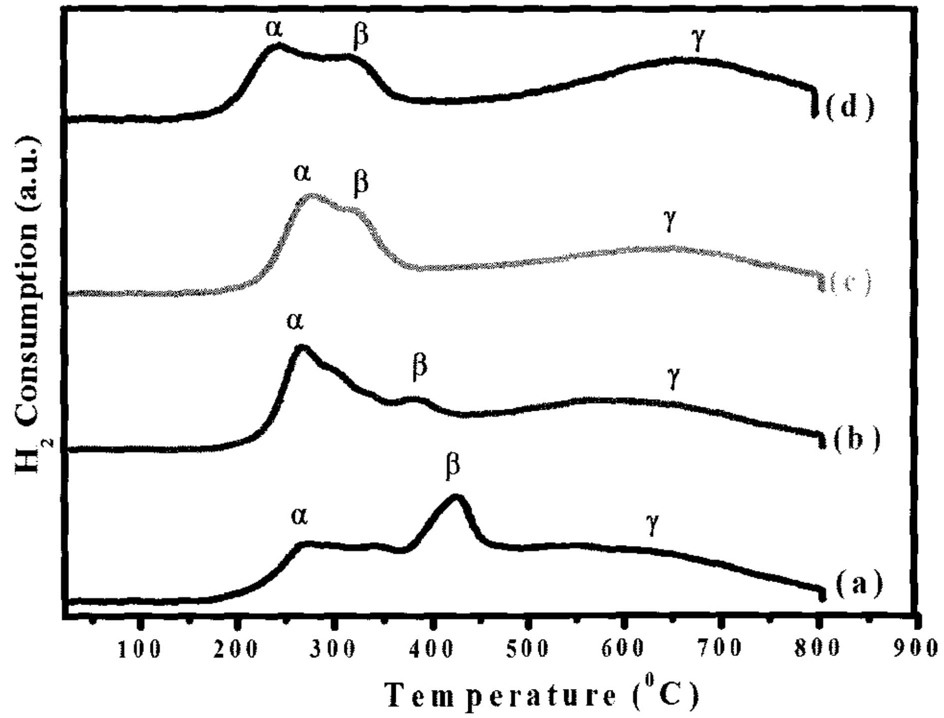

Figure 4.36: TPR Profile of (a) CZC350, (b) CZC450, (c) CZC500 and (d) CZC550 catalysts

Moreover, position of peak (β) was shifted to higher temperature range with increasing the degree of calcination temperature. Similar trend was also observed for peak (α), although the position trend is not distinct as observed for peak (α) Table 4.23. The trend can be attributed to growth of particles with degree of calcination temperature. This also suggests greater interaction between Cu and catalyst support. Moreover, fraction of reduction peak (α) was observed to be intensified when calcination temperature was raised from 350- 450 ^{0}C, but subsequently reduced with further increase in calcination temperature. Almost similar tendency was recorded for reduction peak (β).

Table 4.23: TPR results of calcined samples

Sample	Total H_2 consumed (μmoles/g)	H_2/Cu	Red. temperature (°C)		H_2 consumed (μmoles/g)		$A_{(\alpha)}/(A_{(\alpha)} + A_{(\beta)})^*$ (%)
			Peak α	Peak β	Peak α	Peak β	
CZC350	2225	0.94	269	423	1312	912	59
CZC450	2172	0.92	266	383	1542	692	71
CZC500	1772	0.75	276	362	1007	765	57
CZC550	1212	0.51	245	327	643	568	53

*Fraction of dispersed copper

~~Since~~ highly dispersed copper is the main active part in Cu-based catalysis, hence, relative abundance of highly dispersed and bulk phase copper was studied and reported in Table 4.23. Calcination temperature affected the distribution of different copper phases on the surface of catalysts. Relative abundance of dispersed copper was incremented by increasing the calcination temperature from 350 to 450 °C. However, further rise in calcination temperature shifted the equation in favor of bulk phase copper. This could also be due to agglomeration and growth of Cu at elevated temperature.

4.4.1.7 Metal-metal interaction and surface analysis

The chemical states of catalyst components were evaluated by XPS (Figure 4.37). XPS spectra of calcined catalysts exhibited peaks for Cu $2p_{3/2}$ at 934 eV and 942 eV as parent and satellite peak, respectively [224]. Similarly, XPS peaks appeared at 954 eV and 962 eV for Cu $2p_{1/2}$ core electrons and satellite excitations. The emergence of the satellite structure is due to the charge transfer transitions from the ligands (O^{2-} ions in case of CuO) into the unfilled (d^9) valence orbital of Cu^{2+} ion. This transition of ligands electrons is not possible in case of Cu^+ or Cu^0 species due to the completely filled (d^{10}) shells. Hence, the satellite structure is a characteristic peak of Cu^{2+} ion. In the current study, the appearance of satellite peaks with concomitant parent peak confirms Cu^{2+} as a predominant Cu oxidation state in all studied catalysts: irrespective of the magnitude of calcination temperature. Furthermore, occurrence of Cu $2p_{3/2}$ at 934 eV with consistent satellite peak also suggests a contribution of tenorite CuO which support the XRD findings.

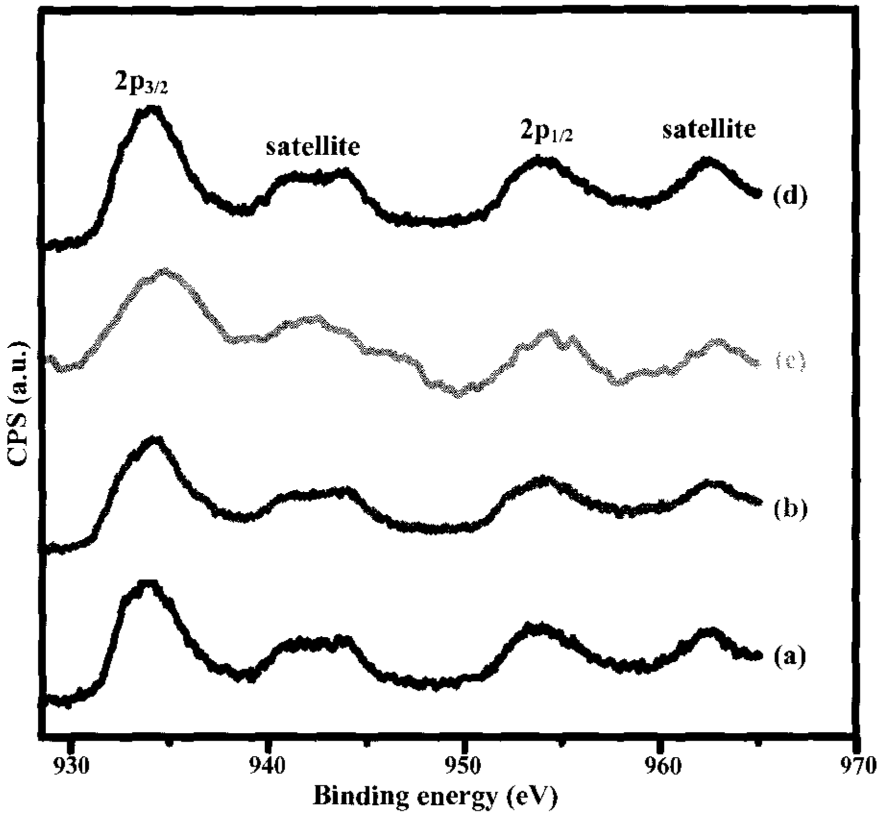

Figure 4.37: XPS Cu2p profile of (a) CZC350, (b) CZC450, (c) CZC500 and (d) CZC550 catalysts

Similarly, a spin–orbit doublet was observed for Zr $3d_{5/2}$ and $3d_{3/2}$ core levels centered at 182.2 eV and 184.6 eV, respectively (Figure 4.38). The appearance of two different binding energy peaks with energy gap of 2.4 eV suggests two different kinds of zirconium ions. The higher binding energy peaks (184.6 eV) represent Zr^{2+} species while lower binding energy peaks (182.2 eV) indicate the existence of pure zirconia in Zr^{4+} form.

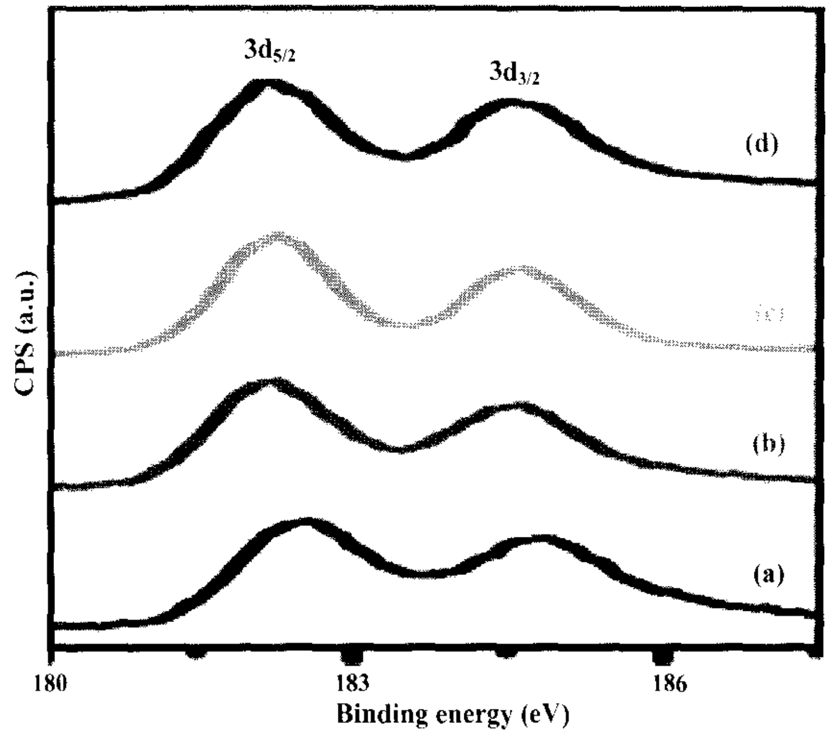

Figure 4.38: XPS Zr 3d spectra of (a) CZC350, (b) CZC450, (c) CZC500 and (d) CZC550 catalysts

The binding energies of Cu $2p_{3/2}$ and Zr $3d_{5/2}$, their FWHM values and Cu/Zr ratio has been documented in Table 4.24.

Table 4.24: XPS data of CZC catalysts calcined at different temperature

Sample	**Binding energy (eV)**		**FWHM (eV)**		**Atomic ratio**
	Cu $2p_{3/2}$	**Zr $3d_{5/2}$**	**Cu $2p_{3/2}$**	**Zr $3d_{5/2}$**	**Cu/Zr**
CZC350	934.14	182.43	4.37	4.69	0.79
CZC450	934.24	182.22	4.55	4.74	1.20
CZC500	934.45	182.28	4.15	4.61	1.05
CZC550	934.12	182.21	4.36	4.73	0.71

The tabulated data shows a slight shift of Cu $2p_{3/2}$ towards higher binding energies with increasing calcination temperature, suggesting a decline in Cu dispersion. According to the XPS results, Cu dispersion is adversely affected by calcination temperature until 500 °C. However, it is increased with further intensification. This is ~~exactly~~ in accordance to the N_2O chemisorption results. In contrast, no significant variation was observed in binding energies of Zr $3d_{5/2}$. The FWHM value of Cu $2p_{3/2}$ was increased for CZC450 as compared to CZC350 catalyst suggesting the distortion in coordination symmetry of Cu^{2+} to highly distorted octahedral symmetry by making additional Cu^{2+}-Cu^{2-} bond with neighbor O^{2-} ions. Unlike Cu $2p_{3/2}$, FWHM values of Zr $3d_{5/2}$ remained also invariant for all catalysts. So in this case no particular information regarding nature and bonding of zirconium ion could be obtained. Furthermore, distribution of surface Cu was also influenced by variation in calcination temperature. Cu/Zr was increased for CZC450 as compared to CZC350 catalyst. Nevertheless, the ratio was adversely affected by further rise in calcination temperature indicating depletion of surface Cu and subsequent enrichment of surface Zr content. Agglomeration of Cu as function of increasing calcination temperature as indicated by TEM results could be one the reasons for Cu/Zr decline.

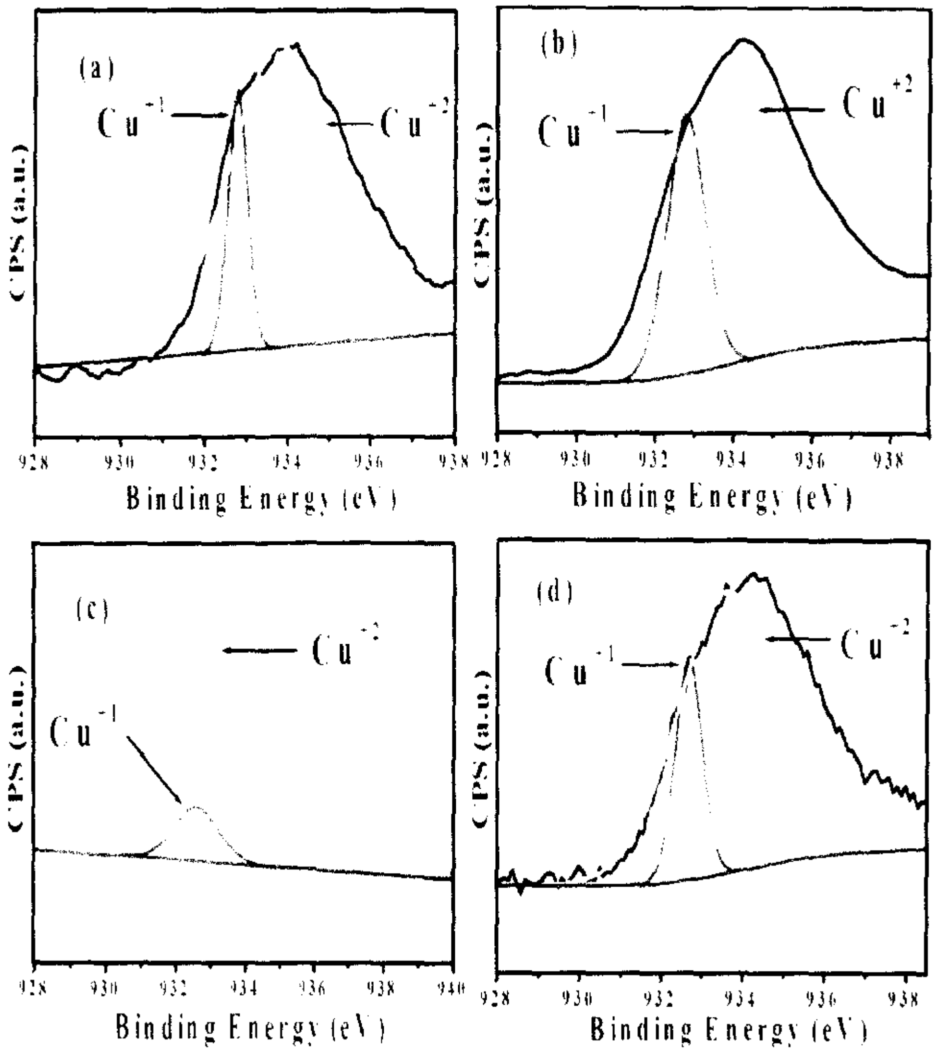

Figure 4.39: Peak fitting curves of $Cu2p_{3/2}$ peak of (a) CZC350, (b) CZC450, (c) CZC500, (d) CZC550 catalysts

In order to identify the different Cu species, the Cu $2p_{3/2}$ peak was resolved in two different peaks, as shown in Figure 4.39. Cupric ion can easily be identified on the basis of coupling phenomenon between unpaired electrons observed in Cu^{2+} while this is lacking in case of metallic and cuprous ion. However, it is quite difficult to differentiate between Cu^{0} and Cu^{1+} because their binding energies and full width at half maximum (FWHM) values are so close that they overlap each other. Cu $2p_{3/2}$ peak observed at 932.7 eV was attributed to Cu^{+} ion while the one observed at 933.7 eV was assigned to Cu^{2+} ion. Furthermore, the existence of two different CuO species is also consistent with the H_2-TPR findings, where CuO with two different kinds of reducibility were also recognized.

4.4.1.8 Basicity and acidic sites of CZC catalysts

The CO_2-TPD profiles of the catalysts are shown in Figure 4.40. The desorption quantities with relative desorption peaks are listed in Table 4.25. The study disclosed significant quantities of basic sites on the surface of all catalysts. Indeed, Lewis basic sites associated with the surface of zirconia are responsible for adsorbing CO_2 [5, 25, 306, 307]. The appearance of desorption peaks are due to the decomposition of carbonate species [307]. Each catalyst exhibited four desorption peaks in the temperature range of 300-690 °C. Desorption peaks below 450 °C were attributed to weak and medium basic sites whereas peaks above 450 °C were ascribed to strong basic sites.

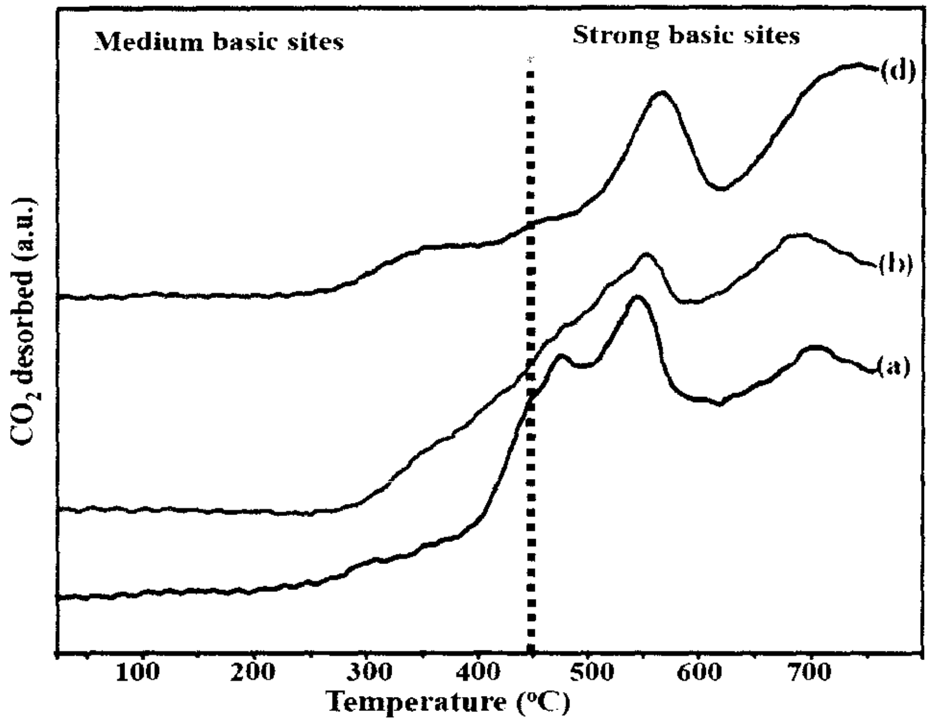

Figure 4.40: CO_2-TPD of (a) CZC350, (b) CZC450, (c) CZC500 and (d) CZC550 catalysts

Comparative study of CO_2-TPD spectra at different calcination temperatures revealed some interesting results. By increasing calcination temperature, the strongly bound CO_2 peaks were shifted to slightly higher temperature, indicating strength of the CO_2 bindings as a function of calcination temperature. On the other hand, no established trend was recorded for TPD peaks ascribed to weakly basic sites. In the literature, monoclinic zirconia is described to display CO_2 desorption peak at higher temperature as compared to tetragonal polymorph. The stronger binding of CO_2 molecules to m-ZrO_2 have been elucidated by different factors like higher concentration of OH groups and carbonate ions on the surface of monoclinic zirconia, relative to tetragonal form [307, 308]. Based on these observations, in our case shifting of strong basic sites peak to higher temperature may also be due to transformation of tetragonal zirconia to monoclinic polymorph. Furthermore, the magnitude of total uptake of CO_2 was inversely affected by rise in calcination temperature (Table 4.25). Total quantity of CO_2 desorbed for catalyst processed at highest calcination temperature of the current study was declined to almost 2/3 of the catalyst calcined at lowest temperature. The drop of CO_2 uptake could be attributed to the growth of zirconia, associated with rise of calcination temperature. This also indicates that smaller size zirconia holds relatively higher concentration of basic sites. Similar observations of reduction in CO_2 adsorption as a function of calcination temperature were also reported by Li et al. [309].

Number and nature of acidic sites were investigated by TPD-NH_3. NH_3-desorption profile of CZC catalysts calcined at different temperature is shown in Appendix C (Figure C3). The values of total number and density of acidic sites are documented in Table 4.25. Desorption signals lower than 200 °C represent weak acidic sites, desorption between 200-400 °C is due to the presence of acidic sites with medium strength while ammonia desorption at more than 400 °C is attributed to strong acidic sites [21]. In the current study, the acidic sites were found over temperature range of 250-700 °C which implies that strength of acidic sites was distributed from medium to strong with no weak acidic site. Although by a closer look at TPD profile of CZC550 a small deflection of desorption can be visualized. However, in some cases NH_3 desorption from weak acidic sites is reported to be the result of hydrogen bonded NH_4^+ rather than desorption of ammonia from the surface of acidic sites of catalyst. Furthermore, acidic sites with moderate strength have been declared as an adequate parameter for evaluation of acidities of the catalysts [310, 311].

Table 4.25: Acidic and basic properties of calcined samples

Catalyst	**Number of total basic sites (mmol/g.cat)**	**Density of total basic sites (mmol/m^2)**	**Number of total acidic sites (mmol/g.cat)**	**Density of total acidic sites (mmol/m^2)**
CZC350	9.40	0.08	0.85	0.007
CZC450	7.13	0.04	0.72	0.004
CZC500	8.71	0.07	0.92	0.007
CZC550	6.02	0.05	0.53	0.004

Quantities of acidic sites recorded in this study are very close to the recently published work of Ning et al. where NH_3-desorption was ascribed to the presence of both Lewis and Bronsted acids sites on surface of zirconia [311]. Increase of calcination temperature affected the acidic profiles of the catalysts. Generally the acidity of catalyst like basicity was reduced by increasing the calcination temperature. Nevertheless, concentration of acidic sites was increased with increasing calcination temperature from 450 °C to 500 °C and ~~was~~ declined on further rise in calcination temperature. The tendency of monoclinic zirconia (*m*-ZrO_2) to have more acidic sites than tetragonal counterpart (*t*-ZrO_2) has consistently been reported in the literature [312, 313]. Based on these observations, the discrepancy could be due to transformation of zirconia from *t*-ZrO_2 form to *m*-ZrO_2 polymorph. The transformation of zirconia was also supported by observing the same trend in basicity profile of CZC catalyst calcined at same temperature. The reduction of acidic sites on further increase of calcination temperature could be attributed to the growth of zirconia, as indicated by TEM measurement. However, owing to the different quantities of total acidic sites and surface area, no clear trend was observed in density of total acidic sites of all studied catalysts.

In conclusion, the overall results indicate that rise in calcination temperature has less affect~~ed~~ the strength of basic sites. Nevertheless, distribution of basic sites has been altered significantly. Moreover, reduction in basicity also indicate lowering of electron-donating potential of electron-rich Zr^{4+}, as higher basicity leads to boost the electron-donating properties of cation [308, 309, 314].

4.4.2 Effect of calcination temperature on catalytic performance of catalysts

CNFs based Cu/ZrO_2 catalysts calcined at different temperature were tested for methanol synthesis as well as conversion of CO_2 and reaction data of all studied catalysts are listed in Table 4.26.

Table 4.26: Activity data of CZC catalysts calcined at different temperature

Catalyst	**Meth. activity (g/kg.cat.h)**	**CO_2 conversion (%)**	**Meth. selectivity (%)**	**$TOF_{MeOH} \times 10^{-3}$ (s^{-1})**
CZC350	27	15	71	1.12
CZC450	34	14	88	1.52
CZC500	24	10	64	2.04
CZC550	17	4	61	1.69

Methanol synthesis rate was improved by raising calcination temperature from 350 to 450 °C. However, it was ~~depressed~~ with further intensification in calcination temperature. Likewise, TOF value of methanol was progressively increased with increasing calcination temperature up to 500 °C and ~~was~~ dropped with maximum ~~degree~~ ~~of~~ calcination temperature ~~in this study~~. Methanol selectivity was significantly increased when calcination temperature was increased from 350 to 450 °C. Nevertheless, methanol selectivity was adversely affected with further intensification of calcination temperature. Similarly, CO_2 hydrogenation was adversely affected by the increasing calcination temperature. The activity pattern of the catalysts calcined at different temperature could be justified by the physiochemical investigations, discussed in the earlier sections.

A comparative study of the activity data of this novel catalyst with the reported literature revealed that the current CZC catalysts showed higher activity for methanol yield and CO_2 conversion as compared to that recorded by Sloczynski et al. over $Ag/ZnO/ZrO_2$ and $Au/ZnO/ZrO_2$ catalysts [278]. Similarly, the results obtained in this study were very much comparable in terms of methanol yield and CO_2 conversion to the work of Liu et al., where they carried out CO_2 hydrogenation over $Cu/Ga_2O_3/ZrO_2$ catalysts [93]. Likewise, magnitude of comparable activity data were reported for carbon nanotube-supported Pd/ZnO catalysts [87].

There has been a general consensus about the involvement of two active sites namely copper (Cu) and zirconia (ZrO_2) for CO_2 hydrogenation to methanol over Cu/ZrO_2 catalysts [5, 25, 315]. More active form of copper is characterized to be the one with higher degree of dispersion and easily reducible form of copper. To demonstrate the relationship between catalyst activity and fraction of dispersed Cu, a plot is presented in Figure 4.41.

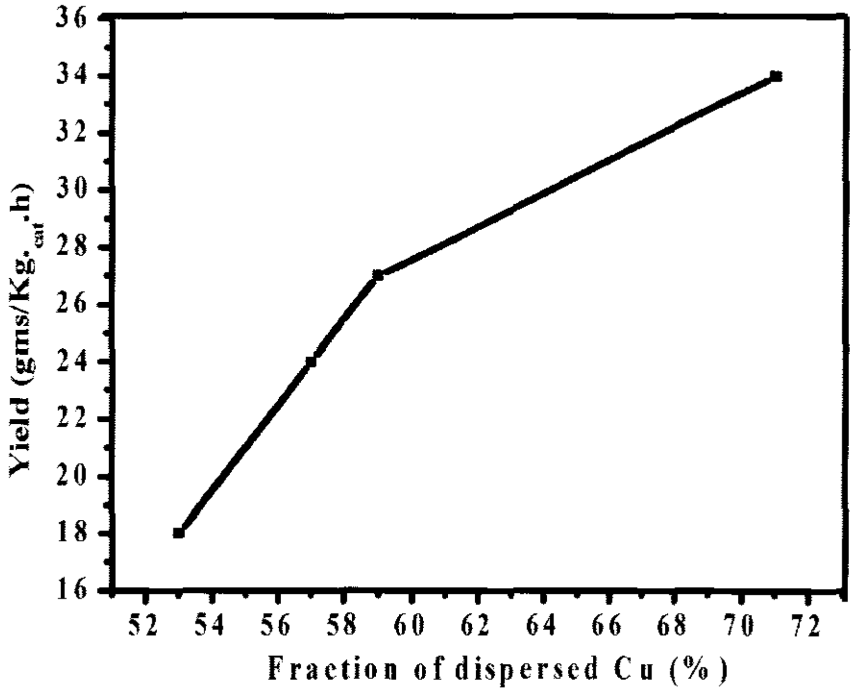

Figure 4.41: Relationship between fraction of dispersed Cu and methanol yield

As depicted in the Figure, rate of methanol formation progressively increased with increasing fraction of dispersed Cu. Obviously, more dispersed Cu will provide more number of active sites to the reacting molecules. Consequently, higher degree of dispersed Cu will lead to higher activity towards methanol formation. The second active site i.e. ZrO_2 has been reported in two different polymorphic forms namely tetragonal and monoclinic form. Rhodes et al. conducted a comparative study between tetragonal and monoclinic polymorphs of ZrO_2 for methanol synthesis and concluded that the latter polymorph of ZrO_2 is 20 times more active than the former one [85]. In this work, activity of catalysts was also affected by phase of zirconia. Rate of methanol formation was enhanced from 27 to 34 (g/kg.cat.h) when calcination temperature was raised from 350 to 450 °C. This could be due to polymorphic transformation of tetragonal ZrO_2 to monoclinic ZrO_2 as suggested by acidity and basicity studies of catalysts. Nevertheless, the trend of catalyst activity with variation in calcination temperature was not persisted any longer and rate of methanol formation decreased ~~was depressed~~ on further increase in calcination temperature. This could be attributed to the growth and sintering of both Cu and ZrO_2 active sites, as indicated by TEM observations.

I mean

Crystallite size of Cu is also an important parameter for CO_2 hydrogenation over Cu based catalysts. To elaborate the influence of Cu crystallite size on the rate of methanol formation and CO_2 conversion, a graph is plotted and is shown in Figure 4.42. As it is evident from the graph that rate of methanol formation gradually reduced with increasing crystallite size of Cu with exception of CZC450 catalyst. On the other hand, CO_2 conversion decreases linearly with growth of Cu crystallite. A similar trend of lower activity with increasing Cu crystallite size was reported by Natesakhawat et al. and Behrens et al. [123, 316]. This is quite understandable as crystals with large size have less surface area and fewer defect sites as compared to small sized crystals.

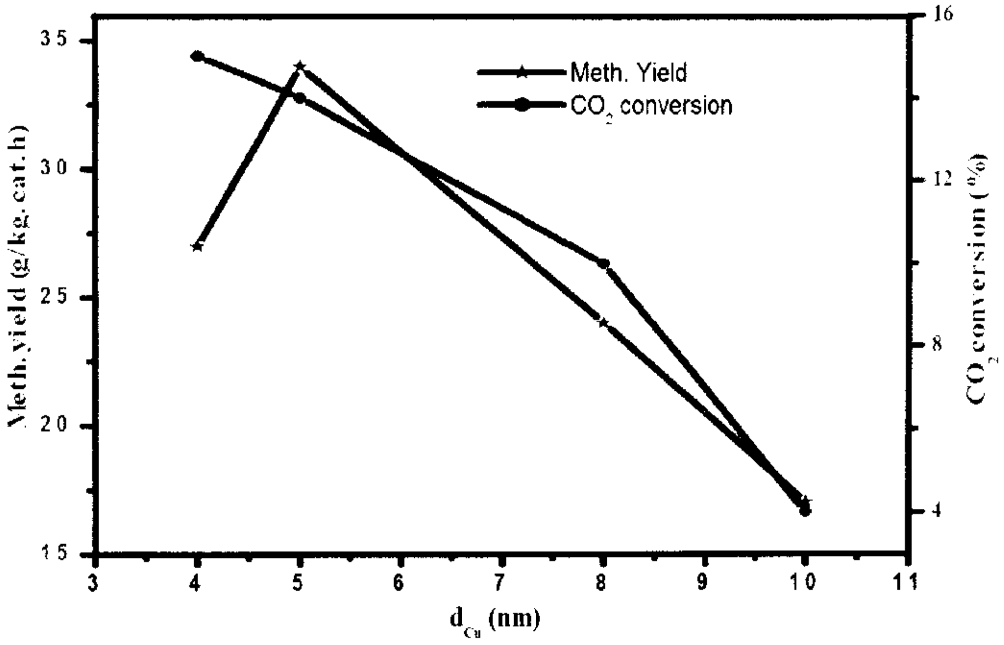

Figure 4.42: Relationship between size of Cu and activity of catalysts

Moreover, smaller Cu particles tend to increase the interfacial area with the neighbor metal oxide [316]. By this mechanism small sized Cu particles promote a synergic effect, leading to increase in the overall performance of the catalyst. The variation of catalysts activities with respect to changes in Cu crystallite size also indicates that CO_2 hydrogenation to methanol is a structure-sensitive reaction.

Based on the reported mechanistic studies, surface area of metallic copper (S_{Cu}) is considered as an important parameter in CO_2 hydrogenation to methanol. Methanol yield has been reported to increase linearly with increasing S_{Cu} [20, 280, 317]. However, in the work of Sun et al., although methanol yield was increased with the increase of S_{Cu} but the relationship was not linear [245]. Nevertheless, the conflicting results of catalysts activity with respect to S_{Cu} has also been reported [89, 282]. Despite all these discrepancies, there is a general consensus that higher value of S_{Cu} is favorable for overall activity of CO_2 hydrogenation. In the recent study, although the trend of methanol formation was not completely aligned with variation of S_{Cu} as highest methanol formation 34 (g/kg.cat.h) was recorded for S_{Cu} = 8.0 as compared to 27 (g/kg.cat.h) for S_{Cu} = 8.6, as depicted by Figure 4.43. On the other hand, a linear relationship was observed between S_{Cu} and CO_2 conversion. The decline in methanol synthesis rate and continuous enhancement in CO_2 conversion for catalyst with highest

S_{Cu} clearly indicates decrease in methanol selectivity. CO formation by reverse water gas shift reaction could be the alternative pathway for CO_2 conversion.

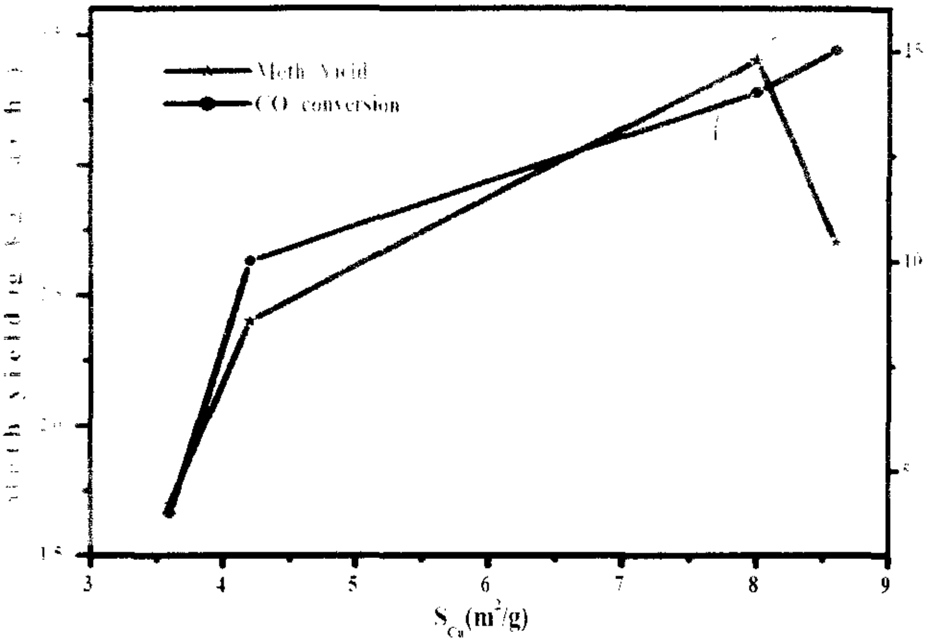

Figure 4.43: Relationship between surface area of Cu and activity of catalysts

To further elaborate the relationship between catalysts activity and S_{Cu}, turnover frequency for methanol production was calculated and is displayed in Table 4.26. According to Boudart's theory, a straight line between TOF and S_{Cu} should be obtained if the catalyst activity is only dependent on S_{Cu} [102, 318]. However, in the current study there is a general trend of decreasing TOF as the S_{Cu} is increased. This further indicates that catalyst activity is not only related to S_{Cu} but other factors like fraction of dispersed Cu in this case, can play a decisive role in determining the activity profile of catalyst. Recently, similar observations were also documented by Ahouari et al. and Sun et al. [89, 245]. Nevertheless, the overall activity of the catalyst, i.e, CO_2 conversion was found to be directly proportional to S_{Cu}. The same trend of CO_2 conversion with respect to S_{Cu} was observed in the recent work of Guo et al. [232]. The increase in CO_2 conversion with increasing S_{Cu} can be described as follows. Increase in S_{Cu} produce more atomic hydrogen on the surface of Cu and will be supplied to ZrO_2 sites by spillover effect. Subsequently with higher concentration of atomic hydrogen, more molecules of CO_2 will be utilized for CO_2 hydrogenation [232].

4.5 Effect of niobium as promoter

Effects of niobium as a promoter on the physicochemical properties and activity pattern of parent catalyst were investigated. The results are briefly discussed as in the following.

4.5.1 Effect of Nb_2O_5 content on physiochemical properties

The influence of Nb_2O_5 content on physicochemical profiles of parent catalysts is discussed below.

4.5.1.1 X-ray diffraction studies

Phase analysis of catalyst components were investigated via XRD technique. XRD profile of Nb promoted CZC catalysts is shown in Figure. 4.44. For comparison purpose, an XRD spectrum of CNFs-O and unloaded CZC catalyst were also included. Hexagonal graphitic planes of CNFs were identified by two prominent peaks at 2θ values of 26° and 44° (JCPDS No. 41-1487). Similarly, diffraction pattern with peaks at 32.6°, 35.5°, 38.7°, 48.8°, 53.6°, 58.3°, 61.67°, 66.4°, 68.1°, 72.3°, and 75.1° on 2θ scale was found to be indexed as monoclinic-phased tenorite CuO with JCPDS card files No. 48-1548 (a = 4.62 Å, b = 3.43 Å, and c = 5.06 Å). A small diffraction peak around 31° was found in XRD profile, indicating zirconia component of the catalyst. However, it disappeared with the incorporation of Nb_2O_5 content. This indicated transformation of zirconia to the amorphous phase with the promotion of Nb_2O_5 loading. Similarly, highly dispersed or very fine crystalline ZrO_2 (crystallite size < 2 nm) could also be the possible reasons. However, peak corresponding to Nb_2O_5 or any Cu-Nb composite was not observed in the XRD spectrum, indicating that Nb_2O_5 existed in amorphous or microcrystalline state, which could not be detected via XRD technique due to low degree of crystallization. An interesting observation was found in the XRD studies whereby the intensification of CuO peaks is dependent on addition of Nb_2O_5 up to 0.8wt.% Nb_2O_5 concentration. The increase in CuO peak intensity with increasing

Nb_2O_5 loading reflects the growth in crystal size. However, CuO peak intensity was decreased with further rise in Nb_2O_5 concentration.

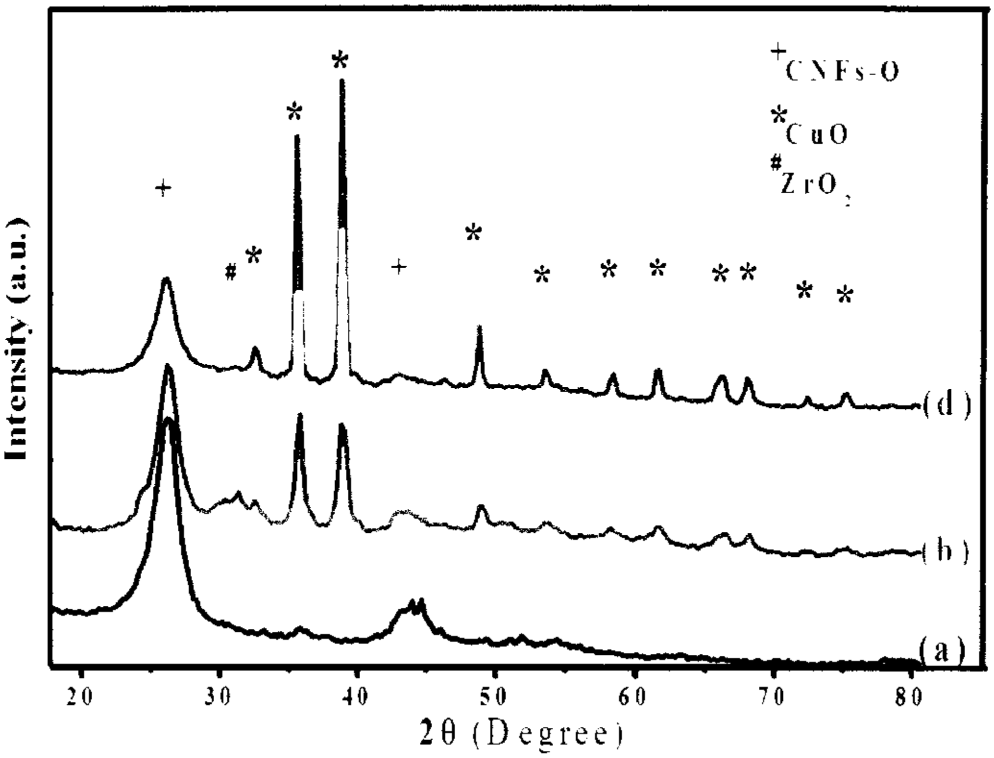

Figure 4.44: XRD profile of (a) CNFs-O, (b) CZC, (c) CZC-Nb0.4, (d) CZC-Nb0.8 and (e) CZC-Nb1.2 catalysts

4.5.1.2 Morphology investigations

TEM images of Nb_2O_5 promoted CZC catalysts are presented in Figure 4.45. Copper and zirconia particles were identified as mentioned in the previous sections. Particles of copper and zirconia are clearly seen in the TEM images. However, Nb_2O_5 particles could not be identified because of their low concentrations. The results demonstrated a homogenous deposition of catalysts particles with low concentrations of Nb_2O_5. Nevertheless, agglomerations of Cu particles were observed when Nb_2O_5 content exceeded 0.8 wt.%.

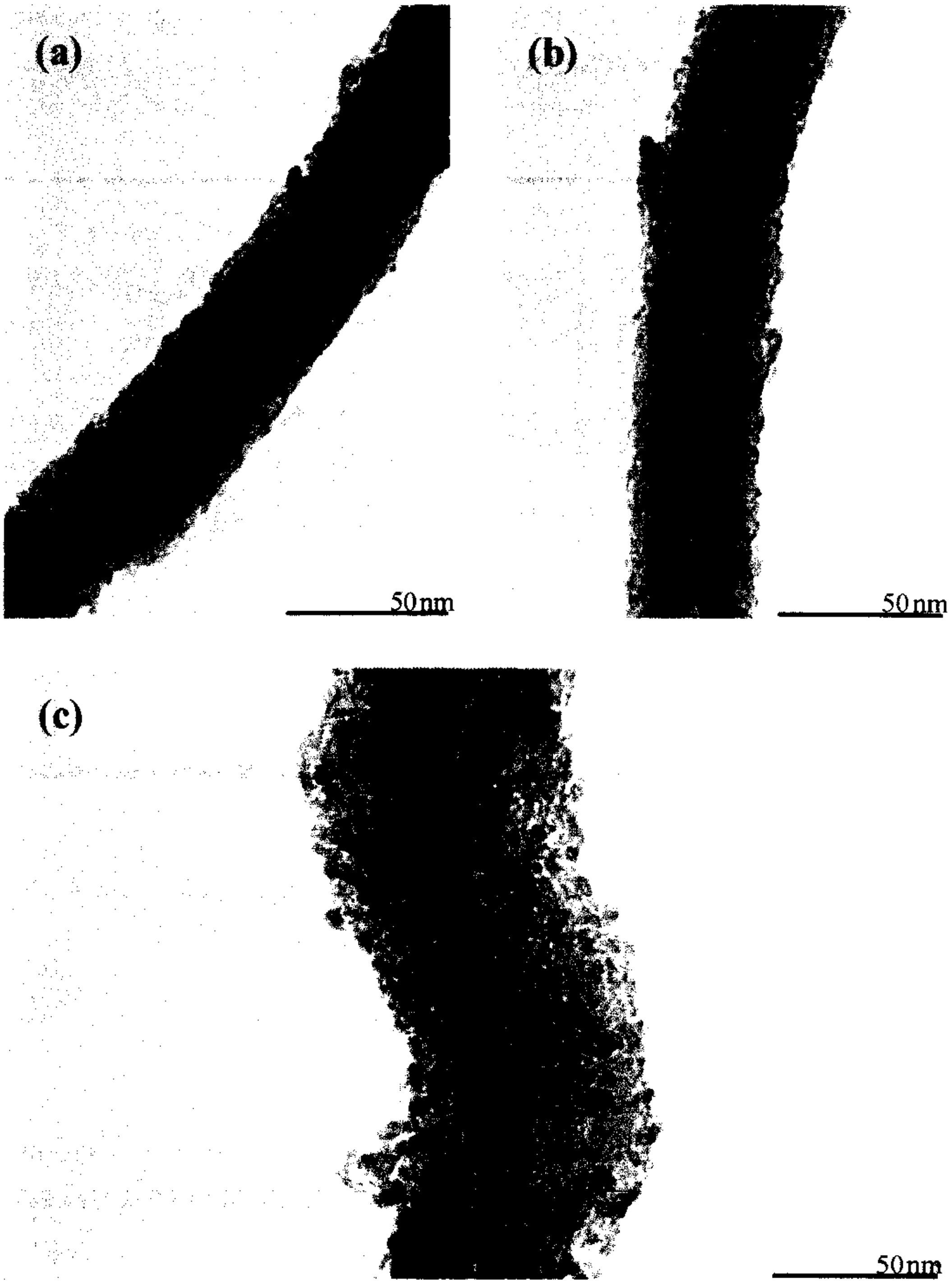

Figure 4.45: TEM images of (a) CZC-Nb0.4, (b) CZC-Nb0.8 and (c) CZC-Nb1.2 catalysts

Table 4.27: Average particle size of catalyst components

Catalysts	**Copper average particle size (nm)**	**Zirconia average particle size (nm)**
CZC-Nb0.4	4	6
CZC-Nb0.8	5	8
CZC-Nb1.2	7	9

Besides, the average particle size of both metal oxides was slightly increased with the increase of Nb_2O_5 content (Table 4.27). This could be due to the agglomeration of metal oxides due to higher interaction as a function of increasing Nb_2O_5 content.

4.5.1.3 BET surface area and pore size distribution

Nitrogen adsorption-desorption isotherms of CZC and Nb_2O_5 promoted CZC catalysts are shown in Figure 4.46. Each catalyst exhibited a typical type-IV isotherm with H4 type hysteresis loops having sharp inflection between p/p^o ranges of 0.90–0.94, indicating mesoporus nature of the synthesized catalysts. The textural properties of CZC catalysts are provided in Table 4.28. BET surface area decreased remarkably from 155 to 108 m^2/g with the incorporation of 0.4 wt.% of Nb_2O_5 to the CZC catalyst. Although, the surface area reduced with further increase of Nb_2O_5 but the change was not very prominent. The decline of surface area with Nb_2O_5 introduction is supported by a drastic decrease in magnitude of total adsorbed gas from 290 to 220 cm^3/g for CZC and CZC-Nb0.8 catalysts, respectively. Similarly, pore volume decreased from 0.39 to 0.29 cm^3/g with the introduction of 0.8 wt.% of Nb_2O_5 to CZC catalysts. Like BET surface area, magnitude of pore volume remained almost constant with further addition of Nb_2O_5. The decline in BET surface area and pore volume could be due to pore-filling by the introduction of Nb_2O_5. In contrast, the pore diameter of the catalyst increased with addition of 0.4 wt.% Nb_2O_5 to the CZC catalyst. However, it remained invariant with further addition of Nb_2O_5.

P/P_o

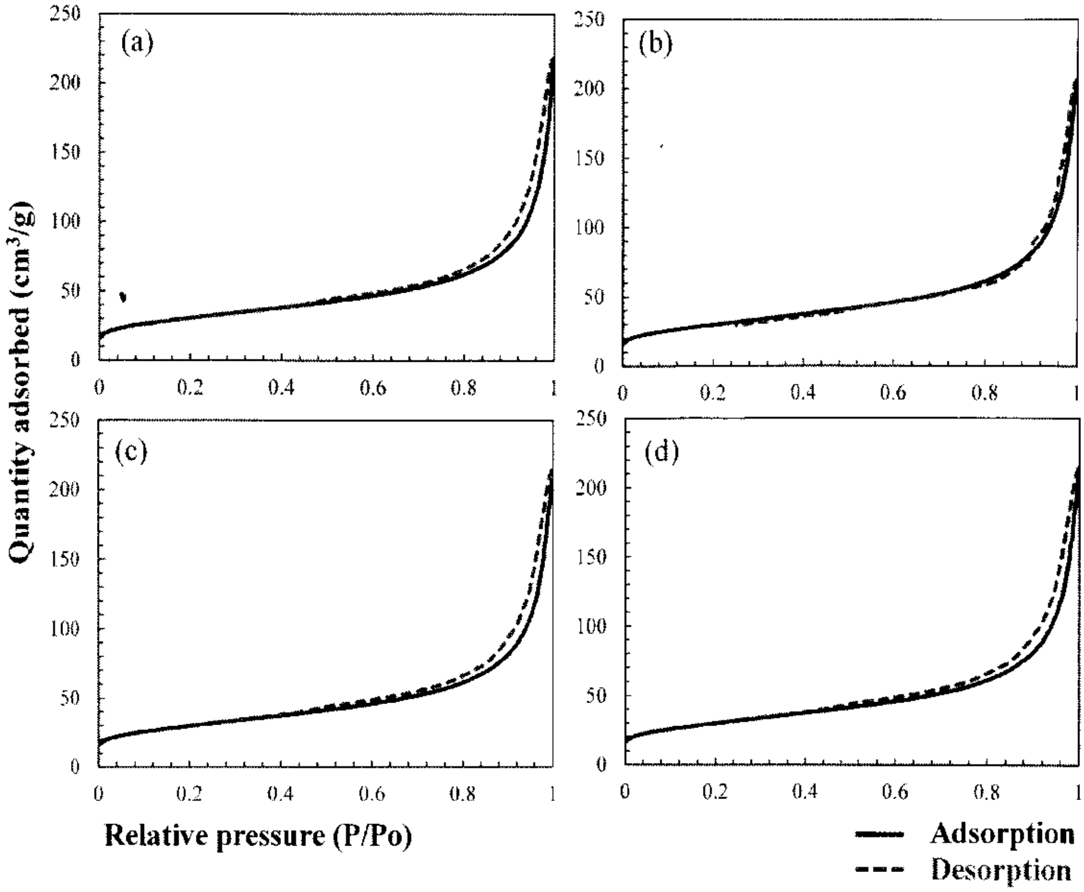

Figure 4.46: N_2 adsorption desorption isotherms of (a) CZC, (b) CZC-Nb0.4, (c) CZC-Nb0.8 and (d) CZC-Nb1.2 catalysts

Table 4.28: Textural properties of CZC and Nb promoted CZC catalysts

Catalyst	**Tot. Ads. gas (cm^3/g)**	**S_{BET} (m^2/g)**	**pore diameter (nm)**	**Pore volume (cm^3/g)**
CZC	290	155	10.1	0.39
CZC-Nb0.4	220	108	11.3	0.30
CZC-Nb0.8	207	104	11.3	0.29
CZC-Nb1.2	213	105	11.2	0.30

|| S: L? c:. Vpore ~

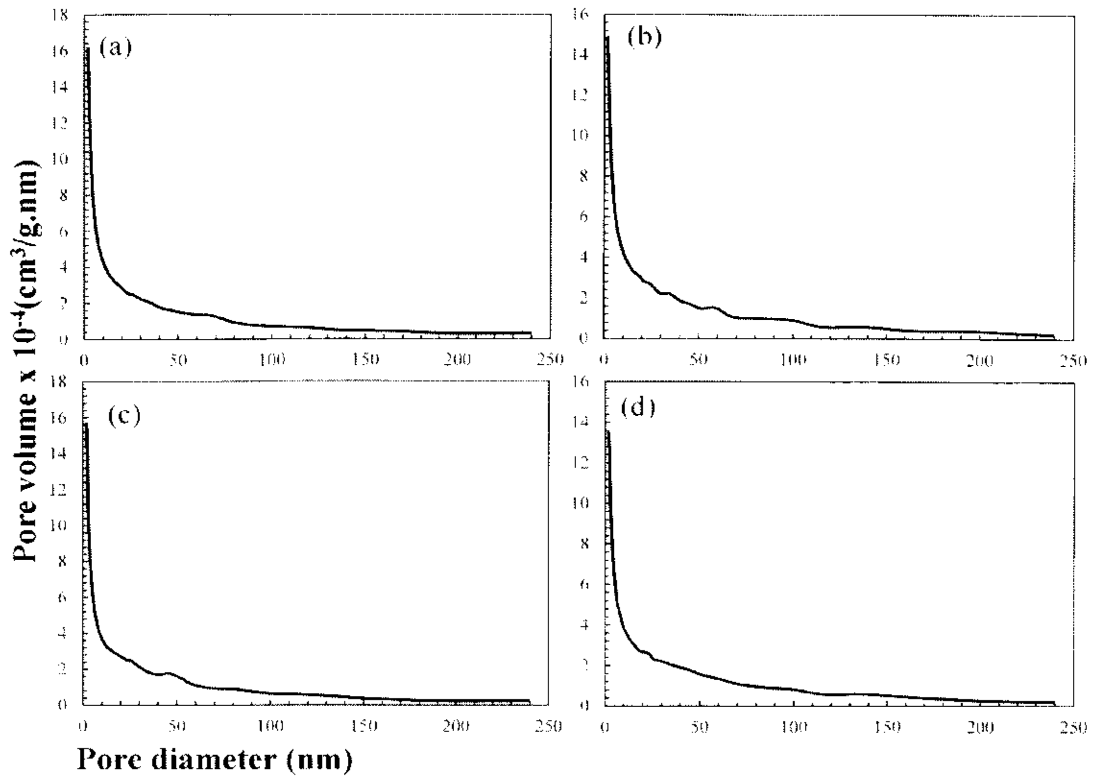

Figure 4.47: Pore size distribution of (a) CZC, (b) CZC-Nb0.4, (c) CZC-Nb0.8 and (d) CZC-Nb1.2 catalysts

Pore size distribution of CZC and Nb promoted CZC catalysts are shown in Figure 4.47. A wide range of pore size distribution staring from 2 to 180 nm was observed. However, majority of the pores were found in the range of 2-15 nm. As evident from the figure, pore size distribution was not affected by introduction of Nb_2O_5 to the parent catalyst.

4.5.1.4 Surface area and dispersion of copper

The surface area of metallic copper (S_{Cu}), Cu dispersion (D_{Cu}), average particle size (d_{Cu}), and relative distribution of metallic copper (R_{Cu}) were measured via N_2O chemisorption, are presented in Table 4.29. As evident from the tabulated data, introduction of Nb_2O_5 content to the parent catalyst had a marked influence on the surface properties of Cu. The surface area of metallic copper increased progressively with the incorporation of Nb_2O_5 content in the parent catalyst and a maximum S_{Cu} of 15.9 m^2/g was obtained for CZC-Nb 0.8 catalyst. However, the S_{Cu} decreased with further rise in concentration of Nb_2O_5 content beyond 0.8 wt.%. Unlike S_{Cu}, dispersion of Cu (D_{Cu}) was adversely affected by incorporation of Nb_2O_5 to the parent CZC catalyst. Besides, the D_{Cu} increased from 15.8 to 17.2 % with the addition of Nb_2O_5 of 0.4 to 0.8 wt.%. However, it remained almost invariant with further addition of Nb_2O_5. On the other hand, the copper particle size was not much affected by variation of Nb_2O_5 content. Distribution of surface copper (R_{Cu}) increased to a maximum with the incorporation of 0.8 wt.% of Nb_2O_5.

Table 4.29: N_2O chemisorption data of Nb promoted CZC catalysts

Sample	S_{Cu} **(m^2/g)**	D_{Cu} **(%)**	d_{Cu} **(nm)**	R_{Cu}
CZC	8.0	22	5	0.34
CZC-Nb0.4	14.4	15.8	6.5	0.88
CZC-Nb0.8	15.9	17.2	6.0	1.00
CZC-Nb1.2	15.4	16.50	6.3	0.97

4.5.1.5 Reducibility studies

To obtain greater insight in the reduction behavior, reducibility of catalysts was studied via TPR technique. TPR profile of CZC and Nb-loaded CZC catalysts are presented in Figure 4.48, while the quantitative evaluation of TPR analysis is documented in Table 4.30. Two distinct TPR peaks were observed in unprompted CZC catalyst with reduction maxima at 260 and 340 °C and denoted as peak α and peak β, respectively. TPR peak α is recognized as reduction peak due to highly dispersed copper while TPR peak β is ascribed to bulk–like CuO [301]. Similarly, according to López-Suárez et al., peak α is assigned to easily reduced form of Cu^{2+} and peak β correspond to less-reducible CuO [270]. However in concomitant to these two traditional peak, a new broad reduction peak (Peak γ) starting at 350 °C with a tail at 490 °C was observed in Nb promoted catalysts. Roma et al. investigated TPR profile of Cu/ Nb_2O_5 catalysts and observed a broad peak for CuO reduction around 450 °C [319]. Based on this observation, Peak γ in the current case could be due to higher interaction of Cu or Cu-

Nb_2O_5 composites. Likewise the occurrence of more than two reduction peaks have also been reported in the literature [320]. Nevertheless, an additional reduction peak was observed at 375 °C for CZC catalysts with maximum Nb_2O_5 concentration. TPR peak at the same magnitude of temperature was also recorded by Courtois et al. and attributed to reduction of bulk CuO [321]. Reduction of Nb_2O_5 is generally reported in the temperature range of 800-900 °C in the literature [322-324]. Therefore in the current study, all the reduction peaks attribute to the CuO reduction. This can be further justified by the fact that magnitude of $Cu/H_2 < 1$ was recorded for each niobium promoted CZC catalysts as evident from Table 4.30.

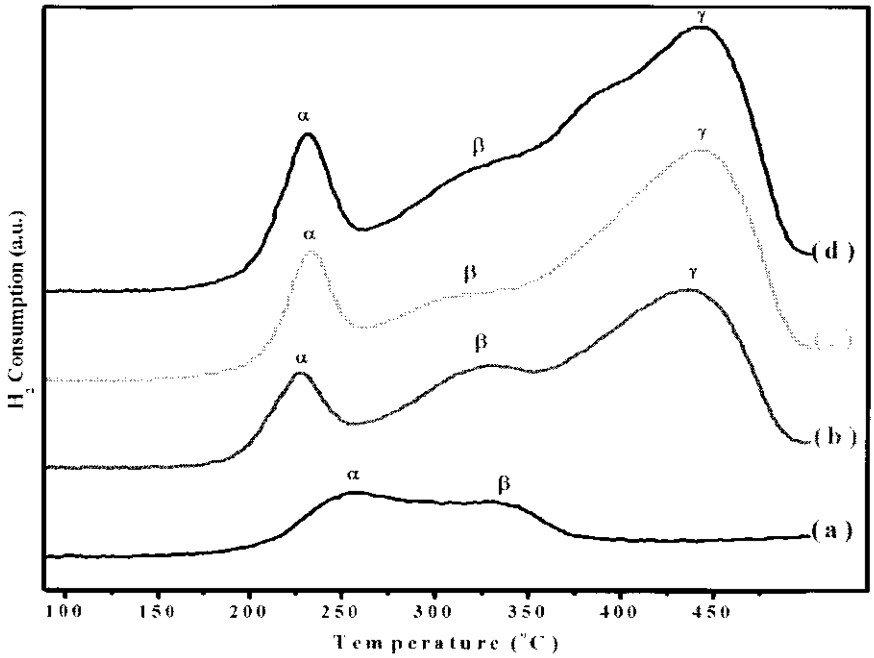

Figure 4.48: TPR profile of (a) CZC, (b) CZC-Nb0.4, (c) CZC-Nb0.8 and (d) CZC-Nb1.2 catalysts

However, Incorporation of Nb_2O_5 resulted some interesting changes in TPR profile of CZC catalysts. Position of TPR peak α was shifted from 260 to 230 °C while a lower temperature shift of almost 10 °C was observed in TPR peak β. The shift of peak α to lower temperature with Nb_2O_5 loading suggested that the incorporation of Nb_2O_5 facilitated the reduction of Cu^{2+}, in agreement with previous works [325-327]. On the other hand, a new peak γ was observed to be centered at 445 °C when CZC catalysts were doped with Nb_2O_5. This transformation of reduction peak was due to formation of a new phase as a result of strong interaction between Cu and dopant Nb_2O_5, as reported in the literature [328-330]. A reduction peak at the same degree of temperature was also reported by Guarido et al. in Cu/ Nb_2O_5 catalyst [331]. Subsequently, incorporation of Nb_2O_5 in CZC catalysts facilitated the reduction of dispersed Cu at one end, but depressed the reducibility of bulk Cu on the other end.

Table 4.30: TPR data of CZC catalysts with different Nb_2O_5 content

Sample	**H_2 consumed (µmoles/g)**	**H_2/Cu**	**Red. temp. (°C) Peak**			**H_2 consumed (µmoles/g) Peak**		
			α	**β**	**γ**	**α**	**β**	**γ**
CZC	2172	0.92	266	340	-	1482	690	-
CZC-Nb0.4	2210	0.94	226	330	437	288	521	1401
CZC-Nb0.8	2239	0.95	235	342	444	291	401	1547
CZC-Nb1.2	2268	0.96	235	355	446	301	517	1450

4.5.1.6 Metal-metal interaction and surface analysis

Figure 4.49 shows the Cu 2p XPS spectra for Nb_2O_5 promoted CZC catalysts. Each catalyst demonstrated Cu $2p_{3/2}$ core electrons peak at 934.4 eV associated with a broad satellite peak around 943 eV. Similarly, core electrons peak for Cu $2p_{1/2}$ was observed at 954 eV accompanied with a shake-up peak around 962 eV. The occurrence of satellite peaks in concomitant to the parental peaks confirmed Cu^{2+} as the predominant oxidation state of Cu in all studied catalysts.

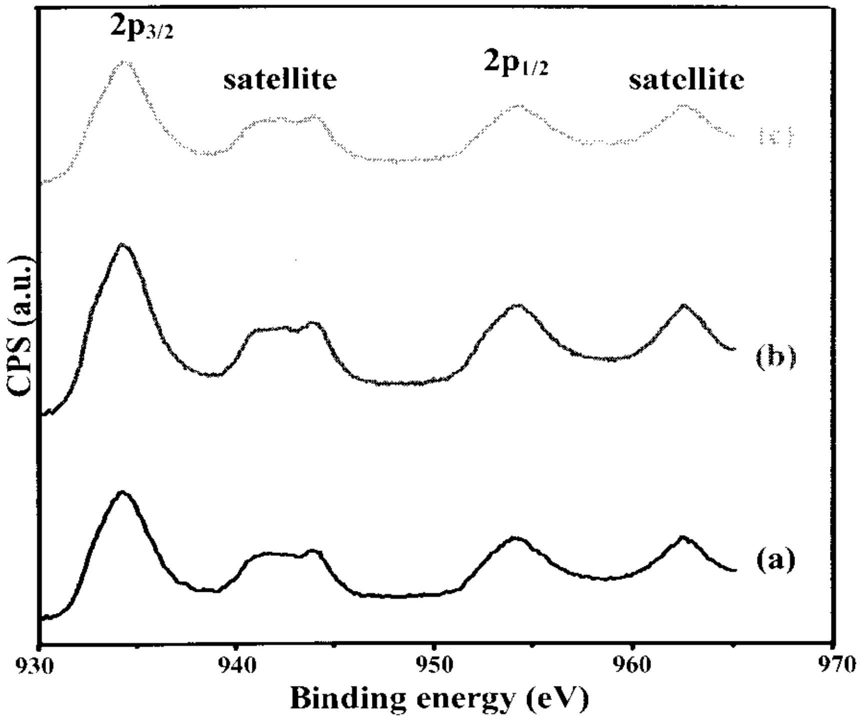

Figure 4.49: XPS of Cu 2p of (a) CZC-Nb0.4, (b) CZC-Nb0.8 and (c) CZC-Nb1.2 catalysts

The binding energies of Cu $2p_{3/2}$ and Zr $3d_{5/2}$ core electrons and their full width at half maximum (FWHM) values, along with Cu/Zr atomic ratio, are documented in Table 4.31. As evident from the tabulated data, binding energies of Cu $2p_{3/2}$ had slightly shifted from 934.10 to 934.24 eV by increasing Nb_2O_5 concentration from 0.4 to 0.8 wt.%, respectively. However, no substantial variation was observed with further rise in Nb_2O_5 content. Similarly, the position of Zr $3d_{5/2}$ on binding energy scale remained almost invariant for different Nb_2O_5 concentrations. Nevertheless, the magnitude of Cu $2p_{3/2}$ FWHM slightly increased from 3.92 to 4.11 eV by increasing Nb_2O_5 concentration from 0.4 to 0.8 wt.%. This indicated the formation of two additional weak Cu^{2+}–Cu^{2-} bonding with neighboring O^{2-} ions, leading to distortion of Cu^{2+} ion coordination symmetry towards a highly distorted octahedral symmetry [97]. On the other hand, FWHM value of Zr $3d_{5/2}$ was not affected by Nb_2O_5 concentration. As a result, no particular information on bonding and nature of Zr^{4+} ions had been obtained. Furthermore, relative atomic ratio of Cu/Zr slightly increased with the increase of Nb_2O_5 content from 0.4 to 0.8 wt.%, suggesting enrichment of surface copper. However, further addition of Nb_2O_5 to the parent catalyst declined the Cu/Zr ratio. This demonstrated the depletion of surface Cu and subsequent enrichment of surface Zr content. Agglomeration of Cu could be one of the reasons for surface Cu depletion.

Table 4.31: XPS data of CZC catalysts with different Nb_2O_5 content

Sample	**Binding energy (eV)**		**FWHM (eV)**		**Atomic Cu/Zr ratio**
	Cu 2p$_{3/2}$	**Zr 3d$_{5/2}$**	**Cu 2p$_{3/2}$**	**Zr 3d$_{5/2}$**	
CZC-Nb0.4	934.10	182.16	3.92	4.57	0.56
CZC-Nb0.8	934.24	182.22	4.11	4.47	0.68
CZC-Nb1.2	934.28	182.18	4.08	4.45	0.52

Likewise, XPS profile of Zr 3d of CZC catalysts with different Nb_2O_5 content is depicted in Figure 4.50. Zirconium ions were identified by two XPS peaks as Zr 3d$_{5/2}$ and Zr 3d$_{3/2}$ with binding energies of 182.2 and 184.6 eV, respectively. The presence of two different XPS peaks with 2.4 eV energy gap indicated the existence of two different types of zirconium ions. Lower binding energy peaks at 182.2 eV ratified the existence of Zr^{4+} as ZrO_2, whereas higher binding energy peaks at 184.6 eV represented Zr^{2+} species [84].

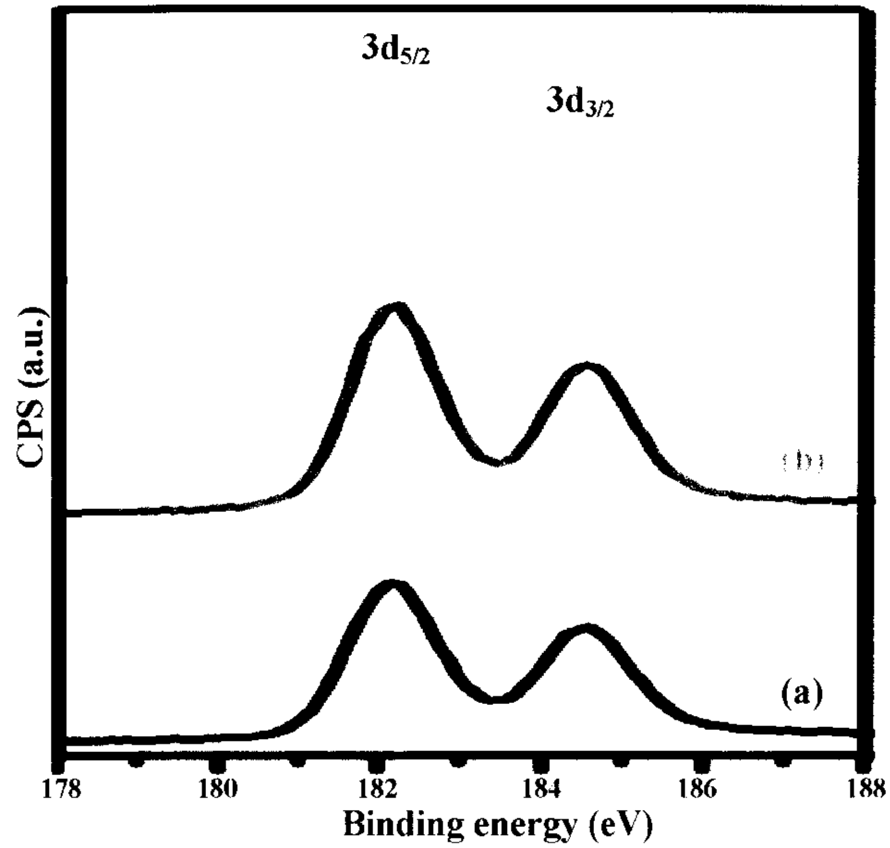

Figure 4.50: XPS Zr 3d spectra of (a) CZC-Nb0.4, (b) CZC-Nb0.8 and (c) CZC-Nb1.2 catalysts

Meanwhile, Cu $2p_{3/2}$ peak of each catalyst was resolved in different peaks to identify the different Cu species and are displayed in Figure 4.51. Cupric ion can easily be recognized due to its characteristic coupling phenomenon between unpaired electrons. However, magnitudes of binding energies of Cu and Cu^{+} were so close that they overlapped each other, hence, these two Cu species could not be differentiated. In the current study, higher energy Cu $2p_{3/2}$ peak observed at 933.7 eV was attributed to Cu^{2+} ion, while a low energy peak centered at 932.7 eV was assigned to Cu^{+} ion. The appearance of two different CuO species in XPS analysis strongly supported the H_2-TPR findings, where step-wise reduction of CuO was recognized.

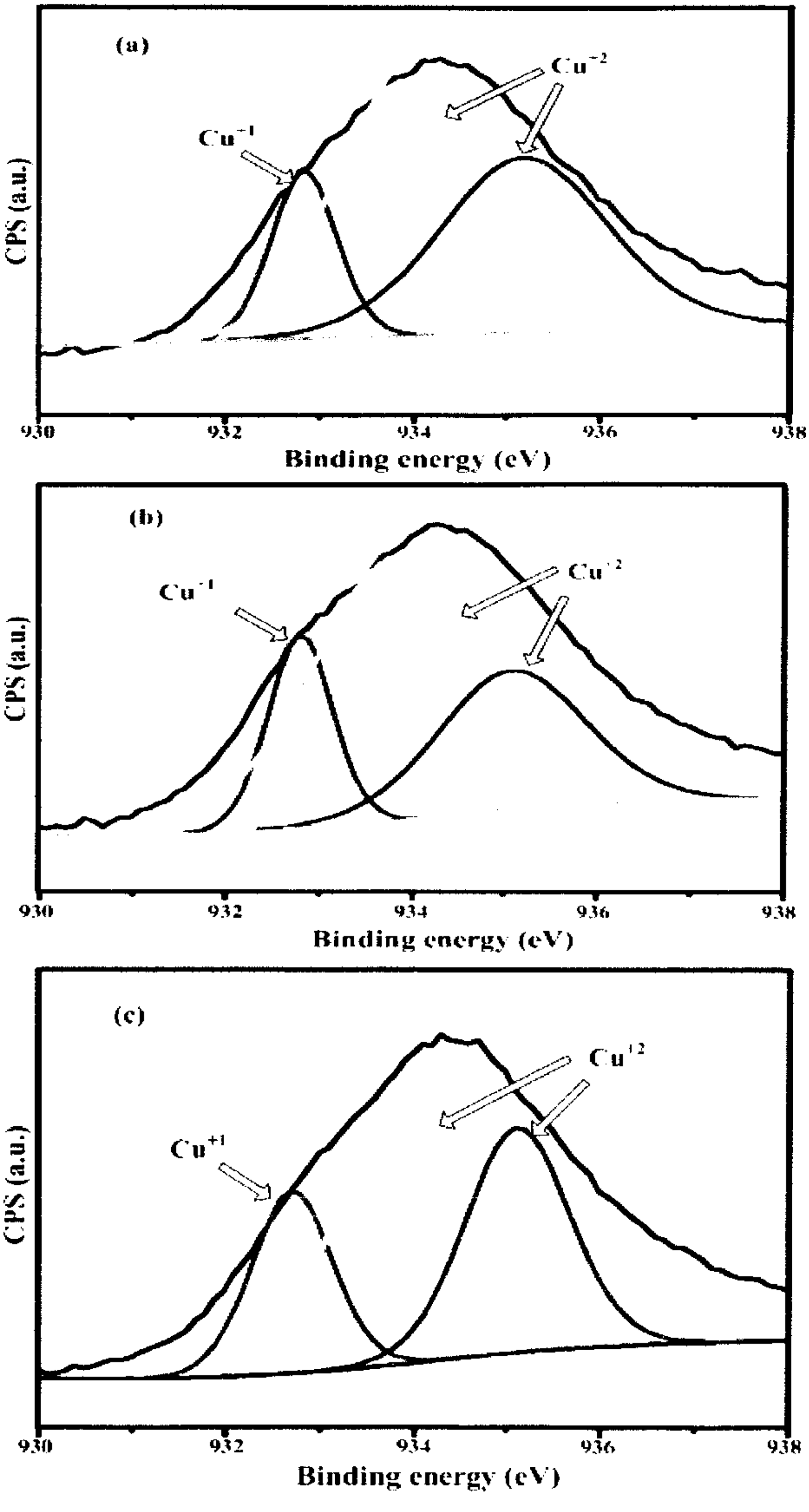

Figure 4.51: XPS Cu 2p peak fitting curves of (a) CZC-Nb0.4, (b) CZC-Nb0.8 and (c) CZC-Nb1.2 catalysts

XPS profile of Nb 3d core electrons of Nb_2O_5 promoted CZC catalysts is displayed in Figure 4.52. Two major peaks were observed for Nb 3d region, Nb $3d_{5/2}$ peak centered at 207 eV and Nb $3d_{3/2}$ peak originated at 210 eV. In order to identify the different forms of niobium oxide, Nb 3d region was deconvoluted in six different peaks. Generally, metallic niobium is characterized by its XPS peak at 202 eV, which was not found in the current case, indicating the absence of Nb metal. However, XPS analysis revealed the existence of Nb in different oxygenated forms. The two main XPS peaks at 207.1 and 209.7 eV were Nb^{5+} (2) peak, which were characteristic peaks for Nb_2O_5 [227, 228]. Another major contribution of niobium oxide form was recognized by Nb^{5+} (1) peak with binding energies of 206.5, 209.16, and 210.09 eV, indicating NbO_6 octahedra. Besides, the existence of these two oxides, XPS peak for NbO_4 was manifested by a small shoulder at 208.1 eV. [332]. The contribution of each oxide to the total niobium oxide was calculated and documented in Table 4.32. Incorporation of Nb_2O_5 content affected the contribution of each oxide. Relative percentage of Nb_2O_5 was increased, whereas contribution of NbO_6 declined with increasing Nb_2O_5 content from 0.4 to 0.8 wt.%. In contrast, the opposite trend was followed when Nb_2O_5 content was further incremented from 0.8 to 1.2 wt.%. However, the contribution of NbO_4 remained almost invariant throughout the range of Nb_2O_5 loadings.

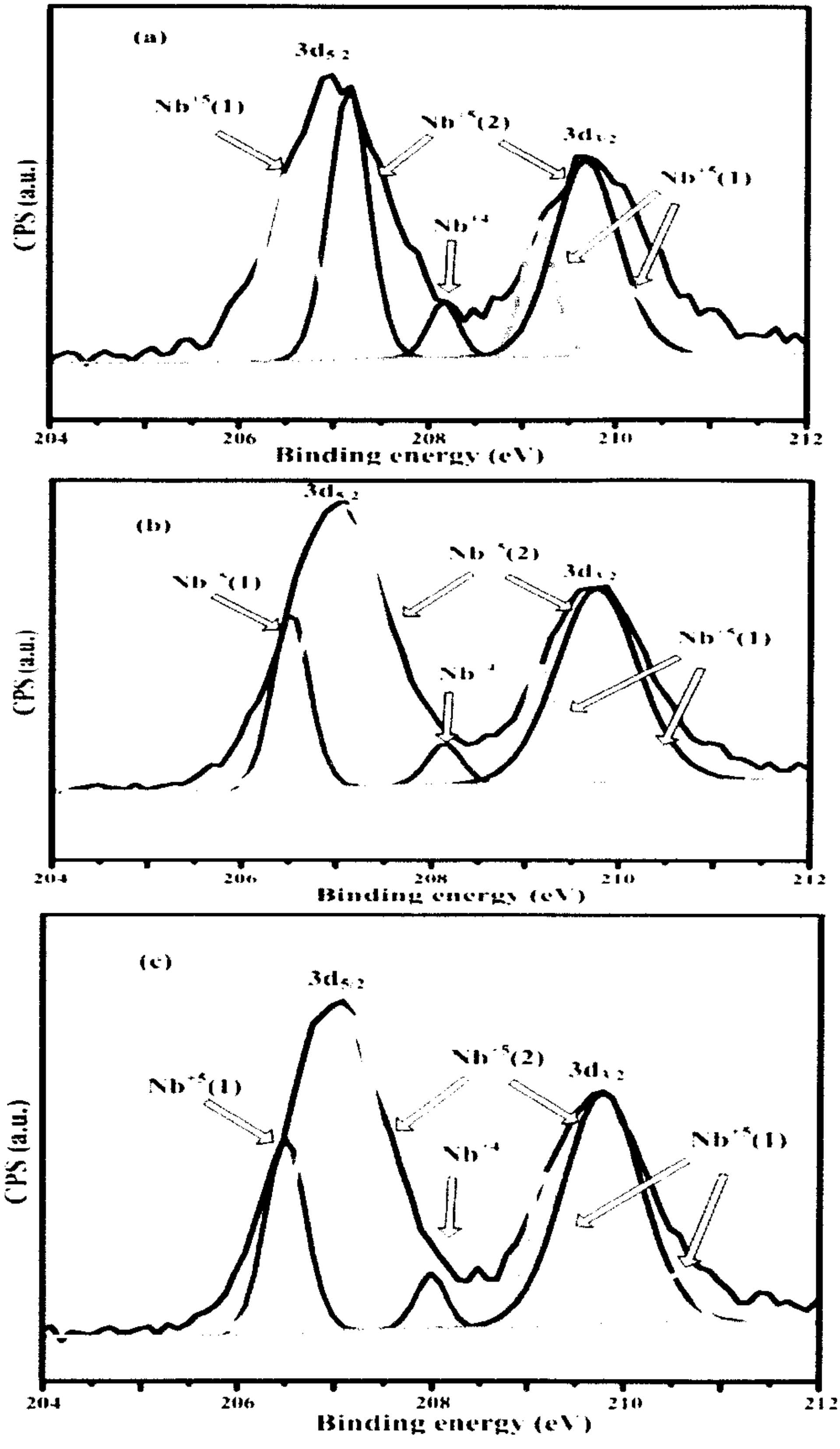

Figure 4.52: XPS Nb 3d peak fitting curves of (a) CZC-Nb0.4, (b) CZC-Nb0.8 and (c) CZC-Nb1.2 catalysts

Table 4.32: Contribution of each oxide to total niobium oxide

Catalyst	iA (%)		
	Nb_2O_5	**NbO_6**	**NbO_4**
CZC-Nb0.4	68	28	4
CZC-Nb0.8	74	23	3
CZC-Nb1.2	71	26	3

iA (%) represents the ratio of Ai/ΣAi (Ai is the area of each peak).

4.5.1.7 Basicity studies

Figure 4.54 shows CO_2 TPD profile of Nb_2O_5 promoted CZC catalysts. Basic sites were found in temperature range of 250-650 °C. The basic sites were classified as medium basic sites (below 450 °C) and strong basic sites (above 450 °C).

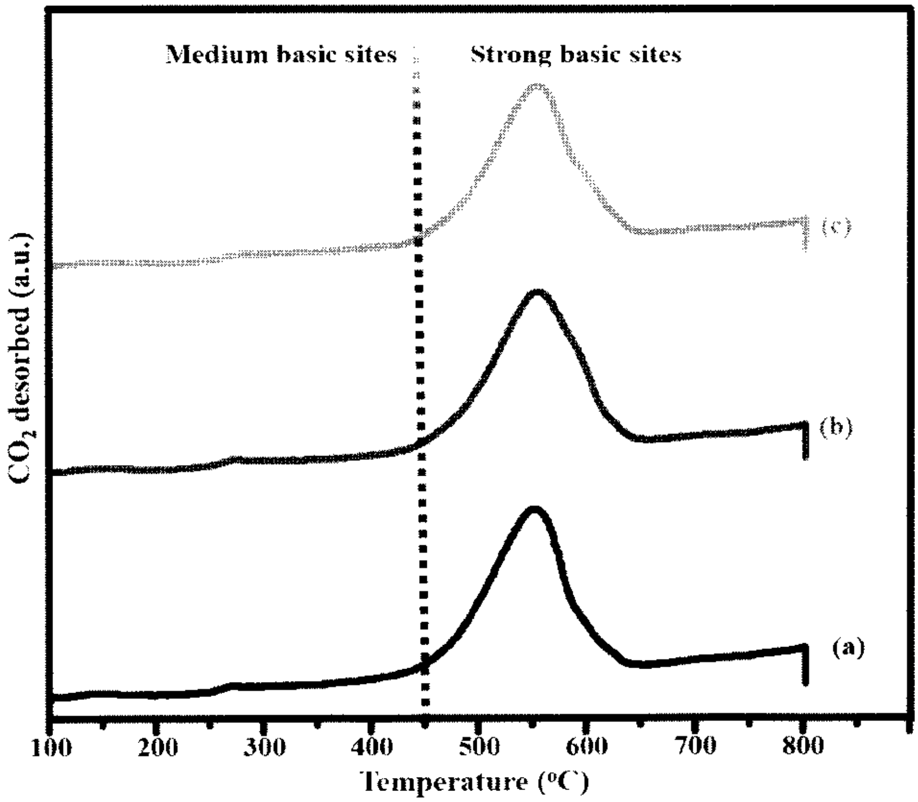

Figure 4.53: CO_2-TPD profile of (a) CZC-Nb0.4, (b) CZC-Nb0.8 and (c) CZC-Nb1.2 catalysts

Irrespective of the Nb_2O_5 concentrations, basic sites were predominantly found in the higher temperature region. This implied that the strength of basic sites was unaffected by variation in Nb_2O_5 content.

The total number of basic sites, their densities, and relative distribution are documented in Table 4.33. The total number of basic sites remained almost constant throughout the range of Nb_2O_5 concentration. Likewise, the densities of total basic sites were also found to be invariant with the variation of Nb_2O_5 concentrations. Meanwhile, the magnitude of medium basic sites slightly increased when Nb_2O_5 concentration increased from 0.4 to 0.8 wt.%. However, the magnitude of medium basic sites declined with further addition of Nb_2O_5 content. Besides, the highest amount of medium basic sites could be one the reasons for higher activity of CZC-Nb0.8 catalyst in the current case.

Table 4.33: CO_2 TPD data of Nb promoted CZC catalysts

Catalyst	**Total basic sites (μmol/g.cat)**	**Density of total basic sites (μmol/m^2)**	**Medium basic sites (μmol/g.cat)**	**Strong basic sites (μmol/g.cat)**
CZC-Nb0.4	333	1.51	33	300
CZC-Nb0.8	331	1.60	39	292
CZC-Nb1.2	334	1.57	34	300

4.5.2 Effect of Nb_2O_5 content on activity of catalysts

Table 4.34 shows the variation of catalysts performance as a function of Nb_2O_5 promotion. The rate of methanol synthesis increased from 32 to 37 (g/kg.cat.h) with the incorporation of Nb_2O_5 to the CZC parent catalyst. Although further addition of Nb_2O_5 improved the activity of the catalyst, but the improvement did not have much significance. Nevertheless, the rate of methanol synthesis was depressed with further incorporation of Nb_2O_5 content. The increment in methanol synthesis rate by Nb_2O_5 promotion could be due to ease in Cu reduction, as indicated by TPR studies. Likewise the increase in methanol synthesis rate could be also justified by improvement in methanol selectivity as a function of Nb_2O_5 introduction to the parent catalyst. On the other hand, CO_2 conversion was adversely affected by Nb_2O_5 addition. Apart from methanol,ethane, hexane and carbon monoxide were also found as by-products in the GC chromatogram of the reaction mixture. On the other hand, CO_2 conversion was adversely effected by Nb_2O_5 promotion to the parent catalyst.

In terms of methanol synthesis, a comparative study of the activity data of this novel catalyst with the reported literature revealed that the current Nb_2O_5 promoted CZC catalysts showed higher activity for methanol yield and CO_2 conversion as compared to that recorded by Sloczynski et al. over $Ag/ZnO/ZrO_2$ and $Au/ZnO/ZrO_2$ catalysts [278]. Similarly, the results obtained in this study were very much comparable in terms of methanol yield and CO_2 conversion to the work of Liu et al., for CO_2 hydrogenation over $Cu/Ga_2O_3/ZrO_2$ catalysts [93]. Similarly, a comparable activity data for methanol synthesis were reported by Liang et al. for carbon nanotube-supported Pd/ZnO catalysts [87]. Nevertheless, at relatively low reaction conditions the activity of the current catalyst system was slightly lower as compared to that reported by Baltes et al. for methanol synthesis over $CuO/ZnO/Al_2O_3$ catalysts [280].

Incorporation of Nb_2O_5 led to a decline the CO_2 conversion from 14 to 10 %. However, CO_2 conversion remained almost constant with further increase in Nb_2O_5 content. Interestingly, it could be inferred from the activity pattern of Nb_2O_5 loaded with CZC catalysts that Nb_2O_5 promotion had a supporting effect on methanol selectivity. Similar observations were also reported by Passos et al., where niobia containing catalysts showed higher selectivity for n-heptane conversion to olefins [114]. Similarly, the turnover frequency (TOF) of methanol synthesis reduced significantly from 1.42 to 0.92 s^{-1} with the incorporation of 0.4 wt.% of Nb_2O_5.

rename

Table 4.34: Activity data of CZC and Nb promoted CZC catalysts

Catalyst	**Meth. activity (g/kg.cat.h)**	**CO_2 conversion (%)**	**Methanol selectivity (%)**	**TOF_{MeOH} (s^{-1})**
CZC	32	14	75	1.42
CZC-Nb0.4	37	10	89	0.92
CZC-Nb0.8	40	9	87	0.89
CZC-Nb1.2	38	8	88	0.88

The higher activity of Nb_2O_5 promoted catalysts that could be explained by significant increase in the copper surface area of the parent catalyst. As evident from Figure 4.54, the introduction of Nb_2O_5 remarkably increased the S_{Cu} of the parent catalyst and the rate of methanol synthesis improved significantly as well. The trend continued with further Nb_2O_5 addition and optimum values of both S_{Cu} and methanol synthesis rate were recorded for CZC catalyst with 0.8wt.% of Nb_2O_5 content. However, the methanol synthesis rate ~~was depressed~~ decreased with maximum concentration of Nb oxide ~~due~~ corresponding to decline in magnitude of S_{Cu}. The tailoring role of S_{Cu} in the activity profile of Nb_2O_5 promoted catalysts showed the importance of metallic Cu surface area.

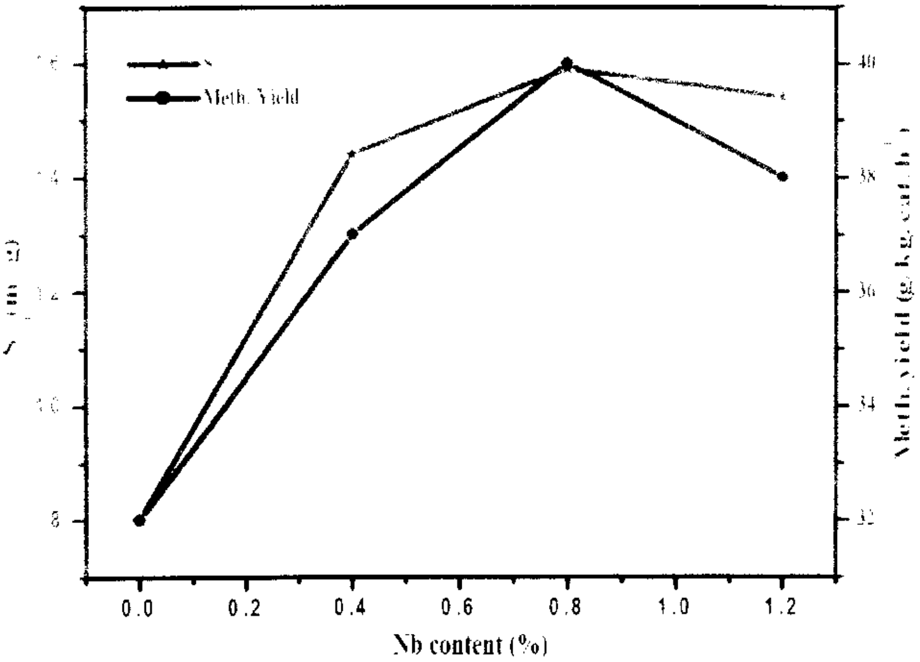

Figure 4.54: Correlation of S_{Cu} and methanol synthesis rate as a consequent of Nb addition

Hence, in order to investigate the role of S_{Cu} in CO_2 hydrogenation to methanol, a graph was plotted between S_{Cu} and TOF of methanol formation.

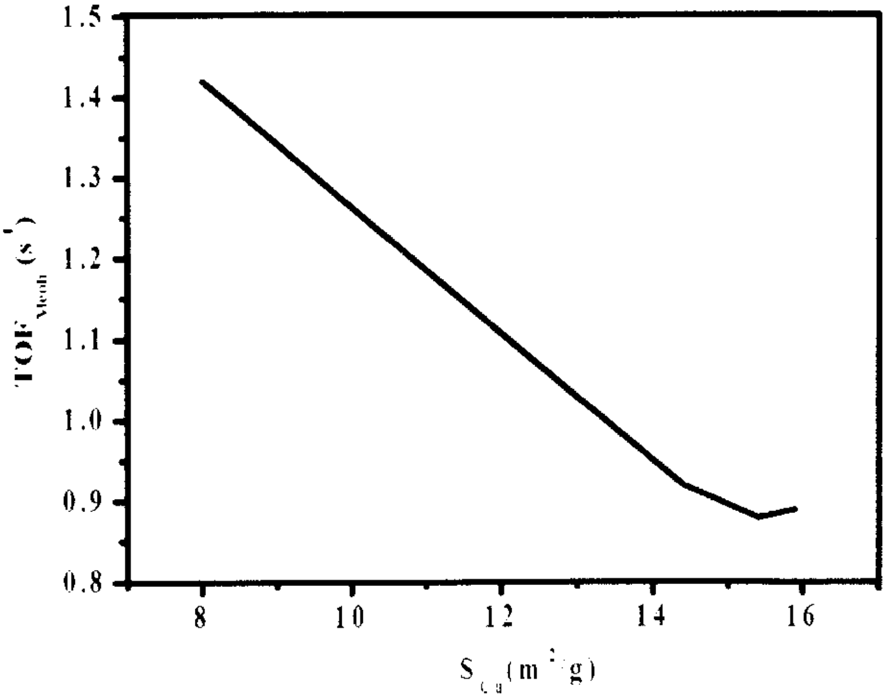

Figure 4.55: Correlation of S_{Cu} and methanol TOF

As evident from the Figure 4.55, TOF decreased with the increase of copper surface area. Generally activity of the copper based catalysts increases linearly with increasing S_{Cu}. However conflicting results have also been reported in the literature [281, 282]. The results obtained in the current study reveal that S_{Cu} is not the only factor to regulate the catalysts activity. Apart from S_{Cu} different factors affecting the catalytic activity have been proposed by different researchers. The higher selectivity of the Nb_2O_5 promoted catalyst could be due to the role of Nb_2O_5 to hold more metallic Cu in promoted CZC catalyst. This can also be justified by increasing S_{Cu} with the introduction of Nb_2O_5 to the parent CZC catalyst. Similar observations were reported by Yoshihara and Cambell for methanol synthesis over Cu/ZnO catalysts [95].

Furthermore, in order to study structure sensitivity behavior of the title reaction, a graph was plotted between copper particles size (d_{Cu}) and TOF of methanol formation. As indicated in Figure 4.56, a sharp decline was observed in magnitude of TOF with increasing d_{Cu} from 5 to 6 nm. Nevertheless, it remained almost constant with further growth of d_{Cu}. This was because of the small variation of d_{Cu} as a consequent of Nb oxide addition.

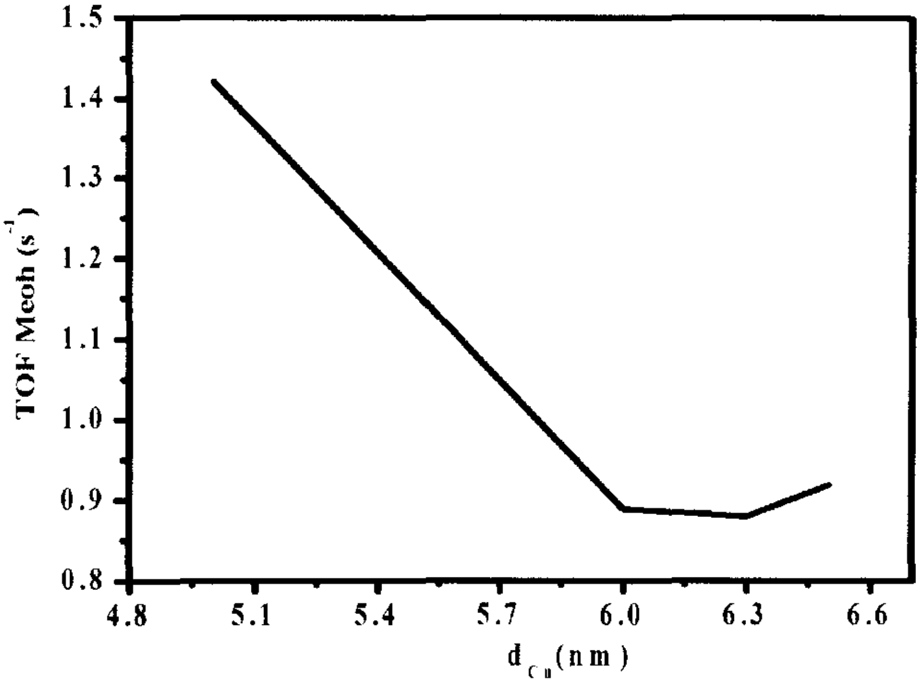

Figure 4.56: Correlation of d_{Cu} and methanol TOF

4.6 Effect of ZnO promoter

Effects of ZnO promoter on the physicochemical properties and activity pattern of parent catalyst were investigated. The results are briefly discussed as in the following.

4.6.1 Effect of ZnO content on physiochemical properties

The influence of ZnO on physicochemical profiles of parent catalysts are discussed below.

4.6.1.1 Quantification of catalyst components

ICP-OES was employed to quantify Cu and ZnO contents and the data are presented in Table 4.35. Magnitudes of both bulk Cu, as well as ZnO measured by ICP, were in very close agreement to the targeted values. This suggested that almost all ZnO were successfully deposited on the catalyst support. This in turn also identified the efficiency of DP method for preparing catalysts with higher loadings of active metals.

Table 4.35: ICP results of CZC catalysts with different ZnO content

Sample	**Target Cu (%)**	**Cu (%) by ICP**	**Target ZnO (%)**	**ZnO (%) by ICP**
CZCZ1	15	14.3	1	0.8
CZCZ2	15	14.8	2	1.7
CZCZ3	15	14.9	3	3.1
CZCZ4	15	14.6	4	3.7

4.6.1.2 X-ray diffraction studies

Phase analysis of catalyst components were investigated by using XRD technique. XRD profile of ZnO promoted CZC catalysts is shown in Figure 4.57. For comparison purpose, an XRD spectra of bare CNFs and unloaded CZC catalyst were also included.

Hexagonal graphitic planes of CNFs were identified as discussed in the previous sections. Similarly, monoclinic-phased tenorite CuO was indexed with JCPDS card files No. 48-1548 (a = 4.62 Å, b = 3.43 Å, and c = 5.06 Å). No diffraction peak was observed for Zn containing compound for ZnO promoted CZC catalysts with ZnO content < 3 wt.%. The absence of diffraction peak of Zn species indicated their amorphous phase at a lower concentration. Similarly, higher dispersion and smaller crystallite size could also be the factors for absence of XRD diffraction. Nevertheless, a sharp diffraction peak at scattering angles 2θ = 36.5° accompanied by small reflection at 32° and 34.5° indicated (101), (100), and (002) crystal planes of ZnO crystal [333]. A small diffraction peak for ZrO_2 around 2θ = 31° found in CZC catalysts disappeared with the introduction of ZnO content. The disappearance of ZrO_2 peak with ZnO addition indicated transformation of zirconia to the amorphous form. However, ZrO_2 diffraction peak re-appeared when ZnO content exceeded 2 wt.%, suggesting lower dispersion of zirconia with higher ZnO loadings. Another interesting observation in XRD studies of ZnO loaded catalysts was the intensification of CuO peaks with increasing ZnO content. This suggested that the degree of CuO crystallization increased with the increase of ZnO loadings.

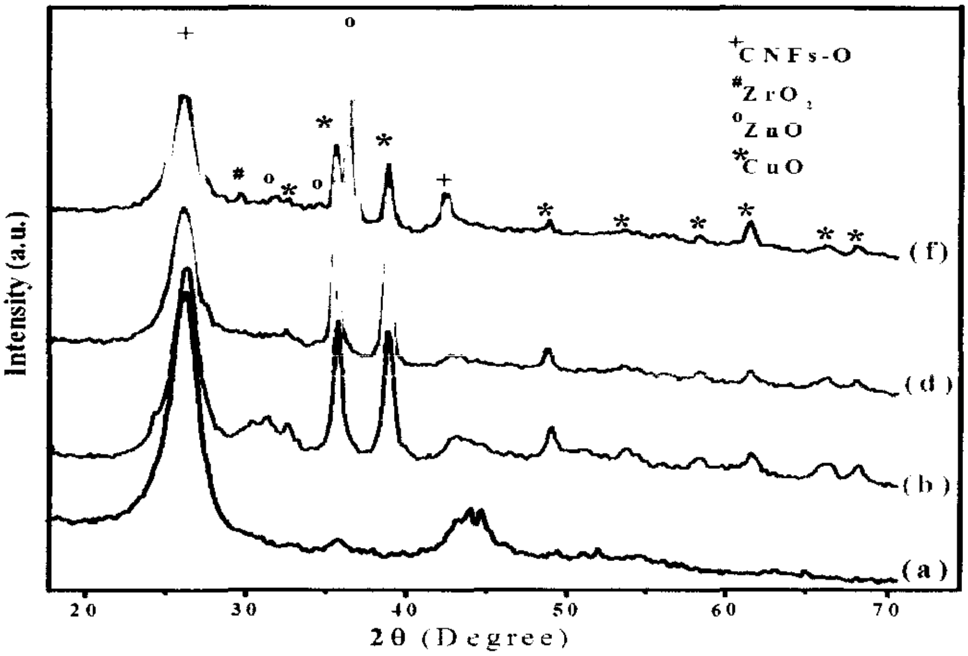

Figure 4.57: XRD profile of (a) CNFs-O, (b) CZC, (c) CZCZ1, (d) CZCZ2, (e) CZCZ3 and (f) CZCZ4 catalysts

4.6.1.3 TEM morphology

TEM was utilized to study the morphology of the catalyst. TEM images of the studied catalysts with magnification of 200 K are presented in Figure 4.58. TEM studies revealed well-distributed particles for CZCZ1 and CZCZ2 with average particle size of 3 and 4 nm, respectively. This well-dispersed morphology was observed with further ZnO addition. However, agglomeration, as well as growth of catalysts particles, was observed when ZnO content was increased beyond 3 wt.%. Consequently, particle size of both metal oxides increased with increasing ZnO content. Furthermore, agglomeration of catalyst particles was observed in the TEM images of the respective catalysts.

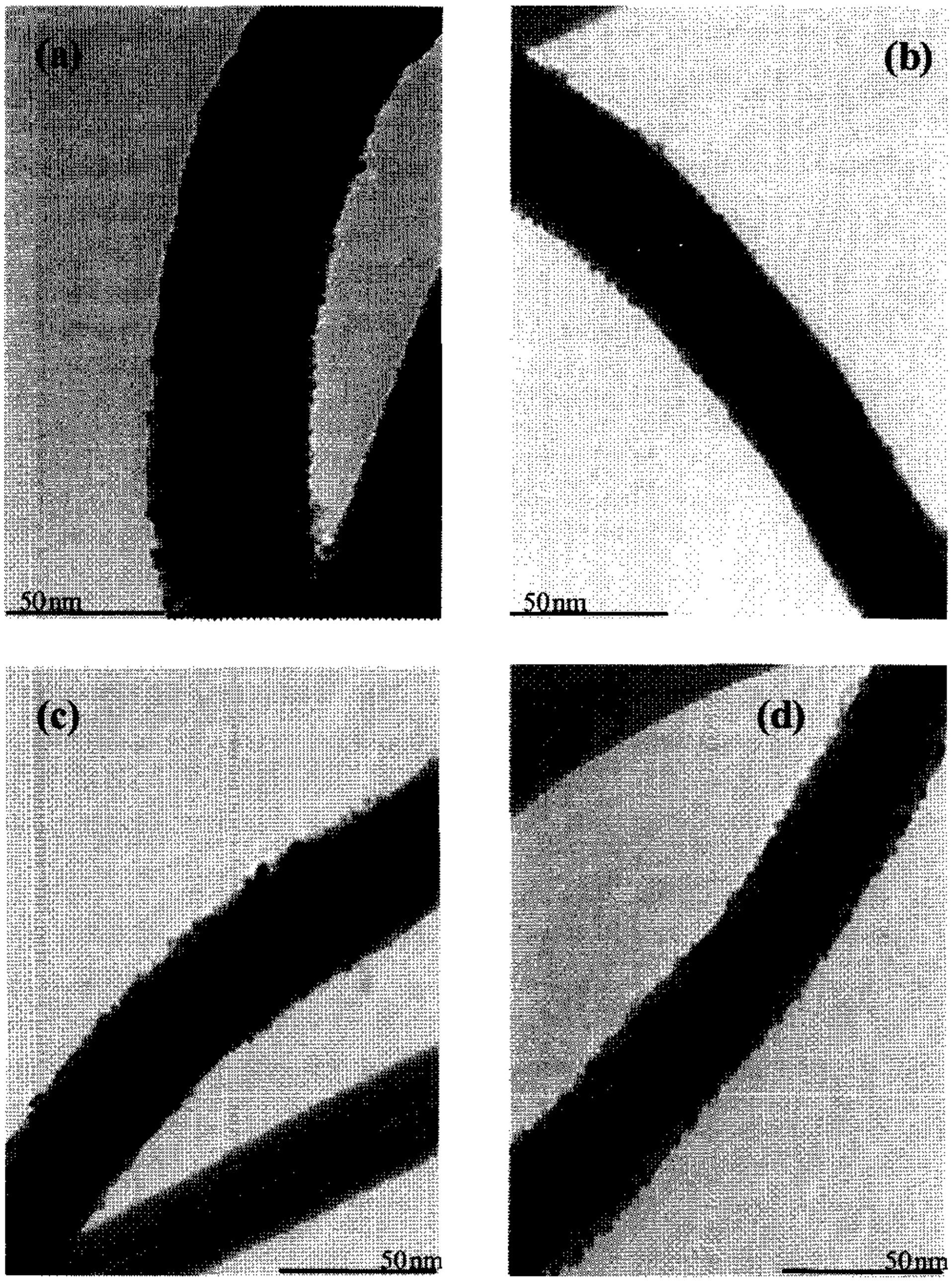

Figure 4.58: TEM images of (a) CZCZ1, (b) CZCZ2, (c) CZCZ3 and (d) CZCZ4 catalysts

4.6.1.4 Textural properties

Nitrogen adsorption-desorption isotherms of ZnO promoted CZC catalysts are shown in Figure 4.59, while pore size distribution is displayed in Appendix C (Figure C4). Each catalyst exhibited a typical type-IV isotherm with H4 type hysteresis loops having sharp inflection between p/po ranges of 0.90–0.94. This unveiled the mesoporous nature of catalyst support.

Textural properties of ZnO promoted CZC catalysts are documented in Table 4.36. The surface area of ZnO promoted catalysts remained almost consistent by increasing ZnO loading up to 3 wt.%. However, it was depressed by further ZnO addition. This had been postulated due to the blockage of pores, as indicated by the decline of pore volume. Similar observations were also observed by Young and Jong [334]. In contrast, the average pore diameter increased from 12.5 to 13.5 nm when ZnO content was doubled from 1 to 2 wt.%, respectively. However, it remained almost constant with further addition of ZnO content.

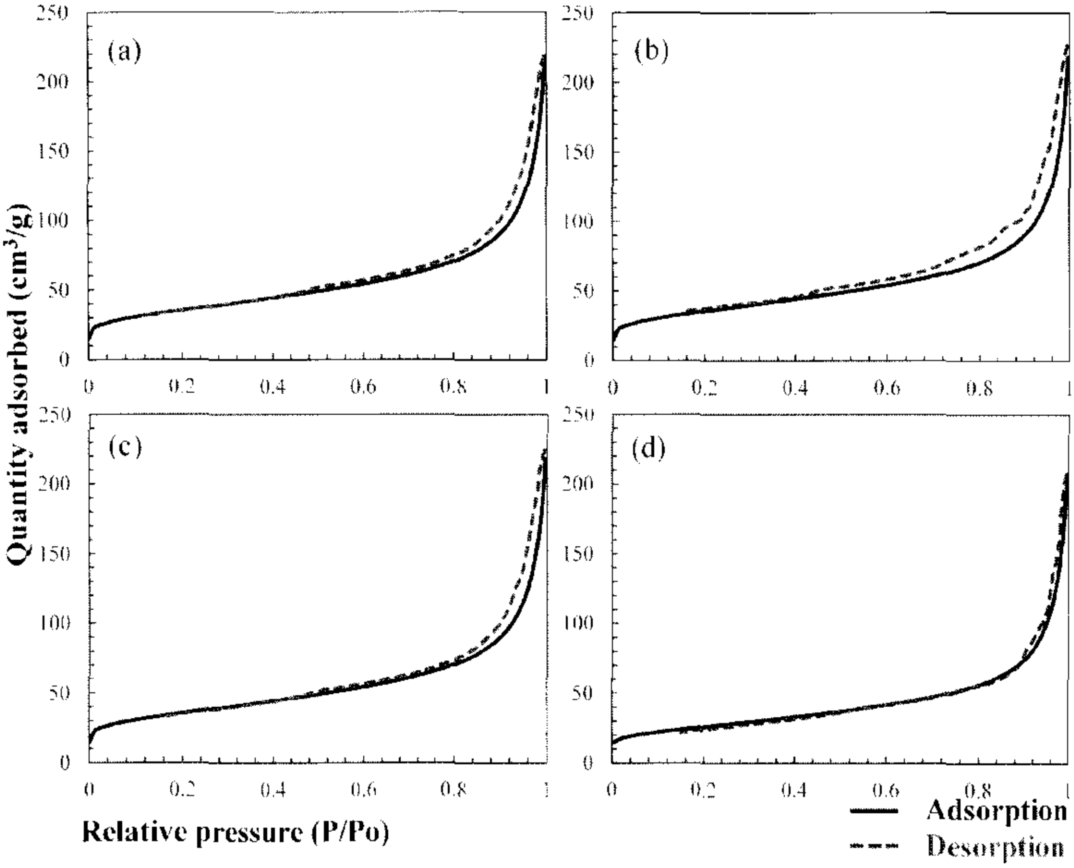

Figure 4.59: N_2 adsorption desorption isotherms of (a) CZCZ1, (b) CZCZ2, (c) CZCZ3 and (d) CZCZ4 catalysts

Table 4.36: Surface properties of CZC catalysts

Sample	**BET surface area (m^2/g)**	**Total pore volume (cm^3/g)**	**Average pore diameter (nm)**
CZCZ1	124	0.28	12.5
CZCZ2	124	0.29	13.5
CZCZ3	122	0.30	13.5
CZCZ4	91	0.27	13.6

4.6.1.5 Surface area and dispersion of copper

The surface area (S_{Cu}), dispersion (D_{Cu}), average particle size (d_{Cu}), and relative distribution (R_{Cu}) of metallic copper were measured via N_2O chemisorption. The N_2O chemisorption data are presented in Table 4.37. As evident from the tabulated data, surface properties of metallic Cu were significantly affected by variation of ZnO content to the parent CZC catalysts. Copper surface area initially decreased from 8.25 to 7.79 m^2/g with incorporation of ZnO concentration in the parent catalyst from 1 to 2 wt.%. The highest S_{Cu} was recorded when ZnO content was increased to 3 wt.%. However, Cu surface area was depressed on further addition of ZnO to the parent CZC catalyst. The maximum S_{Cu} for CZCZ3 could be one of the reasons of its highest activity to methanol synthesis. In contrast, the magnitude of Cu dispersion first was increased, and then, decreased with increasing ZnO content from 1-2 and 2-3 wt.%, respectively. However, it ~~was~~ significantly declined for CZC catalyst with maximum concentration of ZnO. Agglomeration of catalyst particles could be one the reasons for lower dispersion, as indicated in XRD and TEM studies.

Table 4.37: N_2O chemisorption data of ZnO promoted CZC catalysts

Catalyst	S_{Cu} **(m^2/g) N_2O**	D_{Cu} **(%) N_2O**	d_{Cu} **(nm) N_2O**	R_{Cu} **N_2O**
CZCZ1	8.25	11.65	8.92	0.44
CZCZ2	7.59	12.29	8.44	0.41
CZCZ3	8.58	10.84	9.63	0.47
CZCZ4	4.95	6.02	17.21	0.36

Contrary to S_{Cu} and D_{Cu}, no substantial variation in d_{Cu} was observed with ZnO incorporation up to 3 wt.%. Nevertheless, it remarkably increased with further addition of ZnO content. Furthermore, the growth in d_{Cu} and the concomitant decline in S_{Cu} and D_{Cu} for catalyst with ZnO content beyond 3 wt.% had been clear manifestation of Cu agglomeration with higher ZnO loadings. Similarly, the distribution of metallic Cu was affected by variation of ZnO content in the parent catalyst. Contribution of surface metallic copper (R_{Cu}) decreased from 0.44 to 0.41 with the increment of ZnO loading from 1-2 wt.%. Nevertheless, it slightly increased with further addition of ZnO. Generally, the R_{Cu} was not much effected with the initial variations of ZnO content, however, it remarkably declined in CZC catalyst with maximum ZnO loadings. The decrease in surface Cu was a consequent of the increasing ZnO content, which implied that Cu was partially embedded in the ZnO phase and the process lingered until the lowest R_{Cu} value was recorded for catalysts with maximum ZnO loadings. More importantly, the increase of ZnO concentration and subsequent Cu embedding offered less exposure to Cu surface and more Cu–Zn interfacial surface area. The correlation between S_{Cu}, D_{Cu}, and d_{Cu} with varying ZnO content had been quite straight forward and has been discussed in the previous sections.

In summarizing the chemisorption results, one can observe that the properties of metallic Cu were not much affected by ZnO loadings up to 3 wt.%. However, these were severely suffered when ZnO concentration exceeded that level. The lower activity of CZCZ4 catalysts could be understood based on the findings of chemisorption.

4.6.1.6 Reducibility studies

TPR profile of CZC catalysts and ZnO promoted CZC catalysts are displayed in Figure 4.60. Likewise, total H_2-uptake, extent of reduction (H_2/Cu), position and distribution of reduction peaks, and relative abundance of dispersed copper are listed in Table 4.38. Two major reduction peaks were observed at 258 and 337 °C, which were designated by peaks α and β, respectively. The presence of two reduction peaks had been consistently reported in copper based catalysts and attributed to the stepwise reduction of Cu ($Cu^{2+} \rightarrow Cu^{+} \rightarrow Cu$) [268]. Similarly, the reduction peak at lower temperature was ascribed to dispersed copper, whereas bulk phase copper was recognized by a reduction peak at a higher temperature. Besides, the incorporation of ZnO to the parent CZC catalyst shifted the positions of both reduction peaks to lower temperature. This indicated that the reduction of CuO was facilitated with the introduction of ZnO promoter. In contrast, reduction peaks were back shifted to slightly higher temperature when ZnO content exceeded 1 wt.%. Since the surface energy of Zn is lower than copper, the shifting of Cu reduction to higher temperature could be due to surface segregation of Zn^{+2}, which made Cu difficult to be reduced. Such observations were also ~~very~~ recently reported by Ying-ming and Li for ZnO promoted Cu–Al catalyst [335]. Furthermore, no TPR peak was observed for ZnO reduction as ZnO is not reducible in the studied temperature range [336-338].

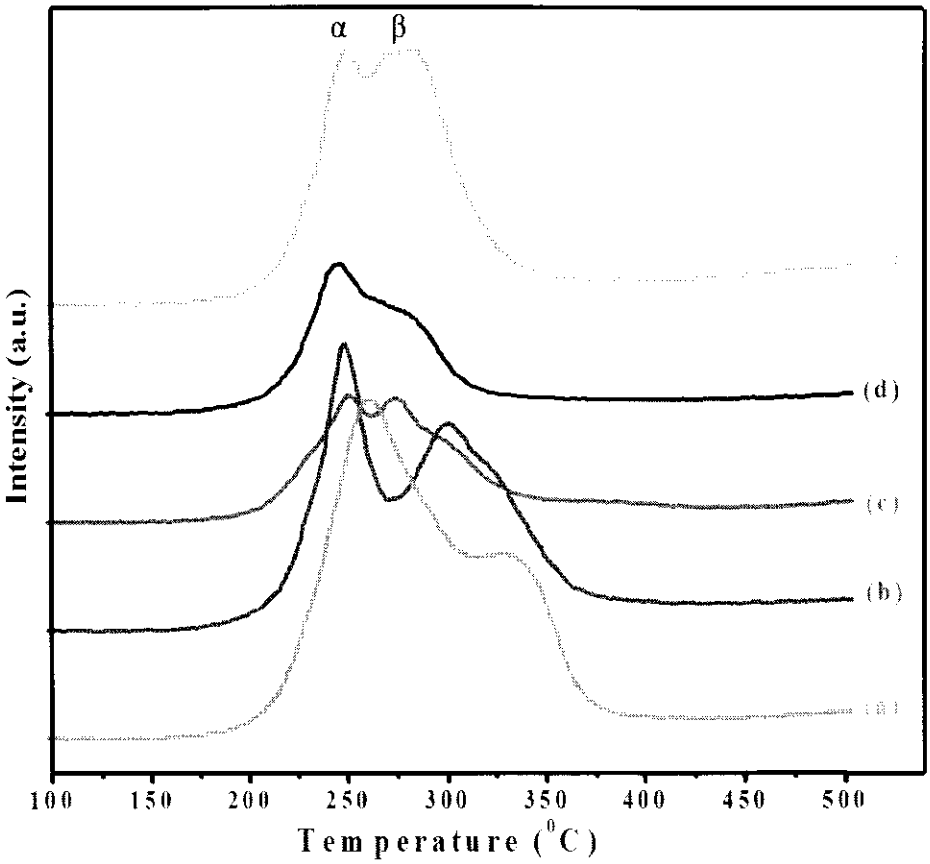

Figure 4.60: TPR profiles of (a) CZC, (b) CZCZ1, (c) CZCZ2, (d) CZCZ3 and (e) CZCZ4

In addition, the magnitude of total H_2-uptake consistently declined with the increase of ZnO content in parent catalyst. This could be due to the embedding of Cu in ZnO matrix with the increasing ZnO concentration. Moreover, H_2/Cu ratio was calculated to analyze the extent of copper reduction as a function of increasing ZnO content. Nevertheless, the ratio decreased from 0.90 to 0.77, suggesting the lesser availability of copper reduction. This decline was continued with further addition of promoter and a minimum value was recorded for catalyst with 3 wt.% of ZnO. This progressive decrease in H_2/Cu ratio further verified the embedding of copper in ZnO matrix. Furthermore, agglomeration of copper with increasing ZnO content had been another vital factor for the decline of H_2/Cu ratio. In this regard, TPR investigations supported the XRD findings where copper agglomeration was identified with increasing ZnO concentration. In addition, the magnitude of H_2/Cu ratio was recorded above 0.50 throughout the range of ZnO concentration. From these observations, another important conclusion that could be drawn is the predominant Cu^{2+} oxidation states of copper in all studied catalysts irrespective of ZnO addition. Distribution of copper was significantly influenced by the variation of ZnO concentration. Peak α was the main reduction peak with 68 % contribution to the total reduced copper in parent CZC catalyst. Although Peak α was still remained the major reduction peak with H_2 consumption of 1842 μmoles/g, but its contribution decreased to 58 %, when ZnO was further promoted to the parent catalyst. On the other hand, the magnitude of Peak α declined, while peak β subsequently increased when ZnO concentration reached 2 wt.%. Consequently, the contribution of peak α was reduced to 45 %. This trend was continued with further rise in ZnO loadings until minimum contribution of Peak α was recorded with highest ZnO content.

Table 4.38: TPR data of ZCC and ZnO promoted CZC catalysts

Sample	**Total H_2 consumed (μmoles/g)**	**H_2/Cu**	**Red. temperature (°C)**		**H_2 consumed (μmoles/g)**		**A (α)/ (A (α) + A (β)) *(%)**
			Peak α	**Peak β**	**Peak α**	**Peak β**	
CZC	2145	0.90	258	337	1455	689	68
CZCZ1	1841	0.77	248	300	1071	770	58
CZCZ2	1786	0.75	252	275	802	984	45
CZCZ3	1566	0.66	250	255	671	895	43
CZCZ4	1771	0.74	255	289	580	1191	33

*Fraction of dispersed copper

4.6.1.7 Metal-metal inteartion and surface analysis

Figure 4.61 displays Cu 2p photoelectron spectra of calcined CZC catalysts with different ZnO content. Two peaks of parent electrons, each one at 934.4 eV representing Cu $2p_{3/2}$ and another parental peak centered in binding energy scale of 954 eV indicating Cu $2p_{1/2}$ peak, were observed. Both peaks were accompanied with a broad satellite peak at a binding energy difference of about 8-9 eV. These satellites peaks were attributed to shake-up transitions by ligand-to-metal 3d charge transfer. These transitions are only allowed in Cu^{2+} due to $3d^9$ configuration of Cu^{2+} ion. Cu^+ cannot undergo such transitions due to $3d^{10}$ configuration. Hence, the emergence of shake-up with the corresponding parental XPS peak was the characterization of Cu^{2+} ions. In the current case, Cu^{2+} was the major oxidation state of copper in all studied catalysts. Furthermore, the position of Cu $2p_{3/2}$ was observed at relatively higher magnitude of binding energies as compared to the bulk copper (933 eV for bulk copper). This suggested that copper was well-dispersed on the surface of CNFs.

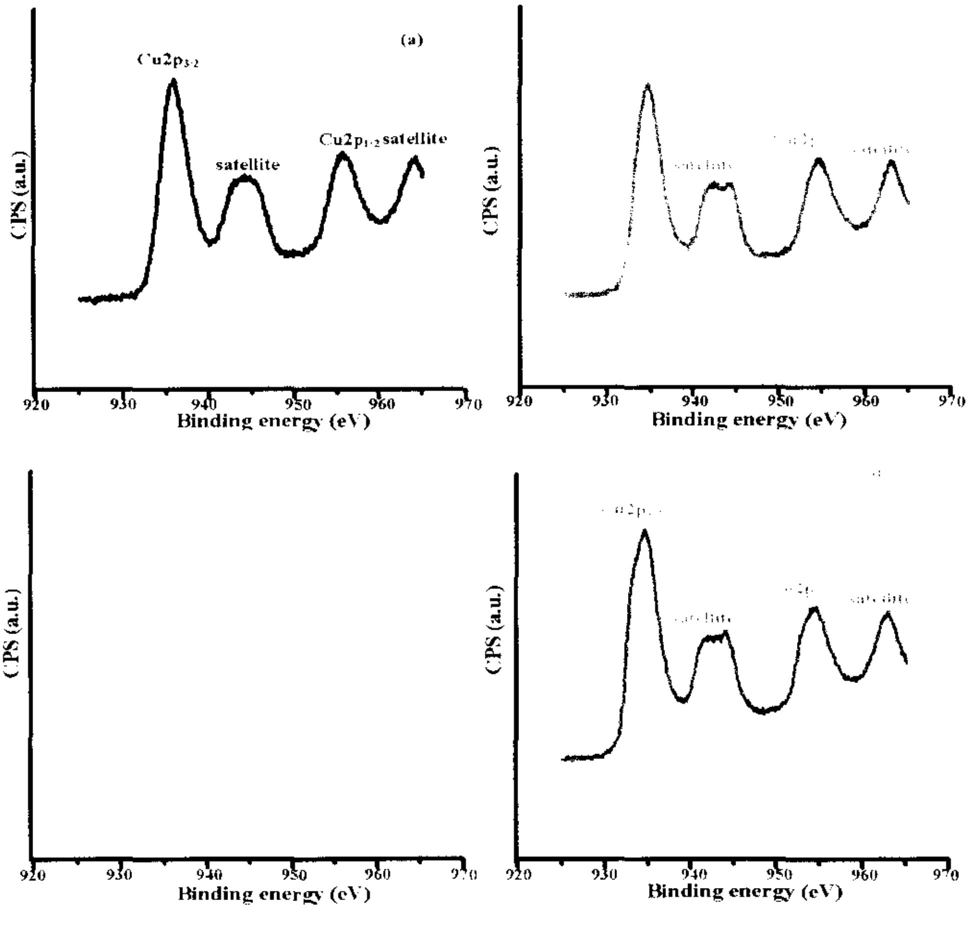

Figure 4.61: Cu2p photoelectron spectra of (a) CZCZ1, (b) CZCZ2, (c) CZCZ3 and (d) CZCZ4 catalysts

Besides, in order to investigate the oxidation chemistry of copper, Cu $2p_{3/2}$ peak was resolved in different peaks. Peak fitting curve of Cu $2p_{3/2}$ is presented in Figure 4.62. Coupling between unpaired electrons is a characteristic phenomenon of cupric ion. Due to this feature, it can easily be differentiated from other copper oxides. However, binding energies of Cu and Cu^+ ions were so close that they could not be identified on this basis. In the current study, three XPS peaks were observed in deconvulated spectra for each catalyst. Cu $2p_{3/2}$ peaks at higher binding energy region (935.1 and 933.7 eV) were ascribed to Cu^{2+} ions. Similarly, Cu^+ species were identified by a small peak at 932.7 eV. The XPS investigations strongly supported the H_2-TPR findings by exhibiting two different forms of copper oxides.

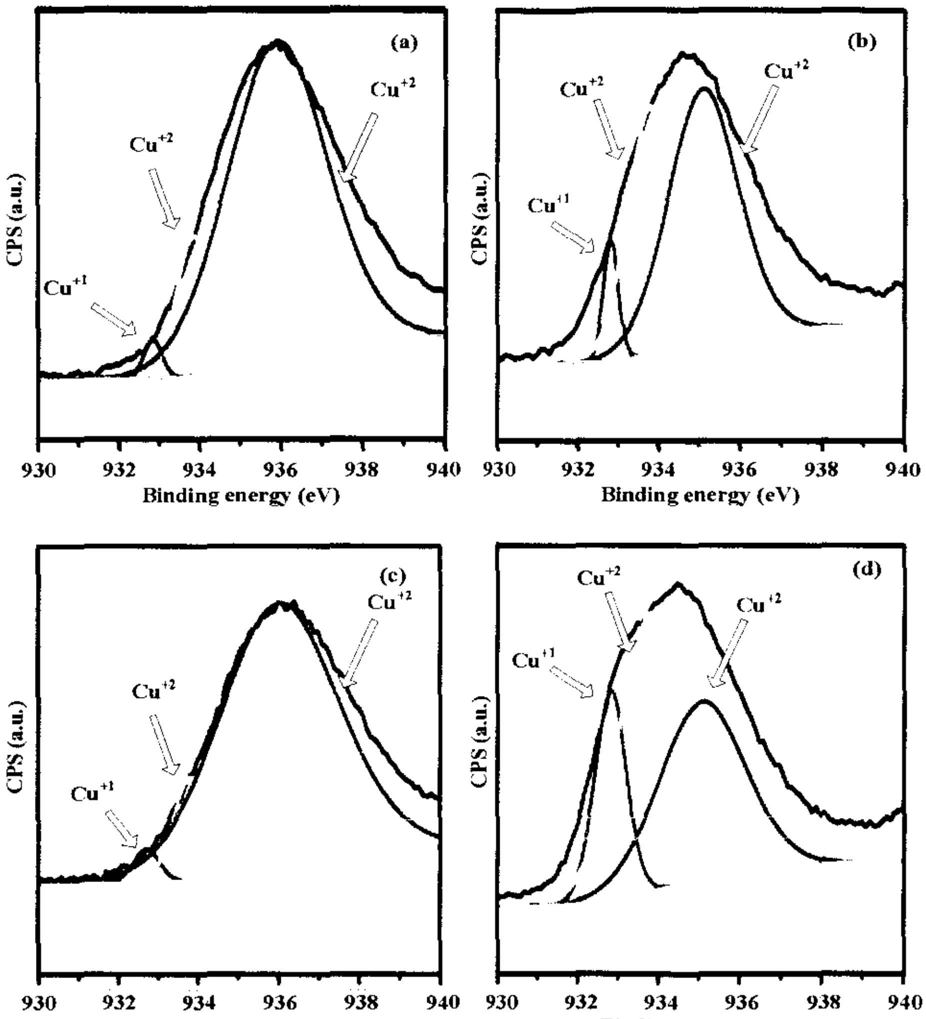

$> Cu^{2+}$?

Figure 4.62: XPS Cu$2p_{3/2}$ fittings curves of (a) CZCZ1, (b) CZCZ2, (c) CZCZ3 and (d) CZCZ4 catalysts

Meanwhile, Figure 4.63 shows Zn 2p XPS profile of ZnO promoted CZC catalysts. The presence of zinc oxide was confirmed in XPS investigations. Two major peaks were recorded with binding energy of 1023 and 1046 eV, representing Zn $2p_{3/2}$ and Zn $2p_{1/2}$, respectively [226]. The intensity of Zn $2p_{3/2}$ gradually increased by increasing ZnO concentration, indicating the enrichment of surface ZnO.

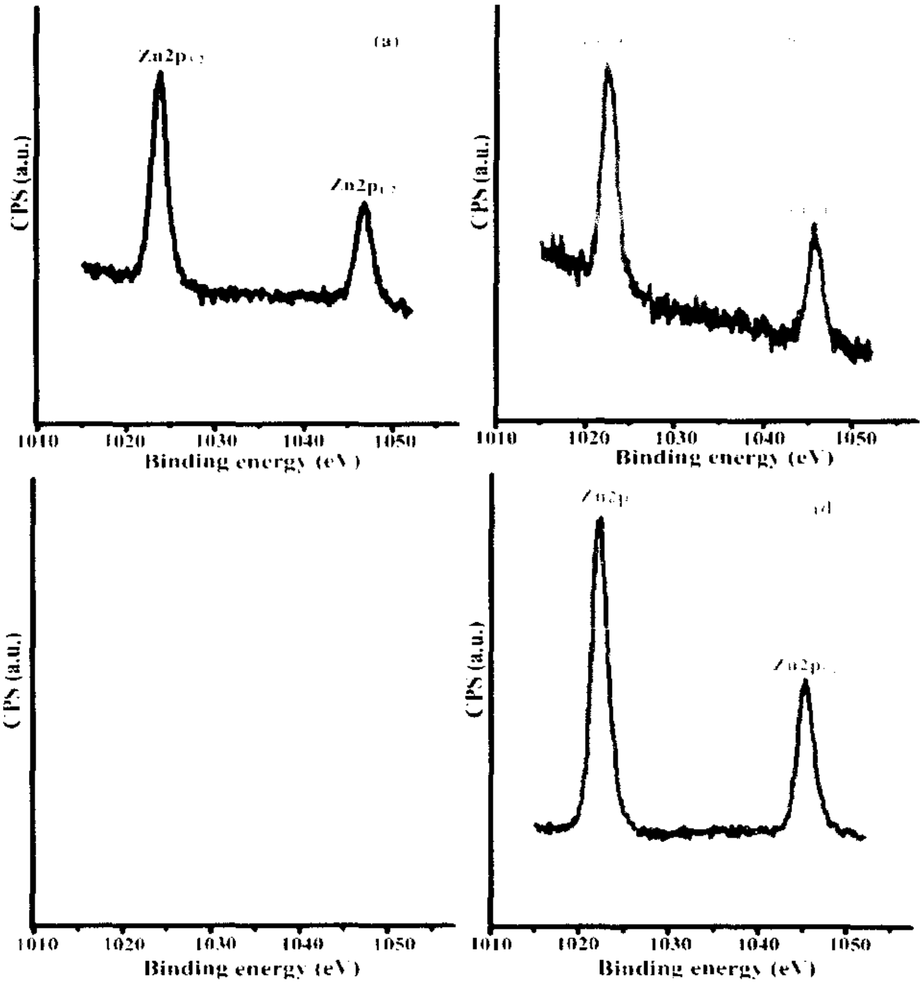

Figure 4.63: XPS Zn2p of (a) CZCZ1, (b) CZCZ2, (c) CZCZ3 and (d) CZCZ4 catalysts

Furthermore, photoelectron spectra of Zn $2p_{3/2}$ were resolved to investigate the different kinds of Zn oxidized states. The deconvoluted spectra of Zn $2p_{3/2}$ are displayed in Figure 4.64. XPS peak at 1021.4 eV exhibited metallic zinc, whereas peaks at 1022.4 and 1023 eV were ascribed to Zn^{2+} in the form of ZnO [339, 340]. The distribution of metallic Zn was affected by variation of ZnO in parent catalyst. Besides, the contribution of surface Zn was improved when ZnO content was doubled. However, further addition of ZnO reduced the surface of Zn metal until no surface zinc was observed in CZC catalyst with maximum amount of ZnO.

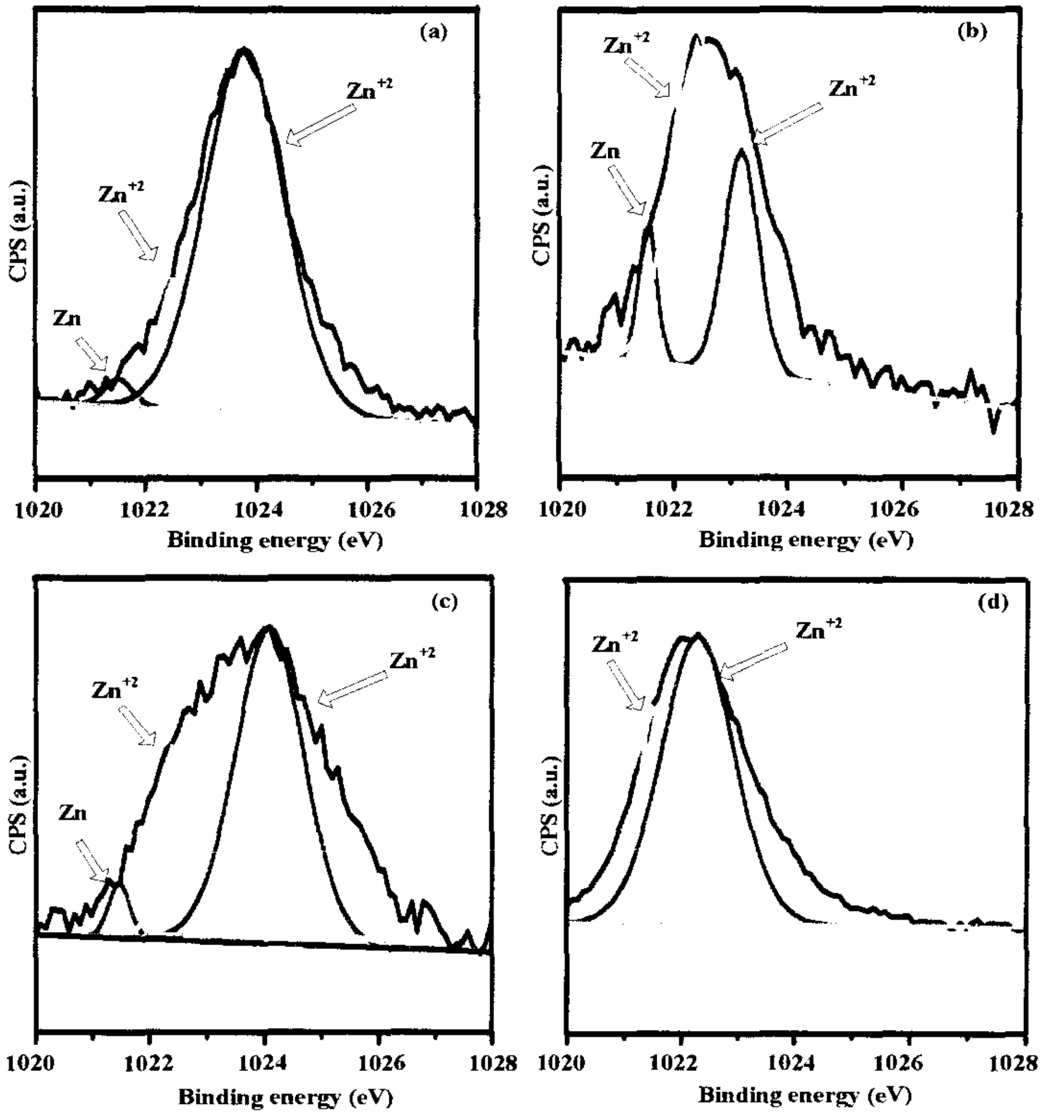

Figure 4.64: $Zn2p_{3/2}$ fitting curves of (a) CZCZ1, (b) CZCZ2, (c) CZCZ3 and (d) CZCZ4 catalysts

The binding energies of Cu $2p_{3/2}$ and Zn $2p_{3/2}$ core electrons and their full width at half maximum (FWHM) values are summarized in Table 4.39. As evident from the tabulated data, the increase in ZnO content from 1 to 2 wt.% shifted the Cu $2p_{3/2}$ peak from 935.82 to 934.50 eV. This shift to lower binding energies had been a consequent of increasing ZnO content, which implied the strengthening of interaction between Cu and ZnO. However, this interaction was diminished when ZnO addition reached 3 wt.%. This was demonstrated by back shifting of Cu $2p_{3/2}$ to higher binding energies. In contrast, Cu $2p_{3/2}$ peak shifted to lower binding energies for catalyst with maximum ZnO concentration that manifested higher interaction between the two metals. The mutual interaction of Cu and Zn as a function of ZnO content was further supported by the similar trend of Zn $2p_{3/2}$ shifting with the increase in ZnO concentration.

Table 4.39: XPS data of CZC catalysts with different ZnO content

Sample	**Binding energy (eV)**		**FWHM (eV)**	
	Cu $2p_{3/2}$	**Zn $2p_{3/2}$**	**Cu $2p_{3/2}$**	**Zn $2p_{3/2}$**
CZCZ1	935.82	1023.72	4.29	3.0
CZCZ2	934.50	1022.42	4.17	2.95
CZCZ3	936.18	1023.91	4.66	4.11
CZCZ4	934.50	1022.0	4.39	3.17

FWHM values of Cu $2p_{3/2}$ peak were also altered by variation on ZnO concentration. The magnitude of FWHM was reduced from 4.29 to 4.17 eV when ZnO content was doubled from its initial 1 wt.% content. Further increment of ZnO concentration in parent catalyst shifted the FWHM values to higher binding energies. This implied that ZnO addition beyond 2 wt.% caused distortion in coordination symmetry of Cu^{2+} ion towards a highly distorted octahedral symmetry. A similar trend was also recorded for FWHM values of Zn $2p_{3/2}$ with increasing ZnO content.

4.6.1.8 Basicity studies

CO_2 TPD was carried out to investigate the magnitude and the strength of basic sites. CO_2 TPD profiles of unpromoted CZC and ZnO promoted CZC catalysts are depicted in Figure 4.65. Basic sites were identified in two different regions. Basic sites below 450 °C were classified as lower and medium basic sites and were denoted by α

region, whereas basic sites above 450 °C were recognized as strong basic sites and had been symbolized as β region.

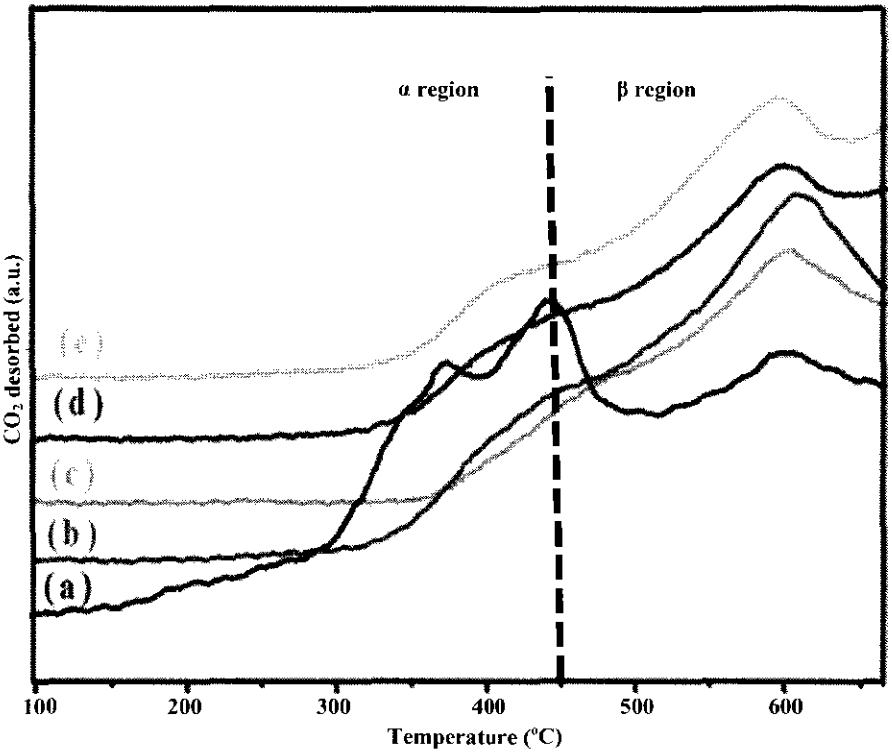

Figure 4.65: CO_2 TPD profile of (a) CZC, (b) CZCZ1, (c) CZCZ2, (d) CZCZ3 and (e) CZCZ4

A broad desorption peak originating around 200 °C with a shoulder at 300 °C was observed for CZC catalysts without ZnO content. This indicated the presence of weak and medium basic sites. Strong basic sites were characterized by another broad desorption peak with desorption maxima around 600 °C. Distribution of basic sites strength was significantly affected by the introduction of ZnO to the parent catalyst. Besides, the positions of desorption peaks in α region were shifted to higher temperature. However, the positions of desorption peaks in β region were invariant. This suggested that basic sites with weak and moderate strength were remarkably affected by the incorporation of ZnO in the parent catalyst.

The total number of basic sites and their densities are documented in Table 4.40. Similar to the distribution of strength, the number of total basic sites and their relative densities were also altered by promotion of ZnO.

Table 4.40: TPD CO_2 data of CZC and ZnO promoted CZC catalysts

Catalyst	Number of total basic sites (mmol/g.cat)	Density of total basic sites (mmol/m^2)
CZC	15.8	0.12
CZCZ1	12.1	0.09
CZCZ2	11.8	0.09
CZCZ3	11.4	0.09
CZCZ4	8.8	0.13

?

how

Zinc oxide is amphoteric in nature, and in the current study, the acidic profile of ZnO was more pronounced. The total number of basic sites was reduced from 15.81 to 12.1 mmol/g.cat when ZnO was incorporated in parent CZC catalyst. This portrayed the acidic character of ZnO in the current catalysts. This was further verified by a progressive decline in the total number of basic sites as a function of increased ZnO content. Similarly, magnitudes of basic sites densities were reduced with the incorporation of ZnO content to the parent catalyst. However, the values were recorded as invariant throughout the ZnO addition range before it was increased for CZC catalyst with highest ZnO loadings. This trend could be justified by the almost constant BET surface area values of the first three ZnO promoted catalysts.

4.6.2 Effect of ZnO content on catalytic performance of catalysts

The ZnO promotion affected the methanol synthesis rate, as well as CO_2 conversion. The reactivity data of the studied catalysts is documented in Table 4.41. The rate of methanol synthesis slightly improved from 32 to 35 g/kg.cat.h when ZnO was incorporated in parent CZC catalysts. The trend of better activity of ZnO loaded CZC catalysts towards methanol synthesis rate was persisted with further rise in ZnO concentration. The optimum amount of ZnO addition to methanol synthesis rate was found to be 3 wt.% before it showed a decline in activity with the maximum ZnO content. The enhanced activity of ZnO loaded CZC catalysts could be due to a synergism between Cu and ZnO. As a result of this synergetic effect, the electronic interaction between Cu and $Zn^{(2-\delta)+}$ created active sites like Cu–O–Zn [121].

Table 4.41: Activity data of CZC and ZnO promoted CZC catalysts

Catalyst	**Meth. activity (g/kg.cat.h)**	**CO_2 conversion (%)**	**Meth. selectivity (%)**	**TOF_{MeOH} X 10^{-3} (s^{-1})**
CZC	32	14	78	1.41
CZCZ1	35	12	80	1.51
CZCZ2	41	10	82	1.92
CZCZ3	45	9	92	1.87
CZCZ4	40	8	83	2.87

Likewise, the better activity of ZnO promoted catalysts could be explained by the fact that it facilitated the adsorption of H_2 species by acting as the binding site for atomic hydrogen. Furthermore, ZnO had been believed to be involved actively in methanol synthesis by creating Zn-methoxy oxide. Methoxy oxide is one of the stable reaction intermediates, which is converted to methanol with further hydrogenation. Similarly, methanol selectivity was progressively enhanced throughout the range of ZnO content. In contrast, CO_2 conversion progressively declined with increasing ZnO content and least conversion was recorded with the highest ZnO loadings. In conclusion, the increase in methanol synthesis rate and concomitant decline in CO_2 conversion as a function of increasing ZnO content indicated that the addition of ZnO improved the selectivity of methanol synthesis. Besides, the turnover frequency of methanol was increased by a factor of 1.07 with the incorporation of ZnO to the parent CZC catalyst. This indicated that ZnO promoter created sites of superior activity, and hence, the activity profile of catalyst was enhanced. Nevertheless, the turnover frequency of methanol progressively increased by increasing ZnO content. A slight decline in TOF was observed when ZnO concentration was increased from 2-3 wt.%. However, the

evidence from? what XPS data

highest value of TOF was recorded for CZC catalysts with maximum concentration of ZnO. A detailed comparative study of the current catalyst for CO_2 hydrogenation to methanol with the literature is displayed in Table 4.42.

Activity data of this novel catalyst with the reported literature revealed that the current ZnO promoted CZC catalysts showed higher activity for methanol yield and CO_2 conversion as compared to that recorded by Sloczynski et al. over Ag/ZnO/ZrO_2 and Au/ZnO/ZrO_2 catalysts [278]. Similarly, the results obtained in this study were very much comparable in terms of methanol yield and CO_2 conversion to the work of Liu et al., for CO_2 hydrogenation over Cu/Ga_2O_3/ZrO_2 catalysts [93]. Similarly, a comparable activity data for methanol synthesis were reported by Liang et al. for carbon nanotube-supported Pd/ZnO catalysts [87]. Nevertheless, at relatively low reaction conditions the activity of the current catalyst system was slightly lower as compared to that reported by Baltes et al. for methanol synthesis over CuO/ZnO/Al_2O_3 catalysts [280].

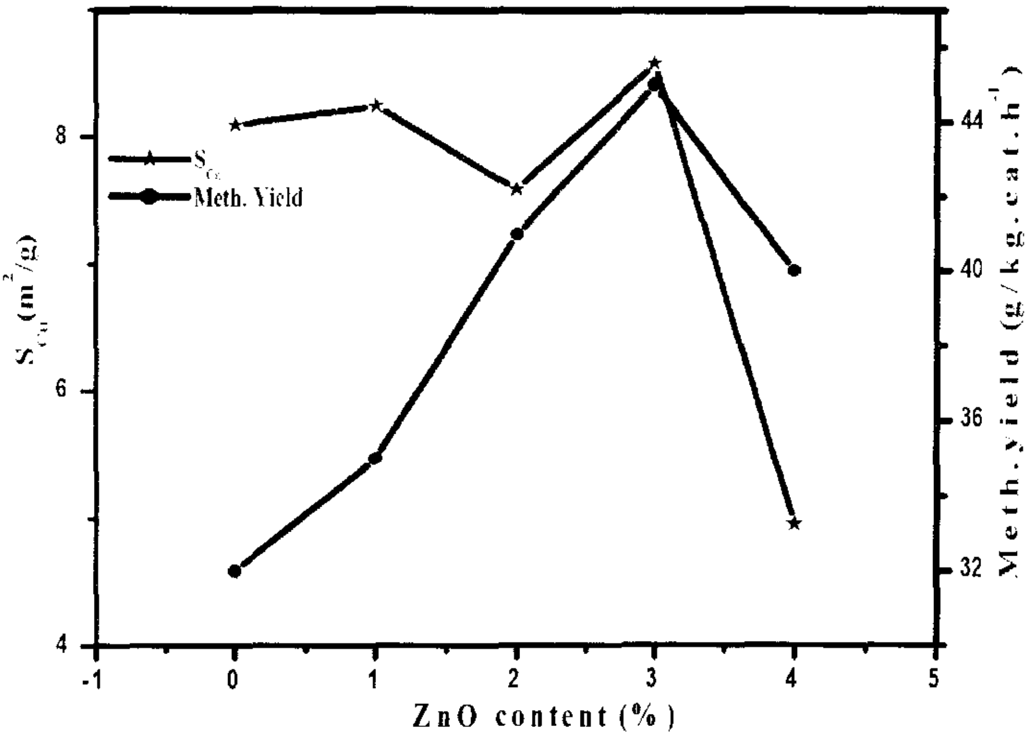

Figure 4.66: correlation of Zn content, Cu surface area and methanol yield

The correlation of ZnO concentration, variation in Cu surface area, and methanol activity are depicted in Figure 4.66. Copper surface area slightly increased with the incorporation of ZnO to the parent catalysts. Consequently, the methanol synthesis rate was also enhanced. Optimum amount of S_{Cu} was recorded for CZC catalyst with 3 wt.% of ZnO content. Similarly, the highest activity was observed for the same catalyst. The decline of methanol activity with maximum ZnO content could be understood by the corresponding decrease in copper surface area.

Table 4.42: Comparative study of the current catalyst for CO_2 hydrogenation to methanol with the literature data

Catalyst	**Reaction conditions**	**Methane activity (g/kg.h)**	**CO_2 conversion (%)**	**Ref.**
CZCZ3	(180°C & 30 bar)	45	9	This work
Pd/ZnO/CNTs	(250°C & 30 bar)	37	6.3	[87]
Pd/ZnO/Al_2O_3	(250°C & 30 bar)	24	4.4	[87]
Pd/ZnO/AC	(250°C & 30 bar)	28	4.9	[87]
Ag/ZrO_2	(230°C & 80 bar)	27	-	[84]
Cu/B_2O_3/ZrO_2	(250°C & 20 bar)	57	16	[93]
Cu/Ga_2O_3/ZrO_2	(250°C & 20 bar)	62	13.7	[93]
Cu/ZnO/ZrO_2	(220°C & 80 bar)	40	2	[278]
Au/ZnO/ZrO_2	(220°C & 80 bar)	19	2	[278]
Ag/ZnO/ZrO_2	(220°C & 80 bar)	15	2	[278]
Cu/ZrO_2	(200°C & 9 bar)	23	1.7	[91]
Cu/ZrO_2/ZnO	(200°C & 9 bar)	48	5.8	[91]
Cu/Zn/SiO_2	(270°C & 20 bar)	62	1.8	[92]
Cu/Zn-Ga/SiO_2	(270°C & 20 bar)	70	3.4	[92]
Cu/ZnO	(180°C & 20 bar)	38	2	[341]
Cu/ZnO.0015 chitosan	(180°C & 20 bar)	70	5	[341]
Cu/ZnO.0030 chitosan	(180°C & 20 bar)	62	3.8	[341]
Cu/ZnO.0045 chitosan	(180°C & 20 bar)	50	3.7	[341]
Ag/Zn	(200°C & 80 bar)	15	-	[84]
Ag/Zn/Zr	(200°C & 80 bar)	23	-	[84]
Cu/Zr	(200°C & 80 bar)	7	-	[84]
Cu/Zn/Zr	(200°C & 80 bar)	42	-	[84]
Cu/ZrO_2	(220°C & 90 bar)	33	-	[342]

Table 4.42 (Continue)

$Cu/Zn/Cr_2O_3$	(195°C & 10 bar)	2.1	-	[105]
$Cu/Zn/Al_2O_3$	(195°C & 10 bar)	4.5	-	[105]
Pd/CeO_2	(195°C & 10 bar)	22	-	[343]
Pd/TiO_2	(195°C & 10 bar)	32	-	[344]
$Pt\text{-}W/SiO_2$	(230°C & 30 bar)	28	-	[345]
$Pt\text{-}Cr/SiO_2$	(200°C & 30 bar)	8.8	-	[345]
$Ag/ZnO/Al_2O_3$	(250°C & 50 bar)	82	-	[29]
$Ag/ZnO\text{-}Ga_2O_3/Al_2O_3$	(250°C & 50 bar)	126	-	[29]
Au/ZnO	(300°C & 50 bar)	51	-	[346]
Pd/SiO_2	(250°C & 41 bar)	10	3	[347]
Cu/SiO_2	(250°C & 41 bar)	6	2.8	[347]
$Cu\text{-}Pd/SiO_2$	(250°C & 41 bar)	35	6.6	[347]
Cu-Pd/MCM-41	(250°C & 41 bar)	21	6.2	[347]
Cu-Pd/SBA-15	(250°C & 41 bar)	23	6.5	[347]
Cu-Pd/MSU-F	(250°C & 41 bar)	13	5.3	[347]
$Cu\text{-}ZnO/Al_2O_3$	(250°C & 41 bar)	55	18.2	[347]
Cu/Zn/Ga	(250°C & 30 bar)	32	3.37	[185]
$Cu(ZnGa)_{MW}$	(250°C & 30 bar)	40	5.48	[185]
$Cu_{MW}(ZnGa)_{MW}$	(250°C & 30 bar)	61	4.48	[185]
Cu	(250°C & 20 bar)	8	9	[348]
Cu/ZnO	(250°C & 20 bar)	11	9	[348]
Cu/ZrO_2	(250°C & 20 bar)	8.7	9	[348]
$Cu/ZnO/ZrO_2$	(250°C & 20 bar)	20	11	[348]
$Cu\text{-}ZnO\text{-}ZrO_2\text{-}MgO/Al_2O_3$	(250°C & 20 bar)	31	12	[348]
$Cu\text{-}ZnO/CeZrO_2$	(250°C & 20 bar)	137	15	[349]
$Cu\text{-}Zn/ZrO_2$- CB	(180°C & 30 bar)	88	3	[186]
$Cu\text{-}Zn/ZrO_2$- CT	(180°C & 30 bar)	60	2	[186]
$Cu\text{-}Zn/ZrO_2$- OX	(180°C & 30 bar)	100	4	[186]

Table 4.42 (Continue)

Cu/Zn/Al/Zr-F	(250°C & 50 bar)	390	22	[350]
La-Cu/ZnO	(250°C & 50 bar)	50	6	[233]
La-Y-Cu/ZnO	(250°C & 50 bar)	40	5	[233]
La-Ce-Cu/ZnO	(250°C & 50 bar)	80	8	[233]
La-Mg-Cu/ZnO	(250°C & 50 bar)	90	9	[233]
La-Zr-Cu/ZnO	(250°C & 50 bar)	100	13	[233]
Cu/ZnO	(240°C & 30 bar)	240	11	[351]
Cu/ZnO	(250°C & 30 bar)	51	12	[352]
Cu-Zn-Zr/Al_2O_3	(250°C & 50 bar)	140	23	[353]
commercial Cu/ZnO/Al_2O_3	(210°C & 50 bar)	32	-	[354]
Cu/ZrO_2	(250°C & 30 bar)	116	1	[355]
Cu/Ga_2O_3	(250°C & 30 bar)	84	1	[355]
Cu/Ga_2O_3/ZrO_2	(250°C & 30 bar)	131	1	[355]

4.7 Kinetic study

Kinetic study of the CO_2 hydrogenation to methanol was conducted in a slurry reactor. The reaction of CO_2 hydrogenation is depicted in the following.

$$CO_2 + 3H_2 \underset{k_2}{\overset{k_1}{\rightleftarrows}} CH_3OH + H_2O \qquad (4.1)$$

To determine the kinetics of CO_2 hydrogenation reaction, it was assumed ~~had been~~ supposed that the concentration of hydrogen was an excess and did not affect the rate of reaction. It was further assumed that water formation had been negligible.

The concentration ratio M $= \dfrac{C_{CHOH}o}{C_{CO_2}0}$, the rate reaction is

$$\frac{dC_{CH_3OH}}{dt} = -\frac{dC_{CO_2}}{dt} = C_{CO_2}o\frac{dX_{CO_2}}{dt} = k_1C_{CO_2} - k_2C_{CH_3OH} \qquad (4.2)$$
$$= k_1(C_{CO_2}o - C_{CO_2}oX_{CO_2}) - k_2(MC_{CO_2}o + C_{CO_2}oX_{CO_2})$$

Where $C_{CO_2}o$, $C_{CH_3OH}o$, $X_{CO_2}e$, $C_{CHOH}e$ and X_{CO_2} is the CO_2 initial concentration, CH_3OH initial concentration, CO_2 equilibrium concentration, CH_3OH equilibrium concentration and fraction of CO_2 conversion, respectively. Calculations for CO_2 concentration and CO_2 conversion versus reaction time at different reaction temperature are shown in Appendix C section C2 and Figure C1, respectively.

$$K_C = \frac{C_{CHOH}e}{C_{CO_2}e} = \frac{M + X_{CO_2}e}{1 - X_{CO_2}e} \qquad (4.3)$$

The equilibrium constant K_C is given as

$$K_C = \frac{k_1}{k_2} \qquad (4.4)$$

Combining equations 4.2, 4.3 and 4.4, the equilibrium conversion is given as

$$\frac{dX_{CO_2}}{dt} = \frac{k_1(M+1)}{M+X_{CO_2}e}(X_{CO_2}e - X_{CO_2}) \qquad (4.5)$$

Integrating equation 4.5 we get

$$-\ln\left(1-\frac{X_{CO_2}}{X_{CO_2}e}\right) = -\ln\frac{C_{CO_2}-C_{CO_2}e}{C_{CO_2}o-C_{CO_2}e} = \frac{M+1}{M+X_{CO_2}e}k_1 t \qquad (4.6)$$

A plot of -ln(1-XCO_2/XCO_2e) versus reaction time had been plotted at different reaction temperatures to give a straight line (Figure 4.67). Therefore, this supported the hypothesis that the reaction is of pseudo-first order.

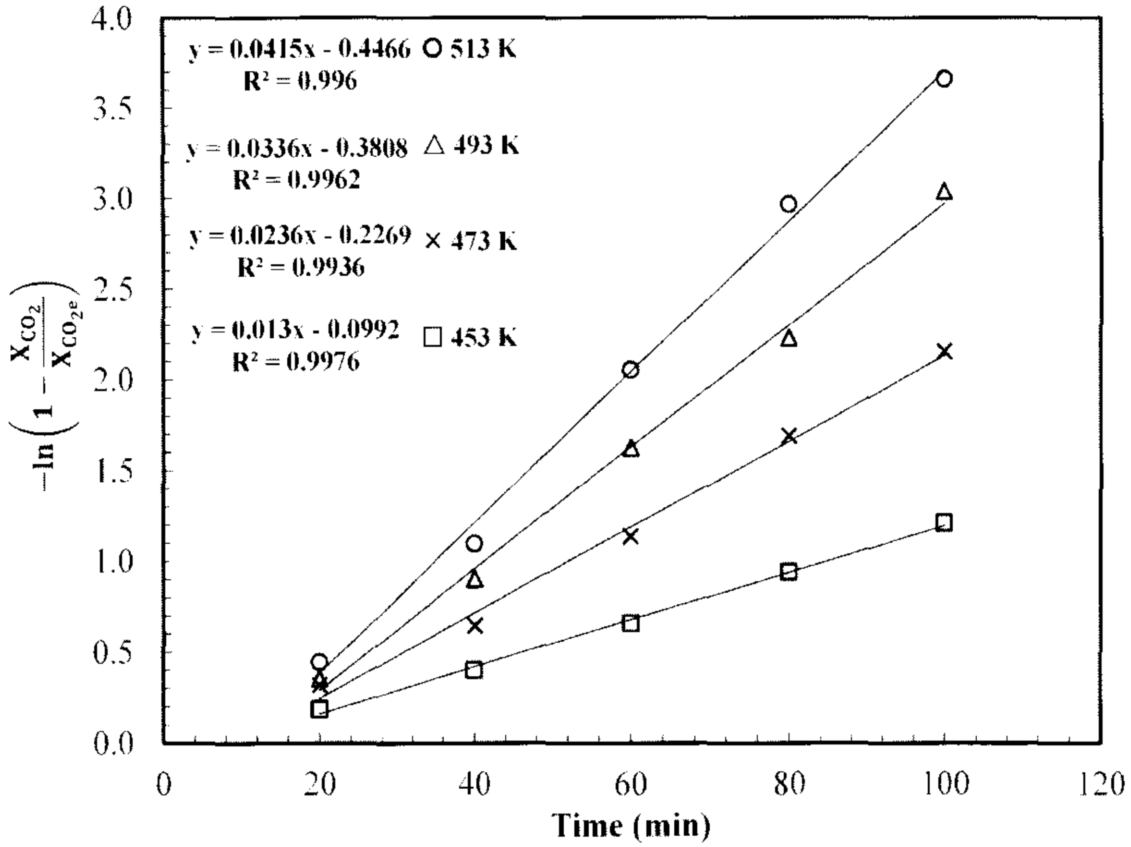

Figure 4.67: Plots of –ln (1-XCO_2/ XCO_2e) versus reaction time at different temperatures

All the plots between the -ln(1-X_{CO_2}/X_{CO_2e}) verses time at different reaction temperatures are linear with slope of $k_1\frac{M+1}{M+X_{Ae}}$ .Rate constant k_1 was obtained from the slope of each curve plotted at different temperature, their magnitudes are shown in Table 4.43.

Table 4.43: Rate constants at different reaction temperature

Reaction temperature (K)	**Rate constant k_1**
453	0.0015
473	0.0033
493	0.0055
513	0.008

4.7.1 Activation energy

The activation energy (Ea) was calculated based on the Svante Arrhenius equation, as represented in Eq. 4.7.

$$k_1 = Ae^{-\frac{Ea}{RT}} \tag{4.7}$$

Where k1 is the rate constants, representing the number of collisions among the reactants that result in a reaction (effective collisions), A is the pre-exponential factor or simply the pre-factor, which represents the total number of collisions (leading to reaction or not), R is the universal gas constant, and Ea is the activation energy, which is necessary for a chemical reaction to occur.

Taking integration of Eq. (4.7), we get,

$$lnk_1 = lnA - \frac{Ea}{R} \cdot \frac{1}{T} \tag{4.8}$$

The activation energy was calculated by plotting lnk1 versus 1/T x 103 (K^{-1}) at different temperatures, as presented in Figure 4.67.

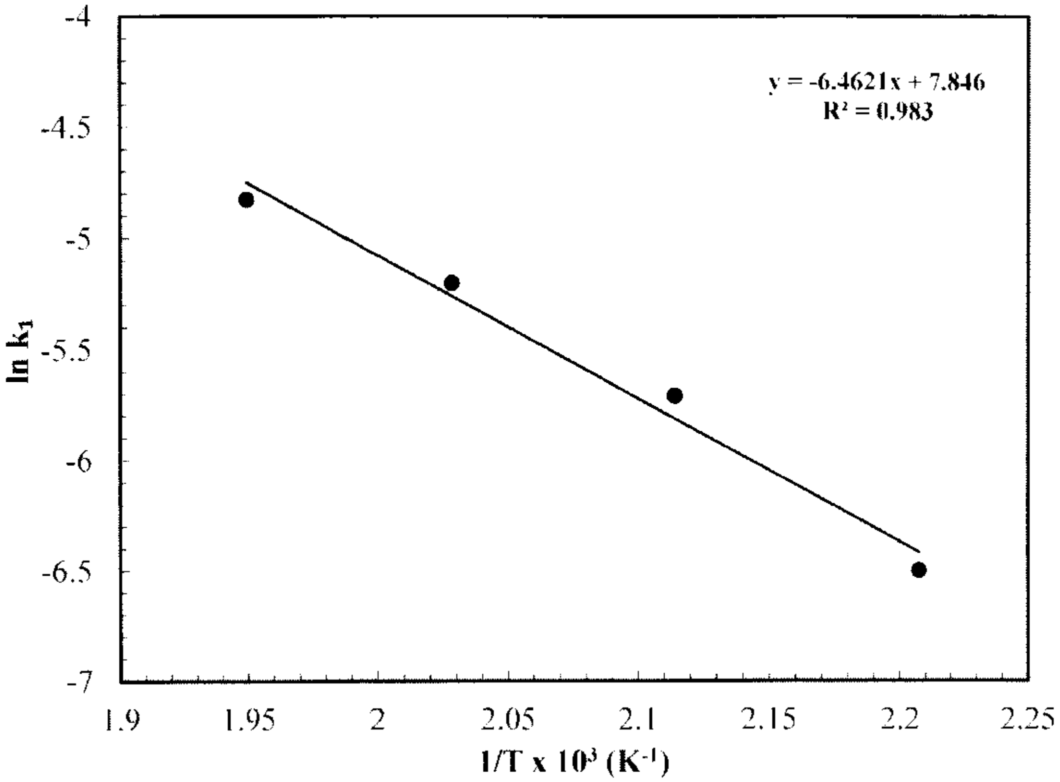

Figure 4.68: Arrhenius plot of CO_2 hydrogenation

Arrhenius plot CO_2 hydrogenation is displayed in Figure 4.68. Activation energy was calculated from the Arrhenius plot in kinetic regime of the reaction. A magnitude of activation energy 51 kJ/mole was obtained for CO_2 hydrogenation. Different values of activation energies, as reported in the literature, are documented in Table 4.44. The magnitude of activation energy in the current study fell within the range of reported value for the same reaction.

Table 4.44: Activation energy of CO_2 hydrogenation

Catalyst	**Activation energy (kJ/mole)**	**Reference**
$Cu/ZrO_2/CNFs$	51	This work
$Cu/ZnO/Al_2O_3$	57	[356]
C301 Cu-Based Catalyst ($Cu/ZnO/Al_2O_3$)	14	[357]
$Cu/ZnO/Al_2O_3$	7	[358]

4.7.2 Reaction temperature

The rate of methanol synthesis was studied in slurry reactor at fixed pressure of 30 bar in a range of 180-240 °C. The correlation of reaction temperature and methanol synthesis rate is displayed by Figure 4.69. The effect of reaction temperature on the CO_2 hydrogenation can be better understood by taking into account three main reactions as under.

$$CO_2 + 3H_2 \rightleftharpoons CH_3OH + H_2O \qquad \Delta H^0{}_{298K} = -49.5\ kJ/mol \qquad (4.9)$$

$$CO_2 + H_2 \rightleftharpoons CO + H_2O \qquad \Delta H^0{}_{298K} = +41.2\ kJ/mol \qquad (4.10)$$

$$CH_3OH \rightleftharpoons CO + 2H_2 \qquad \Delta H^0{}_{298K} = +90.64\ kJ/mol \qquad (4.11)$$

As CO_2 hydrogenation to methanol has exothermic reaction (reaction 4.9), so thermodynamically, it is favorable at low temperature. However, due to higher stability of CO_2, some adequate energy is required to overcome the energy barrier. Moreover, the rate of methanol synthesis increases kinetically with the increase in reaction temperature. Therefore, the methanol productivity is controlled by both kinetics, as well as thermodynamics. A maximum methanol synthesis rate is obtained by the critical point, where the reaction is transformed from kinetics to thermodynamics. This critical point of reaction depends on a number of reaction reactivity factors like the nature of catalyst, the number of active sites, and the exposure of active sites to the reacting molecules. Therefore, literature regarding critical point is not univocal and different

explain

degrees of temperature are reported by different catalysts and operating systems. Similarly, reverse water gas shift reaction (RWGS) is also associated with the main CO_2 hydrogenation to methanol (reaction 4.10). As RWGS is exothermic in nature, so rise in reaction temperature facilitates this reaction. Likewise, increase in reaction temperature can also bring about the decomposition of methanol to CO, as evident by reaction 4.11. In the current case, methanol synthesis rate was increased with the increase in reaction temperature. The optimum rate was observed at 220 °C before it was declined at the highest reaction temperature of 240 °C. A similar trend of reaction temperature and methanol synthesis rate was also recorded by Xin et al., over Cu/Zn/Al/Zr fibrous catalyst [202]. Recent investigations of methanol yield as a function of reaction temperature also revealed a similar dependency of methanol synthesis by CO_2 hydrogenation route [102]. The decline of methanol synthesis rate at the highest reaction temperature could be due to the selectivity of RWGS reactions. This can also be further justified by the fact that RWGS reactions has higher apparent activation energy as compared to the methanol formation [95, 359]. Therefore, the CO formation rate had been faster compared to methanol formation at higher reaction temperature. Likewise, the decomposition of methanol to CO at higher reaction temperature could also be one of the reasons of decrease in methanol synthesis rate.

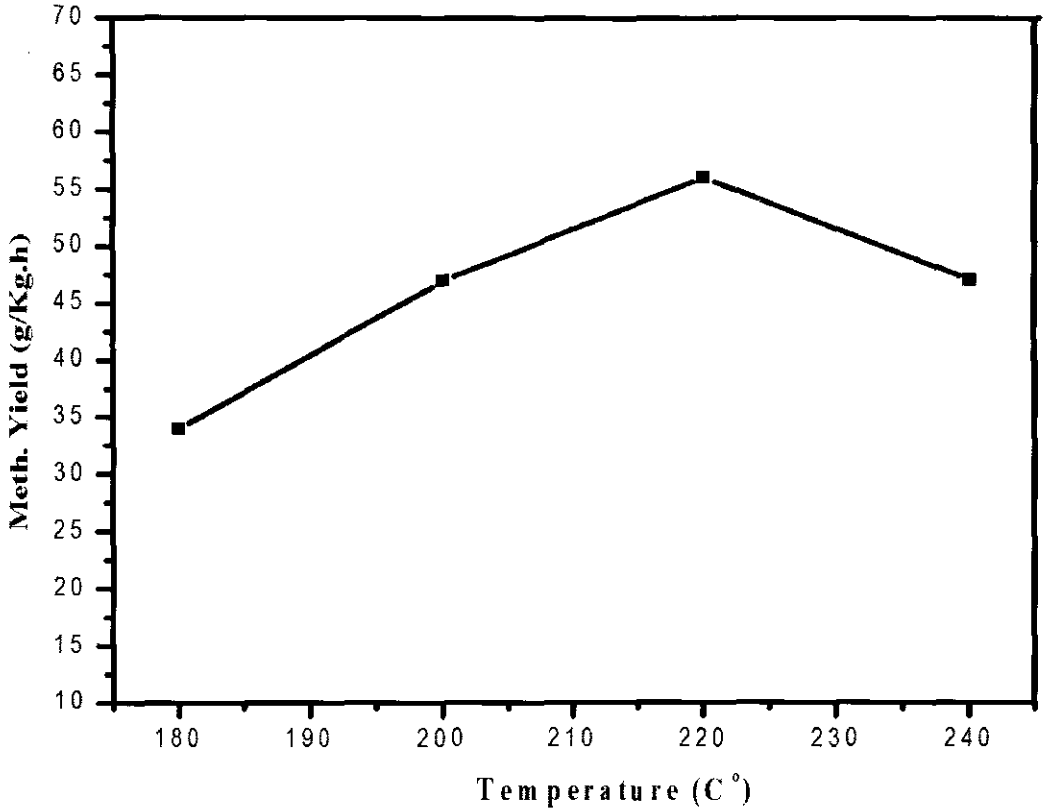

Figure 4.69: Correlation of reaction temperature and methanol synthesis rate

4.7.3 Effect of pressure

Methanol synthesis by CO_2 hydrogenation was also studied at different pressures like 20, 30, and 40 bar. Figure 4.70 shows the correlation of reaction pressure and methanol synthesis rate. As observed, the CO_2 hydrogenation to methanol is a molecule reducing reaction (reaction 7.1), so, thermodynamically it is best facilitated at higher pressure. In the current study, a linear relationship was observed between pressure and methanol synthesis rate. Methanol synthesis rate increased from 45 to 57 g/kg. h when pressure was increased from 20 to 30 bar. A similar trend of increasing rate was continued with further rise in pressure and maximum rate was obtained with the highest reaction pressure.

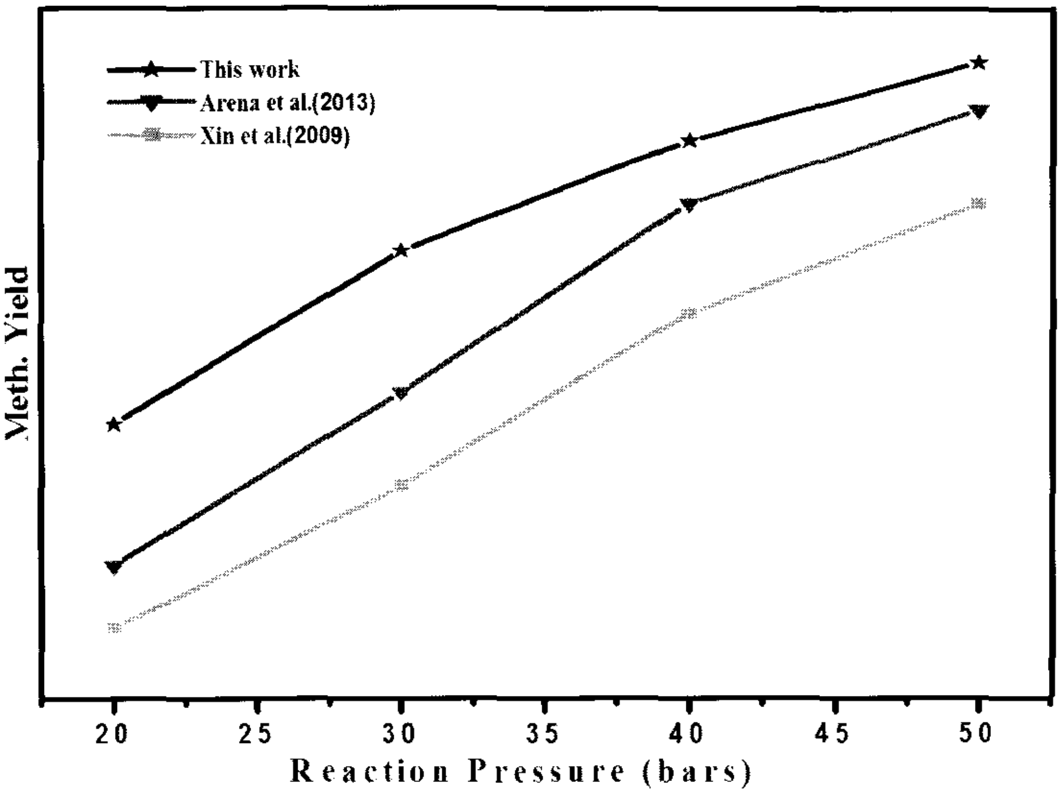

Figure 4.70: Correlation of reaction pressure and methanol synthesis rate

These observations were in good agreement with the work of Arena et al., and Xin et al. [8, 202]. Thermodynamically, the process had been faster at higher reaction pressure. However, too high pressure demands higher requirement of materials strength, high cost of operation, and it is associated with safety problems.

4.7.4 Feed gas composition

CO_2 hydrogenation to methanol was also studied by varying feed gas composition. Figure 4.71 displays the rate of methanol synthesis as a function of increasing H_2/CO_2 ratio. The rate of methanol synthesis increased from 32 to 41 g/kg. h when the H_2/CO_2 ratio was increased from 0.8 to 1.5. Similar trend was also observed with further increase in H_2/CO_2 ratio. This trend is quite instable if the stoichiometric chemistry of CO_2 hydrogenation is considered.

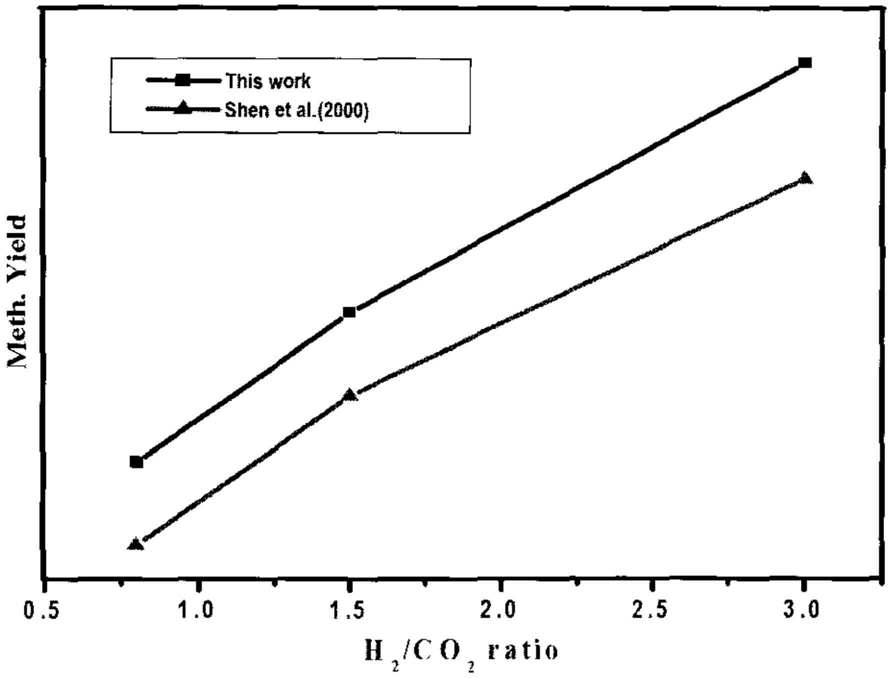

Figure 4.71: Correlation of H_2/CO_2 ratio and methanol synthesis rate

As evident from equation 4.10, the H_2/CO_2 ratio of unity had been favorable for the formation of CO as the main product. However, the rate of methanol synthesis was enhanced by increasing H_2/CO_2 ratio. This could be justified by equation 4.9, where higher H_2/CO_2 ratio was desirable for better methanol yield. This could be one of the reasons of lower activity of catalyst to methanol synthesis with H_2/CO_2 ratio < 3.0. In addition, Shen et al., reported similar observations for methanol synthesis via CO_2 hydrogenation over $Cu/Zr/Al_2O_3$ catalyst [208].

4.7.5 Artificial neural networks modeling

Artificial neural networks (ANN) model was utilized to study the kinetics of CO_2 hydrogenation to methanol. Feed-forward back propagation network type of network was used for the data evaluation. Experimental data was evaluated by four different algorithms, namely trainlm, trainbr, traingda, and traingdm. The model was fed with three inputs (Reaction temperature, pressure, and time interval) and a single target value as methanol synthesis rate of the reaction data.

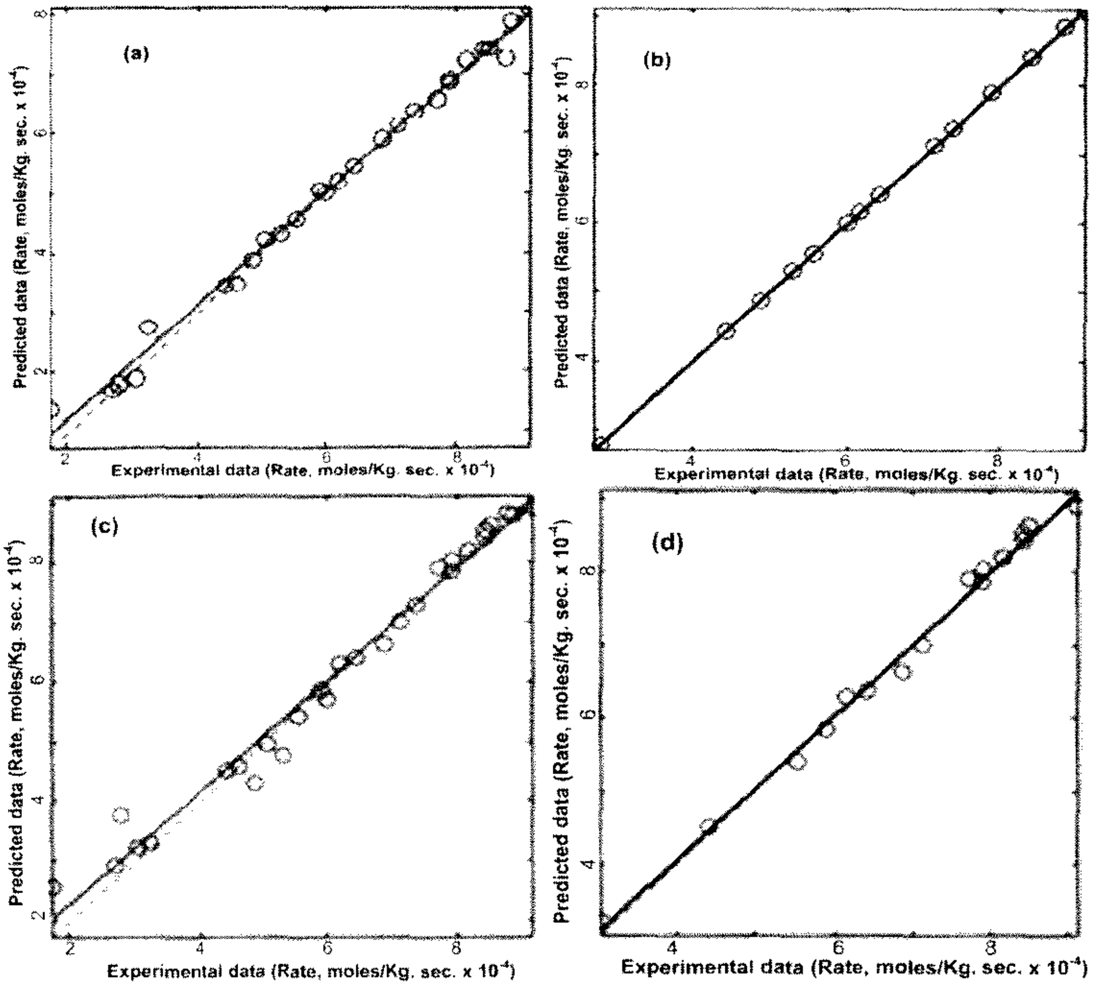

Figure 4.72: Predicted results versus experimental data for (a) LM, (b) SCG (c) BR and (d) GDA algorithm with ten neurons in the hidden layer

As it is evident from Figure 4.72, the experimental data versus predicted data for all selected algorithms showed good agreement. This indicated excellent accuracy of the neural network in estimating the reaction rate in methanol synthesis via CO_2 hydrogenation. Recently, Amini et al., [360] investigated the effects of oxygenated additives in propane dehydrogenation over Pt–Sn/ć-Al_2O_3 catalyst. Hence, ANN model was employed for the conversion of propane with 11 neurons in the hidden layer. The experimental data of propane conversion fitted best with the model predicted data.

CHAPTER 5

CONCLUSION AND FUTURE RECOMMENDATIONS

5.1 Conclusion

In this work, CNFs based Cu/ZrO_2 catalysts were developed for investigating CO_2 hydrogenation to methanol in a three phase reactor. The study began with the activation of catalyst support to create new functional groups (OH, C=O etc.) on the surface of CNFs. The presence of functional groups on the surface of CNFs was confirmed by FT-IR, XPS, TGA and BET techniques. CNFs based Cu/ZrO_2 catalysts were successfully synthesized by deposition precipitation method. The synthesized catalysts were characterized by various techniques. Activity studies were conducted in high pressure autoclave (Parr 4593 with a regulator Parr 4848) reactor. First, the composition of the catalyst was optimized in terms of Cu concentration. In this context, CNFs based Cu/ZrO_2 catalysts with different Cu concentrations were prepared via deposition precipitation method. Variation in Cu content affected both physiochemical properties, as well as activity profiles of catalyst, remarkably. Physiochemical investigation suggested 15 wt.% of Cu as the optimum amount for the studied catalysts. Reactions studies further validated the characteristic data by providing maximum methanol productivity rate for catalyst with 15 wt.% content. After optimization of Cu content, the catalyst was loaded with different concentrations of ZrO_2. The number of total basic sites was increased by increasing zirconia content. Activity of catalyst was enhanced with the addition of ZrO_2 to the parent catalysts and optimum activity was recorded for catalysts with 15 wt.% of ZrO_2 content. After optimization of active sites, the optimized catalyst was investigated for a suitable calcination temperature. Investigations studies for calcination temperature were conducted by calcining the screened catalysts in terms of both active components at different temperatures like 350, 450, 500, and 550 °C. Variation in the degree of calcination temperature affected both physiochemical properties, as well as activity profiles of catalyst, remarkably. Meanwhile, surface area and fraction of dispersed Cu were enhanced when calcination temperature was raised from 350 to 450 °C, which resulted in better performance of the catalyst. Nevertheless, growth and sintering of catalyst particles and reduction of both S_{Cu} and S_{BET} surface area at elevated calcination temperature led to depress the overall activity of $Cu.ZrO_2$/CNFs catalyst for methanol synthesis in slurry reactor. A linear relationship between catalyst activity towards CO_2 conversion and its S_{Cu} was observed. After identifying the optimum calcination temperature, parent catalyst was introduced with different promoters in order to investigate the effect of the promoter on the catalyst for methanol synthesis via CO_2 hydrogenation. Incorporation of Nb_2O_5 promoter to the parent catalyst remarkably increased surface area of metallic copper. Likewise, introduction of Nb_2O_5 promoter to the parent catalyst enhanced the activity of catalyst and optimum activity was recorded with 0.8 wt.% of Nb_2O_5 oxide concentration. Besides, the incorporation of ZnO improved the rate of methanol synthesis and the maximum rate was recorded with CZC catalyst with 3 wt.% of ZnO. However, CO_2 hydrogenation was adversely proportional to the addition of ZnO loadings. The most efficient catalyst was found with composition of Cu (15 wt.%)-ZrO_2 (15 wt.%)-ZnO (3 wt.%)/CNFs having methanol synthesis rate of 45 g/kg.cat.h and 9 % CO_2 conversion.

Furthermore, kinetic studied revealed that CO_2 hydrogenation to methanol follows the pseudo first order kinetics. Similarly, CO_2 hydrogenation to methanol was also investigated in terms of reaction variables. Methanol synthesis rate was significantly altered with variation in reaction temperature. Methanol synthesis rate was initially increased with a rise in the reaction temperature and the highest rate was observed at 220 °C before it declined with further increase in temperature. Likewise, the influence of reaction pressure was investigated by conducting the methanol synthesis at different magnitudes of total pressure. It was concluded from the pressure variation study that the rate of methanol synthesis progressively enhanced as a function of increasing total pressure. Finally, the methanol synthesis rate was also optimized in terms of feed gas ratio. The study concluded that a linear relationship existed between the rate of methanol synthesis and the increasing H_2/CO_2 ratio.

5.2 Future recommendations

Based on the above conclusion, future work in this regard is recommended as

- Bimetallic catalysts were prepared by deposition precipitation methods. Other preparation methods could also be employed to investigate the dispersion and interaction of metals on the surface of CNFs
- Besides ZnO and Nb_2O_5, the catalyst could be tested for the title reaction with other promoters
- In order to understand the reaction pathway, the in-depth mechanistic study of the title reaction should be performed
- The title reaction could be tested in the slurry reactor by incorporating other active metals like Pd metal to the parent catalyst

REFERENCES

[1] K. Kochloefl, *Steam Reforming, in Handbook of Heterogeneous Catalysis* vol. 04: Wiley-VCH GmbH, Weinheim, 1997.

[2] F. Arena, K. Barbera, G. Italiano, G. Bonura, L. Spadaro, and F. Frusteri, "Synthesis, characterization and activity pattern of Cu–ZnO/ZrO2 catalysts in the hydrogenation of carbon dioxide to methanol," *Journal of Catalysis,* vol. 249, pp. 185-194, 2007.

[3] G. C. Chinchen, P. J. Denny, J. R. Jennings, M. S. Spencer, and K. C. Waugh, "Synthesis of Methanol: Part 1. Catalysts and Kinetics," *Appl. Catal.,* vol. 36, pp. 1-65, 1988.

[4] J. C. J. Bart and R. P. A. Sneeden, "Copper-zinc oxide-alumina methanol catalysts revisited," *Catal. Today,* vol. 2, pp. 1-124, 1987.

[5] F. Arena, G. Italiano, K. Barbera, S. Bordiga, G. Bonura, L. Spadaro, *et al.*, "Solid-state interactions, adsorption sites and functionality of Cu-ZnO/ZrO_2 catalysts in the CO_2 hydrogenation to CH_3OH," *Appl. Catal., A,* vol. 350, pp. 16-23, 2008.

[6] M. S. Israf Ud Din, Duvvuri Subarao, Abdul Naeem, "Homogeneous Deposition Precipitation Method for Synthesis of Carbon Nanofibre Based Cu-ZrO_2 Catalyst for Hydrogenation of CO_2 to Methanol," *Applied Mechanics and Materials* vol. 246, pp. 83-87, 2014.

[7] J. Weigel, R. A. Koeppel, A. Baiker, and A. Wokaun, "Surface Species in CO and CO_2 Hydrogenation over Copper/Zirconia: On the Methanol Synthesis Mechanism," *Langmuir,* vol. 12, pp. 5319-5329, 1996.

[8] F. Arena, G. Mezzatesta, G. Zafarana, G. Trunfio, F. Frusteri, and L. Spadaro, "Effects of oxide carriers on surface functionality and process performance of the Cu–ZnO system in the synthesis of methanol via CO_2 hydrogenation," *J. Catal.,* vol. 300, pp. 141-151, 2013.

[9] Q.-Y. Sun, L.-W. Ding, G. P. Lomonossoff, Y.-B. Sun, M. Luo, C.-Q. Li, *et al.*, "Improved expression and purification of recombinant human serum albumin from transgenic tobacco suspension culture," *Journal of Biotechnology,* vol. 155, pp. 164-172, 2011.

[10] L. C. Grabow and M. Mavrikakis, "Mechanism of methanol synthesis on cu through CO 2 and CO hydrogenation," *ACS Catalysis,* vol. 1, pp. 365-384, 2011.

[11] S. Zander, "Preparation and characterization of Cu/ZnO catalysts for methanol synthesis," PhD, Technische Universität Berlin, 2013.

[12] X.-M. Liu, G. Q. Lu, Z.-F. Yan, and J. Beltramini, "Recent Advances in Catalysts for Methanol Synthesis via Hydrogenation of CO and CO_2," *Ind. Eng. Chem. Res.,* vol. 42, pp. 6518-6530, 2003.

[13] Z.-J. Zuo, L. Wang, P.-D. Han, and W. Huang, "Methanol synthesis by CO and CO_2 hydrogenation on Cu/γ-Al_2O_3 surface in liquid paraffin solution," *Appl. Surf. Sci.,* vol. 290, pp. 398-404, 2014.

[14] G. A. Olah, "After oil and gas: methanol economy," *Catal. Lett.,* vol. 93, pp. 1-2, 2004.

[15] C. Yang, Z. Ma, N. Zhao, W. Wei, T. Hu, and Y. Sun, "Methanol synthesis from CO_2-rich syngas over a ZrO_2 doped CuZnO catalyst," *Catal. Today,* vol. 115, pp. 222-227, 2006.

[16] D. J. F. Myles R. Allen, Chris Huntingford, Chris D. Jones, Jason A. Lowe, Malte Meinshausen, Nicolai Meinshausen, "Warming caused by cumulative carbon emissions towards the trillionth tonne," *Nature* vol. 458, pp. 1163-1166, 2009.

[17] M. Eby, K. Zickfeld, A. Montenegro, D. Archer, K. J. Meissner, and A. J. Weaver, "Lifetime of Anthropogenic Climate Change: Millennial Time Scales of Potential CO_2 and Surface Temperature Perturbations," *Journal of Climate,* vol. 22, pp. 2501-2511, 2009.

[18] F. J. Thomas L. Frölicher, "Reversible and irreversible impacts of greenhouse gas emissions in multi-century projections with the NCAR global coupled carbon cycle-climate model," *Climate Dynamics,* vol. 35, pp. 1439-1459, 2010.

[19] V. K. A. Nathan P. Gillett, Kirsten Zickfeld,Shawn J. Marshal & William J. Merryfield, "Ongoing climate change following a complete cessation of carbon dioxide emissions," *NATURE GEOSCIENCE,* vol. 4, pp. 83-87, 2011.

[20] M. Saito, T. Fujitani, M. Takeuchi, and T. Watanabe, "Development of copper/zinc oxide-based multicomponent catalysts for methanol synthesis from carbon dioxide and hydrogen," *Appl. Catal., A,* vol. 138, pp. 311-318, 1996.

[21] T. Inui, H. Hara, T. Takeguchi, and J.-B. Kim, "Structure and function of Cu-based composite catalysts for highly effective synthesis of methanol by hydrogenation of CO_2 and CO," *Catal. Today,* vol. 36, pp. 25-32, 1997.

[22] K. Fujimoto and Y. Yu, "Spillover effect on the stabilization of Cu-Zn catalyst for CO_2 hydrogenation to methanol," in *Stud. Surf. Sci. Catal.* vol. Volume 77, K. F. T. U. T. Inui and M. Masai, Eds., ed: Elsevier, 1993, pp. 393-396.

[23] A. T. Aguayo, J. Ereña, D. Mier, J. M. Arandes, M. Olazar, and J. Bilbao, "Kinetic Modeling of Dimethyl Ether Synthesis in a Single Step on a $CuO-ZnO-Al_2O_3/\gamma-Al_2O_3$ Catalyst," *Ind. Eng. Chem. Res.,* vol. 46, pp. 5522-5530, 2007.

[24] J. Ereña, R. Garoña, J. M. Arandes, A. T. Aguayo, and J. Bilbao, "Effect of operating conditions on the synthesis of dimethyl ether over a CuO-ZnO-Al_2O_3/NaHZSM-5 bifunctional catalyst," *Catal. Today,* vol. 107–108, pp. 467-473, 2005.

[25] I. A. Fisher and A. T. Bell, "In-SituInfrared Study of Methanol Synthesis from H_2/CO_2 over Cu/SiO_2 and $Cu/ZrO_2/SiO_2$," *J. Catal.,* vol. 172, pp. 222-237, 1997.

[26] D. Bianchi, T. Chafik, M. Khalfallah, and S. J. Teichner, "Intermediate species on zirconia supported methanol aerogel catalysts: III. Adsorption of carbon monoxide on copper containing solids," *Appl. Catal., A,* vol. 112, pp. 57-73, 1994.

[27] J. Wambach, A. Baiker, and A. Wokaun, "CO_2 hydrogenation over metal/zirconia catalysts," *PCCP,* vol. 1, pp. 5071-5080, 1999.

[28] C. Li, X. Yuan, and K. Fujimoto, "Development of highly stable catalyst for methanol synthesis from carbon dioxide," *Appl. Catal., A,* vol. 469, pp. 306-311, 2014.

[29] S. Sugawa, K. Sayama, K. Okabe, and H. Arakawa, "Methanol synthesis from CO_2 and H_2 over silver catalyst," *Energy Convers. Manage.*, vol. 36, pp. 665-668, 1995.

[30] J. Toyir, P. R. r. de la Piscina, J. L. G. Fierro, and N. s. Homs, "Highly effective conversion of CO_2 to methanol over supported and promoted copper-based catalysts: influence of support and promoter," *Appl. Catal., B*, vol. 29, pp. 207-215, 2001.

[31] R. Takahashi, S. Sato, T. Sodesawa, M. Yoshida, and S. Tomiyama, "Addition of zirconia in Ni/SiO_2 catalyst for improvement of steam resistance," *Appl. Catal., A*, vol. 273, pp. 211-215, 2004.

[32] S. Iijima, "Helical microtubules of graphitic carbon," *Nature*, vol. 354, pp. 56-58, 1991.

[33] F. Salman, C. Park, and R. T. K. Baker, "Hydrogenation of crotonaldehyde over graphite nanofiber supported nickel," *Catal. Today*, vol. 53, pp. 385-394, 1999.

[34] C. Park and R. T. K. Baker, "Catalytic Behavior of Graphite Nanofiber Supported Nickel Particles. 2. The Influence of the Nanofiber Structure," *The Journal of Physical Chemistry B*, vol. 102, pp. 5168-5177, 1998.

[35] J. H. Bitter, J. K. P. De, D. L. M. K. Van, and D. A. J. Van, "Carbon nanofibre composites, preparation and use," ed: Google Patents, 2005.

[36] J. K. Chinthaginjala, K. Seshan, and L. Lefferts, "Preparation and Application of Carbon-Nanofiber Based Microstructured Materials as Catalyst Supports," *Ind. Eng. Chem. Res.*, vol. 46, pp. 3968-3978, 2007.

[37] J. L. B. F. Nelize Maria de Almeida Coelhoa, Cuong Pham-Huub, Ricardo Vieiraa, "Carbon Nanofibers: a Versatile Catalytic Support," *Materials Research*, vol. 11, pp. 353-357, 2008.

[38] M.-J. Ledoux and C. Pham-Huu, "Carbon nanostructures with macroscopic shaping for catalytic applications," *Catal. Today*, vol. 102–103, pp. 2-14, 2005.

[39] C. P.-H. Marc-Jacques Ledoux, "Carbon nanostructures with macroscopic shaping for catalytic applications," *Catal. Today*, vol. 102-013, pp. 2-14, 2005.

[40] A. Chambers, T. Nemes, N. M. Rodriguez, and R. T. K. Baker, "Catalytic Behavior of Graphite Nanofiber Supported Nickel Particles. 1. Comparison with Other Support Media," *J. Phys. Chem. B*, vol. 102, pp. 2251-2258, 1998.

[41] C. Pham-Huu, N. Keller, G. Ehret, L. c. J. Charbonniere, R. Ziessel, and M. J. Ledoux, "Carbon nanofiber supported palladium catalyst for liquid-phase reactions: An active and selective catalyst for hydrogenation of cinnamaldehyde into hydrocinnamaldehyde," *J. Mol. Catal. A: Chem.*, vol. 170, pp. 155-163, 2001.

[42] I. P. P. V. V. Chesnokov, N. A. Zaitseva, V. I. Zaikovskii, V. V. Molchanov, "Effect of the Structure of Carbon Nanofibers on the State of an Active Component and on the Catalytic Properties of Pd/C Catalysts in the Selective Hydrogenation of 1,3-Butadiene," *Kinet. Catal.*, vol. 43, pp. 838-846, 2002.

[43] M. L. Toebes, Y. Zhang, J. Hájek, T. Alexander Nijhuis, J. H. Bitter, A. Jos van Dillen, *et al.*, "Support effects in the hydrogenation of cinnamaldehyde over carbon nanofiber-supported platinum catalysts: characterization and catalysis," *J. Catal.*, vol. 226, pp. 215-225, 2004.

[44] W. Wang, S. Wang, X. Ma, and J. Gong, "Recent advances in catalytic hydrogenation of carbon dioxide," *Chem. Soc. Rev.*, vol. 40, pp. 3703-3727, 2011.

[45] M. R. Rahimpour, "A two-stage catalyst bed concept for conversion of carbon dioxide into methanol," *Fuel Process. Technol.*, vol. 89, pp. 556-566, 2008.

[46] M. R. Rahimpour and K. Alizadehhesari, "Enhancement of carbon dioxide removal in a hydrogen-permselective methanol synthesis reactor," *Int. J. Hydrogen Energy*, vol. 34, pp. 1349-1362, 2009.

[47] R. P. W. J. Struis and S. Stucki, "Verification of the membrane reactor concept for the methanol synthesis," *Appl. Catal., A*, vol. 216, pp. 117-129, 2001.

[48] G. Chen and Q. Yuan, "Methanol synthesis from CO_2 using a silicone rubber/ceramic composite membrane reactor," *Sep. Purif. Technol.*, vol. 34, pp. 227-237, 2004.

[49] F. Gallucci, L. Paturzo, and A. Basile, "An experimental study of CO_2 hydrogenation into methanol involving a zeolite membrane reactor," *Chemical Engineering and Processing: Process Intensification*, vol. 43, pp. 1029-1036, 2004.

[50] F. Gallucci and A. Basile, "A theoretical analysis of methanol synthesis from CO_2 and H_2 in a ceramic membrane reactor," *Int. J. Hydrogen Energy*, vol. 32, pp. 5050-5058, 2007.

[51] X. Zhai, J. Shamoto, H. Xie, Y. Tan, Y. Han, and N. Tsubaki, "Study on the deactivation phenomena of Cu-based catalyst for methanol synthesis in slurry phase," *Fuel*, vol. 87, pp. 430-434, 2008.

[52] X. Zhang, L. Zhong, Q. Guo, H. Fan, H. Zheng, and K. Xie, "Influence of the calcination on the activity and stability of the $Cu/ZnO/Al_2O_3$ catalyst in liquid phase methanol synthesis," *Fuel*, vol. 89, pp. 1348-1352, 2010.

[53] V. M. Palekar, H. Jung, J. W. Tiemey, and I. Wender, "Slurry phase synthesis of methanol with a potassium methoxide/copper chromite catalytic system," *Appl. Catal., A*, vol. 102, pp. 13-34, 1993.

[54] P. J. A. Tijm, F. J. Waller, and D. M. Brown, "Methanol technology developments for the new millennium," *Appl. Catal., A*, vol. 221, pp. 275-282, 2001.

[55] S. Lee and A. Sardesai, "Liquid phase methanol and dimethyl ether synthesis from syngas," *Top. Catal.*, vol. 32, pp. 197-207, 2005.

[56] A. Cybulski, "Liquid-phase methanol synthesis: Catalysts, mechanism, kinetics, chemical equilibria, vapor-liquid equilibria, and modeling - A review," *Cat. Rev. - Sci. Eng.*, vol. 36, pp. 557-615, 1994.

[57] J.-Q. Zeng, N. Tsubaki, and K. Fujimoto, "The promoting effect of alcohols in a new process of low-temperature synthesis of methanol from $CO/CO_2/H_2$," *Fuel*, vol. 81, pp. 125-127, 2002.

[58] L. Datsevich, "Technological Reasons for the Selection of Fixed-Bed Reactors," in *Conventional Three-Phase Fixed-Bed Technologies*. vol. 7, ed: Springer New York, 2012, pp. 7-9.

[59] G. Centi and S. Perathoner, "Advances in Catalysts and Processes for Methanol Synthesis from CO_2," in *CO_2: A Valuable Source of Carbon*, M. D. Falco, G. Iaquaniello, and G. Centi, Eds., ed: Springer London, 2013, pp. 147-169.

[60] J. Ma, N. Sun, X. Zhang, N. Zhao, F. Xiao, W. Wei, *et al.*, "A short review of catalysis for CO_2 conversion," *Catal. Today*, vol. 148, pp. 221-231, 2009.

[61] Y. Liu, Y. Zhang, T. Wang, and N. Tsubaki, "Efficient conversion of carbon dioxide to methanol using copper catalyst by a new low-temperature hydrogenation process," *Chem. Lett.*, vol. 36, pp. 1182-1183, 2007.

[62] G. Bonura, F. Arena, G. Mezzatesta, C. Cannilla, L. Spadaro, and F. Frusteri, "Role of the ceria promoter and carrier on the functionality of Cu-based catalysts in the CO_2-to-methanol hydrogenation reaction," *Catal. Today*, vol. 171, pp. 251-256, 2011.

[63] L. Ma, T. Tran, and M. Wainwright, "Methanol Synthesis from CO_2 Using Skeletal Copper Catalysts Containing Co-precipitated Cr_2O_3 and ZnO," *Top. Catal.*, vol. 22, pp. 295-304, 2003.

[64] F. Arena, G. Italiano, K. Barbera, G. Bonura, L. Spadaro, and F. Frusteri, "Basic evidences for methanol-synthesis catalyst design," *Catal. Today*, vol. 143, pp. 80-85, 2009.

[65] H.-d. Zhuang, S.-f. Bai, X.-m. Liu, and Z.-f. Yan, "Structure and performance of Cu/ZrO_2 catalyst For the synthesis of methanol from CO_2 hydrogenation," *J. Fuel Chem. Technol.*, vol. 38, pp. 462-467, 2010.

[66] W. H. HG Guo, JL Shen, HZ Liu, "Studies on deactivation of copper-based mathanol synthesis catalysts," *Industrial Catalysis*, vol. 11, pp. 39-42, 2003.

[67] I. Eswaramoorthi, V. Sundaramurthy, N. Das, A. K. Dalai, and J. Adjaye, "Application of multi-walled carbon nanotubes as efficient support to NiMo hydrotreating catalyst," *Appl. Catal., A*, vol. 339, pp. 187-195, 2008.

[68] J. M., "The Role of Carbon Nanotubes in the Hydrogenation of Carbon Monoxide," Southern Illinois University Carbondale, 2009.

[69] A. Bill, "carbon dioxide hydrogenation to methanol at low pressure and temperature," PhD, Ecole Polytechnique Federale De Lausanne, 1997.

[70] Z. U. W. Yangyang Liu, Hong-Cai Zhou, "Recent advances in carbon dioxide capture with metal-organic frameworks," *Greenhouse Gases: Science and Technology*, vol. 2, pp. 239–259, 2012.

[71] G. A. Olah, "Towards Oil Independence Through Renewable Methanol Chemistry," *Angew. Chem. Int. Ed.*, vol. 52, pp. 104-107, 2013.

[72] G. A. Olah, "Beyond Oil and Gas: The Methanol Economy," *Angew. Chem. Int. Ed.*, vol. 44, pp. 2636-2639, 2005.

[73] G. A. Olah, A. Goeppert, and G. K. S. Prakash, "Chemical Recycling of Carbon Dioxide to Methanol and Dimethyl Ether: From Greenhouse Gas to Renewable, Environmentally Carbon Neutral Fuels and Synthetic Hydrocarbons," *The Journal of Organic Chemistry*, vol. 74, pp. 487-498, 2008.

[74] C. M.W., "Thermodynamic Values," *american chemical society and american institute of physics for the national beureu*, vol. 14, 1985.

[75] T. H. P. R. H. Schultz, "Technical and Economic Assessment of Methanol Production from Biogas," Master, University of Aalborg, Denmark, 2012.

[76] M. Sahibzada, I. S. Metcalfe, and D. Chadwick, "Methanol Synthesis from $CO/CO_2/H_2$ over $Cu/ZnO/Al_2O_3$ at Differential and Finite Conversions," *J. Catal.*, vol. 174, pp. 111-118, 1998.

[77] K. Klier, "Methanol Synthesis," in *Advances in Catalysis*. vol. Volume 31, H. P. D.D. Eley and B. W. Paul, Eds., ed: Academic Press, 1982, pp. 243-313.

[78] F. Studt, F. Abild-Pedersen, J. Varley, and J. Nørskov, "CO and CO_2 Hydrogenation to Methanol Calculated Using the BEEF-vdW Functional," *Catal. Lett.*, vol. 143, pp. 71-73, 2013.

[79] N. P. Hansen JB, *Handbook of heterogeneous catalysis*: Wiley, Weinheim, 2008.

[80] L. C. Grabow and M. Mavrikakis, "Mechanism of Methanol Synthesis on Cu through CO_2 and CO Hydrogenation," *ACS Catalysis,* vol. 1, pp. 365-384, 2011.

[81] Z. Huo, M. Hu, X. Zeng, J. Yun, and F. Jin, "Catalytic reduction of carbon dioxide into methanol over copper under hydrothermal conditions," *Catal. Today,* vol. 194, pp. 25-29, 2012.

[82] S. G.A., *introduction to surface chemistry and catalysis*: Wiley, 1994.

[83] R. A. Köppel, C. Stöcker, and A. Baiker, "Copper- and Silver–Zirconia Aerogels: Preparation, Structural Properties and Catalytic Behavior in Methanol Synthesis from Carbon Dioxide," *J. Catal.,* vol. 179, pp. 515-527, 1998.

[84] R. Grabowski, J. Słoczyński, M. Śliwa, D. Mucha, R. P. Socha, M. Lachowska, *et al.*, "Influence of Polymorphic ZrO_2 Phases and the Silver Electronic State on the Activity of Ag/ZrO_2 Catalysts in the Hydrogenation of CO_2 to Methanol," *ACS Catalysis,* vol. 1, pp. 266-278, 2011.

[85] M. D. Rhodes and A. T. Bell, "The effects of zirconia morphology on methanol synthesis from CO and over catalysts: Part I. Steady-state studies," *J. Catal.,* vol. 233, pp. 198-209, 2005.

[86] L. Fan and K. Fujimoto, "Promotive SMSI Effect for Hydrogenation of Carbon Dioxide to Methanol on a Pd/CeO_2 Catalyst," *J. Catal.,* vol. 150, pp. 217-220, 1994.

[87] X.-L. Liang, X. Dong, G.-D. Lin, and H.-B. Zhang, "Carbon nanotube-supported Pd–ZnO catalyst for hydrogenation of CO_2 to methanol," *Appl. Catal., B,* vol. 88, pp. 315-322, 2009.

[88] M. Saito, "R&D activities in Japan on methanol synthesis from CO_2 and H_2," *Catalysis Surveys from Asia,* vol. 2, pp. 175-184, 1998.

[89] H. Ahouari, A. Soualah, A. Le Valant, L. Pinard, P. Magnoux, and Y. Pouilloux, "Methanol synthesis from CO_2 hydrogenation over copper based catalysts," *React. Kinet. Catal. Lett.,* vol. 110, pp. 131-145, 2013.

[90] C. V. Ovesen, B. S. Clausen, J. Schiøtz, P. Stoltze, H. Topsøe, and J. K. Nørskov, "Kinetic Implications of Dynamical Changes in Catalyst Morphology during Methanol Synthesis over Cu/ZnO Catalysts," *J. Catal.,* vol. 168, pp. 133-142, 1997.

[91] Y. Nitta, O. Suwata, Y. Ikeda, Y. Okamoto, and T. Imanaka, "Copper-zirconia catalysts for methanol synthesis from carbon dioxide: Effect of ZnO addition to $Cu-ZrO_2$ catalysts," *Catal. Lett.,* vol. 26, pp. 345-354, 1994.

[92] J. Toyir, P. Ramírez de la Piscina, J. L. G. Fierro, and N. s. Homs, "Catalytic performance for CO_2 conversion to methanol of gallium-promoted copper-based catalysts: influence of metallic precursors," *Appl. Catal., B,* vol. 34, pp. 255-266, 2001.

[93] X.-M. Liu, G. Q. Lu, and Z.-F. Yan, "Nanocrystalline zirconia as catalyst support in methanol synthesis," *Appl. Catal., A,* vol. 279, pp. 241-245, 2005.

[94] S. Bailey, G. F. Froment, J. W. Snoeck, and K. C. Waugh, "A DRIFTS study of the morphology and surface adsorbate composition of an operating methanol synthesis catalyst," *Catal. Lett.,* vol. 30, pp. 99-111, 1994.

[95] J. Yoshihara and C. T. Campbell, "Methanol Synthesis and Reverse Water–Gas Shift Kinetics over Cu(110) Model Catalysts: Structural Sensitivity," *J. Catal.,* vol. 161, pp. 776-782, 1996.

[96] J. Liu, J. Shi, D. He, Q. Zhang, X. Wu, Y. Liang, *et al.*, "Surface active structure of ultra-fine Cu/ZrO_2 catalysts used for the CO_2+H_2 to methanol reaction," *Appl. Catal., A*, vol. 218, pp. 113-119, 2001.

[97] Y.-W. Suh, S.-H. Moon, and H.-K. Rhee, "Active sites in Cu/ZnO/ZrO_2 catalysts for methanol synthesis from CO/H_2," *Catal. Today*, vol. 63, pp. 447-452, 2000.

[98] Y. Nitta, O. Suwata, Y. Ikeda, Y. Okamoto, and T. Imanaka, "Copper-zirconia catalysts for methanol synthesis from carbon dioxide: Effect of ZnO addition to Cu-ZrO_2 catalysts
" *Catal. Lett.*, vol. 26, pp. 345-354, 1994.

[99] Z. Xu, Z. Qian, and H. Hattori, "Mechanistic Study of the Hydrogenation of Carbon Dioxide to Methanol over Supported Rhenium and Copper-Zinc Catalysts," *Bull. Chem. Soc. Jpn.*, vol. 64, pp. 3432-3437, 1991.

[100] X. An, J. Li, Y. Zuo, Q. Zhang, D. Wang, and J. Wang, "A Cu/Zn/Al/Zr Fibrous Catalyst that is an Improved CO_2 Hydrogenation to Methanol Catalyst," *Catal. Lett.*, vol. 118, pp. 264-269, 2007.

[101] X. Guo, D. Mao, S. Wang, G. Wu, and G. Lu, "Combustion synthesis of CuO–ZnO–ZrO_2 catalysts for the hydrogenation of carbon dioxide to methanol," *Catal. Commun.*, vol. 10, pp. 1661-1664, 2009.

[102] X. Guo, D. Mao, G. Lu, S. Wang, and G. Wu, "Glycine–nitrate combustion synthesis of CuO–ZnO–ZrO_2 catalysts for methanol synthesis from CO_2 hydrogenation," *J. Catal.*, vol. 271, pp. 178-185, 2010.

[103] M. Z. V. Santos, C.P. Bergmann and J.M. Hohemberger, "Correlation between thermal treatment and tetragonal/monoclinic nanostructured zirconia powder obtained by sol-gel process," *Rev.Adv.Mater.Sci*, vol. 17, pp. 62-70, 2008.

[104] K. Jung and A. Bell, "Effects of Zirconia Phase on the Synthesis of Methanol over Zirconia-Supported Copper," *Catal. Lett.*, vol. 80, pp. 63-68, 2002.

[105] T. Tagawab, G. Pleizier, and Y. Amenomiya, "Methanol synthesis from CO_2+H_2 I. characterization of catalysts by TPD," *Appl. Catal.*, vol. 18, pp. 285-293, 1985.

[106] K. Tanabe, "Catalytic application of niobium compounds," *Catal. Today*, vol. 78, pp. 65-77, 2003.

[107] S. Furukawa, A. Tamura, T. Shishido, K. Teramura, and T. Tanaka, "Solvent-free aerobic alcohol oxidation using Cu/Nb_2O_5: Green and highly selective photocatalytic system," *Appl. Catal., B*, vol. 110, pp. 216-220, 2011.

[108] R. R. C. M. Silva, M. Schmal, R. Frety, and J. A. Dalmon, "Effect of the support on the fischer-tropsch synthesis with Co/Nb_2O_5 catalysts," *J. Chem. Soc., Faraday Trans.*, vol. 89, pp. 3975-3980, 1993.

[109] Z. Hu, K. Kunimori, and T. Uchijima, "Interaction of hydrogen and oxygen with niobia-supported and niobia-promoted rhodium catalysts," *Appl. Catal.*, vol. 69, pp. 253-268, 1991.

[110] T. Iizuka, Y. Tanaka, and K. Tanabe, "Hydrogenation of carbon monoxide and carbon dioxide over supported rhodium catalysts," *J. Mol. Catal. A: Chem.*, vol. 17, pp. 381-389, 1982.

[111] A. Frydman, D. G. Castner, C. T. Campbell, and M. Schmal, "Carbon monoxide hydrogenation on Co-Rh/Nb_2O_5 catalysts," *J. Catal.*, vol. 188, pp. 1-13, 1999.

[112] M. Schmal and A. Frydman, "Carbon monoxide hydrogenation on Co-Rh/Nb_2O_5 catalysts," *J. Catal.*, vol. 188, pp. 1-13, 1999.

[113] T. Ushikubo, Y. Hara, and K. Wada, "Catalytic activities of niobium oxide for the liquid-phase hydrogenation of maleic anhydride and hydration of succinonitrile," *Catal. Today,* vol. 16, pp. 525-535, 1993.

[114] F. B. Passos, D. A. G. Aranda, R. R. Soares, and M. Schmal, "Effect of preparation method on the properties of Nb_2O_5 promoted platinum catalysts," *Catal. Today,* vol. 43, pp. 3-9, 1998.

[115] S. Ali, N. A. Mohd Zabidi, and D. Subbarao, "Effect of niobium promoters on iron-based catalysts for Fischer-Tropsch reaction," *J. Fuel Chem. Technol.,* vol. 40, pp. 48-53, 2012.

[116] T. Ushikubo and K. Wada, "Catalytic properties of hydrated tantalum oxide," *Appl. Catal.,* vol. 67, pp. 25-38, 1990.

[117] B. Denise and R. P. A. Sneeden, "Oxide-supported copper catalysts prepared from copper formate: Differences in behavior in methanol synthesis from CO/H_2 and CO_2/H_2 mixtures," *Appl. Catal.,* vol. 28, pp. 235-239, 1986.

[118] T. Inui, T. Takeguchi, A. Kohama, and K. Tanida, "Effective conversion of carbon dioxide to gasoline," *Energy Convers. Manage.,* vol. 33, pp. 513-520, 1992.

[119] H. Y. Chen, L. Chen, J. Lin, K. L. Tan, and J. Li, "Comparative surface studies of high-Zn-level and commercial $Cu/ZnO/Al_2O_3$ catalysts," *J. Phys. Chem. B,* vol. 102, pp. 1994-2000, 1998.

[120] K. Sun, W. Lu, F. Qiu, S. Liu, and X. Xu, "Direct synthesis of DME over bifunctional catalyst: surface properties and catalytic performance," *Appl. Catal., A,* vol. 252, pp. 243-249, 2003.

[121] Y. Kanai, T. Watanabe, T. Fujitani, T. Uchijima, and J. Nakamura, "The synergy between Cu and ZnO in methanol synthesis catalysts," *Catal. Lett.,* vol. 38, pp. 157-163, 1996.

[122] H. Y. Chen, S. P. Lau, L. Chen, J. Lin, C. H. A. Huan, K. L. Tan, *et al.*, "Synergism between Cu and Zn sites in Cu/Zn catalysts for methanol synthesis," *Appl. Surf. Sci.,* vol. 152, pp. 193-199, 1999.

[123] M. Behrens, F. Studt, I. Kasatkin, S. Kühl, M. Hävecker, F. Abild-Pedersen, *et al.*, "The Active Site of Methanol Synthesis over $Cu/ZnO/Al_2O_3$ Industrial Catalysts," *Science,* vol. 336, pp. 893-897, 2012.

[124] B. K. Min, A. K. Santra, and D. W. Goodman, "Understanding silica-supported metal catalysts: Pd/silica as a case study," *Catal. Today,* vol. 85, pp. 113-124, 2003.

[125] W. Juszczyk and Z. Karpiński, "Characterization of supported palladium catalysts: II. $PdSiO_2$," *J. Catal.,* vol. 117, pp. 519-532, 1989.

[126] J. F. Lambert and M. Che, "The molecular approach to supported catalysts synthesis: state of the art and future challenges," *J. Mol. Catal. A: Chem.,* vol. 162, pp. 5-18, 2000.

[127] K. V. R. Chary, C. Praveen Kumar, P. Venkat Ramana Rao, and V. Venkat Rao, "Dispersion and reactivity of V_2O_5 catalysts supported on Al_2O_3–ZrO_2," *Catal. Commun.,* vol. 5, pp. 479-484, 2004.

[128] J. M. Dominguez, J. L. Hernandez, and G. Sandoval, "Surface and catalytic properties of Al_2O_3–ZrO_2 solid solutions prepared by sol–gel methods," *Appl. Catal., A,* vol. 197, pp. 119-130, 2000.

[129] Y. Nie, "Surface silanization of carbon nanofibers and nanotubes for altering the properties of epoxy composites," Ph.D., der Technischen Universität Ilmenau, 2012.

[130] B. M. Philippe Serp, "CHAPTER 1 Carbon (Nano)materials for Catalysis," in *Nanostructured Carbon Materials for Catalysis*, ed: The Royal Society of Chemistry, 2015, pp. 1-45.

[131] V. Jiménez, P. Panagiotopoulou, P. Sánchez, J. L. Valverde, and A. Romero, "Synthesis and characterization of ruthenium supported on carbon nanofibers with different graphitic plane arrangements," *Chem. Eng. J.*, vol. 168, pp. 947-954, 2011.

[132] M. K. v. d. L. J.H. Bitter, A.G.T. Slotboom, A.J. van Dillen, K.P. de Jong, "Synthesis of Highly Loaded Highly Dispersed Nickel on Carbon Nanofibers by Homogeneous Deposition–Precipitation," *Catal. Lett.*, vol. 89, pp. 139-142, 2003.

[133] D. B. Thakur, R. M. Tiggelaar, T. M. C. Hoang, J. G. E. Gardeniers, L. Lefferts, and K. Seshan, "Ruthenium catalyst on carbon nanofiber support layers for use in silicon-based structured microreactors, Part I: Preparation and characterization," *Appl. Catal., B*, vol. 102, pp. 232-242, 2011.

[134] T. G. Ros, A. J. van Dillen, J. W. Geus, and D. C. Koningsberger, "Surface Oxidation of Carbon Nanofibres," *Chemistry – A European Journal*, vol. 8, pp. 1151-1162, 2002.

[135] P. Serp, M. Corrias, and P. Kalck, "Carbon nanotubes and nanofibers in catalysis," *Appl. Catal., A*, vol. 253, pp. 337-358, 2003.

[136] K. L. Klein, A. V. Melechko, T. E. McKnight, S. T. Retterer, P. D. Rack, J. D. Fowlkes, *et al.*, "Surface characterization and functionalization of carbon nanofibers," *J. Appl. Phys.*, vol. 103, pp. -, 2008.

[137] R. Gao, C. D. Tan, and R. T. K. Baker, "Ethylene hydroformylation on graphite nanofiber supported rhodium catalysts," *Catal. Today*, vol. 65, pp. 19-29, 2001.

[138] R. T. K. Baker, K. Laubernds, A. Wootsch, and Z. Paál, "Pt/Graphite Nanofiber Catalyst in n-Hexane Test Reaction," *J. Catal.*, vol. 193, pp. 165-167, 2000.

[139] R. Vieira, C. Pham-Huu, N. Keller, and M. J. Ledoux, "New carbon nanofiber/graphite felt composite for use as a catalyst support for hydrazine catalytic decomposition," *Chem. Commun.*, pp. 954-955, 2002.

[140] M. R. Cuervo, E. Asedegbega-Nieto, E. Díaz, A. Vega, S. Ordóñez, E. Castillejos-López, *et al.*, "Effect of carbon nanofiber functionalization on the adsorption properties of volatile organic compounds," *J. Chromatogr. A*, vol. 1188, pp. 264-273, 2008.

[141] S. S. Barton, M. J. B. Evans, E. Halliop, and J. A. F. MacDonald, "Acidic and basic sites on the surface of porous carbon," *Carbon*, vol. 35, pp. 1361-1366, 1997.

[142] H. Ago, T. Kugler, F. Cacialli, W. R. Salaneck, M. S. P. Shaffer, A. H. Windle, *et al.*, "Work Functions and Surface Functional Groups of Multiwall Carbon Nanotubes," *J. Phys. Chem. B*, vol. 103, pp. 8116-8121, 1999.

[143] C. Prado-Burguete, A. Linares-Solano, F. Rodríguez-Reinoso, and C. S.-M. de Lecea, "The effect of oxygen surface groups of the support on platinum dispersion in Pt/carbon catalysts," *J. Catal.*, vol. 115, pp. 98-106, 1989.

[144] R. Anderson, "Structure of Metallic Catalysts," *Academic Press, London*, p. 81, 1975.

[145] D. B. Mawhinney, V. Naumenko, A. Kuznetsova, J. T. Yates Jr, J. Liu, and R. E. Smalley, "Surface defect site density on single walled carbon nanotubes by titration," *Chem. Phys. Lett.*, vol. 324, pp. 213-216, 2000.

[146] B. L. Mojet, M. S. Hoogenraad, A. J. van Dillen, J. W. Geus, and D. C. Koningsberger, "Coordination of palladium on carbon fibrils as determined by XAFS spectroscopy," *J. Chem. Soc., Faraday Trans.*, vol. 93, pp. 4371-4375, 1997.

[147] T. G. Ros, D. E. Keller, A. J. van Dillen, J. W. Geus, and D. C. Koningsberger, "Preparation and Activity of Small Rhodium Metal Particles on Fishbone Carbon Nanofibres," *J. Catal.*, vol. 211, pp. 85-102, 2002.

[148] M. RUTA, "Novel Catalytic Applications of Carbon Nanofi bers on Sintered Metal Fibers Filters as Structured Supports," *Thesis,* 2008.

[149] R. W. Cahn, "Physics of graphite: B.T. Kelly (Applied Science Publishers, London, 1981) pp. 477. price: £48," *J. Nucl. Mater.*, vol. 114, p. 116, 1983.

[150] J. A. Díaz, M. Martínez-Fernández, A. Romero, and J. L. Valverde, "Synthesis of carbon nanofibers supported cobalt catalysts for Fischer–Tropsch process," *Fuel,* vol. 111, pp. 422-429, 2013.

[151] T. H. Yoong Ahm Kim, Morinobu Endo, Mildred S. Dresselhaus, "Carbon Nanofibers," *Springer Handbook of Nanomaterials,* 2013.

[152] T. G. Ros, A. J. van Dillen, J. W. Geus, and D. C. Koningsberger, "Surface Structure of Untreated Parallel and Fishbone Carbon Nanofibres: An Infrared Study," *ChemPhysChem,* vol. 3, pp. 209-214, 2002.

[153] M. K. van der Lee, A. J. van Dillen, J. W. Geus, K. P. de Jong, and J. H. Bitter, "Catalytic growth of macroscopic carbon nanofiber bodies with high bulk density and high mechanical strength," *Carbon,* vol. 44, pp. 629-637, 2006.

[154] M. J. Ledoux, R. Vieira, C. Pham-Huu, and N. Keller, "New catalytic phenomena on nanostructured (fibers and tubes) catalysts," *J. Catal.*, vol. 216, pp. 333-342, 2003.

[155] K. P. De Jong and J. W. Geus, "Carbon Nanofibers: Catalytic Synthesis and Applications," *Catalysis Reviews,* vol. 42, pp. 481-510, 2000.

[156] N. M. Rodriguez, M.-S. Kim, and R. T. K. Baker, "Carbon Nanofibers: A Unique Catalyst Support Medium," *The Journal of Physical Chemistry,* vol. 98, pp. 13108-13111, 1994.

[157] M. K. van der Lee, J. van Dillen, J. H. Bitter, and K. P. de Jong, "Deposition Precipitation for the Preparation of Carbon Nanofiber Supported Nickel Catalysts," *JACS,* vol. 127, pp. 13573-13582, 2005.

[158] A. J. Plomp, D. S. Su, K. P. d. Jong, and J. H. Bitter, "On the Nature of Oxygen-Containing Surface Groups on Carbon Nanofibers and Their Role for Platinum Deposition—An XPS and Titration Study," *J. Phys. Chem. C,* vol. 113, pp. 9865-9869, 2009.

[159] J. Dusza, G. Blugan, J. Morgiel, J. Kuebler, F. Inam, T. Peijs, *et al.*, "Hot pressed and spark plasma sintered zirconia/carbon nanofiber composites," *J. Eur. Ceram. Soc.*, vol. 29, pp. 3177-3184, 2009.

[160] M. L. Toebes, M. K. van der Lee, L. M. Tang, M. H. Huis in 't Veld, J. H. Bitter, A. J. van Dillen, *et al.*, "Preparation of Carbon Nanofiber Supported Platinum and Ruthenium Catalysts: Comparison of Ion Adsorption and Homogeneous Deposition Precipitation," *J. Phys. Chem. B,* vol. 108, pp. 11611-11619, 2004.

[161] C. Park and R. T. K. Baker, "Catalytic Behavior of Graphite Nanofiber Supported Nickel Particles. 3. The Effect of Chemical Blocking on the Performance of the System," *J. Phys. Chem. B,* vol. 103, pp. 2453-2459, 1999.

[162] T. G. Ros, A. J. van Dillen, J. W. Geus, and D. C. Koningsberger, "Modification of Carbon Nanofibres for the Immobilization of Metal Complexes: A Case Study with Rhodium and Anthranilic Acid," *Chemistry – A European Journal,* vol. 8, pp. 2868-2878, 2002.

[163] M. L. Toebes, F. F. Prinsloo, J. H. Bitter, A. J. van Dillen, and K. P. de Jong, "Influence of oxygen-containing surface groups on the activity and selectivity of carbon nanofiber-supported ruthenium catalysts in the hydrogenation of cinnamaldehyde," *J. Catal.,* vol. 214, pp. 78-87, 2003.

[164] C. Pham-Huu, N. Keller, L. J. Charbonniere, R. Ziessel, and M. J. Ledoux, "Carbon nanofiber supported palladium catalyst for liquid-phase reactions. An active and selective catalyst for hydrogenation of C=C bonds," *Chem. Commun.,* pp. 1871-1872, 2000.

[165] J.-M. Nhut, R. Vieira, L. Pesant, J.-P. Tessonnier, N. Keller, G. Ehret, *et al.*, "Synthesis and catalytic uses of carbon and silicon carbide nanostructures," *Catal. Today,* vol. 76, pp. 11-32, 2002.

[166] I. Kang, Y. Y. Heung, J. H. Kim, J. W. Lee, R. Gollapudi, S. Subramaniam, *et al.*, "Introduction to carbon nanotube and nanofiber smart materials," *Composites Part B: Engineering,* vol. 37, pp. 382-394, 2006.

[167] H. W. F. Guo H G, Shen J L, Liu H Z, "Studies on deactivation of copper-based methanol synthesis catalysts," *Industrial Catalysis,* vol. 11, p. 39, 2003.

[168] X. T. C. Yin Y Q, Su J X, Wang H T, Lu Y L, Feng X S, Li S B, "Study for adsorptive behavior of CO and H_2 on Cu-ZnO based catalyst.," *Natural Gas Chemical Industry,* vol. 14, p. 373, 2000.

[169] J. T. Richardson, "Principles of Catalyst Development," *BOOK,* 1989.

[170] G. L. Bezemer, P. B. Radstake, U. Falke, H. Oosterbeek, H. P. C. E. Kuipers, A. J. van Dillen, *et al.*, "Investigation of promoter effects of manganese oxide on carbon nanofiber-supported cobalt catalysts for Fischer–Tropsch synthesis," *J. Catal.,* vol. 237, pp. 152-161, 2006.

[171] L. A. M. Hermans and J. W. Geus, "Interaction Of Nickel Ions With Silica Supports During Deposition-Precipitation," in *Stud. Surf. Sci. Catal.* vol. Volume 3, P. G. P. J. B. Delmon and G. Poncelet, Eds., ed: Elsevier, 1979, pp. 113-130.

[172] C. J. G. Van Der Grift, P. A. Elberse, A. Mulder, and J. W. Geus, "Preparation of silica-supported copper catalysts by means of deposition-precipitation," *Appl. Catal.,* vol. 59, pp. 275-289, 1990.

[173] M. L. Toebes, F. F. Prinsloo, J. H. Bitter, A. J. van Dillen, and K. P. de Jong, "Synthesis and characterization of carbon nanofiber supported ruthenium catalysts," in *Stud. Surf. Sci. Catal.* vol. Volume 143, D. E. D. V. P. G. P. A. J. J. A. M. P. R. E. Gaigneaux and G. Poncelet, Eds., ed: Elsevier, 2000, pp. 201-208.

[174] K. P. de Jong, "Deposition Precipitation Onto Pre-Shaped Carrier Bodies. Possibilities and Limitations," in *Stud. Surf. Sci. Catal.* vol. Volume 63, P. A. J. P. G. G. Poncelet and B. Delmon, Eds., ed: Elsevier, 1991, pp. 19-36.

[175] P. Burattin, M. Che, and C. Louis, "Characterization of the Ni(II) Phase Formed on Silica Upon Deposition−Precipitation," *J. Phys. Chem. B,* vol. 101, pp. 7060-7074, 1997.

[176] A. J. v. D. J. W. Geus, G. Ertl, H.Knözinger, J. Weitkamp, *Handbook on Heterogeneous Catalysis* vol. 1: Weinheim, 1997.

[177] P. C. M. van Stiphout, H. Donker, C. R. Bayense, J. W. Geus, and F. Versluis, "Electrochemically Controlled Deposition-Precipitation. A New Method for the Production of Supported Catalysts," in *Stud. Surf. Sci. Catal.* vol. Volume 31, P. G. P. A. J. B. Delmon and G. Poncelet, Eds., ed: Elsevier, 1987, pp. 55-70.

[178] P. Burattin, M. Che, and C. Louis, "Molecular Approach to the Mechanism of Deposition−Precipitation of the Ni(II) Phase on Silica," *J. Phys. Chem. B,* vol. 102, pp. 2722-2732, 1998.

[179] J. W. Geus, "Production and Thermal Pretreatmewt of Supported Catalysts," in *Stud. Surf. Sci. Catal.* vol. Volume 16, P. G. G. Poncelet and P. A. Jacobs, Eds., ed: Elsevier, 1983, pp. 1-33.

[180] K. Y. Koo, U. H. Jung, and W. L. Yoon, "A highly dispersed Pt/γ-Al_2O_3 catalyst prepared via deposition–precipitation method for preferential CO oxidation," *Int. J. Hydrogen Energy,* vol. 39, pp. 5696-5703, 2014.

[181] A. Guerrero-Ruiz, P. Badenes, and I. Rodríguez-Ramos, "Study of some factors affecting the Ru and Pt dispersions over high surface area graphite-supported catalysts," *Appl. Catal., A,* vol. 173, pp. 313-321, 1998.

[182] S. Song, Z. Sheng, Y. Liu, H. Wang, and Z. Wu, "Influences of pH value in deposition-precipitation synthesis process on Pt-doped TiO2 catalysts for photocatalytic oxidation of NO," *Journal of Environmental Sciences,* vol. 24, pp. 1519-1524, 2012.

[183] P. Burattin, M. Che, and C. Louis, "Metal Particle Size in Ni/SiO_2 Materials Prepared by Deposition−Precipitation: Influence of the Nature of the Ni(II) Phase and of Its Interaction with the Support," *J. Phys. Chem. B,* vol. 103, pp. 6171-6178, 1999.

[184] G. L. Bezemer, P. B. Radstake, V. Koot, A. J. van Dillen, J. W. Geus, and K. P. de Jong, "Preparation of Fischer–Tropsch cobalt catalysts supported on carbon nanofibers and silica using homogeneous deposition-precipitation," *J. Catal.,* vol. 237, pp. 291-302, 2006.

[185] W. Cai, P. R. de la Piscina, J. Toyir, and N. Homs, "CO_2 hydrogenation to methanol over CuZnGa catalysts prepared using microwave-assisted methods," *Catal. Today,* vol. 242, Part A, pp. 193-199, 2015.

[186] G. Bonura, M. Cordaro, C. Cannilla, F. Arena, and F. Frusteri, "The changing nature of the active site of Cu-Zn-Zr catalysts for the CO_2 hydrogenation reaction to methanol," *Appl. Catal., B,* vol. 152–153, pp. 152-161, 2014.

[187] P. Gao, F. Li, H. Zhan, N. Zhao, F. Xiao, W. Wei, *et al.*, "Influence of Zr on the performance of Cu/Zn/Al/Zr catalysts via hydrotalcite-like precursors for CO_2 hydrogenation to methanol," *J. Catal.,* vol. 298, pp. 51-60, 2013.

[188] P. Gao, F. Li, L. Zhang, N. Zhao, F. Xiao, W. Wei, *et al.*, "Influence of fluorine on the performance of fluorine-modified Cu/Zn/Al catalysts for CO_2 hydrogenation to methanol," *Journal of CO_2 Utilization,* vol. 2, pp. 16-23, 2013.

[189] C. H. Bartholomew, "Mechanisms of catalyst deactivation," *Appl. Catal., A,* vol. 212, pp. 17-60, 2001.

[190] J.-S. Kim, S.-B. Lee, M.-C. Kang, K.-W. Lee, M.-J. Choi, and Y. Kang, "Promotion of CO_2 hydrogénation to hydrocarbons in three-phase catalytic (Fe-Cu-K-Al) slurry reactors," *Korean J. Chem. Eng.*, vol. 20, pp. 967-972, 2003.

[191] K. Zhang, H. Song, D. Sun, S. Li, X. Yang, Y. Zhao, *et al.*, "Low-temperature methanol synthesis in a circulating slurry bubble reactor," *Fuel,* vol. 82, pp. 233-239, 2003.

[192] T. K. Sherwood and E. J. Farkas, "Studies of the slurry reactor," *Chem. Eng. Sci.*, vol. 21, pp. 573-582, 1966.

[193] B. J. Liaw and Y. Z. Chen, "Liquid-phase synthesis of methanol from CO_2/H_2 over ultrafine CuB catalysts," *Appl. Catal., A,* vol. 206, pp. 245-256, 2001.

[194] Y.-Z. Chen, B.-J. Liaw, and B.-J. Chen, "One-step synthesis of methanol from CO/H_2 at low temperature over ultrafine CuB catalysts," *Appl. Catal., A,* vol. 236, pp. 121-128, 2002.

[195] L. Fan, Y. Sakaiya, and K. Fujimoto, "Low-temperature methanol synthesis from carbon dioxide and hydrogen via formic ester," *Appl. Catal., A,* vol. 180, pp. L11-L13, 1999.

[196] K. M. Kim, H. C. Woo, M. Cheong, J. C. Kim, K. H. Lee, J. S. Lee, *et al.*, "Chemical equilibria and catalytic reaction of gas-phase methanol synthesis from methyl formate," *Appl. Catal., A,* vol. 83, pp. 15-30, 1992.

[197] N. Tsubaki, M. Ito, and K. Fujimoto, "A New Method of Low-Temperature Methanol Synthesis," *J. Catal.*, vol. 197, pp. 224-227, 2001.

[198] R. Yang, Y. Zhang, Y. Iwama, and N. Tsubaki, "Mechanistic study of a new low-temperature methanol synthesis on Cu/MgO catalysts," *Appl. Catal., A,* vol. 288, pp. 126-133, 2005.

[199] L. Shi, W. Shen, G. Yang, X. Fan, Y. Jin, C. Zeng, *et al.*, "Formic acid directly assisted solid-state synthesis of metallic catalysts without further reduction: As-prepared Cu/ZnO catalysts for low-temperature methanol synthesis," *J. Catal.*, vol. 302, pp. 83-90, 2013.

[200] N. Tsubaki, J. Zeng, Y. Yoneyama, and K. Fujimoto, "Continuous synthesis process of methanol at low temperature from syngas using alcohol promoters," *Catal. Commun.*, vol. 2, pp. 213-217, 2001.

[201] T. Fujitani and J. Nakamura, "The chemical modification seen in the Cu/ZnO methanol synthesis catalysts," *Appl. Catal., A,* vol. 191, pp. 111-129, 2000.

[202] X. An, Y. Zuo, Q. Zhang, and J. Wang, "Methanol Synthesis from CO_2 Hydrogenation with a Cu/Zn/Al/Zr Fibrous Catalyst," *Chin. J. Chem. Eng.*, vol. 17, pp. 88-94, 2009.

[203] G.-X. Qi, X.-M. Zheng, J.-H. Fei, and Z.-Y. Hou, "Low-temperature methanol synthesis catalyzed over $Cu/\gamma\text{-}Al_2O_3\text{–}TiO_2$ for CO_2 hydrogenation," *Catal. Lett.*, vol. 72, pp. 191-196, 2001.

[204] B. Tidona, C. Koppold, A. Bansode, A. Urakawa, and P. Rudolf von Rohr, "CO_2 hydrogenation to methanol at pressures up to 950 bar," *The Journal of Supercritical Fluids,* vol. 78, pp. 70-77, 2013.

[205] W.-J. S. Ki-Won Jun, and Kyu-Wan Lee, "Concurrent Production of Methanol and Dimethyl Ether from Carbon Dioxide Hydrogenation : Investigation of Reaction Conditions," *Bull. Korean Chem. Soc,* vol. 20, pp. 993-998, 1999.

[206] G. H. Graaf, E. J. Stamhuis, and A. A. C. M. Beenackers, "Kinetics of low-pressure methanol synthesis," *Chem. Eng. Sci.*, vol. 43, pp. 3185-3195, 1988.

[207] A. Bansode and A. Urakawa, "Towards full one-pass conversion of carbon dioxide to methanol and methanol-derived products," *J. Catal.*, vol. 309, pp. 66-70, 2014.

[208] W.-J. Shen, K.-W. Jun, H.-S. Choi, and K.-W. Lee, "Thermodynamic investigation of methanol and dimethyl ether synthesis from CO_2 Hydrogenation," *Korean J. Chem. Eng.*, vol. 17, pp. 210-216, 2000.

[209] W. McCulloch and W. Pitts, "A logical calculus of the ideas immanent in nervous activity," *The bulletin of mathematical biophysics*, vol. 5, pp. 115-133, 1943.

[210] D. E. Rumelhart, G. E. Hinton, and R. J. Williams, "Learning representations by back-propagating errors," *Nature*, vol. 323, pp. 533-536, 1986.

[211] R. Rallo, J. Ferre-Giné, A. Arenas, and F. Giralt, "Neural virtual sensor for the inferential prediction of product quality from process variables," *Computers & Chemical Engineering*, vol. 26, pp. 1735-1754, 2002.

[212] D. Himmelblau, "Applications of artificial neural networks in chemical engineering," *Korean J. Chem. Eng.*, vol. 17, pp. 373-392, 2000.

[213] E. Arce-Medina and J. I. Paz-Paredes, "Artificial neural network modeling techniques applied to the hydrodesulfurization process," *Mathematical and Computer Modelling*, vol. 49, pp. 207-214, 2009.

[214] S. Alamolhoda, M. Kazemeini, A. Zaherian, and M. R. Zakerinasab, "Reaction kinetics determination and neural networks modeling of methanol dehydration over nano γ-Al_2O_3 catalyst," *Journal of Industrial and Engineering Chemistry*, vol. 18, pp. 2059-2068, 2012.

[215] P. Szymczyk and M. Szymczyk, "Classification of geological structure using ground penetrating radar and Laplace transform artificial neural networks," *Neurocomputing*, vol. 148, pp. 354-362, 2015.

[216] J. L. Fontaine and A. Germain, "Model-based neural networks," *Computers & Chemical Engineering*, vol. 25, pp. 1045-1054, 2001.

[217] F. ç. Larachi, "Neural network kinetic prediction of coke burn-off on spent MnO_2/CeO_2 wet oxidation catalysts," *Appl. Catal., B*, vol. 30, pp. 141-150, 2001.

[218] M. Fullana, F. Trabelsi, and F. Recasens, "Use of neural net computing for statistical and kinetic modelling and simulation of supercritical fluid extractors," *Chem. Eng. Sci.*, vol. 55, pp. 79-95, 2000.

[219] R. M. Malek Abbaslou, J. Soltan, and A. K. Dalai, "Iron catalyst supported on carbon nanotubes for Fischer–Tropsch synthesis: Effects of Mo promotion," *Fuel*, vol. 90, pp. 1139-1144, 2011.

[220] W. Zhu, L. Wang, S. Liu, and Z. Wang, "Characterization and catalytic behavior of silica-supported copper catalysts prepared by impregnation and ion-exchange methods," *React. Kinet. Catal. Lett.*, vol. 93, pp. 93-99, 2008.

[221] C. J. G. Van Der Grift, A. Mulder, and J. W. Geus, "Characterization of silica-supported copper catalysts by means of temperature-programmed reduction," *Appl. Catal.*, vol. 60, pp. 181-192, 1990.

[222] H. M. Rietveld, "Line profiles of neutron powder-diffraction peaks for structure refinement," *Acta Crystallographica*, vol. 22, pp. 151-152, 1967.

[223] B. Feuerbacher, B. Fitton, and R. F. Willis, *Photoemission and the electronic properties of surfaces*: John Wiley & Sons, 1978.

[224] Y. Matsumura, "Stabilization of $Cu/ZnO/ZrO_2$ catalyst for methanol steam reforming to hydrogen by coprecipitation on zirconia support," *J. Power Sources*, vol. 238, pp. 109-116, 2013.

[225] D. Durán-Martín, M. Ojeda, M. L. Granados, J. L. G. Fierro, and R. Mariscal, "Stability and regeneration of $Cu–ZrO_2$ catalysts used in glycerol hydrogenolysis to 1,2-propanediol," *Catal. Today*, vol. 210, pp. 98-105, 2013.

[226] R. Bhattacharjee and I. M. Hung, "Effect of different concentration Li-doping on the morphology, defect and photovoltaic performance of Li–ZnO nanofibers in the dye-sensitized solar cells," *Mater. Chem. Phys.*, vol. 143, pp. 693-701, 2014.

[227] N. Özer, T. Barreto, T. Büyüklimanli, and C. M. Lampert, "Characterization of sol-gel deposited niobium pentoxide films for electrochromic devices," *Sol. Energy Mater. Sol. Cells*, vol. 36, pp. 433-443, 1995.

[228] C. Zhou, Y. Zhao, L. Shang, Y. Cao, L.-Z. Wu, C.-H. Tung, *et al.*, "Facile preparation of black Nb^{4+} self-doped $K_4Nb_6O_{17}$ microspheres with high solar absorption and enhanced photocatalytic activity," *Chem. Commun.*, vol. 50, pp. 9554-9556, 2014.

[229] H. J, "Indutrial Catalysis: A practical approach," *Wiley-WCH*, 2006.

[230] a. A. A. Damjanovic L, "Heterogeneous catalysis on solids in handbook of thermal analysis and calorimetry," *Elsevier*, 2008.

[231] G. V. Sagar, P. V. R. Rao, C. S. Srikanth, and K. V. Chary, "Dispersion and reactivity of copper catalysts supported on Al_2O_3-ZrO_2," *The Journal of Physical Chemistry B*, vol. 110, pp. 13881-13888, 2006.

[232] X. Guo, D. Mao, G. Lu, S. Wang, and G. Wu, "The influence of La doping on the catalytic behavior of Cu/ZrO_2 for methanol synthesis from CO_2 hydrogenation," *J. Mol. Catal. A: Chem.*, vol. 345, pp. 60-68, 2011.

[233] H. Zhan, F. Li, P. Gao, N. Zhao, F. Xiao, W. Wei, *et al.*, "Methanol synthesis from CO_2 hydrogenation over La–M–Cu–Zn–O (M = Y, Ce, Mg, Zr) catalysts derived from perovskite-type precursors," *J. Power Sources*, vol. 251, pp. 113-121, 2014.

[234] J. W. Evans, M. S. Wainwright, A. J. Bridgewater, and D. J. Young, "On the determination of copper surface area by reaction with nitrous oxide," *Appl. Catal.*, vol. 7, pp. 75-83, 1983.

[235] X.-L. Du, Q.-Y. Bi, Y.-M. Liu, Y. Cao, H.-Y. He, and K.-N. Fan, "Tunable copper-catalyzed chemoselective hydrogenolysis of biomass-derived [gamma]-valerolactone into 1,4-pentanediol or 2-methyltetrahydrofuran," *Green Chem.*, vol. 14, pp. 935-939, 2012.

[236] J. R. H. Ross, "Heterogeneous catalysis fundamentals and applications " *book*, 2012.

[237] S. J. S. Gregg, K.S.W., "Adsorption, Surface Area and Porosity; 2nd ed," *Academic Press: London*, 1982.

[238] D. Peña, A. Griboval-Constant, C. Lancelot, M. Quijada, N. Visez, O. Stéphan, *et al.*, "Molecular structure and localization of carbon species in alumina supported cobalt Fischer–Tropsch catalysts in a slurry reactor," *Catalysis Today*, vol. 228, pp. 65-76, 2014.

[239] R. Zhao, J. G. Goodwin Jr, and R. Oukaci, "Attrition assessment for slurry bubble column reactor catalysts," *Applied Catalysis A: General*, vol. 189, pp. 99-116, 1999.

[240] X. Zhang, Z. Li, Q. Guo, H. Zheng, and K. Xie, "Selective synthesis of mixed alcohols from syngas over catalyst Fe2O3/Al2O3 in slurry reactor," *Fuel Processing Technology,* vol. 91, pp. 379-382, 2010.

[241] X. Sun and G. W. Roberts, "Synthesis of higher alcohols in a slurry reactor with cesium-promoted zinc chromite catalyst in decahydronaphthalene," *Applied Catalysis A: General,* vol. 247, pp. 133-142, 2003.

[242] M. Crivello, C. Pérez, E. Herrero, G. Ghione, S. Casuscelli, and E. Rodríguez-Castellón, "Characterization of AlCu and AlCuMg mixed oxides and their catalytic activity in dehydrogenation of 2-octanol," *Catal. Today,* vol. 107, pp. 215-222, 2005.

[243] P. Reubroycharoen, T. Yamagami, T. Vitidsant, Y. Yoneyama, M. Ito, and N. Tsubaki, "Continuous low-temperature methanol synthesis from syngas using alcohol promoters," *Energy & fuels,* vol. 17, pp. 817-821, 2003.

[244] J. Hagen, "Industrial Catalysis, a practical approach, 1999," ed: Wiley-VCH.

[245] Q. Sun, Y.-L. Zhang, H.-Y. Chen, J.-F. Deng, D. Wu, and S.-Y. Chen, "A Novel Process for the Preparation of Cu/ZnO and Cu/ZnO/Al_2O_3 Ultrafine Catalyst: Structure, Surface Properties, and Activity for Methanol Synthesis from CO_2+H_2," *J. Catal.,* vol. 167, pp. 92-105, 1997.

[246] Y. Nie, "Surface silanization of carbon nanofibers and nanotubes for altering the properties of epoxy composites " PhD, Ilmenau University of Technology, 2012.

[247] G. Ovejero, J. L. Sotelo, M. D. Romero, A. Rodríguez, M. A. Ocaña, G. Rodríguez, *et al.*, "Multiwalled Carbon Nanotubes for Liquid-Phase Oxidation. Functionalization, Characterization, and Catalytic Activity," *Ind. Eng. Chem. Res.,* vol. 45, pp. 2206-2212, 2006.

[248] A. G. Osorio, I. C. L. Silveira, V. L. Bueno, and C. P. Bergmann, "H_2SO_4/HNO_3/HCl—Functionalization and its effect on dispersion of carbon nanotubes in aqueous media," *Appl. Surf. Sci.,* vol. 255, pp. 2485-2489, 2008.

[249] H. Xu, X. Wang, Y. Zhang, and S. Liu, "Single-Step in Situ Preparation of Polymer-Grafted Multi-Walled Carbon Nanotube Composites under 60Co γ-Ray Irradiation," *Chem. Mater.,* vol. 18, pp. 2929-2934, 2006.

[250] J.-H. Zhou, Z.-J. Sui, J. Zhu, P. Li, D. Chen, Y.-C. Dai, *et al.*, "Characterization of surface oxygen complexes on carbon nanofibers by TPD, XPS and FT-IR," *Carbon,* vol. 45, pp. 785-796, 2007.

[251] N. Tena, R. Aparicio-Ruiz, and D. L. García-González, *Use of polar and nonpolar fractions as additional information sources for studying thermoxidized virgin olive oils by FTIR%B 2014*, 2014.

[252] J. Coates, "Interpretation of infrared spectra, a practical approach," *Encyclopedia of analytical chemistry,* 2000.

[253] N. Tena, R. Aparicio-Ruiz, and D. García-González, "Use of polar and nonpolar fractions as additional information sources for studying thermoxidized virgin olive oils by FTIR," *Grasas y Aceites,* vol. 65, p. e030, 2014.

[254] C.-M. Chen, Y.-M. Dai, J. G. Huang, and J.-M. Jehng, "Intermetallic catalyst for carbon nanotubes (CNTs) growth by thermal chemical vapor deposition method," *Carbon,* vol. 44, pp. 1808-1820, 2006.

[255] B. Neppolian, Q. Wang, H. Yamashita, and H. Choi, "Synthesis and characterization of ZrO_2–TiO_2 binary oxide semiconductor nanoparticles:

Application and interparticle electron transfer process," *Appl. Catal., A,* vol. 333, pp. 264-271, 2007.

[256] J. B. Ko, C. M. Bae, Y. S. Jung, and D. H. Kim, "Cu–ZrO_2 Catalysts for Water-gas-shift Reaction at Low Temperatures," *Catal. Lett.*, vol. 105, pp. 157-161, 2005.

[257] I. C. Freitas, S. Damyanova, D. C. Oliveira, C. M. P. Marques, and J. M. C. Bueno, "Effect of Cu content on the surface and catalytic properties of Cu/ZrO_2 catalyst for ethanol dehydrogenation," *J. Mol. Catal. A: Chem.*, vol. 381, pp. 26-37, 2014.

[258] M. SHAHMIRI, N. A. IBRAHIM, N. ZAINUDDIN, N. ASIM, B. Bakhtyar, A. Zaharim, *et al.*, "Effect of pH on the synthesis of CuO nanosheets by quick precipitation method," *Wseas Transactions on Environmental and Development,* vol. 9, pp. 137-146, 2013.

[259] A. S. Ethiraj and D. J. Kang, "Synthesis and characterization of CuO nanowires by a simple wet chemical method," *Nanoscale research letters,* vol. 7, pp. 1-5, 2012.

[260] S. Jayakumar, P. V. Ananthapadmanabhan, K. Perumal, T. K. Thiyagarajan, S. C. Mishra, L. T. Su, *et al.*, "Characterization of nano-crystalline ZrO_2 synthesized via reactive plasma processing," *Materials Science and Engineering: B,* vol. 176, pp. 894-899, 2011.

[261] C. Zhou, Z. Liu, X. Du, D. R. G. Mitchell, Y.-W. Mai, Y. Yan, *et al.*, "Hollow nitrogen-containing core/shell fibrous carbon nanomaterials as support to platinum nanocatalysts and their TEM tomography study," *Nanoscale research letters,* vol. 7, pp. 1-11, 2012.

[262] K. V. R. Chary, G. V. Sagar, D. Naresh, K. K. Seela, and B. Sridhar, "Characterization and Reactivity of Copper Oxide Catalysts Supported on TiO_2–ZrO_2," *J. Phys. Chem. B,* vol. 109, pp. 9437-9444, 2005.

[263] Y. Xie, S. Heo, S. Yoo, G. Ali, and S. Cho, "Synthesis and Photocatalytic Activity of Anatase TiO_2 Nanoparticles-coated Carbon Nanotubes," *Nanoscale Research Letters,* vol. 5, pp. 603-607, 2010.

[264] B. L. Kirsch and S. H. Tolbert, "Stabilization of Isolated Hydrous Amorphous and Tetragonal Zirconia Nanoparticles Through the Formation of a Passivating Alumina Shell," *Adv. Funct. Mater.*, vol. 13, pp. 281-288, 2003.

[265] F. Kazemi, A. Saberi, S. Malek-Ahmadi, S. Sohrabi, H. Rezaie, and M. Tahriri, "Novel Method of synthesis of metasatable tetragonal zirconia nanopowder at low temperatures," *Ceramics-Silikáty,* vol. 55, pp. 26-30, 2011.

[266] O. A. Yeshchenko, I. M. Dmitruk, A. A. Alexeenko, and A. M. Dmytruk, "Size-dependent melting of spherical copper nanoparticles embedded in a silica matrix," *Physical Review B,* vol. 75, p. 085434, 2007.

[267] C.-Y. Huang and S. R. Sheen, "Synthesis of nanocrystalline and monodispersed copper particles of uniform spherical shape," *Mater. Lett.*, vol. 30, pp. 357-361, 1997.

[268] J. Y. Yan, W. M. H. Sachtler, and H. H. Kung, "Effect of Cu loading and addition of modifiers on the stability of Cu/ZSM-5 in lean NOx reduction catalysis," *Catal. Today,* vol. 33, pp. 279-290, 1997.

[269] P. Da Costa, B. Modén, G. D. Meitzner, D. Ki Lee, and E. Iglesia, "Spectroscopic and chemical characterization of active and inactive Cu species

in NO decomposition catalysts based on Cu-ZSM5," *PCCP,* vol. 4, pp. 4590-4601, 2002.

[270] F. E. López-Suárez, A. Bueno-López, and M. J. Illán-Gómez, "Cu/Al_2O_3 catalysts for soot oxidation: Copper loading effect," *Appl. Catal., B,* vol. 84, pp. 651-658, 2008.

[271] J. P. Espinós, J. Morales, A. Barranco, A. Caballero, J. P. Holgado, and A. R. González-Elipe, "Interface Effects for Cu, CuO, and Cu_2O Deposited on SiO_2 and ZrO_2. XPS Determination of the Valence State of Copper in Cu/SiO_2 and Cu/ZrO_2 Catalysts," *J. Phys. Chem. B,* vol. 106, pp. 6921-6929, 2002.

[272] Z. Liu, M. D. Amiridis, and Y. Chen, "Characterization of CuO Supported on Tetragonal ZrO_2 Catalysts for N_2O Decomposition to N_2," *J. Phys. Chem. B,* vol. 109, pp. 1251-1255, 2005.

[273] S. D. Jones, L. M. Neal, M. L. Everett, G. B. Hoflund, and H. E. Hagelin-Weaver, "Characterization of ZrO_2-promoted Cu/ZnO/nano-Al_2O_3 methanol steam reforming catalysts," *Appl. Surf. Sci.,* vol. 256, pp. 7345-7353, 2010.

[274] Y. Okamoto, K. Fukino, T. Imanaka, and S. Teranishi, "Surface characterization of copper(II) oxide-zinc oxide methanol-synthesis catalysts by x-ray photoelectron spectroscopy. 1. Precursor and calcined catalysts," *The Journal of Physical Chemistry,* vol. 87, pp. 3740-3747, 1983.

[275] G. Avgouropoulos and T. Ioannides, "TPD and TPSR study of CO interaction with CuO–CeO2 catalysts," *Journal of Molecular Catalysis A: Chemical,* vol. 296, pp. 47-53, 2008.

[276] O. Mihai, C. R. Widyastuti, S. Andonova, K. Kamasamudram, J. Li, S. Y. Joshi, *et al.*, "The effect of Cu-loading on different reactions involved in NH3-SCR over Cu-BEA catalysts," *Journal of Catalysis,* vol. 311, pp. 170-181, 2014.

[277] E.-Y. Choi, I.-S. Nam, and Y. G. Kim, "TPD Study of Mordenite-Type Zeolites for Selective Catalytic Reduction of NO by NH3," *Journal of Catalysis,* vol. 161, pp. 597-604, 1996.

[278] J. Słoczyński, R. Grabowski, A. Kozłowska, P. Olszewski, J. Stoch, J. Skrzypek, *et al.*, "Catalytic activity of the M/($3ZnO \cdot ZrO_2$) system (M=Cu, Ag, Au) in the hydrogenation of CO_2 to methanol," *Appl. Catal., A,* vol. 278, pp. 11-23, 2004.

[279] W. X. Pan, R. Cao, D. L. Roberts, and G. L. Griffin, "Methanol synthesis activity of CuZnO catalysts," *J. Catal.,* vol. 114, pp. 440-446, 1988.

[280] C. Baltes, S. Vukojević, and F. Schüth, "Correlations between synthesis, precursor, and catalyst structure and activity of a large set of CuO/ZnO/Al_2O_3 catalysts for methanol synthesis," *J. Catal.,* vol. 258, pp. 334-344, 2008.

[281] H. Ahouari, A. Soualah, A. Le Valant, L. Pinard, P. Magnoux, and Y. Pouilloux, "Methanol synthesis from CO_2 hydrogenation over copper based catalysts," *Reaction Kinetics, Mechanisms and Catalysis,* vol. 110, pp. 131-145, 2013.

[282] H. Berndt, V. Briehn, and S. Evert, "Reliability of pulse-chromatographic nitrous oxide titrations of the copper surface area on Cu-ZnO-MeOx catalysts in connection with the characterization of their thermostability," *Appl. Catal., A,* vol. 86, pp. 65-69, 1992.

[283] Q. Pan, J. Peng, T. Sun, S. Wang, and S. Wang, "Insight into the reaction route of CO_2 methanation: Promotion effect of medium basic sites," *Catal. Commun.,* vol. 45, pp. 74-78, 2014.

[284] B. Vahid, N. Saghatoleslami, H. Nayebzadeh, and A. Maskooki, "Preparation of Nano-Size Al-Promoted Sulfated Zirconia and the Impact of Calcination Temperature on Its Catalytic Activity," *Chem. Biochem. Eng. Q.*, vol. 26, pp. 71-77, 2012.

[285] F. Song, Y. Tan, H. Xie, Q. Zhang, and Y. Han, "Direct synthesis of dimethyl ether from biomass-derived syngas over Cu–ZnO–Al_2O_3–$ZrO_2(x)$/γ-Al_2O_3 bifunctional catalysts: Effect of Zr-loading," *Fuel Process. Technol.*, vol. 126, pp. 88-94, 2014.

[286] U. De La Torre, B. Pereda-Ayo, and J. R. González-Velasco, "Cu-zeolite NH3-SCR catalysts for NOx removal in the combined NSR–SCR technology," *Chem. Eng. J.*, vol. 207–208, pp. 10-17, 2012.

[287] C. Torre-Abreu, M. F. Ribeiro, C. Henriques, and G. Delahay, "Characterisation of CuMFI catalysts by temperature programmed desorption of NO and temperature programmed reduction. Effect of the zeolite Si/Al ratio and copper loading," *Appl. Catal., B*, vol. 12, pp. 249-262, 1997.

[288] R. Bulánek, B. Wichterlová, Z. Sobalík, and J. Tichý, "Reducibility and oxidation activity of Cu ions in zeolites: Effect of Cu ion coordination and zeolite framework composition," *Appl. Catal., B*, vol. 31, pp. 13-25, 2001.

[289] T. Nanba, S. Masukawa, J. Uchisawa, and A. Obuchi, "Characterization of Cu species on SiO_2 and ZSM-5 by temperature-programmed reduction by ammonia," *J. Therm. Anal. Calorim.*, vol. 113, pp. 793-802, 2013.

[290] G. Delahay, B. Coq, and L. Broussous, "Selective catalytic reduction of nitrogen monoxide by decane on copper-exchanged beta zeolites," *Appl. Catal., B*, vol. 12, pp. 49-59, 1997.

[291] S. Damyanova, P. Grange, and B. Delmon, "Surface Characterization of Zirconia-Coated Alumina and Silica Carriers," *J. Catal.*, vol. 168, pp. 421-430, 1997.

[292] S. Damyanova, L. Petrov, and P. Grange, "XPS characterization of zirconium-promoted CoMo hydrodesulfurization catalysts," *Appl. Catal., A*, vol. 239, pp. 241-252, 2003.

[293] C. C. Chusuei, M. A. Brookshier, and D. W. Goodman, "Correlation of Relative X-ray Photoelectron Spectroscopy Shake-up Intensity with CuO Particle Size," *Langmuir*, vol. 15, pp. 2806-2808, 1999.

[294] S. G. Botta, J. A. Navio, M. a. C. Hidalgo, G. M. Restrepo, and M. I. Litter, "Photocatalytic properties of ZrO_2 and Fe/ZrO_2 semiconductors prepared by a sol–gel technique," *Journal of Photochemistry and Photobiology A: Chemistry*, vol. 129, pp. 89-99, 1999.

[295] M. L. W. Victoria and J. S. Kevin, "The Effect of Calcination Temperature on the Properties and Hydrodeoxygenation Activity of Ni_2P Catalysts Prepared Using Citric Acid," in *Novel Materials for Catalysis and Fuels Processing*. vol. 1132, ed: American Chemical Society, 2013, pp. 287-300.

[296] P. Górska, A. Zaleska, E. Kowalska, T. Klimczuk, J. W. Sobczak, E. Skwarek, *et al.*, "TiO_2 photoactivity in vis and UV light: The influence of calcination temperature and surface properties," *Appl. Catal., B*, vol. 84, pp. 440-447, 2008.

[297] P. D. L. Mercera, J. G. van Ommen, E. B. M. Doesburg, A. J. Burggraaf, and J. R. H. Ross, "Zirconia as a support for catalysts Influence of additives on the thermal stability of the porous texture of monoclinic zirconia," *Appl. Catal.*, vol. 71, pp. 363-391, 1991.

[298] D. Y. Yoon, J.-H. Park, H.-C. Kang, P. S. Kim, I.-S. Nam, G. K. Yeo, *et al.*, "DeNOx performance of Ag/Al_2O_3 catalyst by n-dodecane: Effect of calcination temperature," *Appl. Catal., B,* vol. 101, pp. 275-282, 2011.

[299] A. Cybula, J. B. Priebe, M.-M. Pohl, J. W. Sobczak, M. Schneider, A. Zielińska-Jurek, *et al.*, "The effect of calcination temperature on structure and photocatalytic properties of Au/Pd nanoparticles supported on TiO_2," *Appl. Catal., B,* vol. 152–153, pp. 202-211, 2014.

[300] B. Valle, B. Aramburu, A. Remiro, J. Bilbao, and A. G. Gayubo, "Effect of calcination/reduction conditions of Ni/La_2O_3–αAl_2O_3 catalyst on its activity and stability for hydrogen production by steam reforming of raw bio-oil/ethanol," *Appl. Catal., B,* vol. 147, pp. 402-410, 2014.

[301] W. P. Dow and T. J. Huang, "Effects of Oxygen Vacancy of Yttria-Stabilized Zirconia Support on Carbon Monoxide Oxidation over Copper Catalyst," *J. Catal.,* vol. 147, pp. 322-332, 1994.

[302] C. D. Taboada, J. Batista, A. Pintar, and J. Levec, "Preparation, characterization and catalytic properties of carbon nanofiber-supported Pt, Pd, Ru monometallic particles in aqueous-phase reactions," *Appl. Catal., B,* vol. 89, pp. 375-382, 2009.

[303] J. A. Díaz, A. R. de la Osa, P. Sánchez, A. Romero, and J. L. Valverde, "Influence of CO_2 co-feeding on Fischer–Tropsch fuels production over carbon nanofibers supported cobalt catalyst," *Catal. Commun.,* vol. 44, pp. 57-61, 2014.

[304] X. Yao, Q. Yu, Z. Ji, Y. Lv, Y. Cao, C. Tang, *et al.*, "A comparative study of different doped metal cations on the reduction, adsorption and activity of CuO/$Ce_{0.67}M_{0.33}O_2$ (M=Zr^{4+}, Sn^{4+}, Ti^{4+}) catalysts for NO+CO reaction," *Appl. Catal., B,* vol. 130–131, pp. 293-304, 2013.

[305] C.-M. Hung, "The effect of the calcination temperature on the activity of Cu–La–Ce composite metal catalysts for the catalytic wet oxidation of ammonia solution," *Powder Technol.,* vol. 191, pp. 21-26, 2009.

[306] I. A. Fisher and A. T. Bell, "In Situ Infrared Study of Methanol Synthesis from H_2/CO over Cu/SiO_2 and Cu/ZrO_2/SiO_2," *J. Catal.,* vol. 178, pp. 153-173, 1998.

[307] K. Pokrovski, K. T. Jung, and A. T. Bell, "Investigation of CO and CO_2 Adsorption on Tetragonal and Monoclinic Zirconia," *Langmuir,* vol. 17, pp. 4297-4303, 2001.

[308] B. Bachiller-Baeza, I. Rodriguez-Ramos, and A. Guerrero-Ruiz, "Interaction of Carbon Dioxide with the Surface of Zirconia Polymorphs," *Langmuir,* vol. 14, pp. 3556-3564, 1998.

[309] N. T. Juan Li, Wei Song, Ensheng Zhan, Wenjie Shen, "Au/ZrO_2 catalysts for low-temperature water gas shift reaction: Influence of particle sizes," *Gold Bulletin,* vol. 42, pp. 48-60, 2009.

[310] K. T. K Basavaiah, N Rajendra Prasad, S G Hiriyanna, K B Vinay, "Determination of amoxycillin in pharmaceutical forms by visible spectrophotometry and HPLC," *Indian J. Chem. Technol.,* vol. 16, pp. 272-277, 2009.

[311] N. Li, G. A. Tompsett, T. Zhang, J. Shi, C. E. Wyman, and G. W. Huber, "Renewable gasoline from aqueous phase hydrodeoxygenation of aqueous sugar solutions prepared by hydrolysis of maple wood," *Green Chem.,* vol. 13, pp. 91-101, 2011.

[312] Z.-Y. Ma, C. Yang, W. Wei, W.-H. Li, and Y.-H. Sun, "Surface properties and CO adsorption on zirconia polymorphs," *J. Mol. Catal. A: Chem.*, vol. 227, pp. 119-124, 2005.

[313] Y. Zhao, W. Li, M. Zhang, and K. Tao, "A comparison of surface acidic features between tetragonal and monoclinic nanostructured zirconia," *Catal. Commun.*, vol. 3, pp. 239-245, 2002.

[314] T. Viinikainen, H. Rönkkönen, H. Bradshaw, H. Stephenson, S. Airaksinen, M. Reinikainen, *et al.*, "Acidic and basic surface sites of zirconia-based biomass gasification gas clean-up catalysts," *Appl. Catal., A,* vol. 362, pp. 169-177, 2009.

[315] D. Bianchi, T. Chafik, M. Khalfallah, and S. J. Teichner, "Intermediate species on zirconia supported methanol aerogel catalysts V. Adsorption of methanol," *Appl. Catal., A,* vol. 123, pp. 89-110, 1995.

[316] S. Natesakhawat, J. W. Lekse, J. P. Baltrus, P. R. Ohodnicki, B. H. Howard, X. Deng, *et al.*, "Active Sites and Structure–Activity Relationships of Copper-Based Catalysts for Carbon Dioxide Hydrogenation to Methanol," *ACS Catalysis,* vol. 2, pp. 1667-1676, 2012.

[317] R. A. Koeppel, A. Baiker, C. Schild, and A. Wokaun, "Effect of Preparation Variables on Catalytic Behaviour of Copper/Zirconia Catalysts for the Synthesis of Methanol from Carbon Dioxide," in *Stud. Surf. Sci. Catal.* vol. Volume 63, P. A. J. P. G. G. Poncelet and B. Delmon, Eds., ed: Elsevier, 1991, pp. 59-68.

[318] S. Bailey and K. C. Waugh, "Comment on the use of temperature-programmed desorption of H_2 as a tool to determine metal surface area of Cu catalysts," *Catal. Lett.*, vol. 17, pp. 371-374, 1993.

[319] M. N. S. C. Roma, D. S. Cunha, G. M. Cruz, and A. J. G. Cobo, "Effects of Cu over Pd based catalysts supported on silica or niobia," *Brazilian Journal of Chemical Engineering,* vol. 17, pp. 937-946, 2000.

[320] X.-m. Z. Gong-Xin Qi, Jin-hua Fei, Zhao-yin Hou, "Promoting efect of titanium on Cu/Ai_20_3 catalyst for CO_2 hydrogenation " *Indian journal of chemistry,* vol. 40A, pp. 588-593, 2001.

[321] V. P. X. Courtois, M. Primet, G. Bergeret, "Influence of small amounts of rhodium on the structure and the reducibility of Cu/Ai_20_3 and Cu/CeO_2-Ai_20_3 catalysts " *Stud. Surf. Sci. Catal.*, vol. 130, pp. 1031-1036, 2000.

[322] F. d. O. Cantão, W. d. C. Melo, L. C. A. Oliveira, A. R. Passos, and A. C. d. Silva, "Utilization of Sn/Nb_2O_5 composite for the removal of methylene blue," *Quim. Nova,* vol. 33, pp. 528-531, 2010.

[323] M. Ziolek, "Niobium-containing catalysts—the state of the art," *Catal. Today,* vol. 78, pp. 47-64, 2003.

[324] C. G. Alonso, A. C. Furtado, M. P. Cantao, O. A. A. Dos Santos, and N. R. C. Fernandes-Machado, "Reactions over Cu/Nb_2O_5 catalysts promoted with Pd and Ru during hydrogen production from ethanol," *Int. J. Hydrogen Energy,* vol. 34, pp. 3333-3341, 2009.

[325] S. Esposito, M. Turco, G. Bagnasco, C. Cammarano, P. Pernice, and A. Aronne, "Highly dispersed sol–gel synthesized Cu–ZrO_2 materials as catalysts for oxidative steam reforming of methanol," *Appl. Catal., A,* vol. 372, pp. 48-57, 2010.

[326] P. H. Matter, D. J. Braden, and U. S. Ozkan, "Steam reforming of methanol to H_2 over nonreduced Zr-containing CuO/ZnO catalysts," *J. Catal.*, vol. 223, pp. 340-351, 2004.

[327] L. C. Wang, Q. Liu, M. Chen, Y. M. Liu, Y. Cao, H. Y. He, *et al.*, "Structural evolution and catalytic properties of nanostructured Cu/ZrO_2 catalysts prepared by oxalate gel-coprecipitation technique," *J. Phys. Chem. C,* vol. 111, pp. 16549-16557, 2007.

[328] C. G. Alonso, A. C. Furtado, M. P. Cantão, O. A. Andreo dos Santos, and N. R. Camargo Fernandes-Machado, "Reactions over Cu/Nb_2O_5 catalysts promoted with Pd and Ru during hydrogen production from ethanol," *Int. J. Hydrogen Energy,* vol. 34, pp. 3333-3341, 2009.

[329] F. B. Noronha, M. Schmal, M. Primet, and R. Frety, "Characterization of palladium-copper bimetallic catalysts supported on silica and niobia," *Appl. Catal.*, vol. 78, pp. 125-139, 1991.

[330] M. P. Maia, M. A. Rodrigues, and F. B. Passos, "Nitrate catalytic reduction in water using niobia supported palladium–copper catalysts," *Catal. Today,* vol. 123, pp. 171-176, 2007.

[331] C. E. M. Guarido, D. V. Cesar, M. M. V. M. Souza, and M. Schmal, "Ethanol reforming and partial oxidation with Cu/Nb_2O_5 catalyst," *Catal. Today,* vol. 142, pp. 252-257, 2009.

[332] G. Zhang, X. Zou, J. Gong, F. He, H. Zhang, S. Ouyang, *et al.*, "Characterization and photocatalytic activity of Cu-doped $K_2Nb_4O_{11}$," *J. Mol. Catal. A: Chem.*, vol. 255, pp. 109-116, 2006.

[333] B. Yadav, R. Srivastava, S. Singh, A. Kumar, and A. Yadav, "Temperature Sensors based on Semiconducting Oxides: An Overview," *arXiv preprint arXiv:1205.2712,* 2012.

[334] Y. I. Pae and J. R. Sohn, "Effect of Al_2O_3 addition and WO_3 modification on catalytic activity of NiO/Al_2O_3-TiO_2/WO_3 for ethylene dimerization," *Bull. Korean Chem. Soc,* vol. 28, p. 1763, 2007.

[335] Y.-m. Zhu and L. Shi, "Zn promoted Cu–Al catalyst for hydrogenation of ethyl acetate to alcohol," *Journal of Industrial and Engineering Chemistry,* vol. 20, pp. 2341-2347, 2014.

[336] M. Liang, W. Kang, and K. Xie, "Comparison of reduction behavior of Fe_2O_3, ZnO and $ZnFe_2O_4$ by TPR technique," *Journal of Natural Gas Chemistry,* vol. 18, pp. 110-113, 2009.

[337] K.-S. Kim, H.-R. Seo, S. Lee, J.-G. Ahn, W. Shin, and Y.-K. Lee, "TPR and EXAFS Studies on Na-Promoted Co/ZnO Catalysts for Ethanol Steam Reforming," *Top. Catal.*, vol. 53, pp. 615-620, 2010.

[338] J. Agrell, M. Boutonnet, I. Melián-Cabrera, and J. L. G. Fierro, "Production of hydrogen from methanol over binary Cu/ZnO catalysts: Part I. Catalyst preparation and characterisation," *Appl. Catal., A,* vol. 253, pp. 201-211, 2003.

[339] A. Peled, B. Dragnea, R. Alexandrescu, and A. Andrei, "Laser-induced photodeposition from ZnS colloid solutions," *Appl. Surf. Sci.*, vol. 86, pp. 538-542, 1995.

[340] Shabnam, C. R. Kant, and P. Arun, "Size and defect related broadening of photoluminescence spectra in ZnO:Si nanocomposite films," *Mater. Res. Bull.*, vol. 47, pp. 901-906, 2012.

[341] T. Witoon, T. Permsirivanich, W. Donphai, A. Jaree, and M. Chareonpanich, "CO_2 hydrogenation to methanol over Cu/ZnO nanocatalysts prepared via a chitosan-assisted co-precipitation method," *Fuel Process. Technol.*, vol. 116, pp. 72-78, 2013.

[342] Y. Nitta, T. Fujimatsu, Y. Okamoto, and T. Imanaka, "Effect of starting salt on catalytic behaviour of Cu-ZrO_2 catalysts in methanol synthesis from carbon dioxide," *Catal. Lett.*, vol. 17, pp. 157-165, 1993.

[343] L. Fan and K. Fujimoto, "Development of an active and stable ceria-supported palladium catalyst for hydrogenation of carbon dioxide to methanol," *Appl. Catal., A*, vol. 106, pp. L1-L7, 1993.

[344] L. Fan and K. Fujimoto, "Hydrogenation of Carbon Dioxide to Methanol by Titania-Supported Palladium Catalyst: Promotive SMSI Effect," *Bull. Chem. Soc. Jpn.*, vol. 67, pp. 1773-1776, 1994.

[345] C. Shao, L. Fan, K. Fujimoto, and Y. Iwasawa, "Selective methanol synthesis from CO_2/H_2 on new SiO_2-supported PtW and PtCr bimetallic catalysts," *Appl. Catal., A*, vol. 128, pp. L1-L6, 1995.

[346] H. Sakurai and M. Haruta, "Synergism in methanol synthesis from carbon dioxide over gold catalysts supported on metal oxides," *Catal. Today*, vol. 29, pp. 361-365, 1996.

[347] X. Jiang, N. Koizumi, X. Guo, and C. Song, "Bimetallic Pd–Cu catalysts for selective CO_2 hydrogenation to methanol," *Appl. Catal., B*, vol. 170–171, pp. 173-185, 2015.

[348] H. Ren, C.-H. Xu, H.-Y. Zhao, Y.-X. Wang, J. Liu, and J.-Y. Liu, "Methanol synthesis from CO_2 hydrogenation over Cu/γ-Al_2O_3 catalysts modified by ZnO, ZrO_2 and MgO," *Journal of Industrial and Engineering Chemistry*.

[349] L. Angelo, K. Kobl, L. M. M. Tejada, Y. Zimmermann, K. Parkhomenko, and A.-C. Roger, "Study of CuZnMOx oxides (M=Al, Zr, Ce, CeZr) for the catalytic hydrogenation of CO_2 into methanol," *Comptes Rendus Chimie*, vol. 18, pp. 250-260, 2015.

[350] P. Gao, F. Li, H. Zhan, N. Zhao, F. Xiao, W. Wei, *et al.*, "Fluorine-modified Cu/Zn/Al/Zr catalysts via hydrotalcite-like precursors for CO_2 hydrogenation to methanol," *Catal. Commun.*, vol. 50, pp. 78-82, 2014.

[351] H. Lei, R. Nie, G. Wu, and Z. Hou, "Hydrogenation of CO_2 to CH_3OH over Cu/ZnO catalysts with different ZnO morphology," *Fuel*.

[352] A. Le Valant, C. Comminges, C. Tisseraud, C. Canaff, L. Pinard, and Y. Pouilloux, "The Cu–ZnO synergy in methanol synthesis from CO_2, Part 1: Origin of active site explained by experimental studies and a sphere contact quantification model on Cu+ZnO mechanical mixtures," *J. Catal.*, vol. 324, pp. 41-49, 2015.

[353] P. Gao, R. Xie, H. Wang, L. Zhong, L. Xia, Z. Zhang, *et al.*, "Cu/Zn/Al/Zr catalysts via phase-pure hydrotalcite-like compounds for methanol synthesis from carbon dioxide," *Journal of CO2 Utilization*, 2015.

[354] M. J. Bos and D. W. F. Brilman, "A novel condensation reactor for efficient CO_2 to methanol conversion for storage of renewable electric energy," *Chem. Eng. J.*, 2014.

[355] P. B. Sanguineti, M. A. Baltanás, and A. L. Bonivardi, "Copper–gallia interaction in Cu–Ga_2O_3–ZrO_2 catalysts for methanol production from carbon oxide(s) hydrogenation," *Appl. Catal., A*, 2014.

[356] W. Yuefa, "Activity of Catalyst for Liquid Phase Methanol Synthesis," *Chin. J. Chem. Eng.,* vol. 10, pp. 63-69, 2002.

[357] Y. N. Junwang Guo, Bijiang Zhang, "Global kinetics study of LPDME process from syngas,"
Journal of Energy Chemistry vol. 9, pp. 331-342, 2000.

[358] G. H. Graaf, P. J. J. M. Sijtsema, E. J. Stamhuis, and G. E. H. Joosten, "Chemical equilibria in methanol synthesis," *Chem. Eng. Sci.,* vol. 41, pp. 2883-2890, 1986.

[359] I. Melián-Cabrera, M. López Granados, and J. L. G. Fierro, "Reverse Topotactic Transformation of a Cu–Zn–Al Catalyst during Wet Pd Impregnation: Relevance for the Performance in Methanol Synthesis from CO_2/H_2 Mixtures," *J. Catal.,* vol. 210, pp. 273-284, 2002.

[360] Y. Amini, M. Fattahi, F. Khorasheh, and S. Sahebdelfar, "Neural network modeling the effect of oxygenate additives on the performance of Pt–Sn/γ-Al_2O_3 catalyst in propane dehydrogenation," *Applied Petrochemical Research,* vol. 3, pp. 47-54, 2013.

LIST OF PUBLICATIONS

Journal Papers

1. Israf Ud Din, Maizatul S. Shaharun, Duvvuri Subbarao, A. Naeem. Synthesis, characterization and activity pattern of carbon nanofibers based copper/zirconia catalysts for carbon dioxide hydrogenation to methanol: Influence of calcination temperature. Journal of power sources. 274 (2015), Pages 619–628

2. Israf Ud Din, Maizatul S. Shaharun, Duvvuri Subbarao, A. Naeem. Zinc Ferrite Nanoparticle Synthesis and Characterization; Effects of Annealing Temperature on the Size of nanoparticles. *Australian Journal of Basic and Applied Sciences*, 7(4): 154-162, 2013

3. Israf Ud Din, Maizatul S. Shaharun, Duvvuri Subbarao, A. Naeem. Homogeneous deposition precipitation method for synthesis of carbon nanofibers based Cu/ZrO_2 catalyst for hydrogenation of CO_2 to methanol. *Applied Mechanics and Materials*. Vols 446 – 447 (2014) pp 83-87

4. Israf Ud Din, Maizatul S. Shaharun, Duvvuri Subbarao, A. Naeem. Synthesis, characterization and activity pattern of carbon nanofibres based Cu/ZrO_2 catalyst in the hydrogenation of carbon dioxide to methanol. *Advanced Materials Research* Vol. 925 (2014) pp 349-353

5. Israf Ud Din, Maizatul S. Shaharun, Duvvuri Subbarao, A. Naeem. Wet chemical route for the synthesis of nickel ferrite nanoparticles, Journal of *Synthesis and Reactivity in Inorganic, Metal-Organic, and Nano-Metal Chemistry* **(In Press)**

Conference Papers

6. Development of Carbon Nanofiber Supported Cu/ZrO2 Catalyst for the Hydrogenation of CO_2 to Methanol. Postgraduate Colloquium for Environmental Research 2013 (POCER 2013), *Malaysia*

7. Synthesis, characterization and activity pattern of carbon nanofibre based Cu/ ZrO_2 catalyst in the hydrogenation of carbon dioxide to methanol. Joint International Conference on Nanoscience, Engineering and Management (BOND21), *Malaysia*

8. Homogeneous deposition precipitation method for synthesis of carbon nanofibers based Cu/ZrO2 catalyst for hydrogenation of CO_2 to methanol. 2013 3rd International Conference on Nanomaterials and Electronics Engineering - ICNEE 2013, *Malaysia*

9. Physicochemical Properties of Carbon nanofibers Supported Cu/ZrO_2 Catalyst.3rd International Conference on Fundamental and Applied Sciences (ICFAS 2014), *Malaysia*

10. The 1st International symposium on catalytic science and technology in sustainable energy and environment (EECAT 2014), *China*

APPENDIX A

CATALYST PREPARATION CALCULATIONS

- Preparation of 15CZC catalysts (15 wt.% Cu, 15 wt.% ZrO_2 and 70 wt.% CNFs-O)

Total amount of catalysts was 4.28 grams with 3 grams of oxidized CNFs. Concentration of both active components are 15 wt.% each.

Section A1: Calculation for Cu component,

$$Amount\ of\ Cu = \frac{total\ weight\ of\ catalyst\ X\ wt\%Cu}{100}$$

$$Amount\ of\ Cu = \frac{4.28\ X\ 15}{100}$$

$$Amount\ of\ Cu = 0.64$$

Then weight of the precursor $Cu(NO_3)_2.6H_2O$

$$weight\ of\ the\ precursor\ = \frac{Molecular\ wt\ of\ precursort\ X\ wt\ of\ Cu}{atomic\ wt\ of\ Cu}$$

$$weight\ of\ the\ precursor\ = \frac{241.6\ X\ 0.64}{63}$$

$$weight\ of\ the\ precursor\ = 2.46\ grams$$

Similarly for zirconia component,

Total amount of catalysts was 4.28 grams with 15 wt.% ZrO_2 loading.

$$Amount\ of\ ZrO_2 = \frac{total\ weight\ of\ catalyst\ X\ wt.\%\ ZrO_2}{100}$$

$$Amount\ of\ ZrO_2 = \frac{4.28\ X\ 15}{100}$$

$$Amount\ of\ ZrO_2 = 0.64$$

Then weight of the precursor Zirconyl nitrate hydrate ($ZrO(NO_3)_2.H_2O$)

$$weight\ of\ the\ precursor\ = \frac{Molecular\ wt\ of\ precursort\ X\ wt\ of\ ZrO_2}{molecular\ wt\ of\ ZrO_2}$$

$$weight\ of\ the\ precursor\ = \frac{231.23\ X\ 0.64}{123}$$

$$weight\ of\ the\ precursor\ = 1.20$$

So 2.46 grams of $Cu(NO_3)_2.6H_2O$, 1.20 grams of ($ZrO(NO_3)_2.H_2O$) and 3 grams of oxidized CNFs were weighted for synthesis of CZC catalysts with 15 wt.% content of Cu and zirconia.

Section A2. Metal concentration calculations

Prior to metal concentration analysis, the instrument was calibrated with the known concentrations of Cu metal. The calibration curve for five different concentrations of Cu (5, 10, 15, 20, 25 and 30 mg/l) is displayed as below.

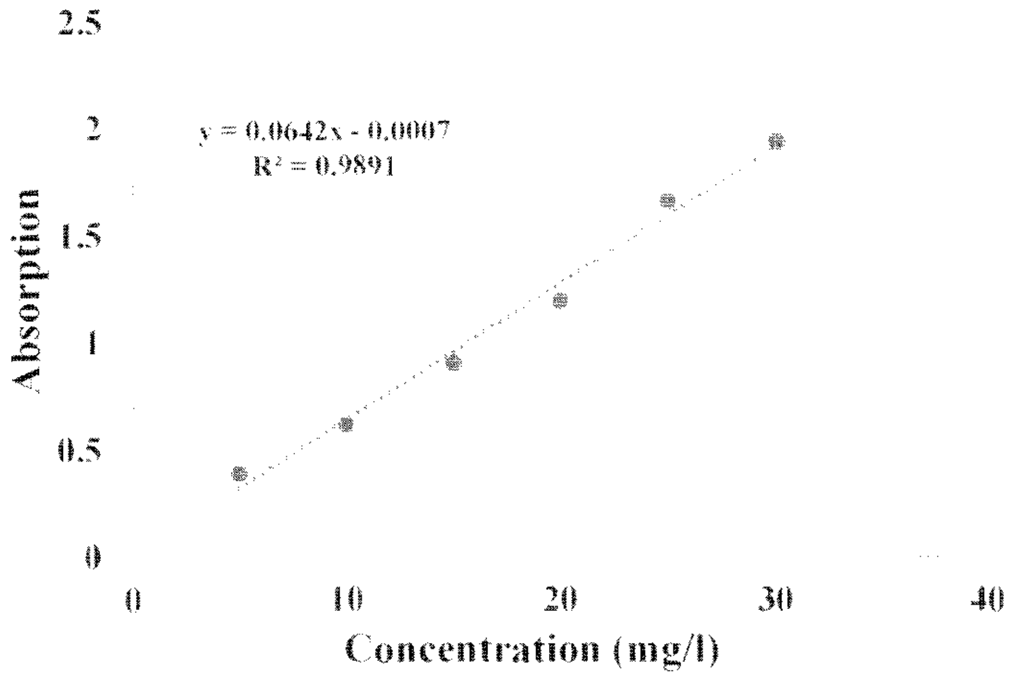

Concentration of metal was calculated from above equation as in the following example.

A 30 mg of sample (CZC15) was digested in total 50 ml of aqua ragia solution. The solution was cooled and diluted to total volume of 250 ml with distilled water. This diluted sample was used for analysis. Absorbance intensity of 1.2 was measured for the sample. The concentration (mg/l) of Cu was calculated from equation.

$$x = \frac{(1.2+0.0007)}{0.0642} = 18\, mg/l$$

Percentage of Cu was calculated as

$$\%\, Cu = (conc\left(\frac{mg}{l}\right) \times DF \times \frac{100}{1000 \times wt\ of\ sample\ (mg)}$$

So, in this case

$$\%\, Cu = 18 \times 250 \times \frac{100}{1000 \times 30}$$
$$= 15$$

APPENDIX B
REACTOR SYSTEM

Section B1: Description and Specification of slurry reactor are as follow

- Parr (Model 4593) moveable reactor
- Total vessel capacity = 100 mL

Other specifications:

Max pressure: 3000 PSI (200 bar)

- Max temperature: 350 °C with PTFE gasket
- Maximum torque: 16 in-lbs
- Impeller, 4 blade: One
- Material of vessel construction: T316 stainless steel
- Variable speed motor, 1/8 HP
- 3000 PSI pressure gauge with rupture disc
- For 230VAC 50Hz one phase power
- ASME vessel safety (pressure) safety certification
- 4848 standalone PID reactor controller with only temperature display

Section B2: Standard operating procedure of slurry reactor

The standard operating procedure of the slurry reactor is given as below.

- First 25 ml of ethanol (reaction solvent) were placed in reactor vessel
- A 0.5 g of reduced sample was suspended in reaction solvent
- The reactor was purged with reactant gases at room temperature to remove any air or other gases
- Reactor was pressurized with reactant gases (mixture of H_2/CO_2 gases with 3:1) to 30 bar
- Reaction temperature was raised to 180 °C
- Catalytic hydrogenation of CO_2 to methanol was carried out for 2 hours
- Liquid samples were collected from liquid sample valve while gases samples were collected from gas sampling valve

- Liquid and gas products were analyzed by flame ionization detector (FID) and thermal conductivity detector (TCD) respectively.

Table B1. Products and their retention time

Serial #	Compound	Retention time	Signal
01	Carbon dioxide	3.428	TCD
02	Methanol	1.511	FID
03	Ethanol	1.616	FID
04	Hydrogen	4.582	TCD
05	Hexane	2.112	FID
06	Ethane	3.409	FID
07	Methane	5.208	TCD
08	Carbon monoxide	5.598	TCD

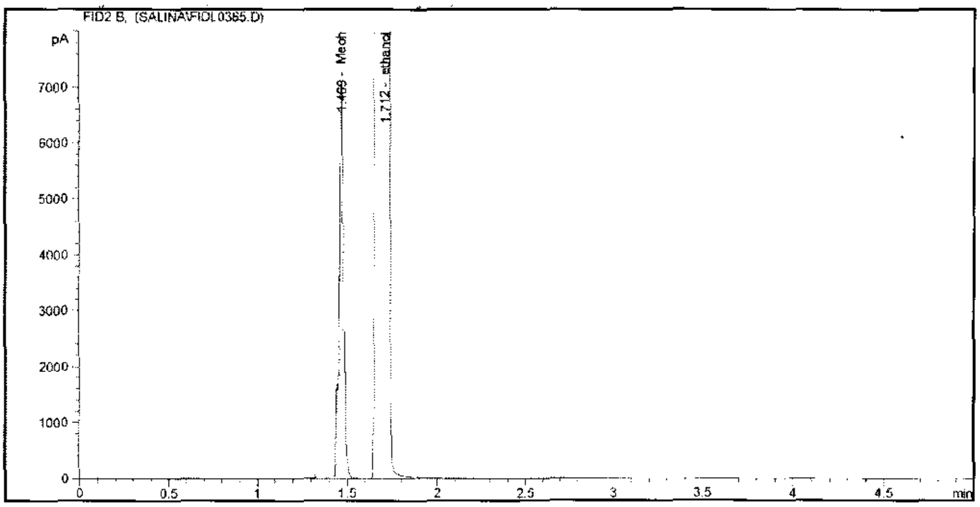

```
RetTime  Type     Area        Amt/Area      Amount    Grp   Name
 [min]           [pA*s]                      [%]
-------|------|----------|----------|----------|--|-----------------
  1.469 PB S   1.18379e4  4.12858e-4    4.88736      MeoH
  1.712 BB S   4.48592e5  2.30175e-4  103.25224      ethanol

Totals :                              108.13960

 Results obtained with enhanced integrator.
================================================================
                     *** End of Report ***
```

Figure B1: Chromatogram of methanol standard and FID detector

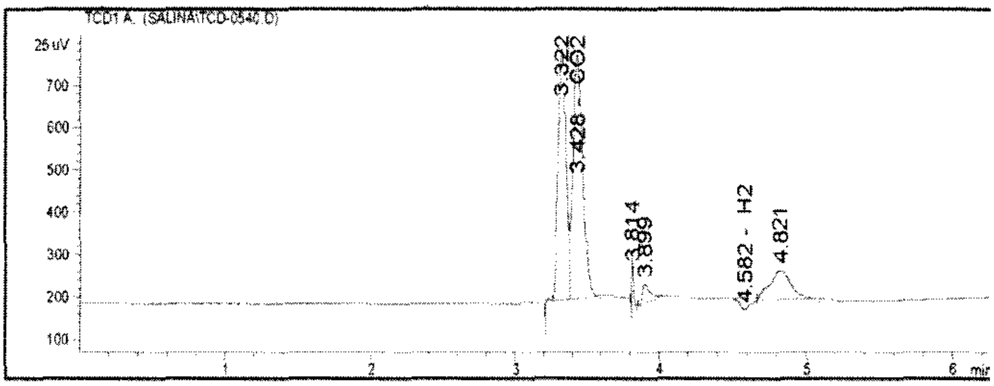

```
RetTime  Type     Area        Amt/Area      Amount    Grp   Name
 [min]          [25 uV*s]                    [%]
-------|------|----------|----------|----------|--|-----------------
  3.426 VB    2635.43626  7.62601e-3   20.09787      CO2
  4.582 BP N   117.16738  6.64081e-1   77.82193      H2
  5.208            -           -           -         CH4
  5.598            -           -           -         CO

Totals :                               97.91980
```

Figure B2: Chromatogram of GC calibration using CO_2 and H_2 gas mixture

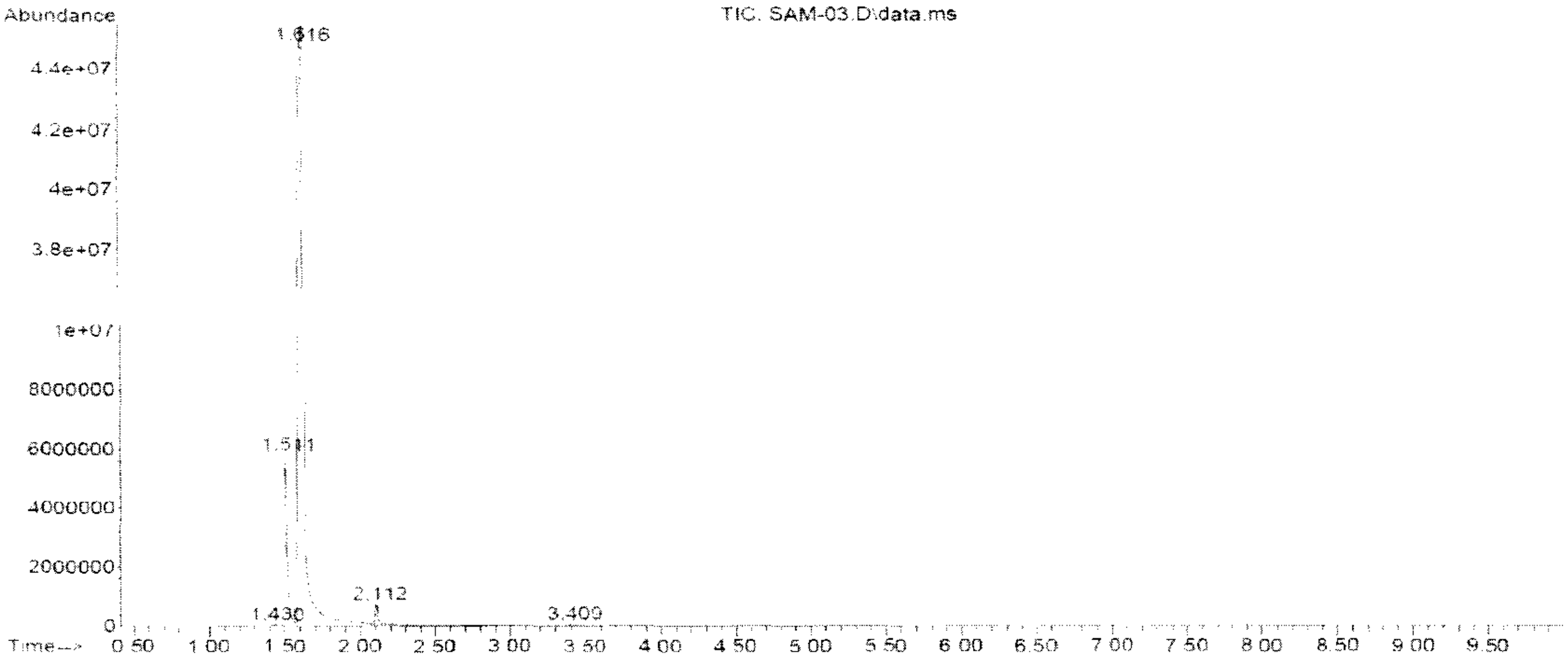

Peak	R.Time	Comp. Name	First Scan	Max. Scan	Last Scan	Peak Height	Corre. Height	% Total
1	1.43	Carbon dioxide	177	208	212	53800	464991	0.00037
2	1.511	Methanol	212	220	231	5535219	72939072	0.05734
3	1.616	Ethanol	231	236	308	2	45090620	1
4	2.112	Hexane	308	313	395	726985	16515194	0.01298
5	3.409	Ethane	490	513	544	60356	1141417	0.0009

Figure B3: GCMS chromatogram of reaction product

APPENDIX C

SUPLEMENTRAY DATA

Table C1: Standard Gibbs free energy of different molecules

Molecule	**Standard Gibbs free energy, ΔG° (kJ/mol)**
CO	-137
CO_2	-394
H_2	0
H_2O	-228
CH_3OH	-162

$$CO + 2H_2 \leftrightarrow CH_3OH \qquad \Delta H^0{}_{298K} = -90.84kJ/mol \qquad (1)$$

$$CO_2 + 3H_2 \leftrightarrow CH_3OH + H_2O \qquad \Delta H^0{}_{298K} = -49.5kJ/mol \qquad (2)$$

ΔG^0 for reaction [1]

$$\Delta G^0 = \Sigma n_p G^O{}_{product} - \Sigma n_r G^O{}_{reactants}$$

$$\Delta G^0 = [1(-162.3)] - [1(-137.1) + 2(0)] = -25.2kJ$$

Equilibrium constant, K for reaction [1]

$$\Delta G^0 = -RTln(K)$$

$$ln(K) = -\Delta G^0/RT$$

$$ln(K) = -\frac{\left(-\frac{25200J}{mol}\right)}{(8.314J mol.K)(298K)} = 10.17$$

$$K = e^{10.17} = 26.14$$

$$K > 1$$

ΔG^0 for reaction [2]

$$\Delta G^0 = \Sigma n_p G^O{}_{product} - \Sigma n_r G^O{}_{reactants}$$

$$\Delta G^0 = [1(-162.3)] - [1(-394.4) + 3(0)] = 232.1kJ$$

Equilibrium constant, K for reaction [1]

$$\Delta G^0 = -RTln(K)$$

$$ln(K) = -\Delta G^0/RT$$

$$ln(K) = -\frac{\left(\frac{232100J}{mol}\right)}{(8.314J mol.K)(298K)} = -93.68$$

$$K = e^{-93.68} = 2.07 \times 10^{-41}$$

$$K < 1$$

Section C1: Cu surface area (S_{Cu}) calculations by N_2O titration method

The following formula was used for S_{Cu} determination.

$$S_{Cu}(m^2/g) = (nCu \times N)/(1.4 \times 10^{19} \times W)$$

Where S_{Cu} is the exposed copper surface area per gram catalyst, W is the weight of the reduced catalyst, n_{Cu} is the number of moles of copper, N is Avogadro's constant

(6.02×10^{23} atoms mol^{-1}), and 1.4×10^{19} is the number of copper atoms per square meter.

The amount of H_2 adsorbed for CZC catalyst was recorded as 187 μmoles/g.cat. So according to stoichiometry ratio number of moles of Cu will be 187 x 2 = 374 μmoles/g.cat. Putting these values in above equation we get.

$$S_{Cu}(m^2/g) = (0.000374 \times 6.02 \times 10^{23})/(1.4 \times 10^{19} \times 1)$$

$$S_{Cu}(m^2/g) = 15.4$$

Section C2: Calculation of CO_2 concentration

According to ideal gas equation

PV=nRT

where P is pressure of gas in atomsphere, V is the volume in Liters, n is the number of moles of gas, R is gas constant (0.0821) and T is the temperature in Kelvin

Rearranging this equation we get

n =PV/RT

Total volume of reaction vessel is 100 ml. 25 ml of ethanol was present in the cell so the net volume of gase is 75 ml. Temperature and pressure of the gas were recorded as 180 °C and 30 bar, respectively. As feed gas was used in ratio of H_2/CO_2 = 3:1, therefore partial pressure of CO_2 was found to be 1/4*30= 7.5 bar, equavalent to 7.4 atom.

Putting the valusc in equation we get

n= 7.4*.075/0.0821*453

n= 0.015 moles

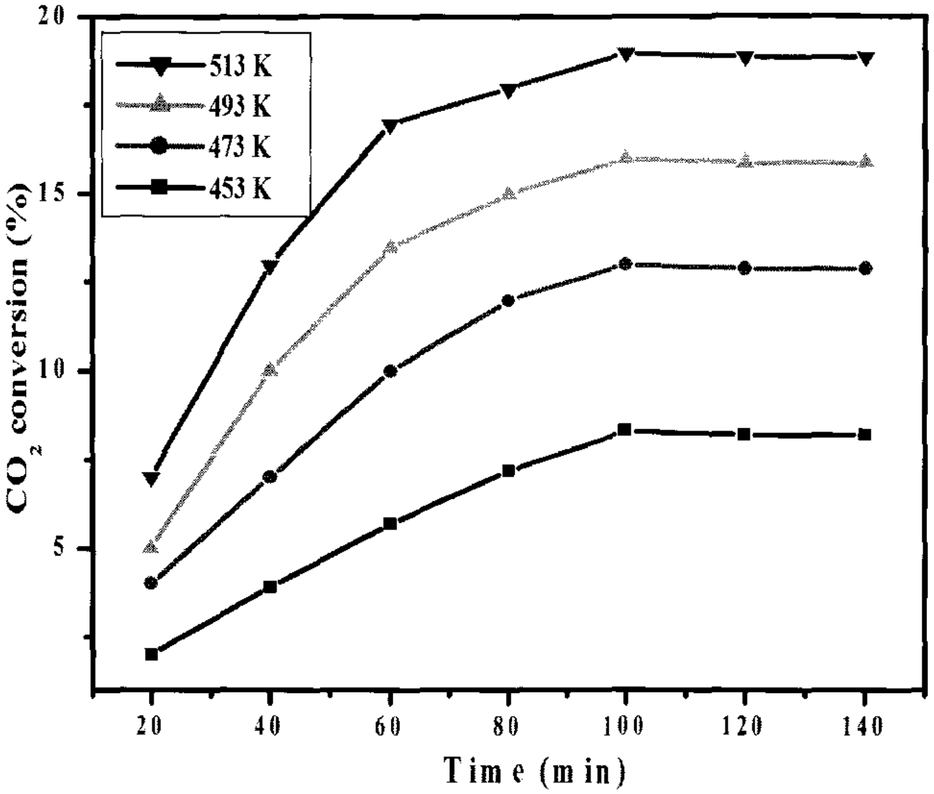

Figure C1: CO_2 conversion versus time at different reaction temperature.

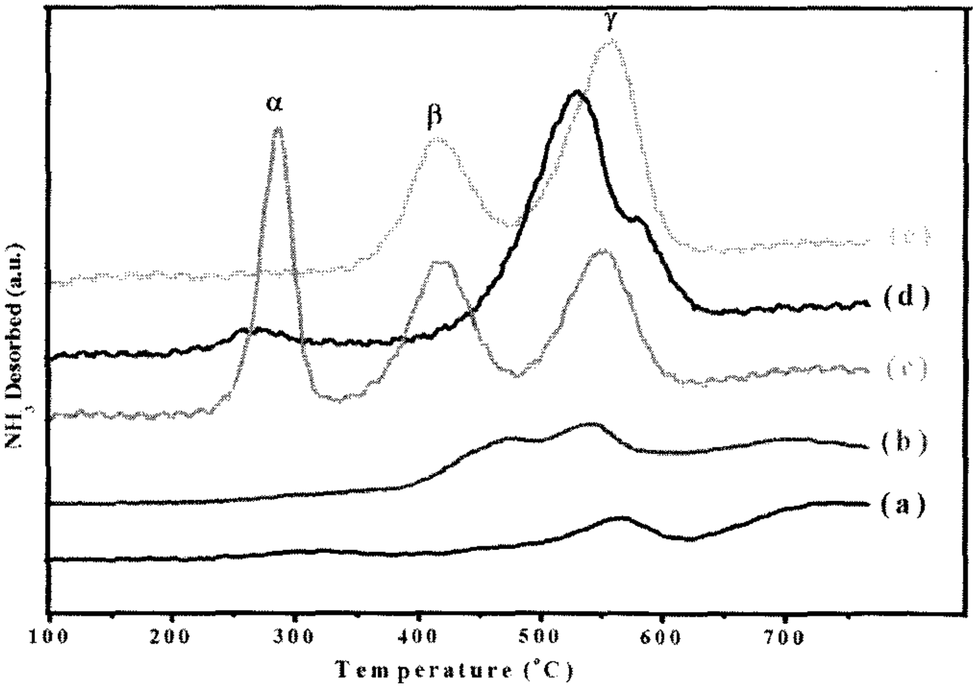

Figure C2: TPD-NH_3 profile of (a) CZC5, (b) CZC10, (c) CZC15, (d) CZC20 and (e) CZC25 catalysts

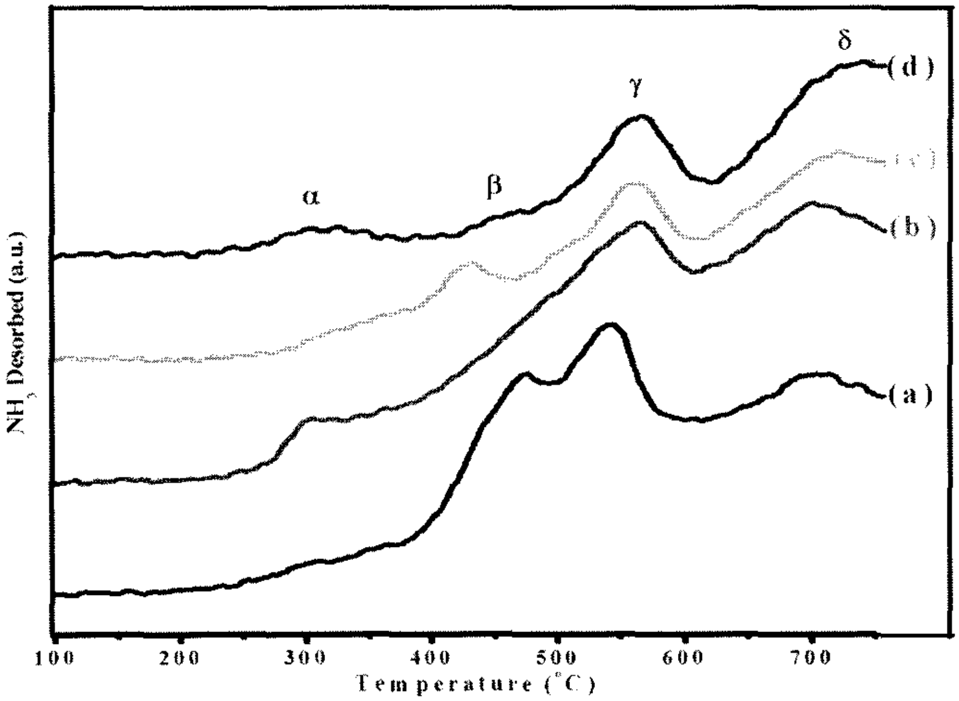

Figure C3: NH_3-TPD profiles of (a) CZC350, (B) CZC450, (C) CZC500 and (d) CZC550 catalysts

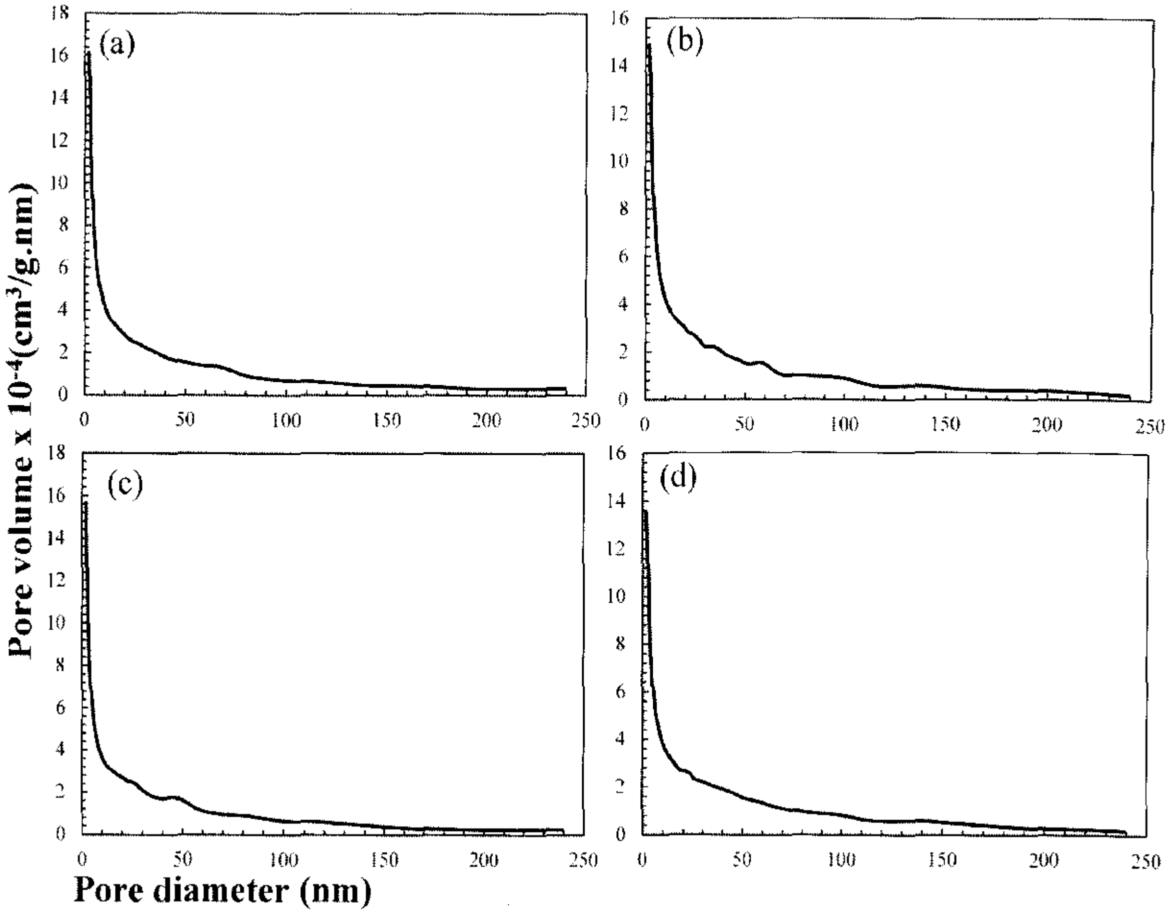

Figure C4: Pore size distribution of (a) CZCZ1, (b) CZCZ2, (c) CZCZ3 and (d) CZCZ4 catalysts